Master's thesis

NTNU
Norwegian University of Science and Technology
Faculty of Engineering
Department of Marine Technology

Vishnu Ramachandran Nair Rajasree

Transverse Viscous Loads in Maneuvering

Master's thesis in Marine Technology
Supervisor: Trygve Kristiansen
June 2022

NTNU
Norwegian University of
Science and Technology

Vishnu Ramachandran Nair Rajasree

Transverse Viscous Loads in Maneuvering

Master's thesis in Marine Technology
Supervisor: Trygve Kristiansen
June 2022

Norwegian University of Science and Technology
Faculty of Engineering
Department of Marine Technology

NTNU
Norwegian University of
Science and Technology

Preface

This master thesis was written as the concluding work for obtaining the degree of Master of Science in Marine Technology. This work was conducted in the Department of Marine Technology of the Norwegian University of Science and Technology (NTNU) in Trondheim, Norway in the spring of 2022.

The topic of this thesis is to improve the transverse viscous loads calculation in maneuvering of ships and is a continuation of the specialisation project carried out in autumn of 2021. The motivation to choose this topic is because only a limited number of experimental or numerical studies have been carried to determine the transient drag coefficient for ship shaped sections and due to the uncertainty regarding the unsteady drag coefficient curves in the literature.

This thesis was work was supervised by Professor Trygve Kristiansen. I am very thankful for the his guidance and support during this thesis. The guidance meetings during this thesis was very useful to keep on-track during this work. I would also like to thank PhD candidate Øyvind Rabliås for providing the python code for simulation. I am also grateful to the engineers at the Laddertanken Laboratory, NTNU, for helping with the model preparation and test setup. Finally, I would like to thank my family and friends for their support during this master's degree.

The reader is expected to have basic understanding of marine hydrodynamics.

Abstract

The main objective of the thesis is to improve the estimation of transverse viscous loads in ship maneuvering. The traditional approach for calculating the transverse viscous loads in most of the maneuvering models is based on empirical methods. 2D+t methods offer a rational method for estimating these loads. A basic input necessary for applying 2D+t method is the transient drag coefficient curves. Hence, as a part of the thesis work, both an experimental and numerical approach is made to obtain the sectional transient drag coefficients of ship-shaped sections. Finally, these are used in a two-time scale maneuvering code to simulate turning circle maneuvers of KCS and DTC vessel and the result is compared against available experimental data.

Contents

List of Tables

List of Figures

Glossary

List of abbreviation

2D	2 Dimensional
3D	3 Dimensional
BVP	Boundary Value Problem
BWD	Backward direction
CFD	Computational fluid dynamics
CMT	Circular Motion Tests
CNC	Computer Numerical Control
DNS	Direct Numerical Simulation
DTC	Duisburg Test Case
EEDI	Energy Efficiency Design Index
EMD	Empirical Mode Decomposition
FWD	Forward direction
HF	High-frequency

IMF	Intrinsic Mode Function
IMO	International Maritime Organization
KCS	Korea Research Institute for Ships and Ocean Engineering Container Ship
KRISO	Korea Research Institute for Ships and Ocean Engineering
LES	Large Eddy Simulations
LF	Low-frequency
MEPC	Marine Environment Protection Committee
MMG	Maneuvering Modeling Group
PMM	Planar Motion Mechanism
RANS	Reynolds-averaged Navier–Stokes
RAO	Response Amplitude Operator
RPS	Revolutions Per Second
SHOPERA	Energy Efficient Safe SHip OPERAtions
SINTEF	The Foundation for Scientific and Industrial Research
STF	Salvesen Tuck Faltinsen
TEU	Twenty-foot equivalent unit

Commonly applied symbols

K_{CF}	Roll moment due to flow separation
N_{CF}	Yaw moment due to flow separation
α	Angle of attack

β	Drift angle, defined as the angle made by the velocity vector with the x_c axis.
β_0	Wave heading angle
β_r	Drift angle
δ	Rudder angle
η_0	Open water efficiency
Λ	Rudder aspect ratio
μ_D	Drifting angle, the offset angle between the wave direction and the line defined by the ship position at which the wave encounter angle is 90 deg. is defined as the drift angle.
$\overline{C_D}$	Mean drag coefficient
$\overline{R}_x, \overline{R}_y\ \overline{N}$	Mean second order wave forces and moment
ϕ	Velocity potential
ψ	Heading angle, defined as the angle between x_c and X_E axes.
ρ	Density of water
a_p	Peak acceleration
A_R	Rudder area
a_x	Acceleration in x-direction
a_x^{acc}	Acceleration directly obtained from the accelerometer without any corrections
a_x^{dry}	Acceleration in x-direction calculated from the carriage speed
a_x^{wet}	Acceleration in x-direction calculated from the carriage speed
C_D	Drag coefficient

C_{D0}	Coefficient for rudder surface friction
C_L	Lift coefficient
C_M	Inertial coefficient
C_Q	Resistance coefficient
C_T	Thrust in non-dimensional form
C_{for}	Force coefficient
D	Drag force
D_p	Propeller diameter
F_c	Correction force to be applied on the force recorded by the force transducer
f_v	Vortex shedding frequency
F_x^{dry}	Force on the model as recorded by the force transducer when the model is towed with the tank empty
F_x^{wet}	Force on the model as recorded by the force transducer when the model is towed in water
F_{drag}	Drag force in the x-direction
F_{hyd}	Force in x-direction due to difference in water level on the upstream and downstream side of the model considering only the hydro-static pressure
F_x	Total force measured in x-direction
Fn	Froude number
g	Acceleration due to gravity
H	Value of the parameter after 20% reduction
h	Water height difference between the upstream and downstream side of the model

H^*	Original value of the parameter
H_D	Drifting distance, defined as the distance between consecutive positions of the ship at which the wave encounter angle is 90 deg.
h_d	Water level height from base of the model
h_{sub}	Submerged length of model
h_{tank}	Water height in the tank
j	Advance coefficient
K_R	Roll moment due to rudder
K_T	Open water thrust coefficient
L	Lift force
L_{PP}	Length between perpendiculars
m	Mass of the model
m_a	Added mass of the model
n	RPS
N_r	Hydrodynamic derivative
N_v	First order hydrodynamic derivative
R	Value of the maneuvering index after 20% reduction in the parameter
r	Bilge radius, Yaw velocity of the vessel
R^*	Original value of the maneuvering index
R_T	Calm water resistance
Rn	Reynolds Number

S	Sensitivity index
St	Strouhal number
T	Thrust, Characteristic length of the model
t_f	Time at which velocity at the inlet at both top and bottom corner is equal to v
u_a	Velocity of advance
u_{RS}	Longitudinal component of the mean inflow velocity to the rudder
v	Inlet velocity
v_∞	Final free stream velocity
v_c	Carriage speed
v_m	Initial flow velocity at the bottom point of the inlet boundary patch
v_{RS}	Transversal component of the mean inflow velocity to the rudder
w	Wake fraction
w_{tank}	Width of the tank
x_r	Location of the rudder
X_{PROP}	Propeller force in the longitudinal direction
Y_R	Positive sway rudder force
Y_{CF}	Sway force due to flow separation
z	Direction perpendicular to the free surface
B	Breadth
C_{th}	Thrust loading coefficient
GM	Metacentric height

KG	Height of the center of gravity above the ship keel
Lpp	Length between perpendiculars
R	Radius of the cylinder
s	Speed of the flow
t	Time, Thrust deduction factor
t_0	Instant at which flow separation start
U	Ship speed

Chapter 1

Introduction

1.1 Background and Motivation

Traditionally, the study of ship dynamics is divided into two fields: maneuvering and seakeeping. As discussed in Abkowitz (1964), maneuvering deals with motion of the ship in the horizontal plane due to the action of control surfaces in the absence of excitation from the sea, whereas seakeeping deals with the motion of the vessel due to excitation forces from the sea. Comparison of the approaches in the two fields is presented in Table 1.1.

The traditional assessment of the maneuvering capability of ships is performed in calm and deep water using 3 degree of freedom (surge-sway-yaw) models (ITTC 2021b). These assessments assume negligible influence of ship motions and external sea conditions such as wave, wind, current, and water depth on the maneuvering capability of the vessel. However, real navigation conditions involve an overlap of maneuvering and seakeeping fields, hence a theory intended to describe the motions of the vessel in seaway needs to combine the seakeeping and maneuvering theories.

Combining the seakeeping and maneuvering theories is very challenging due to the difference in the nature of hydrodynamic forces which is involved (Schoop-Zipfel 2017). Viscosity plays a major role in the maneuvering forces. 'Slow motion' derivatives are used to describe this effect. These derivatives are derived using model testing and are evaluated at zero frequency. In seakeeping, the viscous forces can be ignored and frequency dependent coefficients obtained using potential flow theory are used to describe the relevant forces.

Over the past decade, there has been an increasing interest in developing models

	Maneuvering	Seakeeping
Environment	Calm water	Seaway
Models	3 DOF models in horizontal plane (surge, sway, yaw). 4DOF models include roll.	6DOF models
Model Type	Non-linear	Linear
Domain	Time-domain	Due to linearity frequency domain models are preferred
Forces	Forces from propulsion systems, control surfaces	Wave loads
Coordinate system	Body-fixed	Equilibrium coordinate system
Forward speed	Studies and model tests are performed at forward speed	Studies and model tests are performed both at zero speed and forward speed

DOF = Degree of Freedom

Table 1.1: Seakeeping vs maneuvering (Adapted from Perez and T. I. Fossen 2006)

for simulating maneuvering behavior of ships, especially in waves both in academia and industry. An example for this is the models to capture broaching, especially for small vessels in waves. Broaching occurs when the speed of the wave is nearly the same or faster than the ship's speed. As a result, the ship looses its steerage and subsequently can cause the vessel to turn and be exposed to beam seas and can cause instantaneous capsizing. These models can be used to develop steering strategies to reduce the risk of capsizing. Further, this increasing interest can be evidenced from the appointment of a specialist committee in ITTC which is exclusively responsible for maneuvering in waves which was established in the 28th International Towing Tank Conference (ITTC 2017). The main aim of the committee is to bridge the gap between calm water maneuvering and classical seakeeping, create guidelines for benchmark tests, and investigate numerical and experimental techniques for maneuvering in waves.

Workshops for Verification and Validation of Ship Manoeuvring Simulation Methods (SIMMAN) have been organized to benchmark the capability of numerical programs to simulate the maneuvering problem through comparison with model test data from various participating towing tanks and institutions such as MOERI (Korea), NMRI (Japan), INSEAN (Italy), HSVA (Germany), MARIN (Holland), BSHC (Bulgaria), IIHR (USA), FORCE Technology (Denmark), FHR (Belgium),

CTO (Poland) and HMRI (Korea). The workshops have been organized in 2008 (*SIMMAN* 2008), 2014(*SIMMAN* 2014) and 2020 (*SIMMAN* 2020). SIMMAN 2020 includes a test case with maneuvering in waves. Based on these workshops ITTC has published benchmarking data for validating maneuvering predictions(ITTC 2021a).

The motivation behind these studies is mainly due to the following reasons :

- Introduction of 2012 EEDI (Energy Efficiency Design Index) regulation by Marine Environment Protection Committee (MEPC) of the International Maritime Organization (IMO) has led to increasing interest among designers and regulators regarding the maneuvering performance in waves. The EEDI regulation encourages the designers to reduce the installed engine power. This raises safety concerns regarding the ability of the vessel to maintain maneuverability under adverse weather conditions. Hence a minimum propulsion power requirement was proposed by IMO through Interim Guidelines 2013. However, the sufficiency of these requirements has been questioned (Papanikolaou et al. 2016). A number of research initiatives including the EU-funded project SHOPERA (Energy Efficient Safe SHip OPERAtions) were aimed at studying and developing numerical tools to study the minimum propulsion and steering requirements for maneuvering in waves.
- Simplified mathematical models of ship maneuvering can be used in the initial design stage to ensure compliance of the design with IMO guidelines MSC.137(76) Standards for Ship Maneuverability.
- Time domain mathematical models can be used in man-in-the-loop simulators for the training of marine officers (ITTC 2014).
- Simulation models are used for statistical analysis of ship safety in waves (Schoop-Zipfel 2017).
- Efficient ship maneuvering models are essential for the development of guidance and navigational systems of autonomous vessels. They are used in predicting the trajectories and in collision avoidance systems (Jin et al. 2020).

1.2 Literature study and review of previous works

The currently available models for maneuvering simulations can be broadly classified into 2 types :

- System-based methods

- CFD based methods

1.2.1 System-based models

The system-based models rely on simplified mathematical models to simulate the vessel behavior. Due to the simplification, they compromise on accuracy however, they are fast and are the only option for real-time simulations. The system-based models can be classified as :

- **Abkowitz model/Regression models** (Abkowitz 1964) These models are based on truncated Taylor series expansion.This model serves as the origin of the term 'maneuvering derivatives' (Sutulo and Guedes Soares 2011) for the regression coefficients. These coefficients are determined from CMT (Circular Motion Tests) or PMM (Planar Motion Mechanism) tests. The drawback of this model is that it does not provide any information regarding the physical phenomena involved, hence it is difficult to translate the results to a different vessel. Also, the computation of the regression coefficients through model testing is a time-consuming and complicated process.

- **Norrbin model** (Norrbin 1970) also called the second order modulus model. The difference between the Abkowitz model and Norrbin model is that in Norrbin model, the forces are represented by non-differentiable functions due to the use of the absolute value function. Hence they do not represent a physical system (Skjetne et al. 2004). For example, the Taylor series expansion of sway force has the term $Y_{vv}v^2$. In the Abkowitz model, this is set to zero to satisfy the symmetry condition. In Norrbin model this term is replaced as $Y_{|v|v}|v|v$. The advantage of this representation is that it models the damping effects more accurately (Skjetne et al. 2004).

- **MMG model** (Yasukawa and Yoshimura 2014) It was standardized by the Japan Society of Naval Architects and Ocean Engineers. It follows a modular approach in which the contributions from different elements (such as hull, propeller, rudder etc.) are calculated separately in different modules and then combined together to find the total hydrodynamic force. This is in contrast to the "whole ship models" proposed by Abkowitz and Norrbin. The MMG approach provides more clarity on the contributions from individual components and helps to identify the dominant phenomenon for different types of vessels as well as for different types of maneuvers. This approach also enables easier validation through the comparison of results from individual modules with experimental data.

The MMG approach is currently the most popular approach adopted in system-based models. Within the MMG approach, 2 methods have been identified for modeling the maneuvering in waves problem :

- **Two time scale approach** This approach separates the high frequency responses due to the first order wave loads from the low frequency responses in the maneuvering problem. The two problems are solved separately with some exchange of information. 2 major works in this domain are from Seo and Y. Kim (2011) and Skejic (2008). The difference between the two works is that Skejic (2008) used the frequency domain approach for seakeeping analysis whereas Seo and Y. Kim (2011) solved the seakeeping problem in the time domain. The second order wave loads in Seo and Y. Kim (2011) is evaluated by the application of 3D boundary element method whereas Skejic (2008) employed strip theory based methods.
- **Hybrid approach** In the hydrid approach, in-contrast to the two time-scale approach, the aim is to integrate both the high-frequency as well as low frequency motions into a single set of equations. This equation is then solved to obtain the responses of a vessel maneuvering in waves. These methods employ convolution integrals to solve the equations. Impulse response function (IRF) or retardation functions are used to transform the frequency domain coefficients into time domain. However, this approach is very time-consuming and not practical for real-time simulations (Skejic 2008). This approach is used by Schoop-Zipfel (2017).

1.2.2 CFD based approach

RANS based CFD solvers are increasingly used to obtain the maneuvering derivatives which are then used to simulate the maneuvers. For example Cura-Hochbaum (2006) conducted virtual PMM test. The maneuvering derivatives were derived from the time-history of the loads from the virtual test. The comparison with model tests shows good agreement.

In most of the CFD simulations, the effect of the propeller is modeled as body forces. The main challenges identified in the CFD based approach as a part of *SIMMAN* 2008 workshop are accurate turbulence modeling, free surface capturing method, improvement in propeller and rudder models, and improved grid resolution near rudder and other appendages.

1.3 Contribution

A complete real-time maneuvering simulation code in python was developed by Øyvind Rabliås who is a PhD candidate at IMT, NTNU. The contribution of the author is limited to making the necessary modification in the code to simulate the maneuvering of Kriso Container Ship (KCS) detailed in Section 2.4 and perform simulations and sensitivity studies presented in Chapter 6.

1.4 Outline of the thesis

Chapter 1 presented the basic motivation for the project.

Chapter 2 decribes functions and limitations of the various modules used in the simulation code. Mathematical models for the modules are presented.

Chapter 3 goes into the details of the non-linear viscous loads module.

Chapter 4 describes the experimental approach to obtain a transient drag coefficient curve which is the basic input for 2D+t methods.

Chapter 5 describes the numerical approaches to obtain a transient drag coefficient curve.

Chapter 6 presents the results of maneuvering simulations.

Chapter 7 presents the conclusions and future work

Chapter 2

Fundamentals of the maneuvering model

The chapter describes the fundamental theoretical principles behind the maneuvering model.

2.1 Assumptions

The main assumptions behind the developed maneuvering model are (Skejic 2008; Xiang 2012):

- The vessels are assumed to have a small to moderate Froude number. This limitation comes from the fact that at these Froude numbers the ship-generated waves are assumed to be small. Hence the free surface behaves like a rigid wall. This permits the use of double body approximation in slender body theory and added mass theory which is the basis for calculating the calm water loads.
- The horizontal and vertical extent of water is assumed to be infinite. The density of water is assumed to be a constant.
- For maneuvering in waves, the effect of waves on the maneuvering motion of the vessel is only accounted for by the second order mean-drift loads. The remaining loads are computed as if the vessel is in calm water. However, it is to be noted that waves can influence the loads on the rudder and propeller which are not accounted for in the current model.
- It is assumed that the calm water hydrodynamic loads, the loads from the

waves, and the viscous loads can be super-imposed linearly.

- The effect of current and wind are not accounted for in the model

2.2 Coordinate System

A short summary of the right-handed coordinate systems employed in the maneuvering model and their purpose is presented below (Rabliås and Kristiansen 2021; Skejic 2008; Xiang 2012):

- **Earth-fixed coordinate system** $OX_EY_EZ_E$ (see Figure 2.1(a)). The positive direction of Z_E axis points upwards with its origin on the free surface. The earth fixed coordinate system is used to define the ship heading and trajectory of the vessel as a function of time.
- **Incident wave coordinate system** $OX_IY_IZ_I$ (see Figure 2.1(a)). The positive direction of Z_I axis points upwards and the X_I is aligned in the wave direction, with its origin the same as that of the earth-fixed coordinate system. This coordinate system is used to define the incident wave with wavelength λ.
- **Body-fixed seakeeping coordinate system** $O_sx_sy_sz_s$ (see Figure 2.1(a)). The positive direction of z_s axis points upwards and passes through the center of gravity of the vessel, positive direction of x_s axis points towards the bow of the vessel, with its origin located on the undisturbed free surface. Since this is a body-fixed coordinate system, it can be used to refer to any point on the vessel. When the vessel has unsteady motion, this reference frame becomes non-inertial.
- **Inertial seakeeping coordinate system** O_sxyz (see Figure 2.1(a)). The positive direction of the z axis points upwards and passes through the center of gravity of the vessel, positive direction of x axis points towards the bow of the vessel, with its origin located on the undisturbed free surface. The inertial seakeeping coordinate system does not oscillate with the ship and it remains fixed at the mean oscillatory position of the vessel. The body-fixed seakeeping coordinate system coincides with the inertial seakeeping coordinate system when the vessel has no unsteady motion. Since the coordinate system is inertial, Bernoulli's equation and Newton's second law can be applied directly without any modification.
- **Maneuvering body-fixed coordinate system** $O_cx_cy_cz_c$ (see Figure 2.1(b)), with z-axis pointing upwards, x-axis pointing towards the bow with its origin located at the center of gravity of the vessel.

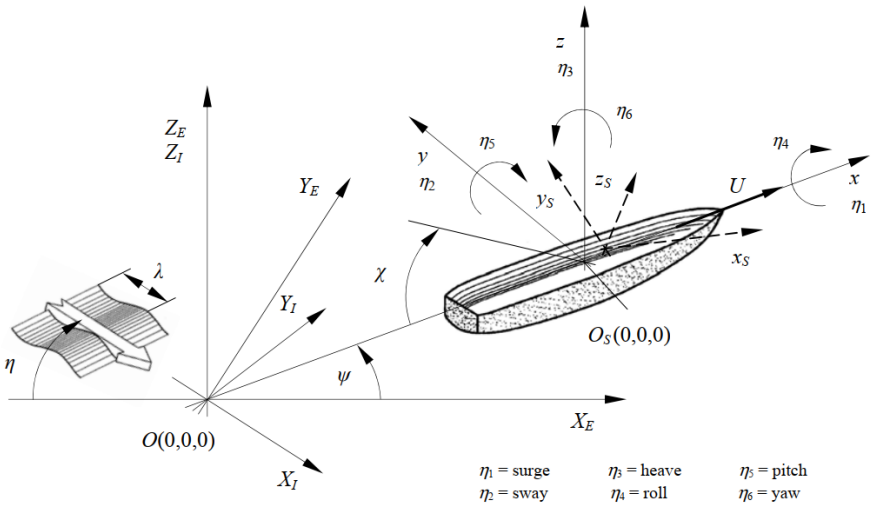

(a) Definition for earth fixed, incident wave, inertial seakeeping and body-fixed seakeeping coordinate systems. Definitions and positive directions for angular and translator displacements are also presented (Skejic 2008)

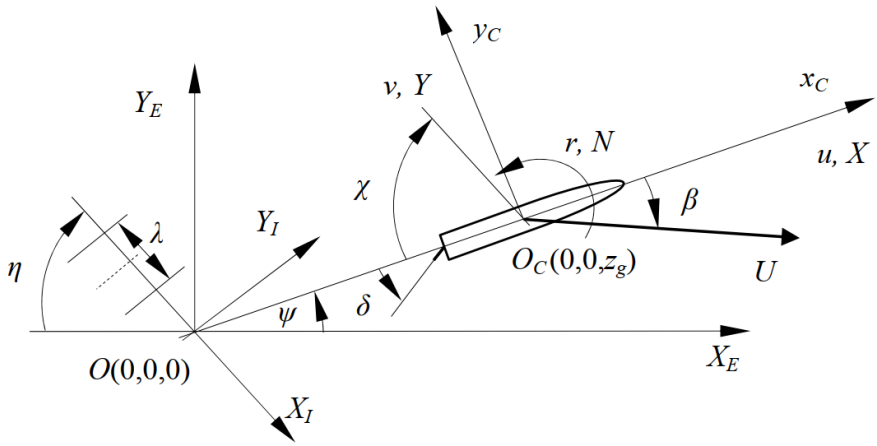

(b) Definition for maneuvering body fixed coordinate system (Skejic 2008)

Figure 2.1: Definition for different coordinate systems used in the maneuvering model

Based on the coordinate systems which are defined, the following important angles are defined :

- Incident wave angle - with respect to the earth-fixed coordinate system η - It is defined as the angle between the positive X_E and X_I axes.

- Heading angle ψ - it is defined as the angle between x_c and X_E axes.
- Drift angle β - defined as the angle made by the velocity vector with the x_c axis.
- Rudder angle δ - defined as the angle between the rudder and positive x_c axis.

2.3 Two-time scale method

In the two time scale approach, the total motion of the vessel is split into a low-frequency (LF) motion connected with the maneuvering and a high frequency (HF) motion connected with the first order wave motions. The total motion of the vessel is considered to be a superposition of the two, as shown in Figure 2.2.

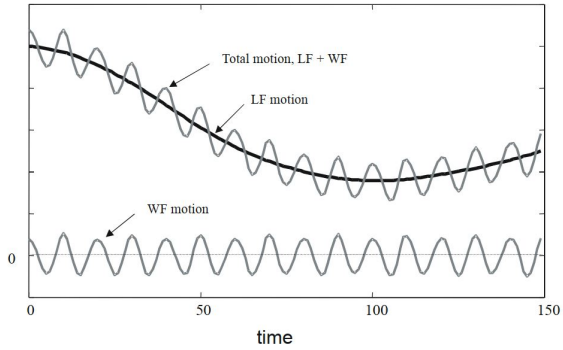

Figure 2.2: Low frequency and high frequency motion components (T. Fossen 2005)

The fundamental assumption behind this approach is that the mean path followed by the vessel is not influenced by the oscillatory motion caused by the first order wave loads. The LF problem and HF problem are solved separately considering some interaction effects. The LF problem is solved in the maneuvering module and HF problem is solved in the seakeeping module. The seakeeping module influences the maneuvering module through the second order wave drift loads and moments. The maneuvering module influences the seakeeping module through the slowly varying ship speed and heading and thereby the encounter frequency. These interactions are indicated in Figure 2.3.

A general limitation of this approach is that, in order to split the ship motion response into high frequency and low frequency components, the seakeeping responses must have a high enough frequency. This implies that, in principle, this method may not provide good results when employed in following sea conditions.

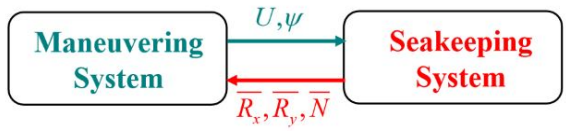

Figure 2.3: Interaction between the seakeeping system and maneuvering system (Greco 2020). U - ship speed, ψ - heading angle, $\overline{R}_x$, $\overline{R}_y$ & $\overline{N}$ are the mean second order wave forces and moment

Another situation where the two-time step model may not give an accurate result was presented by Schoop-Zipfel (2017) in the simulations of S-175 container ship. For a particular wavelength ($\lambda/L_{PP} = 0.7$) it was observed that the ship was not able to turn against the waves and hence gets "trapped" in the two-time scale model which did not occur in the unified theory approach. This occurred in the case where the second order wave drift loads were large i.e. the wave drift yaw moment was larger than the maximum steering moment. The oscillating linear wave loads have instances where it produces moments that support the turning direction. This helped the vessel in counteracting the large mean drift loads in the unified theory. Since these oscillating linear wave loads are not present in the two-time scale approach, the vessel gets "trapped" and cannot turn against the waves.

2.4 Test cases

Two test vessels are referred to in the thesis :

- **Duisburg Test Case (DTC)** - It is a Post-Panamax 14000 TEU container ship developed at the Institute of Ship Technology, Ocean Engineering and Transport Systems (ISMT) - University of Duisburg-Essen (Moctar et al. 2012). It has single screw propulsion and is fitted with a bulbous bow and has a large bow flare. It is also fitted with a bilge keel consisting of 5 segments on each side of the hull, each with a length of 14.85 m and a height of 0.4 m. Experimental data for maneuvering tests for the vessel in calm water, regular waves, as well as irregular waves, is available in Rabliås and Kristiansen (2021, 2022).

- **KRISO (Korea Research Institute for Ships and Ocean Engineering) Container Ship (KCS)** - It is a 3600 TEU Container ship model (*NMRI* 2022). It has single screw propulsion and is fitted with a bulbous bow. Experimental data for maneuvering tests for the vessel in calm water and regular waves is publicly available as the vessel is a test case for *SIMMAN* (2020). The vessel has a low GM, hence the test case underlines the importance of 4-DOF (surge-sway-yaw-roll) maneuvering models in predicting ac-

Particulars	KCS	DTC	
Length between perpendiculars (Lpp)	230	355	m
Breadth (B)	32.2	51	m
Draft	10.8	14.5	m
Displacement	52030	173467	m^3
C_B	0.651	0.661	
GM	0.6	5.1	m
k_{44}/B	0.40	0.398	-
k_{55}/Lpp	0.25	0.246	-
k_{66}/Lpp	0.25	0.246	-

Table 2.1: Main particulars of test cases

curate maneuvers as compared to 3-DOF (surge-sway-yaw) models (ITTC 2021a).

The main particulars of the vessels are presented in Table 2.1.

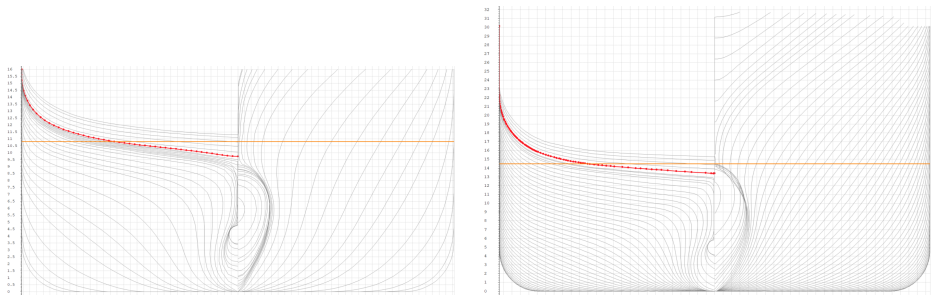

(a) KCS **(b)** DTC

Figure 2.4: Body plan for the test vessels. The yellow line indicates the design draft of the vessels and the section marked in red indicates the separation section.

Body plan of the vessel is shown in Figure 2.4. It is assumed that flow separation occurs at a section ahead of the transom stern and this separation section is indicated in red in Figure 2.4. This section is important for calculating lifting effects associated with the hull as per Söding (1982). The exact location of the separation section depends on the curvature of the hull at the aft end (Skejic 2008). In this work, the section just aft of the propeller plane is assumed to be the separation section.

2.5 4-DOF maneuvering equation

The 4-DOF (surge-sway-roll-yaw) equation of motion is given as (Rabliås and Kristiansen 2021; Skejic 2008):

$$
\begin{bmatrix} M & 0 & 0 & 0 \\ 0 & M & 0 & 0 \\ 0 & 0 & I_{44} & -I_{46} \\ 0 & 0 & -I_{64} & I_{66} \end{bmatrix} \begin{bmatrix} \dot{u} \\ \dot{v} \\ \dot{p} \\ \dot{r} \end{bmatrix} + \begin{bmatrix} 0 & -Mr & 0 & 0 \\ 0 & 0 & 0 & Mu \\ 0 & 0 & 0 & 0 \\ 0 & 0 & 0 & 0 \end{bmatrix} \begin{bmatrix} u \\ v \\ p \\ r \end{bmatrix} =
$$

$$
\begin{bmatrix} X_{\dot{u}} & 0 & 0 & 0 \\ 0 & Y_{\dot{v}} & Y_{\dot{p}} & Y_{\dot{r}} \\ 0 & K_{\dot{v}} & K_{\dot{p}} & K_{\dot{r}} \\ 0 & N_{\dot{v}} & N_{\dot{p}} & N_{\dot{r}} \end{bmatrix} \begin{bmatrix} \dot{u} \\ \dot{v} \\ \dot{p} \\ \dot{r} \end{bmatrix} + \begin{bmatrix} 0 & -C_{TN}Y_{\dot{v}}r & -Y_{\dot{p}}r & -Y_{\dot{r}}r \\ 0 & 0 & 0 & X_{\dot{u}}u \\ 0 & 0 & 0 & 0 \\ 0 & -X_{\dot{u}}u & 0 & 0 \end{bmatrix} \begin{bmatrix} u \\ v \\ p \\ r \end{bmatrix} +
$$

$$
\begin{bmatrix} 0 & 0 & 0 & 0 \\ 0 & Y_v & Y_p & Y_r \\ 0 & K_v & K_p & K_r \\ 0 & N_v & N_p & N_r \end{bmatrix} \begin{bmatrix} u \\ v \\ p \\ r \end{bmatrix} - \begin{bmatrix} 0 & 0 & 0 & 0 \\ 0 & 0 & 0 & 0 \\ 0 & 0 & C_{44} & 0 \\ 0 & 0 & 0 & 0 \end{bmatrix} \begin{bmatrix} \int_0^t u dt \\ \int_0^t (v + z_G p + u\psi) dt \\ \phi \\ \psi \end{bmatrix} + \begin{bmatrix} X_R \\ Y_R \\ K_R \\ N_R \end{bmatrix} +
$$

$$
\begin{bmatrix} X_{PROP} \\ Y_{PROP} \\ K_{PROP} \\ N_{PROP} \end{bmatrix} + \begin{bmatrix} X_{CF} \\ Y_{CF} \\ K_{CF} \\ N_{CF} \end{bmatrix} + \begin{bmatrix} \overline{R}_X \\ \overline{R}_Y \\ \overline{R}_K \\ \overline{R}_N \end{bmatrix} \quad (2.1)
$$

- The terms on the left side of the Equation (2.1) are the inertial terms. They are expressed in the body-fixed coordinate system. The terms on the right side of the equation represent the hydrodynamics loads.
- The terms $X_{\dot{u}}$, $Y_{\dot{v}}$, $Y_{\dot{p}}$, $Y_{\dot{r}}$, $K_{\dot{v}}$, $K_{\dot{p}}$, $K_{\dot{r}}$, $N_{\dot{v}}$, $N_{\dot{r}}$, $N_{\dot{p}}$ are the maneuvering coefficients which are the zero-frequency added mass coefficients. Y_v, Y_p, Y_r, K_v, K_p, K_r, N_v, N_r, N_p are the maneuvering coefficients which are also built up based on the zero-frequency added mass coefficients (Söding 1982).
- C_{TN} is an empirical coefficient that takes a value between 0.2 and 0.8 (Skejic 2008). The term $-C_{TN}Y_{\dot{v}r}$ causes involuntary speed loss in turning circle maneuver. It represents the longitudinal component of centrifugal force. For KCS simulations C_{TN} is set to 0.5.
- X_R, Y_R, K_R and N_R are the rudder forces and moments calculated as described in Section 2.8.

- X_{PROP}, Y_{PROP}, K_{PROP} and N_{PROP} are the propeller forces and moments as described in Section 2.7.
- X_{CF}, Y_{CF}, K_{CF} and N_{CF} are the viscous forces and moments calculated as described in Chapter 3. It is noted that X_{CF} is set to zero as this component is already included while calculating the resistance of the vessel. The roll moment K_{CF} is calculated by assuming the cross-flow force to act at 0.65T where T is the draft of the vessel.
- $\overline{R}_X$, $\overline{R}_Y$, $\overline{R}_K$ and $\overline{R}_N$ are the mean second order drift forces and moments calculated as described in Section 2.9.

2.6 Seakeeping module

The overall objective of the seakeeping module in the code is :

- Calculate the zero frequency limit added mass coefficients. This is used to compute the terms $X_{\dot{u}}$, $Y_{\dot{v}}$, $Y_{\dot{p}}$, $Y_{\dot{r}}$, $K_{\dot{v}}$, $K_{\dot{p}}$, $K_{\dot{r}}$, $N_{\dot{v}}$, $N_{\dot{r}}$ and $N_{\dot{p}}$. Other maneuvering coefficients (lifting terms) are also calculated using the zero-frequency added mass coefficient based on Söding (1982).
- Compute the second order mean drift forces and moments. One of the inputs necessary for this is the motion response of the vessel for a given encounter frequency and wave heading angle.

2.6.1 Linear ship motions

The seakeeping analysis in the present code is performed using 2D strip theory. Strip theory simplifies the complex 3D flow around the vessel into 2D problems by dividing the underwater portion of the hull into a number of strips. Each strip represents a 2D boundary value problem (BVP) which is solved to obtain the 2D coefficients. The 2D coefficients are then integrated along the length of the vessel to obtain an approximation of the 3D coefficients (O. M. Faltinsen 1990; Skejic 2008). STF strip theory by Salvesen et al. (1970) is used in the current code which accounts for the effect of forward speed. The complete formulation including the exact 3D BVP and its subsequent linearization and BVP formulation for 2D sections is presented in Skejic (2008). The important features and limitations of this approach are summarised below (Salvesen et al. 1970; Skejic 2008):

- STF theory is a linear theory. This means that the theory assumes a linear relationship between the wave-induced responses and the wave amplitude. Hence, the wave steepness is small.

- The initial transients is neglected and steady-state conditions are assumed.
- STF theory is applicable to displacement vessels i.e $Fn \leq 0.4$. The underlying assumption here is that there is no longitudinal hydrodynamic interaction between the different cross-sections of the hull. For $Fn > 0.4$, 2D+t theory is a more appropriate strip theory.
- In principle, radiation loads can be calculated using strip theory only when the radiated waves from the vessel during forced oscillation have a wavelength that is small compared to the breadth of the vessel or in other words at high encounter frequencies. However, strip theory provides a good engineering estimate of the responses and is usually applied at all frequencies.
- The total velocity potential associated with a vessel moving with forward speed consists of contributions from uniform steady flow associated with the constant forward speed, a time-dependent perturbation potential associated with the vessel motions, and a time-independent or steady perturbation potential which is associated with the steady wave pattern generated by the vessel when it moves with a constant forward speed. In STF theory, the contribution from the steady perturbation potential is neglected under the assumption that they are small.
- STF theory assumes the hull to be slender meaning draft and breadth of the hull are much smaller than the length of the vessel. This results in the surface normal component in the x-direction being much smaller than the surface normal component in y and z-directions.
- The correction for forward speed in STF theory considers the change in the direction of normals to the 2D ship sections due to pitch and yaw motion and also due to the lifting effects associated with the separation section. Figure 2.5 shows the influence of forward speed correction on the 3D added mass coefficient in heave A_{33} and damping coefficient in heave B_{33} for KCS vessel obtained using STF theory.

In the code, the 2D BVP is solved to obtain the 2D radiation coefficients. This is integrated along the length to obtain the 3D values. The diffraction forces are computed using Haskind-Hanaoka relation. Hence the diffraction BVP is not solved. The diffraction loads are obtained from the radiation potential and incident wave potential. Roll damping is accounted by using Ikeda et al. (1978).

Comparison of RAO (Response Amplitude Operator) obtained from the code and from ShipX(VERES) for KCS vessel for zeros forward speed and with a forward

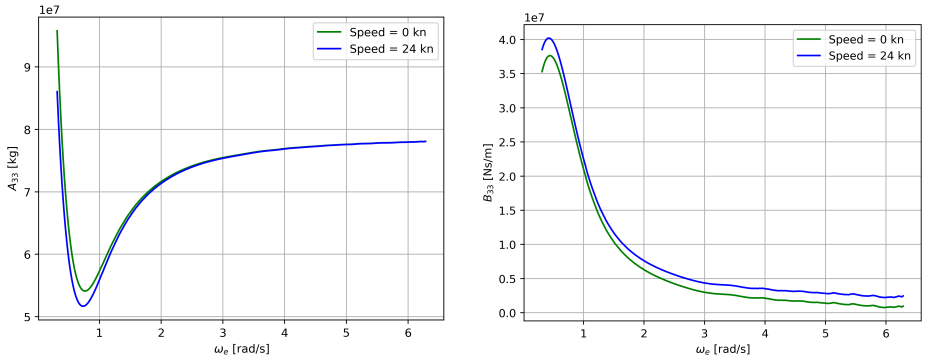

(a) Added mass coefficient **(b)** Damping coefficient

Figure 2.5: 3D added mass coefficient in heave A_{33} and damping coefficient B_{33} for KCS vessel for zero speed and forward speed of 24 knots from STF strip theory

speed of 24 knots is shown in Figures 2.6 and 2.7. ShipX [1] is a hydrodynamic workbench developed by SINTEF. Comparing the results, some differences are seen in the RAO for roll motion, both at zeros speed and at 24 knots. This is probably due to the differences in the empirical formulations used for determining the roll damping. However, overall there is good agreement between the results.

2.7 Propulsion module

The purpose of the propulsion module is to calculate the propeller-induced forces and moments.

The main inputs required for the module are :

- Calm water resistance curve
- Propeller open water performance curve
- Wake fraction
- Thrust deduction factor

The first step is to calculate the self-propulsion RPS which is required to achieve the desired speed in calm water. This RPS is maintained as a constant during the maneuvers. The calculations can be summarised in the following steps :

[1] https://www.sintef.no/en/software/shipx/

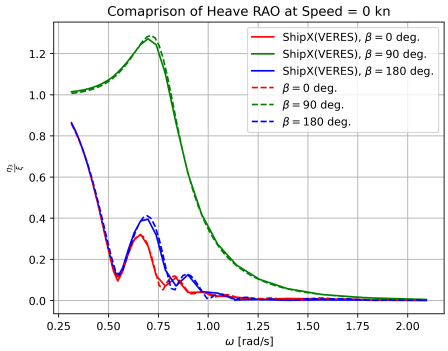

(a) RAO for heave motion

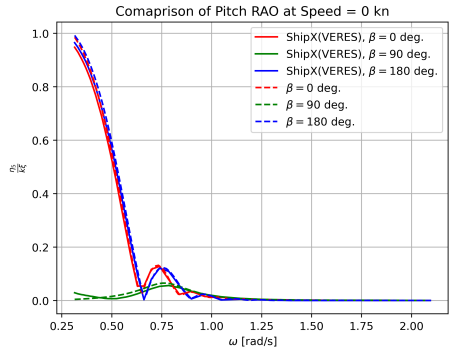

(b) RAO for pitch motion

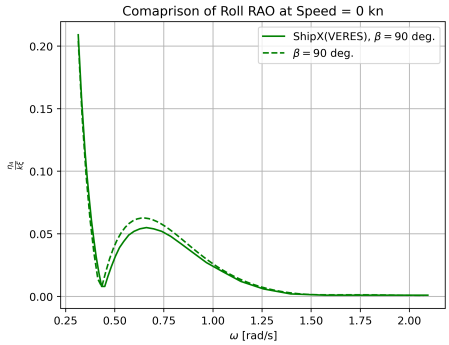

(c) RAO for roll motion

Figure 2.6: Comparison of RAO obtained for KCS from ShipX(VERES) and from the program for Speed = 0 kn. The dashed lines show the output from the current code and the solid lines shows the output from ShipX(VERES)

- For the input approach speed, the calm water resistance R_T is obtained from the calm water resistance curve. Then the required thrust (T) can be calculated as :

$$T = \frac{R_T}{1-t} \tag{2.2}$$

  where t is the thrust deduction factor.

- The velocity of advance, u_a takes into account the wake fraction. This can be calculated as :

$$u_a = u(1-w) \tag{2.3}$$

  where u is the ship speed and w is the wake fraction.

- The thrust can then be expressed in the non-dimensional form as C_T:

$$C_T = \frac{T}{\rho D_p^2 u_a^2} \tag{2.4}$$

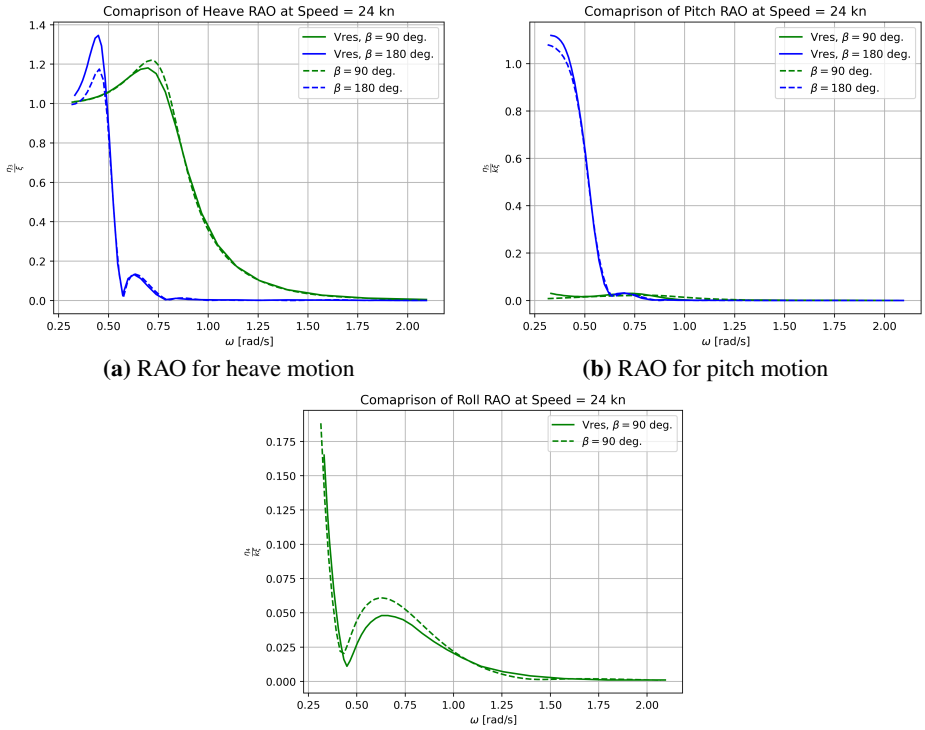

(a) RAO for heave motion

(b) RAO for pitch motion

(c) RAO for roll motion

Figure 2.7: Comparison of RAO obtained for KCS from ShipX(VERES) and from the program for Speed = 24 kn. The dashed lines show the output from the current code and the solid lines shows the output from ShipX(VERES)

where ρ is the density of water, D_p is the propeller diameter.

- The open water curve of the propeller indicates the relation between the open water thrust coefficient K_T and advance coefficient j.

$$K_T = \frac{T}{\rho n^2 D_p^4} \tag{2.5}$$

where T is the thrust and n is the RPS.

$$j = \frac{u_a}{nD_p} \tag{2.6}$$

It can be observed from Equations (2.4)–(2.6) that :

$$\frac{K_T}{j^2} = C_T \tag{2.7}$$

- Therefore the advance coefficient j^* which corresponds to the self propulsion point can be calculated by plotting $\frac{K_T}{j^2}$ against j for all the values of j. j^* corresponds to the point at which $\frac{K_T}{j^2} = C_T$. From j^* the self propulsion RPS can be calculated as :

$$n = \frac{u_a}{D_p j^*} \tag{2.8}$$

Once the self propulsion RPS is determined as described above the propeller force in the longitudinal direction is computed as :

$$X_{PROP} = -R_T(u) + (1-t)T(j) \tag{2.9}$$

In single-screw propelled vessels, the operation of the propeller results in a flow asymmetry. This can lead to a lateral force and yaw moment. These effects are accounted for by the coefficients Y_{PT} and N_{PT}. For the simulations of KCS vessel, these have been ignored as reliable experimental data of these coefficients could not be found in the published literature.

The calm water resistance curve for KCS is shown in Figure 2.8. This was obtained by extrapolation of model test data obtained from J. Kim (2021). The form factor k was taken to be 0.106 based on the data presented in Korkmaz et al. (2019).

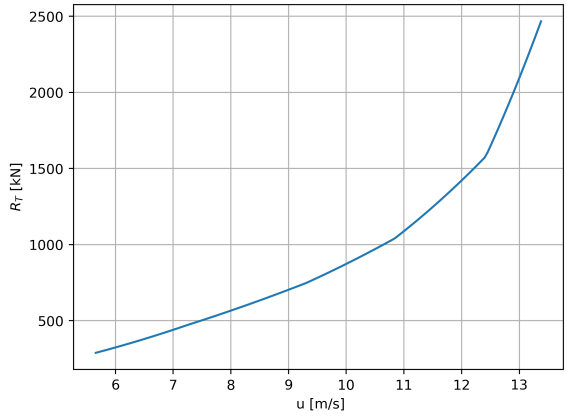

Figure 2.8: Calm water resistance curve for KCS (R_T is the total resistance of the vessel, u is the speed of the vessel)

The propeller data and open curve data for KCS are as per data provided by MARIN in *SIMMAN* 2020. The open water curve is presented in Figure 2.9.

The wake fraction w and the thrust deduction factor t for KCS are taken as 0.143 and 0.2112 based on the data presented in Kinaci et al. (2018).

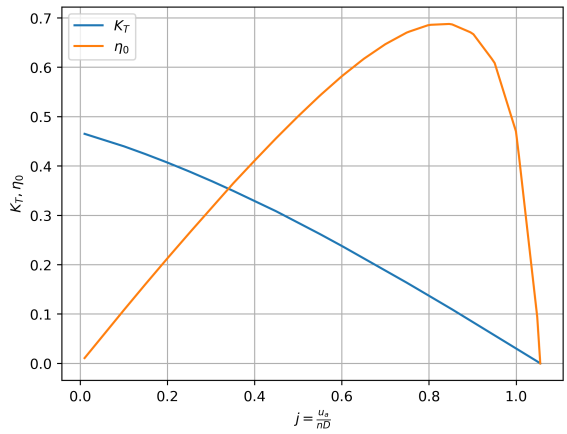

Figure 2.9: Open water propeller curve curve for KCS (K_T is the thrust coefficient, η_0 is the open water efficiency, j is the advance coefficient)

2.8 Rudder module

The purpose of the rudder module is to calculate the forces and moments induced by the rudder. The computational model for rudder is exemplified in Figure 2.10. The rudder deflection angle is δ. u_{RS} and v_{RS} are longitudinal and transversal components of the mean inflow velocity to the rudder V_R.

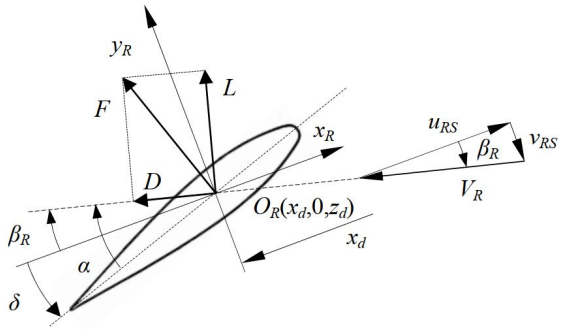

Figure 2.10: Rudder model (Skejic 2008)

The calculations involved in the rudder module is summarised below :

- First the inflow velocities to the rudder is calculated as :

$$u_{rs} = u_a(1 + k_m(\sqrt{1 + C_{th}} - 1)) \tag{2.10}$$

Here C_{th} is the thrust loading coefficient given by :

$$C_{th} = \frac{T(j)}{0.5\rho u_a^2 \pi D_p^2/4} \tag{2.11}$$

This term appears in the equation to account for the slip-stream from the propeller. The factor k_m accounts for the distance between the rudder and propeller and varies between 0.5 and 1. For the simulations with KCS, k_m is taken as 0.55.

$$v_{rs} = v + x_r r \tag{2.12}$$

x_r is the location of the rudder and v is sway velocity and r is the yaw velocity of the vessel.

- Based on u_r and v_r, the lift and drag force can be computed as:

$$L = \frac{1}{2} C_L \rho A_r (u_r^2 + v_r^2) \tag{2.13}$$

$$D = \frac{1}{2} C_D \rho A_r (u_r^2 + v_r^2) \tag{2.14}$$

where A_R is the rudder area. The lift and drag coefficient, C_L and C_D can be obtained from Bertram (2012) as :

$$C_L = 2\pi \frac{\Lambda(\Lambda + 0.7)}{(\Lambda + 1.7)^2} \sin\alpha + C_Q \sin\alpha |\sin\alpha| \cos\alpha \tag{2.15}$$

$$C_D = \frac{C_L^2}{\pi\Lambda} + C_Q |\sin\alpha|^3 + C_{D0} \tag{2.16}$$

where Λ is the rudder aspect ratio, C_Q is the resistance coefficient which is approximately taken as 1. The angle of attack $\alpha = \delta + \beta_r$.

The drift angle β_r for the rudder can be calculated as :

$$\beta_r = tan^{-1}\left(\frac{-v_r}{u_r}\right) \tag{2.17}$$

C_{D0} is the coefficient for rudder surface friction and can be calculated as

$$C_{D0} = 2.5 \frac{0.075}{(\log Re - 2)^2} \tag{2.18}$$

- The computed lift and drag forces can then be resolved to the ship-fixed coordinate system as :

$$X_R = L \sin\beta_r - D \cos\beta_r \tag{2.19}$$

$$Y_R = L \cos\beta_r + D \sin\beta_r \tag{2.20}$$

$$N_R = x_r Y_R \tag{2.21}$$

The roll moment due to rudder K_R is assumed to be 0.

For the simulation with KCS the rudder data is obtained from *SIMMAN* (2008). The rudder dimensions are presented in Figure 2.11.

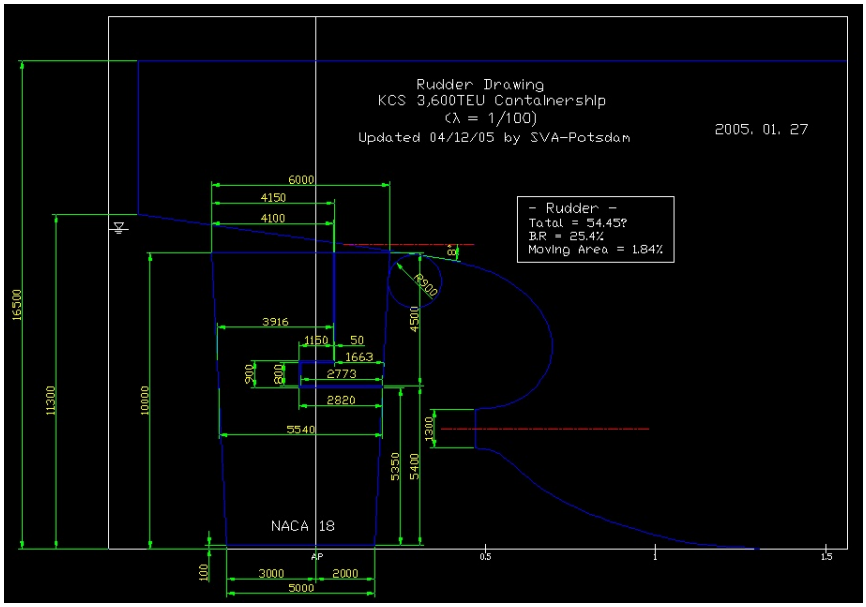

Figure 2.11: KCS rudder dimensions (*SIMMAN* 2008)

2.9 Mean second order drift load Module

In the code mean second order drift loads in x-direction $\overline{R}_X$, in y-direction $\overline{R}_Y$ and yaw moment $\overline{R}_N$ is calculated by combining two theories (Rabliås and Kristiansen 2021):

- If the relative wavelength is approximately above $\lambda/L \geq 0.5$, then the drift loads are dominated by ship motions. In this range, the drift loads are calculated by using the direct pressure integration method by O. Faltinsen et al. (1980).
- If the wavelength is approximately lower $\lambda/L \leq 0.5$, then the drift loads are dominated by the wave reflections. In this range, the drift loads are calculated by using the asymptotic theory of O. Faltinsen et al. (1980).

The two theories are combined by using the expression :

$$\overline{R}_X = (1 - R^2)\overline{R}_{X,1} + R^2\overline{R}_{X,2} \tag{2.22}$$

where $\overline{R}_{X,1}$ is mean drift load in x-direction calculated using direct pressure integration and $\overline{R}_{X,2}$ is mean drift load in x-direction calculated by asymptotic theory. R is a function that combines the results from the two theories and is proposed by Fujii and Takahashi (1975).

$$R = \frac{\pi I_1(kd)}{\sqrt{\pi^2[I_1(kd)]^2 + [K_1(kd)]^2}} \tag{2.23}$$

Here I_1 and K_1 are the modified Bessel function of the first and second kind respectively, k is the wavenumber and d is the ship draft. The same formulation is also applied to sway and yaw mean drift forces.

2.10 Numerical integration - Runge-Kutta method

This chapter briefly describes the time-stepping procedure and algorithm used to solve the 4-DOF maneuvering equation. Fourth order Runge-Kutta scheme is used for time integration of Equation (2.1). The general form of the equation can be represented as :

$$\frac{dX}{dt} = f(t, X) \tag{2.24}$$

X is the vector containing the variables which we want to integrate and $X(t_0) = X_0$ is the value of X at the initial time $t = t_0$ which is known. If h is the time step, then the value of X at the next time step can be calculated as :

$$X_{i+1} = X_i + \frac{1}{6}h(k_1 + 2k_2 + 2k_3 + k_4) \tag{2.25}$$

where

$$\begin{aligned} k_1 &= f(t_i, X_i) \\ k_2 &= f(t_i + \frac{h}{2}, X_i + h\frac{k_1}{2}) \\ k_3 &= f(t_i + \frac{h}{2}, X_i + h\frac{k_2}{2}) \\ k_4 &= f(t_i + h, X_i + hk_3) \end{aligned} \tag{2.26}$$

To integrate Equation (2.1), the X vector is defined as :

$$X = [x \;\; u \;\;\; y \;\; v \;\; \phi \;\; p \;\; \psi \;\; r \;\; X_0 \;\; Y_0 \;\; \Phi \;\; \Psi]^T \tag{2.27}$$

In Equation (2.27), X_0, Y_0, Φ, Ψ are in global inertial coordinate system as defined in Section 2.2.

To apply the Runge-Kutta formulas given in Equation (2.26), an expression for $\dot{X}$ has to be determined.

$$\dot{X} = [\dot{x} \;\; \dot{u} \quad \dot{y} \;\; \dot{v} \;\; \dot{\phi} \;\; \dot{p} \;\; \dot{\psi} \;\; \dot{r} \;\; \dot{X}_0 \;\; \dot{Y}_0 \;\; \dot{\Phi} \;\; \dot{\Psi}]^T \tag{2.28}$$

- $\dot{x}$, $\dot{y}$, $\dot{\phi}$ and $\dot{\psi}$ are respectively u, v, p and r
- $\dot{X}_0$, $\dot{Y}_0$, $\dot{\Phi}$ and $\dot{\Psi}$ are determined using Euler rotation matrix as (Skejic 2008):

$$\begin{bmatrix} \dot{X}_0 \\ \dot{Y}_0 \\ \dot{\Phi} \\ \dot{\Psi} \end{bmatrix} = \begin{bmatrix} \cos\psi & -\sin\psi\cos\phi & 0 & 0 \\ \sin\psi & \cos\psi\cos\phi & 0 & 0 \\ 0 & 0 & 1 & 0 \\ 0 & 0 & 0 & \cos\phi \end{bmatrix} \begin{bmatrix} u \\ v \\ p \\ r \end{bmatrix} \tag{2.29}$$

- $\dot{u}$, $\dot{v}$, $\dot{p}$ and $\dot{r}$ can be obtained from rearranging Equation (2.1)

Making these modifications, it is possible to express $\dot{X}$ as :

$$M\dot{X} = F(t, X) \tag{2.30}$$

Here M is 12x12 matrix which contains mass and added mass terms and F is 12x1 matrix which contains rest of the terms which arises out of rearranging Equation (2.1). Hence, the expression of $\dot{X}$ can be obtained as :

$$\dot{X} = M^{-1}F(t, X) \tag{2.31}$$

which is in the same form as Equation (2.24).

Since the M matrix has only the mass and added mass terms, it is required to invert this matrix only once for a simulation.

2.11 Two-time scale algorithm

The algorithm for the two-time scale approach of Skejic (2008) is presented in Figure 2.12. The main steps involved are :

- The main vessel particulars and incident wave characteristics (wave period, wave amplitude, and wave direction) are input into the program. A predetermined threshold for the difference in heading angle $\Delta\psi_c$ is provided for updating the second order mean drift loads. In the current code, a threshold is also applied on the vessel speed given by $\sqrt{u^2 + v^2}$.

- At the first time step, t_1, the seakeeping module solves the zero-frequency limits for added mass coefficients and outputs the maneuvering coefficients to the maneuvering module. The loads from other modules such as propulsion loads, rudder loads, and viscous loads are also provided to the maneuvering module.

- The time-stepping procedure is performed in the maneuvering module. The instantaneous change in ship heading in a time step is given by $\Delta\psi_i$. The total change in the heading since the last update of mean second order loads is $\Sigma\Delta\psi_i$. This is then compared against the threshold value $\Delta\psi_c$. If this is exceeded, then the mean second order loads are updated in the next iteration. In the current code, the drift loads are also updated if the ship speed given by $\sqrt{u^2 + v^2}$ exceeds a set threshold.

- This process is repeated until we reach the last time step.

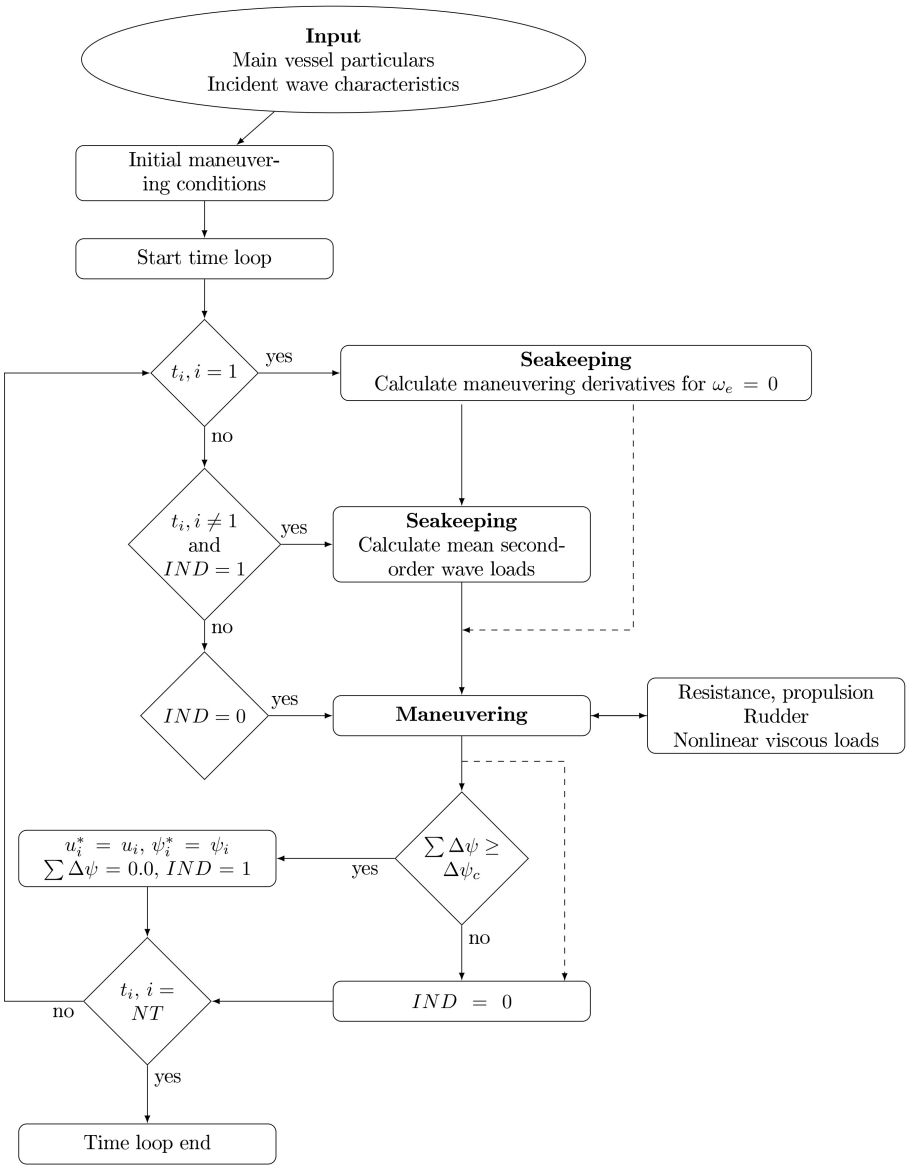

Figure 2.12: Algorithm for two-time scale approach of Skejic (2008) (Schoop-Zipfel 2017)

Chapter 3

Non-linear viscous loads

The objective of the non-linear viscous loads module is to account for loads that occur due to the viscous effects of water. A significant contribution to the non-linear viscous loads is the loads arising from flow separation resulting in a pressure loss. A semi-empirical formulation is used to model these loads.

The non-linear viscous loads are decomposed into those arising from flow separation in the longitudinal direction and those associated with flow separation in the transverse direction of the vessel. The loads in the longitudinal direction are accounted for in the resistance of the vessel. Hence the module only computes the loads due to the flow separation in the transverse direction.

Sectional loads arising from pressure loss can be estimated using the sectional drag coefficient C_D, local transverse velocity $v + xr$ and the sectional drafts $T(x)$. The general formulation for the transverse viscous force Y_{CF}, yaw moment N_{CF}, and roll moment K_{CF} can be expressed as :

$$Y_{CF} = -0.5\rho \int_L C_D(v + xr)|v + xr|T(x)dx \tag{3.1}$$

$$N_{CF} = -0.5\rho \int_L C_D(v + xr)|v + xr|T(x)xdx \tag{3.2}$$

$$K_{CF} = -Y_{CF}(KG - 0.65T) \tag{3.3}$$

where,

Y_{CF}	Sway force due to flow separation
N_{CF}	Yaw moment due to flow separation
K_{CF}	Roll moment due to flow separation
ρ	Density of the fluid
C_D	Sectional drag coefficient
v	sway velocity
r	yaw velocity
x	x-coordinate of the section
T(x)	sectional still water draft
KG	height of the center of gravity above the ship keel

It is a common practice to assume C_D to be a constant value for the hull and this value is tuned based on experience. However, the non-linear drag force component becomes dominant when the drift angle is large. Hence an accurate estimate of this component is essential for simulating tight turns (Hooft 1994).

The estimation of sectional drag coefficient C_D is challenging as it is very sensitive to the local flow and form parameters of the vessel. Section 3.1 summarises the various factors affecting the steady-state sectional drag coefficient.

3.1 Factors affecting the sectional drag coefficient

The important parameters influencing the sectional drag coefficient of the vessel are :

- **Flow regime** The flow regime influences the location of the flow separation point. The flow separation occurs further downstream in turbulent flow as compared to laminar flow due to the larger fluid-momentum exchange in turbulent flows. Hence the drag coefficient is expected to be lower in turbulent flow regimes. Aarsnes (1984) studied the effect of different flow regimes on the sectional drag coefficient. From Figure 3.1 it can be observed that in subcritical conditions i.e. laminar flow there are two vortical structures indicating two separation points whereas in transcritical conditions i.e. in turbulent flow, there is only one separation point as the flow remains attached. Hence, the drag coefficient obtained is different in these two cases.

- **Free surface effects** The action of the free surface can be approximated to that of a splitter plate under the rigid wall assumption of the free surface. It forces the wake of the flow to be symmetric (O. M. Faltinsen 1990). The drag coefficient is lower in the case of symmetric wake compared to the case of alternate vortex shedding. Hence the influence of the free surface is to reduce the drag coefficient.

(a) Subcritical condition **(b)** Transcritical condition

Figure 3.1: Influence of flow regimes on flow separation (Aarsnes 1984)

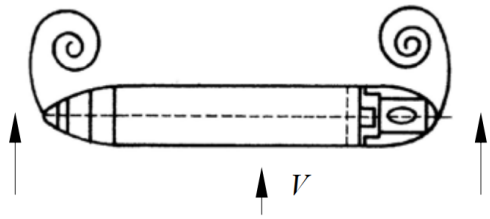

Figure 3.2: Vortical structures at ship ends (O. M. Faltinsen 1990)

- **Three-dimensional effects** Flow separation at the ends of the body leads to the formation of vortical structures as shown in Figure 3.2. The induced velocity due to these vortices tends to reduce the local inflow velocity at the ends. Hence the drag force contribution from the end sections reduces (Aarsnes 1984). The reduction factor for the drag coefficient for KCS hull is shown in Figure 3.4.
- **Cross sectional shape** The B/D ratio, bilge keels, and bilge radius influences the drag coefficient. B/D ratio does not have a large influence on the drag coefficient unless it becomes sufficiently small (< 0.8). When the bilge radius is increased the drag coefficient reduces due to the reduced intensity of the vortex shedding. Bilge keel forces the flow to be similar to the flow around a rectangular section with sharp corners, hence increasing the drag coefficient.

3.2 Estimation of drag coefficient

Rabliås and Kristiansen (2021) proposed four methods for estimation of the drag coefficient - one is based on the cross-flow approach and the other three are based on 2D+t theory. The methods are exemplified and the results, when they are applied to KCS and DTC hull, are presented. Further the 2D+t methods proposed by Rabliås and Kristiansen (2021) were modified to utilise the results of 2D CFD simulations performed in Section 5.9.1.

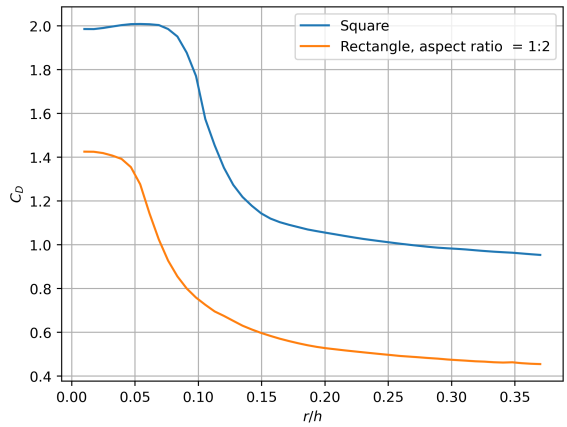

Figure 3.3: Steady drag coefficient against the ratio of bilge radius(r) and 2d for square and rectangular section with b/2d = 2 (Hoerner 1965)

3.2.1 Cross-flow method

The basic assumption behind the cross-flow approach is that the longitudinal component of the flow velocity does not influence the transverse drag. It only depends on the local transverse velocity component. Hence, the different cross-sections are considered to be hydrodynamically independent. Transverse force per unit length is computed for each cross-section using the steady value of the drag coefficient and integrated along the length to obtain the total 3D transverse force. This approach is valid for drift which ranges from $\approx 45 - 60$ deg. to 90 deg. i.e. when the longitudinal velocity component of flow velocity is small.

The procedure for estimation of the drag coefficient by cross-flow approach is summarised below :

- For sections which can be approximated as rectangular with a bilge radius, the breadth (B), draft (T), and bilge radius (r) is determined. The drag coefficient when $r \rightarrow 0$ ($C_{D,sharp}$) and $r \rightarrow \infty$ is obtained from Figure 3.3, from the limiting values at the left and right ends of the plot for a square and rectangular section with $\frac{b}{2d} = 2$. The limiting values for the required $\frac{b}{2d}$ is then computed by interpolation between these two values.

- The effect of bilge radius is accounted by using the expression

$$C_D = C_1 e^{-kr/d} + C_2$$

with k = 6. The value of C_2 can be determined by setting $r \rightarrow \infty$. Value of C_2 will be the limiting value obtained above when $r \rightarrow \infty$. When $r \rightarrow 0$,

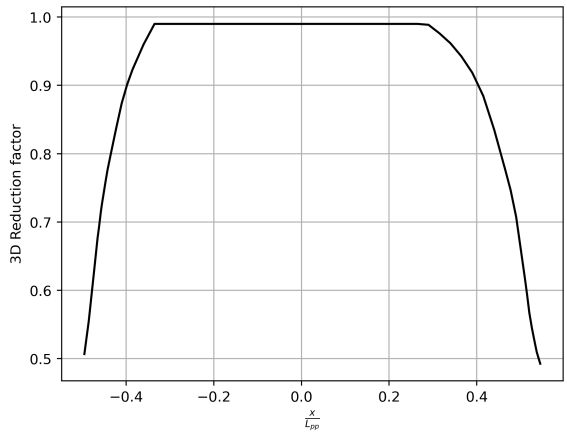

Figure 3.4: Reduction factor for C_D along the hull for KCS vessel considering three-dimensional effects from Aarsnes (1984)

$C_1 + C_2 = C_{D,sharp}$. C_1 can then be determined from this expression. Hence, C_D including the bilge radius can be computed.

- The effect of bilge keel is considered by setting the bilge radius of the section to zero i.e. a sharp bilge is considered.
- To consider the free-surface effects, the drag coefficient is reduced by 27.3% (Shen 2018).
- To account for three-dimensional effects, a reduction factor is applied as shown in Figure 3.4. The reduction factor is obtained by considering a similar trend as in Aarsnes (1984).
- For sections which cannot be approximated as rectangular with a bilge radius especially at the fore and aft ends, the steady drag of a similar section from Aarsnes (1984) is used.

Based on this procedure the drag coefficient obtained for KCS and DTC hull is shown in Figures 3.5(a) and 3.5(b). From the plots, it can be observed that there is a sudden jump in drag coefficient around the midship section in the DTC hull which is not present in KCS. This is due to the presence of bilge keel in DTC hull which was accounted by considering the drag coefficient of these sections to be equal to $C_{D,sharp}$.

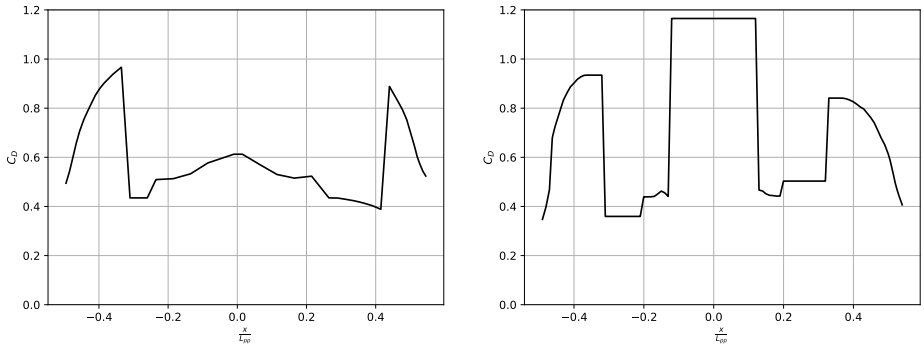

(a) KCS vessel

(b) DTC vessel (Rabliås and Kristiansen 2021)

Figure 3.5: Drag coefficient obtained using cross-flow approach.

3.2.2 2D+t method

When the longitudinal velocity component is significant, there will be a certain length starting from the bow where the flow remains attached to the hull and then the flow separation develops along the hull as shown in Figure 3.6. This means that the flow at a cross-section is influenced by the previous cross-sections and hence now the different cross-sections are not hydrodynamically independent and the 2D+t theory captures this influence by establishing an analogy between the variation of drag coefficient along the length of the hull to the time-varying drag coefficient in an impulsively started flow.

Consider a 2D+t coordinate system as shown in Figure 3.7. The π plane is earth fixed and the ship passes through the plane. At any instant τ, the coordinate of the section passing through the π plane can be obtained from the relation :

$$x_b - x_p = u(t) \cdot (\tau - \tau_0) \tag{3.4}$$

where x_b is the x-coordinate of the bow, x_p is the x-coordinate of the section passing through the π plane, both in the body-fixed coordinate system and τ_0 is the time instant at which the bow touches the π plane. Observing the motion in the π plane, it represents a time-varying geometry interacting with a transverse flow and as different cross-section passes through the plane, there will be a development of a vortex along the length of the hull. Hence within the π plane, the space coordinate is transformed into a time coordinate. At a time instant t, let the vessel have a forward speed $u(t)$, transverse speed $v(t)$ and yaw velocity $r(t)$. In order to calculate the drag coefficient variation long the length of the vessel, the transverse

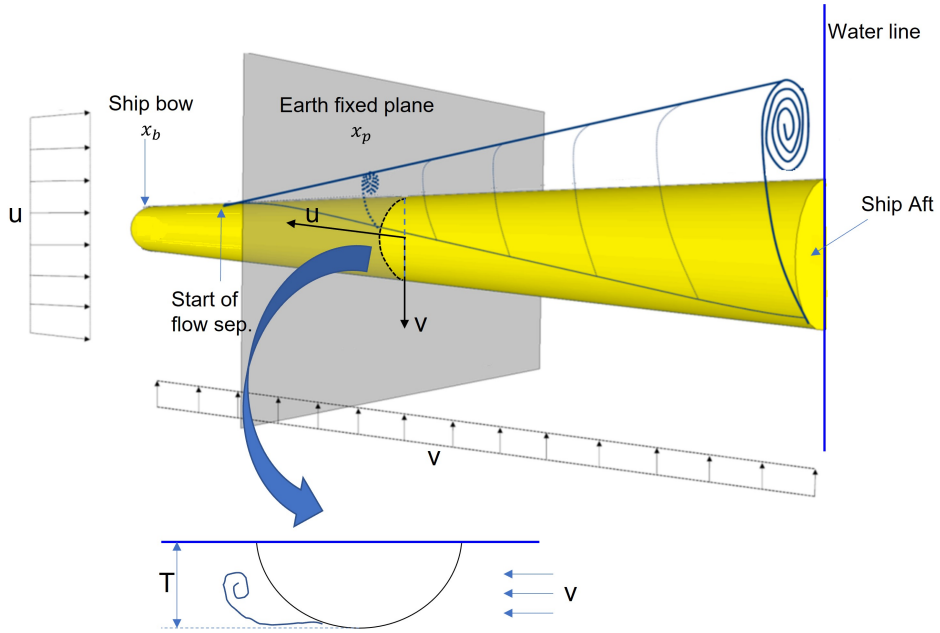

Figure 3.6: 2D+t theory for a ship moving with constant forward speed u and constant transverse speed v towards starboard (Figure adapted from Alsos and Odd M. Faltinsen (2018)). Yaw velocity is taken as zero. Flow separation starts from a certain distance from the bow of the vessel and developes along the hull.

distance moved by ship in the π plane has to be calculated as :

$$\begin{aligned} s_y &= \int_{\tau_0}^{\tau} [v(t) + x_p(\tau) r(t)] d\tau \\ &= v(t) \frac{x_b - x_p}{u(t)} + \frac{r(t)}{u(t)} [x_b(x_b - x_p) - \frac{1}{2}(x_b - x_p)^2] \end{aligned} \tag{3.5}$$

The non-dimensional time can be obtained as :

$$t^* = \frac{|s_y|}{T} \tag{3.6}$$

where T is the sectional draft. The non-dimensional time can then be used to determine the C_D for the section based on the time-varying drag coefficient of an impulse started flow for that particular section.

From Equations (3.5) and (3.6), the non-dimensional time for a given cross section and hence the drag coefficient distribution along the length of the hull will vary at each time step based on the drift angle ($tan^{-1}(\frac{-v}{u})$) and the ratio $\frac{r}{u}$. Figure 3.8

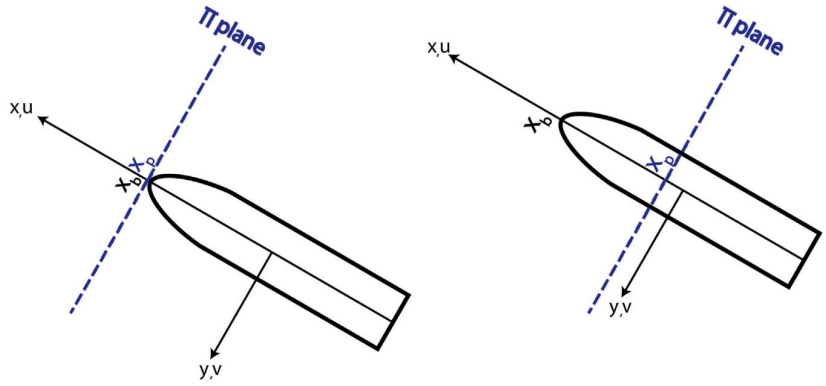

Figure 3.7: 2D+t coordinate system (Rabliås and Kristiansen 2021)

shows the variation of t^* along the DTC hull for different drift angles keeping u = 16 knots and r = 0.5 deg./sec. It can be observed that when $r \neq 0$, the variation of t^* along the hull will have a non-linear nature. The sudden increase in t^* towards the aft end is due to the small draft of these sections. The unusual nature of t^* for drift angle $\alpha = -5°$ is noted and will be discussed in detail in Section 6.4.1.

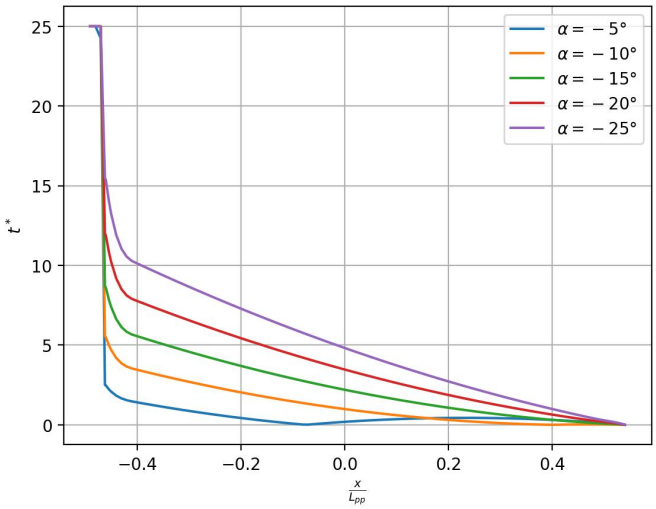

Figure 3.8: Variation of t^* along the hull for different drift angles for DTC hull using Equations (3.5) and (3.6). Forward speed u = 16 knots, r = -0.5 deg./sec and v is calculated based on drift angle. t^* is limited to 25 as the drag coefficient is expected to reach the steady-state value by this non-dimensional time

2D sectional shape of the vessel is varying in x-direction, hence in principle, to

apply 2D+t method in the ship maneuvering problem, the transient drag coefficient curve for each cross-section has to be obtained. Then the C_D for a given cross-section can be obtained from the corresponding transient drag coefficient curve at the t^* calculated for the cross-section. However, since the transient drag coefficient curve is not available for all the cross-sections, simplified methods are sought and 3 variants of the 2D+t method have been proposed by Rabliås and Kristiansen (2021). The difference in the methods arises from the approximations which are made to obtain the time-varying C_D curve for each cross-section along the hull.

2D+t^0 method

In 2D+t^0 method, the time-dependent C_D curve for a cross-section is obtained from a similar section in Aarsnes (1984) which is scaled to have the same steady drag coefficient for the section as computed in the cross-flow approach.

Based on this approach, the variation of the drag coefficient curve for KCS and DTC vessels are presented in Figures 3.9(a) and 3.9(b) respectively. The plots are generated by considering $u = 16$ knots and v is calculated based on the drift angle. The yaw rate is kept a constant at -0.5 deg./s. Five different time series for drag coefficient from Aarsnes (1984) is used in the DTC and KCS vessels.

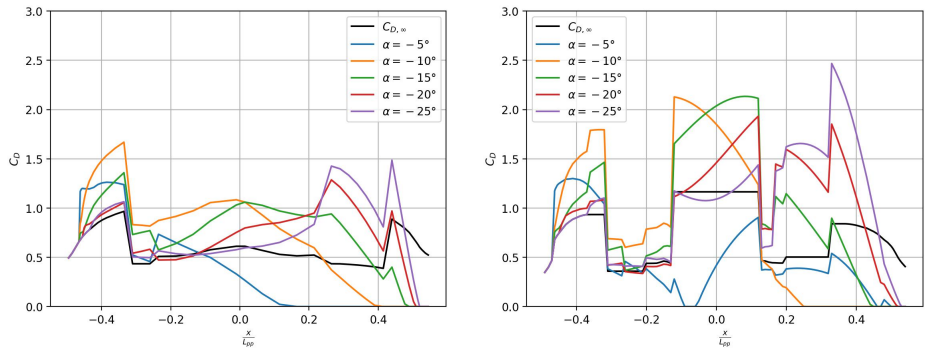

(a) KCS vessel **(b)** DTC vessel

Figure 3.9: Variation of C_D along the hull from 2D+t^0 method for different drift angles. Forward speed u = 16 knots, r = -0.5 deg./sec and v is calculated based on drift angle. The black curve indicates the C_D from cross flow approach.

The drag coefficient is initially zero at the forward end for some distance until the point where the flow separation starts. Then the drag coefficient increases following the selected time series. Towards the aft end, it can be seen that the drag coefficient coincides with the steady value. The discontinuities and jumps in the drag coefficient curve are caused when the time series is changed as well as due to the different scaling of the time series based on the value of the steady drag

coefficient at the section. Further, the drag coefficient for the DTC hull at $\alpha = -5°$ goes to zero near the midship of the vessel which is probably not physical. This is discussed in detail in Section 6.4.1.

As pointed out by Rabliås and Kristiansen (2021), the discontinuities and jumps in the drag coefficient curve are not physically consistent with a vortex developing along the hull. The next two methods attempt to resolve this issue.

2D+t^{cyl} method

In this method, the time-dependent C_D curve is obtained by scaling the drag coefficient curve for a cylinder from Sarpkaya (1966) such that the steady-state value of C_D is equal to the mean of the drag coefficients obtained in the cross-flow approach. The motivation for this is to obtain a smooth curve for C_D along the length of the vessel.

The resulting drag coefficient variation along the length of the hull is presented in Figures 3.10(a) and 3.10(b) for KCS and DTC hull respectively. The forward speed $u = 16$ knots and yaw velocity $r = -0.5$ deg./s in the plots.

The result (except for $\alpha = -5°$ for DTC vessel) is more consistent with the physical assumptions of the 2D+t approach. Again the sudden increase in the drag coefficient towards the aft end is due to the low draft of these sections leading to a jump in the non-dimensional time.

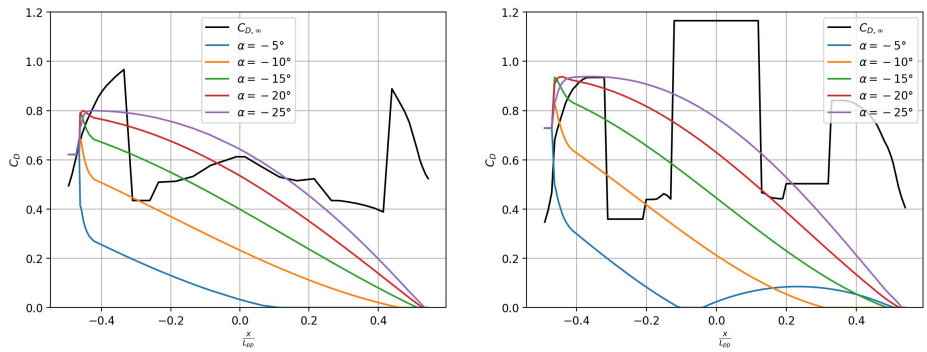

(a) KCS vessel **(b)** DTC vessel

Figure 3.10: Variation of C_D along the hull from 2D+t^{cyl} method for different drift angles. Forward speed u = 16 knots, r = -0.5 deg./sec and v is calculated based on drift angle. The black curve indicates the C_D from cross flow approach.

2D+t method

In this method the time-dependent C_D curve is generated in such a way that for a given cross-section, the time rate of change of C_D is obtained from a similar section from Aarsnes (1984), which is scaled so that the steady-state value is same as that obtained from the cross-flow approach for the section. Hence in contrast to the 2D+t^0 method, scaled $\frac{dC_D}{dt}$ is used instead of scaled C_D for a similar section from Aarsnes (1984). Once the time rate of change of C_D or $\frac{dC_D}{dt}$ is determined for each section along the hull, then the curve $C_D^*(t')$ is generated by integrating $\frac{dC_D}{dt}$ along the hull as shown in Equation (3.7).

$$C_D^*(t') = C_D(t_0) + \int_{t_0}^{t'} \frac{dC_D(t)}{dt} dt \tag{3.7}$$

with $C_D(t_0) = 0$ at the bow of the vessel. Then as $t' \to \infty$, the value of C_D must go towards the steady-state value. Assuming that the steady-state value is the mean value of C_D as obtained from the cross-flow approach, the entire curve is scaled so that near the aft section where $t^* > 10$, the final C_D curve will show the steady-state value. For Aarsnes (1984) sections as seen in Figure 4.2, it is assumed that steady-state occurs at $t^* \geq 10$. However, when integrating $\frac{dC_D}{dt}$ at some drift angles t^* may be less than 10 even at the aft section i.e. the steady-state is not reached. In this case, additional fictitious sections are considered towards the aft of the vessel so that the steady-state is reached and the value of C_D at the final section is used for scaling.

This results in a smooth curve which at the same time will account for the geometric variation of the cross-section in the x-direction and is more consistent with the assumption of a vortex developing along the hull. The resulting drag coefficient variation along the length of the hull is presented in Figures 3.11(a) and 3.11(b) for KCS and DTC hull respectively. The forward speed $u = 16$ knots and yaw velocity $r = -0.5$ deg./s in the plots.

Comparison of C_D curve obtained from the four methods against experimental results obtained from segmented model tests shown in Figure 4.4 indicate that the trend of C_D distribution presented by 2D+t method is the best fit for experimental data.

2D+t$^{0,\ 2D\text{-}CFD}$ method

This method is a modification of the 2D+t^0 method which was proposed by Rabliås and Kristiansen (2021). Instead of using scaled drag curves of Aarsnes (1984), the smoothed transient drag coefficient curves generated by using 2D RANS simulations described in Section 5.9.1 are used. Smoothing is necessary as in the sub-

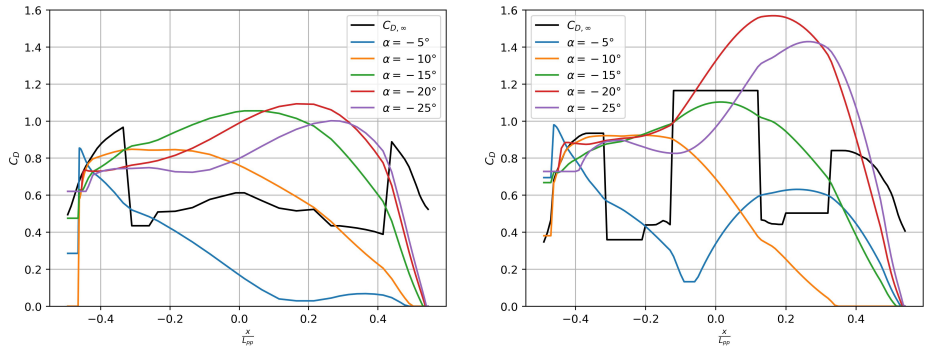

(a) KCS vessel **(b)** DTC vessel

Figure 3.11: Variation of C_D along the hull from 2D+t method for different drift angles. Forward speed u = 16 knots, r = -0.5 deg./sec and v is calculated based on drift angle. The black curve indicates the C_D from cross flow approach.

sequent method (2D+t$^{\text{2D-CFD}}$) the slope $\frac{dC_D}{dt}$ has to be calculated. A comparison between the transient drag coefficient curve obtained from 2D RANS simulations and smoothed curves for DTC vessel is presented in Figure 3.12. A good agreement is seen between the smoothed and the original version.

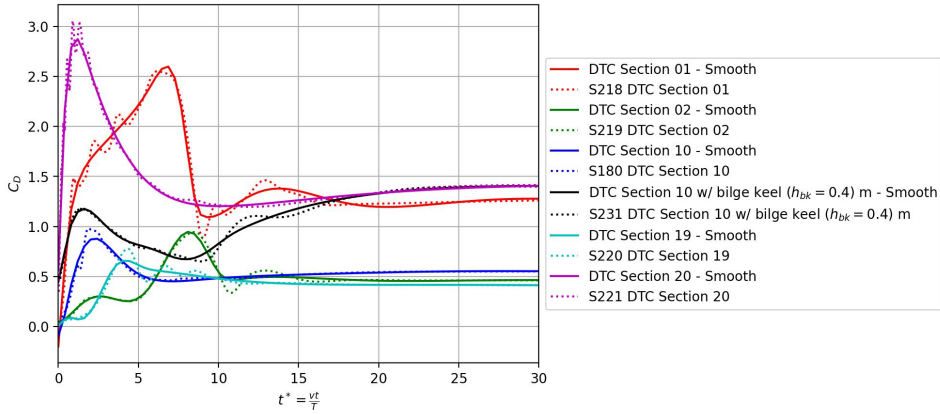

Figure 3.12: Comparison between transient drag coefficient for DTC vessel sections obtained from 2D-CFD and smoothed curves. The reference for section numbers are shown in Figure 5.21(b). Sections marked as SXXX are the 2D RANS simulation results.

Following the same procedure as used in 2D+t^0 method, the final resulting drag coefficient variation along the length of the hull is presented in Figure 3.13 for DTC hull. The forward speed $u = 16$ knots and yaw velocity $r = -0.5$ deg./s in the plot.

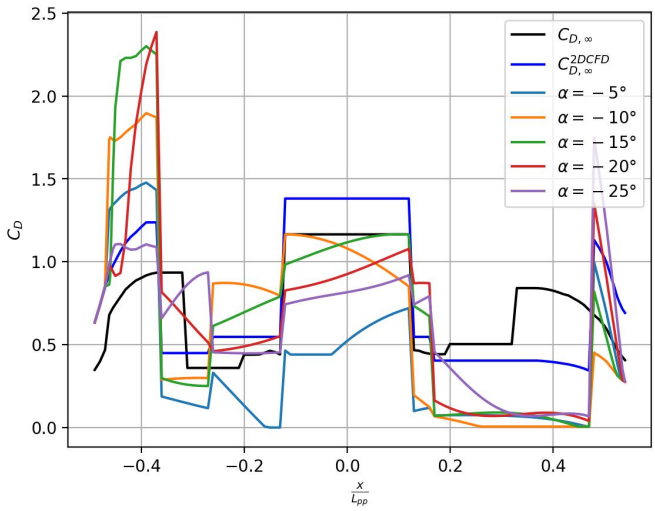

Figure 3.13: Variation of C_D along the hull from 2D+t$^{0,2d\text{-}CFD}$ method for different drift angles. Forward speed u = 16 knots, r = -0.5 deg./sec and v is calculated based on drift angle. The black curve indicates the C_D from cross flow approach using empirical methods described in Section 3.2.1 whereas the blue curve is based on the steady value obtained from 2D CFD.

2D+t$^{2D\text{-}CFD}$ method

Similar to 2D+t^{0,CFD} method, 2D+t$^{2D\text{-}CFD}$ is a modification of the original 2D+t method of Rabliås and Kristiansen (2021). Instead of using slopes from scaled Aarsnes (1984) curves, the smoothed curves shown in Figure 3.12 is used. Further, it was also found necessary to smooth extensively the curve of $\frac{dC_D}{dt}$ to obtain a physically meaningful drag coefficient variation along the hull.

Following the same procedure as used in 2D+t method, the final resulting drag coefficient variation along the length of the hull is presented in Figure 3.14 for DTC hull. The forward speed $u = 16$ knots and yaw velocity $r = -0.5$ deg./s in the plot.

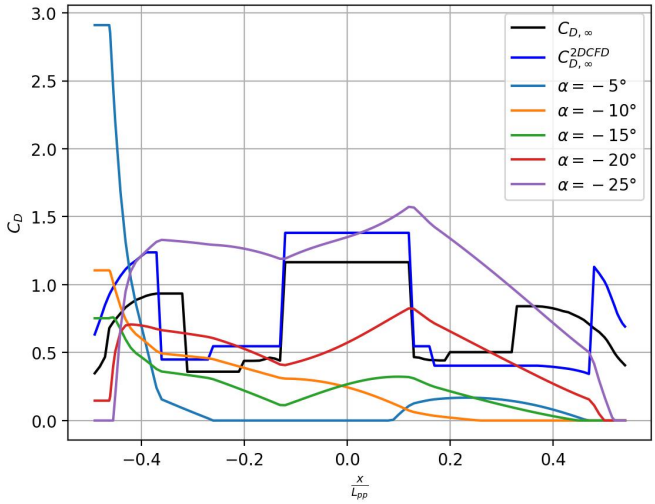

Figure 3.14: Variation of C_D along the hull from 2D+t$^{\text{2d-CFD}}$ method for different drift angles. Forward speed u = 16 knots, r = -0.5 deg./sec and v is calculated based on drift angle. The black curve indicates the C_D from cross flow approach using empirical methods described in Section 3.2.1 whereas the blue curve is based on the steady value obtained from 2D CFD.

Chapter 4

Experimental study of non-linear viscous loads

4.1 Motivation

The unsteady sectional drag coefficient is the basic input for the calculation of the non-linear viscous loads on the vessel during maneuvering, using the 2D+t methods proposed by Rabliås and Kristiansen (2021) as elaborated in Chapter 3. An experimental study to determine the transient sectional drag coefficient is motivated by the following :

- **Uncertainty regarding the unsteady drag coefficient curves in the literature**: Sarpkaya (1966) experimentally determined the unsteady drag coefficient curve for a circular cylinder for Reynolds numbers in the range 15000 to 120000. A single curve for the development of the drag coefficient over time was obtained for the whole range of Reynolds number and it was noted that there was no significant influence of Reynolds number on the obtained curve. This curve is plotted in Figure 4.1. C_D is plotted against non-dimensional time, which is given as $t^* = \frac{vt}{R}$, where v is the steady flow speed, t is the time and R is the radius of the cylinder. The drag coefficient increases rapidly and achieves a peak value close to 1.6 at the non-dimensional time $t^* = 8$ and then reduces to a steady-state average value of 1.2. Further in an updated report from Sarpkaya (1978) for Re = 32000, the peak value is ≈ 1.6 which occurs at $t^* = 5$. Hall (1987) attributed the difference in the curves obtained in Sarpkaya (1966) and Sarpkaya (1978) to the differences in the experimental facility - the latter had a more rapid initial acceleration at the start-up than the former, thus the latter is believed to be a more accur-

ate representation of flow around impulsively started cylinder. The results of high resolution DNS (Direct Numerical Simulation) performed by Koumoutsakos and Leonard (1995) for Re of 9500 indicates a peak value of 1.9 which occurs close to $t^* = 4$. The numerical result from Rumsey (1988) indicates a peak value of 1.4 which occurs close to $t^* = 3.5$. The different curves for unsteady drag coefficient for cylinder obtained from literature are presented in Figure 4.1. It is observed that they do not agree with each other regarding the timescale at which the drag coefficient develops nor the peak value of the drag coefficient.

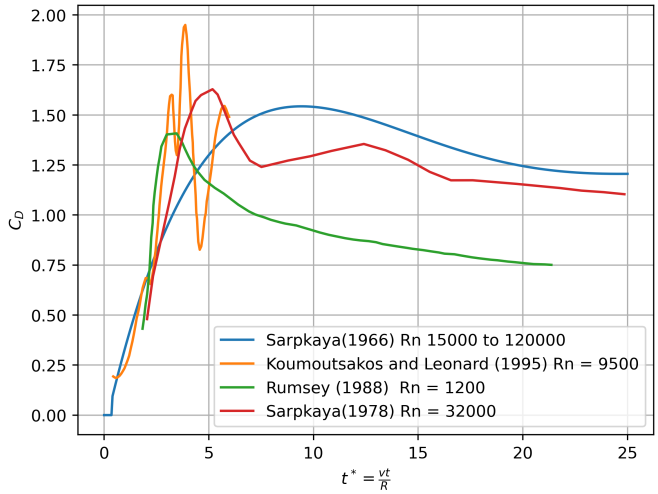

Figure 4.1: Comparison of the unsteady drag coefficient for circular cylinder from different sources in the literature (Sarpkaya (1966), Koumoutsakos and Leonard (1995), Rumsey (1988) and Sarpkaya (1978)). The drag coefficient is plotted against non-dimensional time defined as $t^* = \frac{vt}{R}$.

- **Limited number of experimental or numerical studies done in literature regarding nature of transient drag coefficient of ship shaped sections** : The development of drag coefficient around circular cylinder has been studied both experimentally as well as numerically, however such information about ship-shaped sections is limited. Aarsnes (1984) used a vortex tracking method to compute the unsteady drag coefficient curve for a 60,000 dwt tanker. Arslan et al. (2016) performed LES calculations to obtain the drag coefficient for the same 2D sections as in Aarsnes (1984), but he does not present the curve for development of the drag coefficient with time. Figure 4.2 indicates the drag coefficient curves from Aarsnes (1984) for the ship sections indicated in Figure 5.14 and the result for circular cylinder ob-

tained from Sarpkaya (1966). It can be observed that the time scale at which the drag coefficient for ship sections achieve the steady value is smaller as compared to the cylinder. It was theorised in Rabliås and Kristiansen (2021) that this may be because the onset of flow separation is almost immediate in case of the ship shaped sections as compared to the case of a circular cylinder.

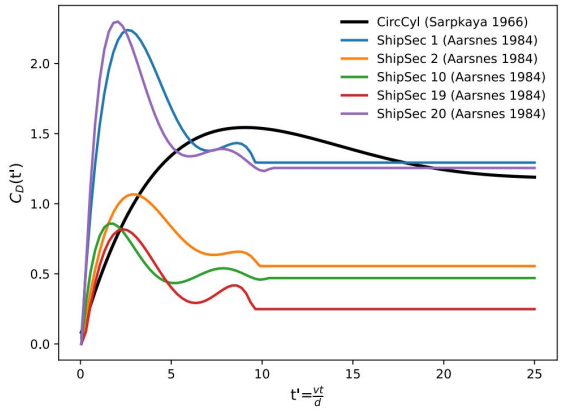

Figure 4.2: Comparison of transient drag coefficient for cylindrical section (Sarpkaya 1966) and ship sections (Aarsnes 1984). The ship sections numbers referred in the figure corresponds to the ship sections presented in Figure 5.14 (from Rabliås and Kristiansen 2021)

Hence, an experimental study to increase the understanding of the behavior of transient sectional drag coefficient was considered to be essential.

4.2 Previous experimental works

A brief summary of three different experimental approaches to quantify the sectional drag coefficient is described below :

- **Vertical water tunnel experiments** Sarpkaya (1966, 1978) used a vertical water tunnel with butterfly valve at the bottom to establish an impulsively started flow across a cylinder. Different accelerations could be realized by changing the rate at which the valve was opened. The acceleration measurements were made by measuring the pressure difference between two pressure taps. Velocity measurements were made by using 4 different methods - using a pitot tube, variable resistance probe, displacement-time curve by using uniformly spaced terminals on the tunnel wall, and also from the motion pictures. In Sarpkaya (1978) the acceleration phase was limited to 0.05

s for steady velocities of about 0.4 m/s whereas in Sarpkaya (1966) the acceleration phase was for about 0.1 s. The results from these experiments are presented in Figure 4.1.

- **Segmented model tests** These experiments were performed by Beukeinian (1989) and Clarke (1972). The basic setup consists of a ship model which is divided into segments. Each segment is then connected to a beam through a stain gauge dynamometer which measures the sway force on the segment. The arrangement is presented in Figure 4.3. The vessel is towed at different drift angles and the linear and non-linear component associated with the sway force is obtained.

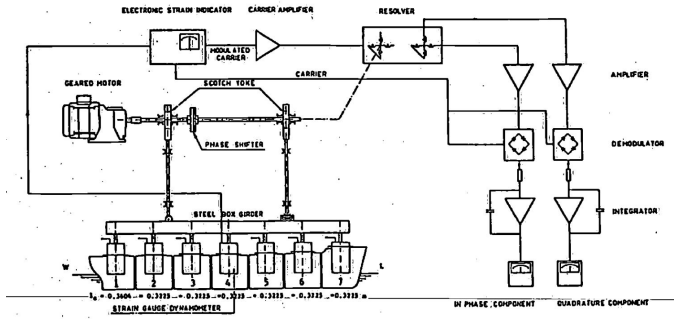

Figure 4.3: Segmented model test (Beukeinian 1989)

Detailed analysis to obtain the linear and non-linear sway force components has been presented by Hooft (1994). The obtained drag coefficient distribution for experiments done by Beukeinian (1989) for Todd 70 hull form at $Fn = 0.15$ is presented in Figure 4.4.

The following conclusions regarding the sectional drag coefficients can be made :

- The drag coefficient at the forward-most section is very large. It is theorized in Hooft (1994) that this is due to the bow wave. This goes against the results of 2D+t theory presented by Rabliås and Kristiansen (2021) in which the drag coefficient is very low at the bow as the effect of the bow wave is not considered in 2D+t theory.
- If this large value of C_D at the bow segment is discounted, the results indicate that for low drift angles C_D increases till it attains a maximum value at some section aft of the bow and then decreases a little as we go further aft. This trend is in agreement with the 2D+t theory presented by Rabliås and Kristiansen (2021).

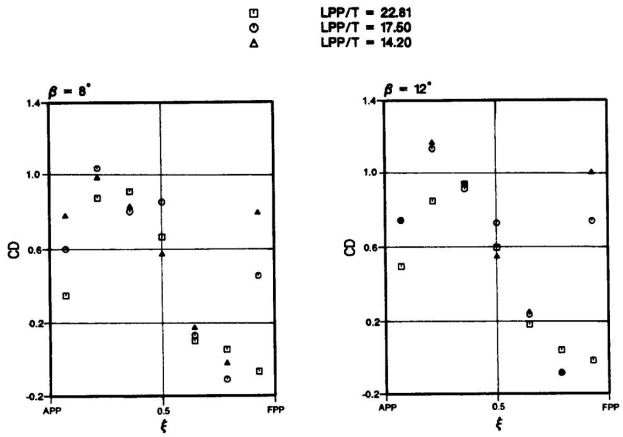

Figure 4.4: Drag coefficient distribution over Todd 70 hull form at Fn = 0.15 for different drafts and drift angle β (Hooft 1994)

– Further it was observed that if the drift angle is higher then the C_D curve is shifted forward. This trend is also in agreement with the 2D+t theory presented by Rabliås and Kristiansen (2021).

- **2D Sectional Model tests** This method was used by Aarsnes (1984). The basic approach was to consider a set of typical cross-sections from the full 3D hull. The cross-sections were selected in such a way that the major cross-sections along the 3D hull are represented. Then, prismatic models are built such that each model has a single cross-section along its entire length. These 2D sectional models were then towed vertically in the towing tank using the arrangement presented in Figure 4.5.

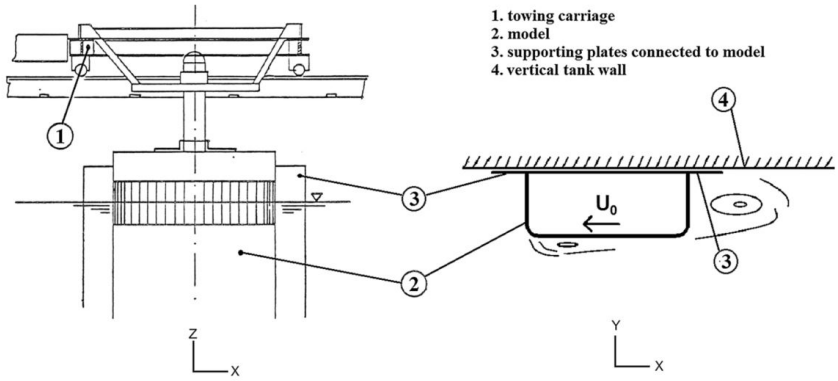

Figure 4.5: Experimental setup used by Aarsnes (1984) (Arslan et al. 2016)

The 2D sectional models have a supporting plate mounted as shown in Figure 4.5 and are towed very close to the vertical wall of the tank. This is done in order to simulate the effect of the free surface in a simplified manner. The model is then towed at small speeds so as to reduce the disturbance on the free surface. The force acting on the models was recorded from which the drag coefficients are obtained. The towing velocity used was 0.3 m/s and the start-up acceleration attained was 0.5 m/s^2.

4.2.1 Discussion on the experimental approaches

The segmented model tests can provide the actual longitudinal distribution of C_D for a given hull form and can be used directly to validate the distributions obtained from different methods proposed by Rabliås and Kristiansen (2021) for different drift angles. However, it does not directly provide the time-varying drag coefficient for individual sections. This can be indirectly obtained by performing the test at different drift angles and speeds. For each drift angle and speed, the value of C_D at a given cross-section will correspond to a particular non-dimensional time. Hence by changing the drift angle and speed, it is theoretically possible to generate the time-varying sectional drag coefficient assuming the drag coefficient of the 3D hull follows the 2D+t theory. However, these tests will require the production of a segmented ship model and the associated instrumentation. Hence, it was decided to focus on the other two methods.

From the previous experimental approaches for the determination of the transient drag coefficient of 2D sections, the major challenges identified are:

- Establishing an impulsively started flow i.e. a near-instantaneous acceleration and thereafter the acceleration goes to zero.
- Instrumentation required to the capture the transient quantities

To perform the experiment based on the approach of Sarpkaya (1966, 1978) in a cavitation tunnel or circulating water tunnel at IMT (Institutt for Marin Teknikk) will require a large pump capacity to have a near-instantaneous start-up of flow and instrumentation to enable the measurement of the acceleration and the transient drag on the test sections. Pursuing a certain degree of simplicity, it was decided to proceed with the sectional-model test approach taken by Aarsnes (1984). Aarsnes (1984) focused on flow visualization which was necessary for developing his vortex tracking method and also provided the pressure distribution around the section in the steady-state. The focus of the current experiments is to record the transient drag on the sections during the start-up.

4.3 Model test

4.3.1 Objectives

The overall objective of the model tests is to determine the transient drag coefficient curve for 2D cross-section accounting for the free surface in a simplified manner. Two models are used and are described below :

- Midship section of DTC hull with and without bilge keel
- Semi-Circular section

4.3.2 Test environment

The experiments were performed in Ladertanken laboratory at NTNU, Tyholt campus. The facility consists of a wave tank of dimensions 13 m x 0.6 m x 1.3 m made from glass to enable visualization. It has a single flap wave generator on one end and a parabolic wave damping beach on the other end.

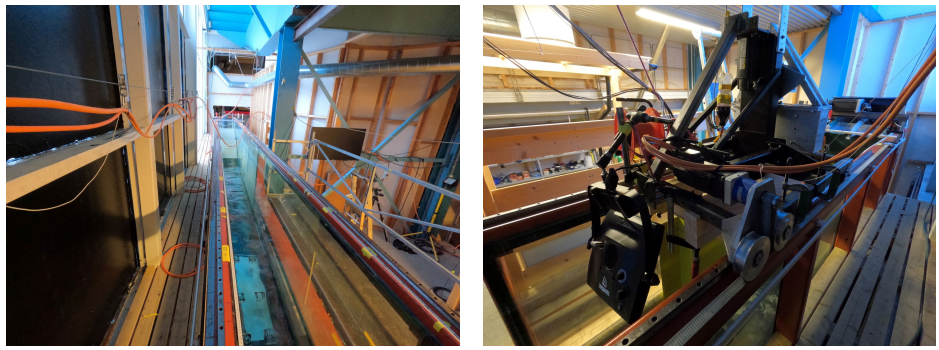

(a) Wave tank **(b)** Towing carriage

Figure 4.6: Laddertanken Laboratory, IMT NTNU

The laboratory has a towing carriage as shown in Figure 4.6(b). The rail length for the towing carriage is approximately 9 m. During the experiment, a rail length of 5 m was utilized due to the limitations associated with the cable length from the amplifier to the instrumentation on the carriage. Since start-up acceleration was very important for these tests, the towing carriage was tested and was found to be capable of producing an acceleration up to 2 m/s^2 (without the model attached).

The water level in the tank was maintained at 1 m. The experimental setup is shown in Figure 4.7.

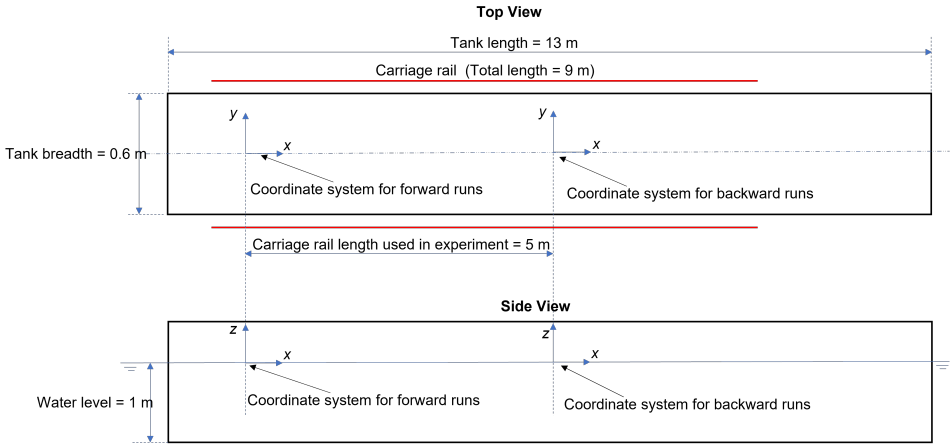

Figure 4.7: Experiment setup (not to scale) and the coordinate system. Zero-balancing is done at the left end of the carriage rails for forward direction runs and at the right end of the carriage rails for backward direction runs. Hence, the origin of the position recording is shifted for forward and backward runs.

Model	Cross Section	Model Mass (kg)
A	DTC midship section	76.25
B	Semi-circular section with radius 145 mm	35.58
C	DTC midship section with bilge keel of height 8 mm	76.25
D	DTC midship section with bilge keel of height 16 mm	76.25

Table 4.1: Model description and model mass (includes ballast mass and the aluminium plate fitted to the model)

4.3.3 Models

The full-scale particulars of DTC are indicated in Section 2.4. The model scale for the DTC section is selected as 1:100. Two different bilge keels with heights of 8 mm and 16 mm can be fitted onto the model. The semi-circular sectional model has a radius equal to the scaled draft of DTC hull. The length of both models is 1080 mm.

The models are designated as shown in Table 4.1. The details of the model are presented in Figure 4.8.

Model construction details

- T-profile was used as the main structural member for the model. This was

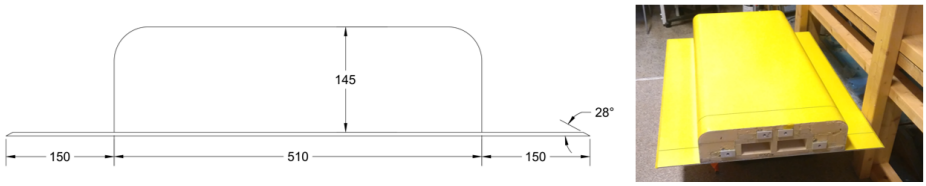

(a) Model A - DTC midship section

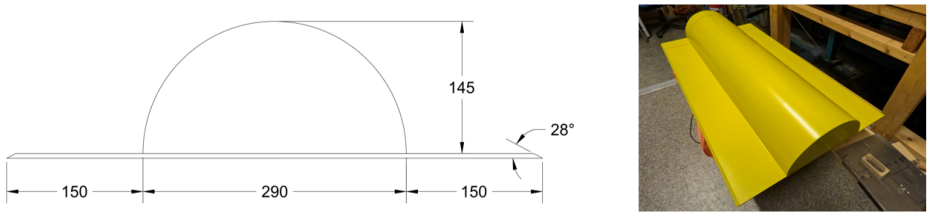

(b) Model B - Semi- circular cross section

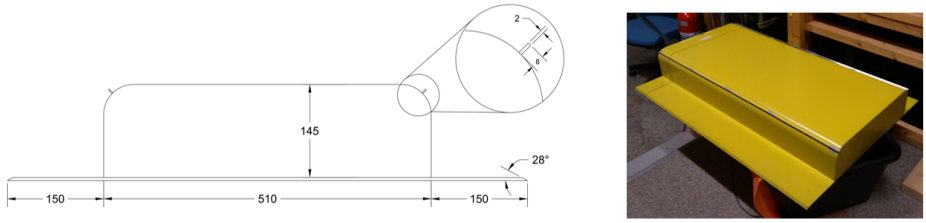

(c) Model C - cross section same as Model A but fitted with a bilge keel of height 8 mm

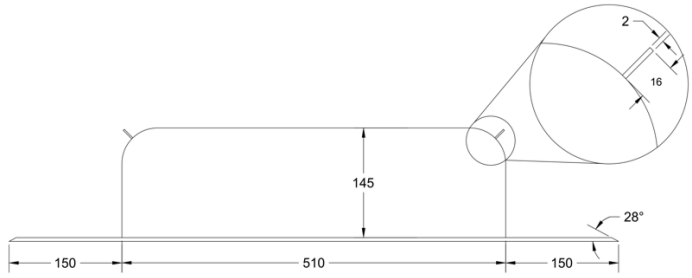

(d) Model D - cross section same as Model A but fitted with a bilge keel of height 16 mm

Figure 4.8: Models used in the experiment

to ensure that the model remains stiff during towing. This was essential to avoid additional hydrodynamic loads arising from the vibration of the model from being registered by the force transducers.

- Divynicell foam was then glued around the T-profile. The surface was then milled using a CNC machine to achieve the desired shape.
- After the testing of Model A (DTC midship section model), a groove was

cut on it to fit the bilge keel.

- Additional ballast weight was added to the model to make it neutrally buoyant so as to reduce back pressure on the force transducers due to the buoyancy of the model.
- The models were fitted with a 5 mm thick honey-comb supporting plate which has an overhang of 150 mm on each side of the model (see Figures 4.8 and 4.9(a)). The edges of the plate were sharpened to make it streamlined with the flow.
- On the top side, the models were provided with bolt holes to permit them to be bolted to a thick aluminum plate (see Figure 4.9(a)). Model A and B were provided with 4 and 3 such connection points respectively.
- The bilge keels were made of an aluminum sheet of thickness 2 mm, heights 8 mm and 16 mm, and length of approximately 1080 mm.

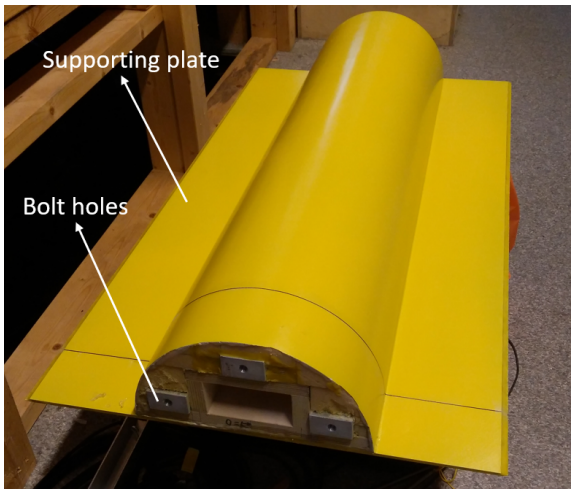

(a) Model B - supporting plate and bolt holes for mating with aluminium plate

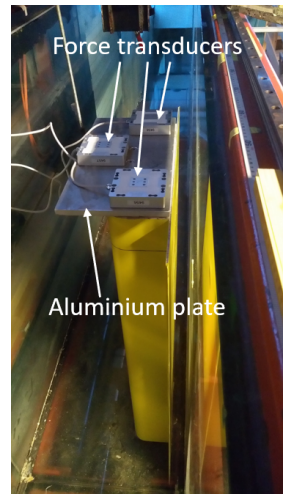

(b) Model A connected to an aluminium plate. The force transducers bolted on to the aluminium plate

Figure 4.9: Model construction and mounting details

4.3.4 Test setup

- The model is mounted on the carriage in such a way that the distance between the tank walls and the supporting plate on the model is approximately 10 mm

and the length of the model is such that once mounted the distance between the base of the model and the tank bottom wall is also approximately 15 mm.

- The thick aluminum plate mounted on the model is then connected to the measurement points of 3 force transducers (see Figure 4.9(b)).
- The force transducers are then connected to another aluminum plate at the top. The arrangement with the force transducer sandwiched between two aluminum plates facilitates easy change of the models. This plate is then bolted to a wooden frame which is fixed to the carriage (see Figure 4.10).

This aluminum plate is then bolted to 3 force transducers

The complete model test setup is shown in Figure 4.10.

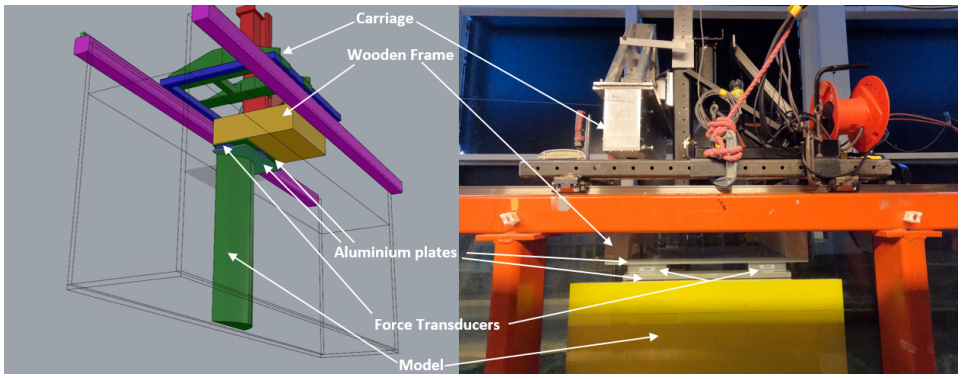

Figure 4.10: Model test setup (3D model visual provided by Trond Innset - Staff Engineer, IMT NTNU)

4.3.5 Model test principles

The following principles are considered during the design of the experiment :

- **Free surface representation** - In potential flow theory, the low frequency boundary condition on the free surface is given as $\frac{\partial \phi}{\partial z} = 0$, where ϕ is the velocity potential and z is in the direction perpendicular to the free surface (O. M. Faltinsen 1990). This implies that the free surface acts as a rigid wall and there is no velocity component perpendicular to it. In the experiment when the model is towed close to the wall, the free surface is assumed to be represented by the tank walls. However, the limitation of this approach is that in the experiments due to viscosity, a no-slip boundary condition is applicable on the tank walls. This results in the velocity component tangential to the wall being zero in addition to the perpendicular component,

which is not the case with a free surface. The error caused due to this is not quantified. To reduce the impact of the no-slip boundary condition on the wall from impacting the flow around the model and especially the vortices formed near the bilge when the model is towed, supporting plates are fitted with an overhang of 150 mm on both sides of the model (see Figure 4.8). This is the same approach adopted by (Aarsnes 1984). Hence within the experiment the free surface is simulated in a simplified manner.

- **2D flow** - The objective of the experiment is to obtain 2D transient drag coefficient, hence the flow around the model is assumed to be 2D. This assumption is violated at the bottom end of the model where there can be cross-flow across the tip and near the free surface. To reduce the error associated with this effect to the extent practically possible, the model length is set up in such a way that the base of the model is very close to the tank bottom wall.

- **Free surface disturbances** - The 2D flow assumption is also violated near the free surface, further disturbances on the free surface can lead to additional loads due to wave radiation. The towing speeds are selected in such a way that the Froude number associated with the breadth of the model is kept less than approximately 0.2 to ensure that the free surface disturbances are minimized. One of the reasons for towing the model in the vertical position rather than towing it horizontally is to reduce the water plane area which in turn reduces the free surface disturbances.

- **Blockage effect** - The model scale is selected in such a way that the model is not too small that the drag loads on it will be very small to be accurately captured by the force transducers. For the model scale of 1:100, the ratio of the scaled draft of the model to the width of the tank is 145/600 $\approx$ 0.25. Hence the flow speed experienced by the model is not the carriage speed. As a first approximation, the conservation of mass principle is applied to obtain a mean speed-up of the flow due to the blockage effect :

$$w_{tank} \cdot h_{tank} \cdot v_c = (w_{tank} \cdot h_{tank} - T \cdot h_{sub}) \cdot v \tag{4.1}$$

where,

w_{tank} width of the tank = 600 mm
h_{tank} water height in the tank = 1000 mm
v_c carriage speed
T draft of the model = 145 mm
v average corrected flow speed
h_{sub} Submerged length of model = h_{tank} - 15 = 985 mm, 15 mm is the gap at the bottom between the tank floor and model base

Substituting in Equation (4.1), the relation between the carriage speed and the average corrected flow speed can be obtained as $v = 1.312 \cdot v_c$.

4.3.6 Instrumentation

The instrumentation used in the tests are summarised below:

- **Force transducers** - 3 force transducers (Forsentek, Model- F3F-1kN) were used measure the forces on the model (see Figure 4.11(a)). Each transducer can output forces in all the three directions (X, Y and Z) has a capacity to measure up to 1 kN. The transducers were arranged and designated as 9456, 9457 and 9458 as shown in Figure 4.11(b).

(a) Forsentek, Model : F3F-1kN force transducer

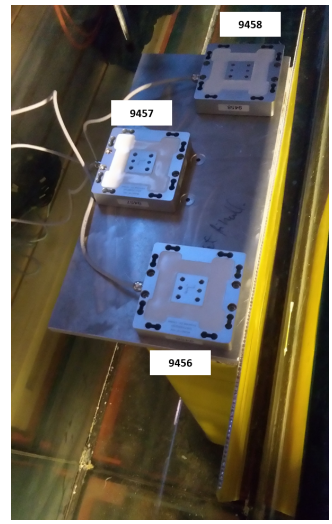

(b) Arrangement of force transducer and its designation

Figure 4.11: Force transducers used in the experiment

3 transducers ensure that the connection between the carriage and the model is rigid and the model will not oscillate due to the force it will experience

when it is towed. Based on the initial estimates, the major contribution to the load on the transducer will be from inertia which occurs during the initial acceleration phase.

The force transducers were calibrated before the start of the experiment. Since it is a triaxial transducer matrix calibration is performed in which a known force is applied in one direction and the response of the transducer is measured in all the three directions. This procedure is applied to generate a matrix of calibration coefficients. The calibration coefficients are then input as equations into the data acquisition software (catmanAP V5.5.1) so that it can output the forces in x, y and z direction of the transducers (refer Figure 4.7 for the definition of the coordinate system). After mounting the 3 transducers it was verified that the axes of the 3 transducers are aligned in the same direction by applying a force on the model in one direction and ensuring that the three transducers give readings of the same sign. The total towing force was then calculated as the sum of the x direction forces of the transducers.

- **Accelerometers** - Two uni-axial accelerometers were used to record the acceleration of the carriage and the model respectively (see Figure 4.12). The accelerometers on the model and the carriage are designated as 16241 and 6239 respectively.

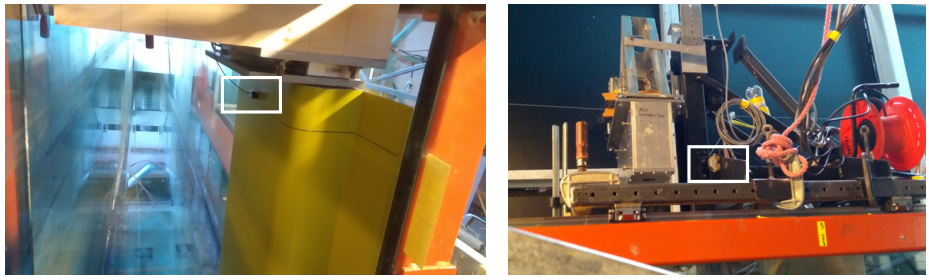

(a) Accelerometer on the model **(b)** Accelerometer on the carriage

Figure 4.12: Accelerometers used in the experiment

The accelerometer on the carriage measures the acceleration of the carriage and the model in the longitudinal direction. This is necessary to calculate the inertial loads (including the added mass loads) on the model during the acceleration phase. The inertial loads have to be subtracted from the total load registered by the transducers to obtain the drag load on the model.

The accelerometer on the model measures the acceleration of the model in the transverse direction at a point above the water level. This is used to

confirm that the model is not having any large undesired vibration during the tests.

- **Wave probes** - The wave heights are measured at two points - one in the forward and one at the aft of the model. These wave probes will be fitted to the carriage. Additionally, 2-3 wave probes will also be used which will be fixed to the tank sides. These probes will be used to confirm that the model does not generate any significant waves when towed.
- **Camera** - This is to capture the flow around the model. Fluorescent particles may be used to have a better visualization of the development of vortices with time around the model.

Sampling Frequency

The sampling frequency used for the force transducers, wave probes and accelerometer is 200 Hz, whereas the the carriage position and carriage speed is obtained from the carriage controller which has a sampling frequency of 50 Hz.

4.3.7 Towing speed and acceleration

Towing speed

The selection of towing speeds for the test took into account two considerations :

- As discussed in Section 4.3.5, the Froude number during towing has to be less than approximately 0.2 to minimise the disturbance of the free surface.
- The range of velocities must cover the realistic transverse velocities which shall be experienced by DTC vessel during maneuvering.

Based on the experiment results for DTC manoeuvers presented in Rabliås and Kristiansen 2021, the speeds for towing were decided as 0.1, 0.2, 0.3, and 0.4 m/s.

4.4 Post-processing

Measurements readings were obtained by towing the model with the test setup described in Section 4.3.4 and with the speeds specified in Section 4.3.7. The measurement readings obtained were not consistent with the theoretical expectations. Section 4.4.1 describes these inconsistencies encountered and Section 4.4.2 describes the possible explanations for these inconsistencies based on additional tests and observations.

In all the subsequent sections, a test case is used to explain the observations. The test case selected is Model A, Run 1, high acceleration run, forward direction, with

carriage speed set as 0.3 m/s. The time history of the wet run and dry run for this case is shown in Figures B.3 and B.19 respectively.

4.4.1 Inconsistencies in measurements readings with respect to theoretical expectations

Accelerometer measurement readings

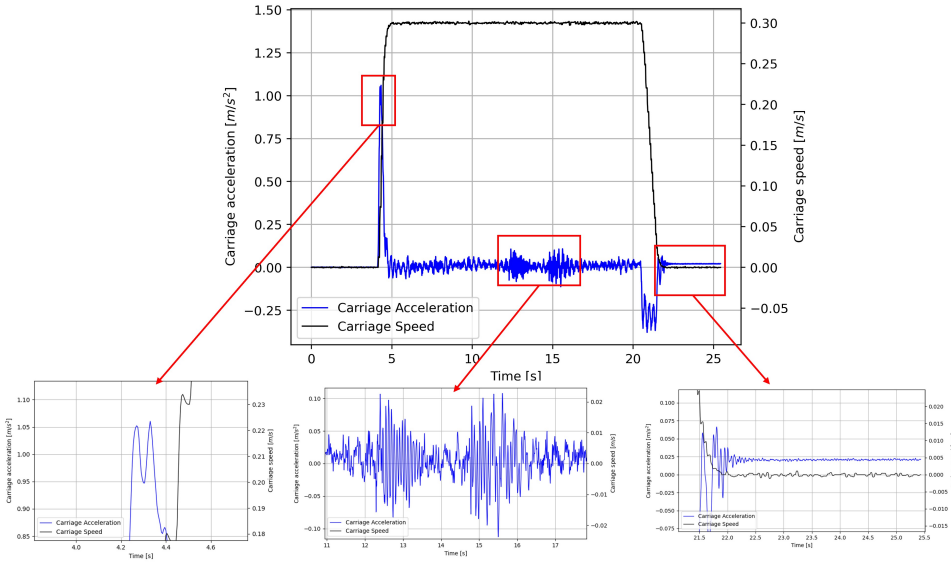

Figure 4.13: Time series for acceleration and velocity measurement of the carriage for model A, run 1, speed 0.3 m/s, forward direction, wet run

The acceleration for the carriage was initially set to 1 m/s^2. Theoretically, it was expected that the acceleration curve would have an instantaneous jump when the carriage starts to move and the acceleration would reach the peak value of 1 m/s^2. Beyond this the acceleration would remain constant at 1 m/s^2 until the carriage achieves the input speed, then the carriage acceleration is expected to go fall to zero and the carriage would move with a constant input speed. The experimentally obtained carriage acceleration and carriage speed for the test case is shown in Figure 4.13. The following observations are noted :

- **Accelerometer reading during the start-up phase** : The carriage is able to achieve a peak instantaneous acceleration value of 1 m/s^2 with a slight overshoot. Post this peak the acceleration has oscillations around 1 m/s^2.The carriage speed reaches the input speed of 0.3 m/s at t $\approx$ 4.9 s starting from rest at t $\approx$ 4.2 s. This average acceleration can be computed as 0.43 m/s^2.

- **Accelerometer readings during the steady speed phase**: Once the carriage reaches the input speed of 0.3 m/s, the carriage acceleration does not go to zero but has oscillations around zero-mean. In particular, these oscillations seem to peak between 12 to 17 s and achieves an amplitude close to 0.1 m/s^2.
- **Accelerometer readings after the carriage stops** : Once the carriage stops moving, the accelerometer reading remains at 0.02 m/s^2 and does not return to zero as expected.

Force transducer measurement readings

Theoretically the force in the x direction F_x recorded by the transducer can be expressed as :

$$F_x = -(m + m_a) \cdot a_x + F_{drag} \tag{4.2}$$

where,

F_x	Total force measured in x-direction
m	mass of the model
m_a	added mass of the model
a_x	acceleration in x-direction
F_{drag}	drag force in the x-direction

F_{drag} consists of the drag component associated with skin friction and the drag component associated with pressure loss due to flow separation. The skin friction component is very small in comparison to the component linked with the flow separation and can be neglected. F_{drag} can be expressed as :

$$F_D = \frac{1}{2}\rho C_D T v|v| \tag{4.3}$$

where,

ρ	density of water in the towing tank
C_D	drag coefficient
T	characteristic length of the model. For ship shaped cross-section models (Model A, C and D) this was taken as the ship draft whereas for the semi-circular cross section model (Model B) this was taken as the radius.
v	flow speed. In the experiment this was taken as the carriage speed corrected for the blockage effect

During the startup, before the occurrence of flow separation, the flow around the model can be assumed to be potential flow. Therefore the transducer is expected to indicate a large negative peak with a magnitude $\approx (m + m_a) \cdot a_x$ in the test case. This approximation holds true only for models without bilge keel. If a bilge keel is present, depending on its size, it can cause flow separation to develop during the startup phase itself.

In the test case (Model A which does not have a bilge keel), to verify if the values obtained from the measurements are physical, a rough estimate of the peak value for the case was calculated. The effect of the free surface was neglected and the cross-sectional shape was approximated as a rectangle with length 0.51 m and breadth of 0.145 m (see Figure 4.8(a)). The immersed length of the model was taken as 0.985 (1 m is the water level and 15 mm gap between the tank bottom and model base). From DNV-RP-H103 (2011) the added mass of this section was obtained as 30.9 kg. Hence the estimated peak value is $(76.25+30.9)\cdot 1 \approx 107\ N$. This is expected to be a crude approximation as this also does not consider the influence of the supporting plate or the tank walls as the model is very close to the wall.

In the steady speed phase the acceleration is expected to be zero, hence there will be no inertial loads. In this phase, a behavior similar to the evolution of drag coefficient shown in Figure 4.2 was expected, with the force slowly increasing from nearly zero to a peak negative value and then decreasing and reaching a negative steady-state value. During the deceleration phase the inertial component reappears and a peak positive value is expected. The force is then expected to go to zero once the carriage stops after the water in the tank settles down.

The force transducer reading and the carriage speed realized for the test case is shown in Figure 4.14. The following observations are noted :

- **Tow force readings during the start-up phase :** The peak value in the force seen during the initial acceleration phase is $\approx$ 130 N which is in general agreement with the estimated value.
- **Tow force readings during the steady speed phase :** In the steady speed state, the behaviour is not as expected. The tow force shows both a high frequency and a low frequency variation. As seen in the time series for acceleration (Figure 4.13), a peak in the oscillation amplitude is seen between 12 to 17 s. Neglecting the high frequency oscillations, the low frequency component appears to change sign and becomes positive between approximately 15 to 20 s. Also, a steady-state value as expected is also not attained.
- **Tow force readings after the carriage stops :** Similar to the accelerometer

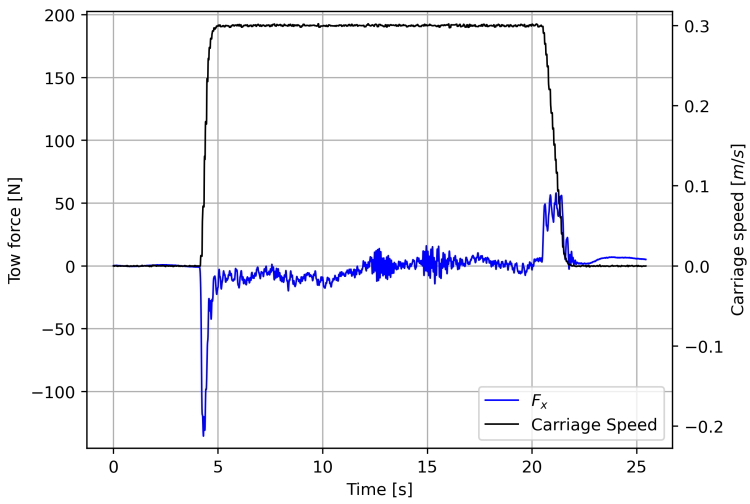

Figure 4.14: Time series for tow force and velocity measurement of the carriage for model A, run 1, speed 0.3 m/s, forward direction, wet run

readings, the tow force readings does not go to zero after the carriage stops even after sufficient time has been allowed for the water to settle down.

4.4.2 Explanation for inconsistencies in measurements readings with respect to theoretical expectations

Startup phase

The reason for the oscillations in acceleration in the startup phase is likely to be connected with mechanism used for driving the carriage. The carriage in Ladder-tanken Laboratory is belt driven as shown in Figure 4.15. The carriage belt runs along the length of the tank and is fixed at the two ends of the tank. The belt has grooves that lock on to the grooves on the motor shaft to propel the carriage when the motor rotates. The carriage and belt could be simplified as a spring-mass system with the belt and the motor speed control introducing stiffness in the system. Post the initial jerk during the start, the system possibly oscillates at its damped natural frequency which is the likely cause for the oscillations seen in the acceleration.

For studying the transient phenomenon connected with impulse start, it was essential to reduce these oscillations in acceleration to the extent practically possible. The following conclusions regarding the acceleration characteristics of the carriage were made based on further tests :

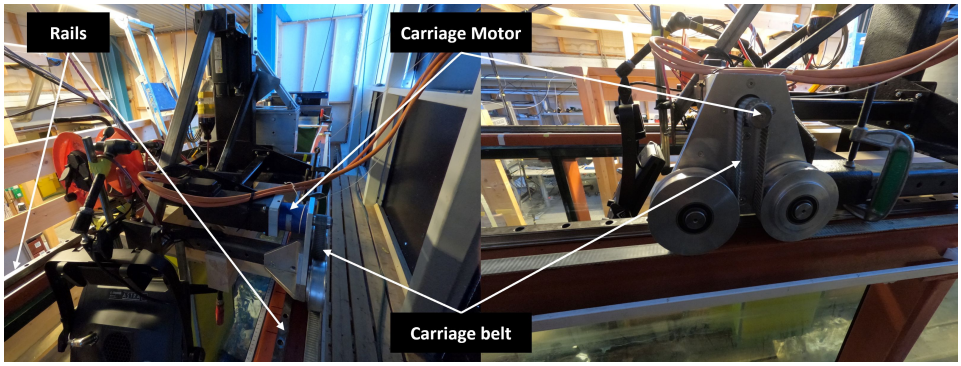

Figure 4.15: Details of the belt driven carriage at Laddertanken Laboratory

- The tension in the belt had a significant impact on the initial oscillations in the acceleration. When the tension in the belt was increased, it resulted in larger oscillations. This is probably because, increase in tension results in a higher stiffness leading to higher damped natural frequency in turn resulting in larger amplitude for oscillation in acceleration.

- Different startup accelerations were tested to find the setting which will reduce the oscillations. The resulting acceleration for 3 such cases, for Model A with carriage speed set to 0.3 m/s is shown in Figure 4.16. The shift of the curves along the time axis for the 3 cases is not important because the time at which the carriage was started was different for each run. The following are noted :

  - For low acceleration runs (acceleration input set to 0.1 m/s^2), there is no single peak in acceleration observed. Since the acceleration is low, the carriage oscillates around 0.1 m/s^2 for a longer time.
  - The maximum startup acceleration achievable is $\approx$ 1.6 m/s^2. However, it is noted that as the acceleration value is increased, the overshoot to the negative side post the initial peak also increases and it takes longer to dampen out the oscillation amplitudes.
  - High acceleration runs (acceleration input set to 1 m/s^2) appeared most promising setting for the testing, however this does not fully conform to the theoretical requirements.

    The quality of the startup accelerations has significant impact on the results of transient drag coefficient as seen from the difference in the curves presented by Sarpkaya (1966) and Sarpkaya (1978) (see Figure 4.1). Hence it was decided to run the models with different acceleration settings. Model A was run with all the three settings (low, high,

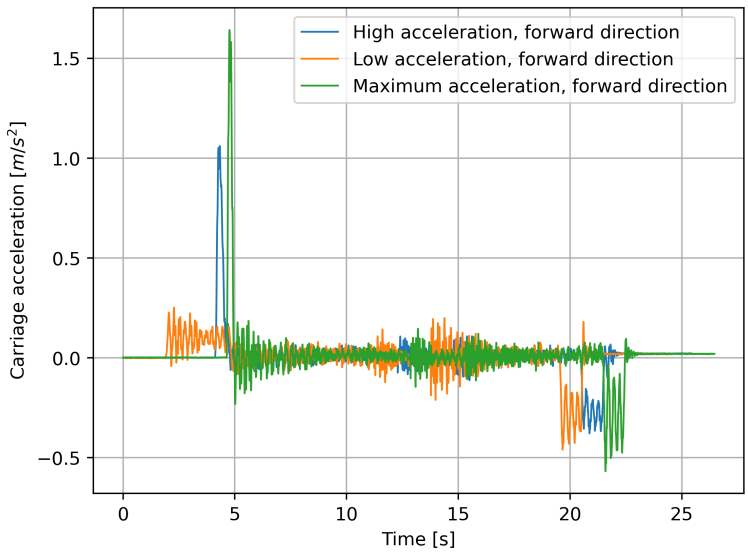

Figure 4.16: Time history for carriage acceleration model A, run 1, speed 0.3 m/s, forward direction, wet run with different startup acceleration values

and maximum acceleration) whereas Model B, C, and D were run with low and high acceleration settings.

– It was also noted that for a given acceleration setting, the input speed for the carriage (v_c) also affects the nature of oscillations during the startup. This can be seen in the acceleration time history plotted in Figure 4.17 for Model A, run with high acceleration settings for different speeds. The shift of the curves along the time axis is not relevant as the carriage was started at different time for different runs. The following observations are made :

  * The oscillations in accelerations near the peak is most prominent for $v_c = 0.4\ m/s$.
  * The overshoot of the acceleration to the negative side is minimum for $v_c = 0.3\ m/s$. This speed with the high acceleration setting was the closest to the theoretical acceleration desired, which could be practically produced with the carriage.

Steady speed phase

The oscillations in the accelerometer readings after the initial acceleration is likely to be connected with the speed control mechanism of the carriage motor and could

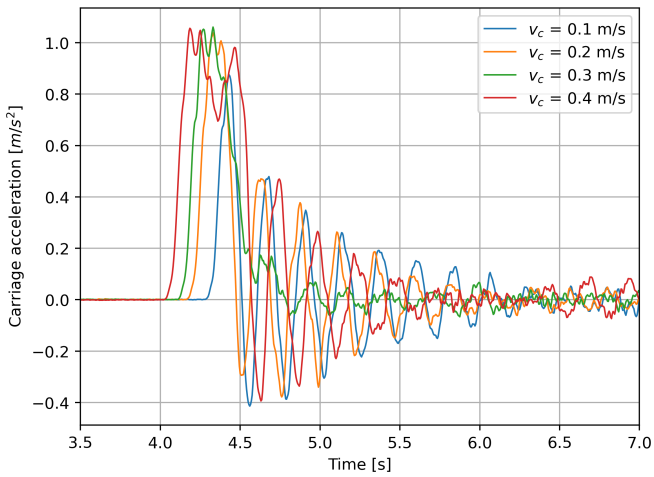

Figure 4.17: Time history for carriage acceleration model A, run 1, forward direction, wet run, high acceleration runs with different input carriage speeds v_c

not be reduced. The tow force and negative of the acceleration are plotted together in Figure 4.18. From the plot it can be observed that the high frequency oscillations seen in the time series plot from the accelerometer are also reflected at a 180 deg. phase difference on the forces registered by the force transducers. Hence it was concluded that the oscillations recorded by the accelerometer are physical and significant enough to induce inertial loads on the model.

The peaks in the oscillation amplitude of tow force and acceleration seen between between 12 to 17 s is probably connected with sudden external load associated with the arrangement which allows the transducer cables from the amplifier to be transferred to the moving carriage as shown in Figure 4.19. The setup used for transferring cables for the motor could not be utilized for the transducers due to limitations on the length of the cables.

The transducer cables were run through a pulley running on rails. To prevent tension on the cables, a rope is tied between the carriage and the pulley. The rope and cable length were adjusted in such a way that it remains slack during the initial start-up and for some time into the steady phase. The sudden peaks are seen in the acceleration and tow force curves are caused when the rope is in tension and the pulled onto to a new position. Even though this happens at the same position, there were slight differences during each repeat runs. Since the model is symmetric in positive and negative x-direction, it was decided to have repeat runs in both directions (forward and backward runs) to try to obtain the complete picture as this disturbance will occur at a different position when the

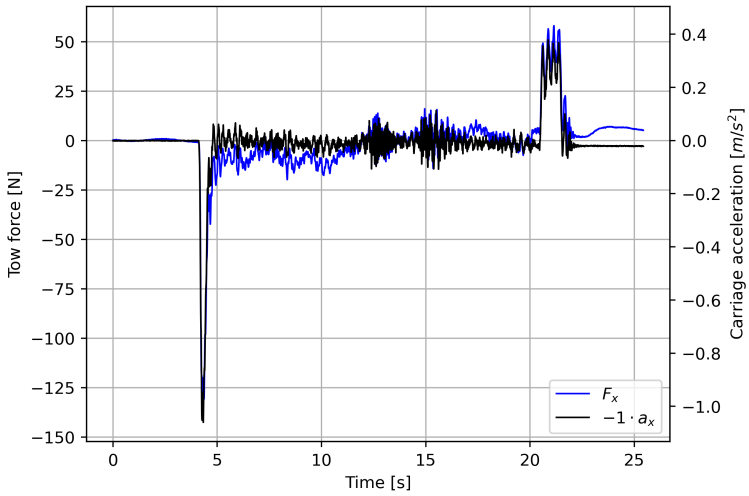

Figure 4.18: Time history for carriage acceleration and tow force model A, run 1, speed 0.3 m/s, forward direction, wet run, high acceleration runs

carriage is run in the other direction. Here forward runs refer to run along positive x-direction and backward run refers to run in negative x-direction (see Figure 4.7 for the definition of the coordinate system). Zero-balancing is done at the start for both the forward and backward runs, this results in a shift of the origin for position recording as shown in Figure 4.7.

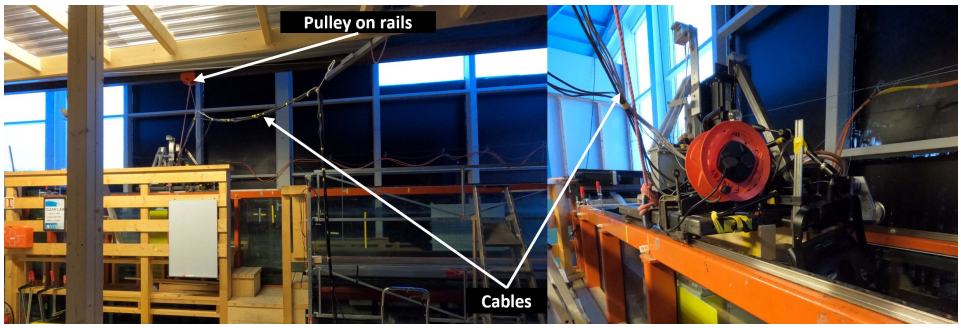

Figure 4.19: Arrangement for transferring transducer cables from the amplifier to be transferred to the moving carriage

After the carriage stops

After the carriage comes to rest it was observed that the force transducer and accelerometer readings do not go back to zero. The following additional tests were conducted to determine the cause for this observation :

- Initially the non-zero readings from the force transducer was suspected to be the consequence of small disturbances of the free surface taking a long time to subside post the run. To test this, the readings were recorded for ≈ 8 minutes post the run. The resulting time series is plotted in Figure 4.20. The following observations are noted :

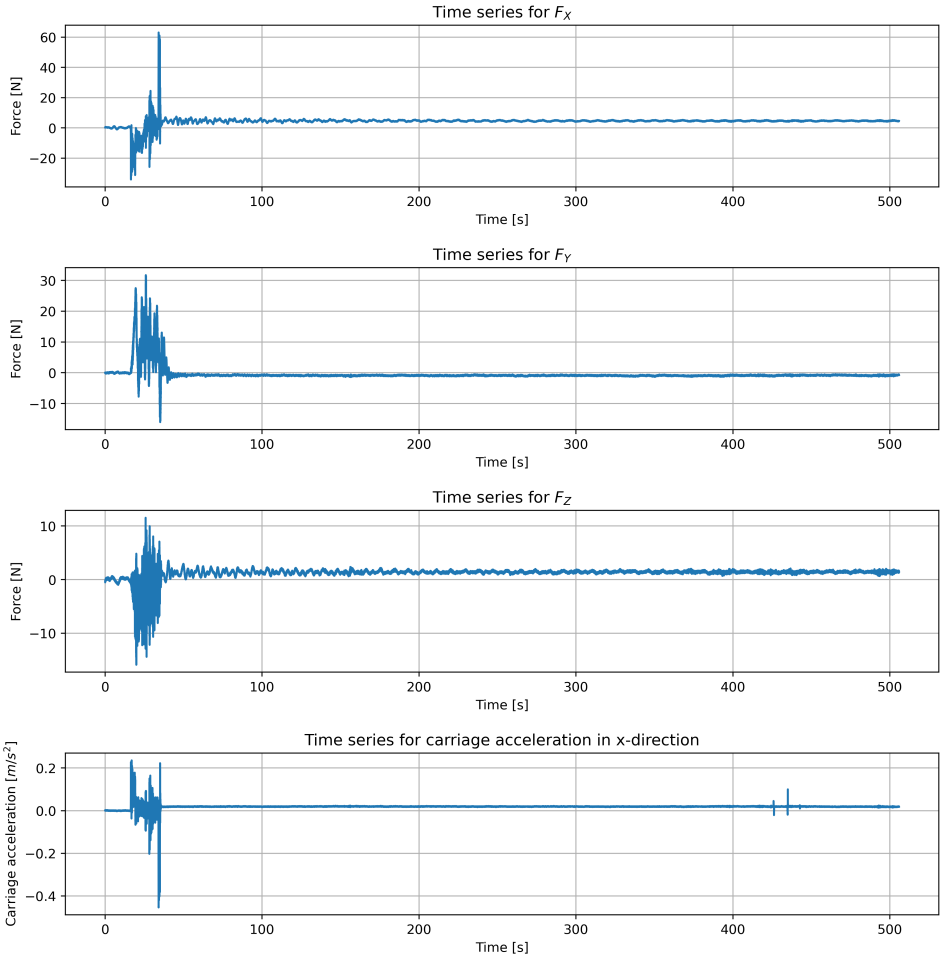

Figure 4.20: Time history of readings from the force transducers and accelerometer recorded for ≈ 8 minutes after stopping the carriage (Model A, forward direction, wet run)

  - Since a triaxial transducers was used, forces in all the 3 directions were recorded. In all the three directions, the transducer output settles to a non-zero value mean value and does not return to zero, even after a long time.

  - The accelerometer on the carriage measuring acceleration in $x-$direction also shows a similar trend.

- Since F_z and a_x showed a mean offset value, it was suspected that the carriage rails have a different gradient at the stopping point compared to the starting point where zero measurement is set. This can result in a component of acceleration due to gravity to act in x- direction of the acceleromemter. This could explain non-zero offset readings in F_Z and a_x. To check this a self-leveling laser and a ruler was used to measure the difference in vertical heights at the starting and stopping point of the carriage. The difference measured was very small ($\approx$ 1-2 mm) which is not significant enough to cause an acceleration component with the magnitude shown by the accelerometer.

- The possibility of drift in the force transducer load cells was investigated by connecting a digital force gauge to the amplifier. Force was applied on the model in different directions using the force gauge and the readings from the transducer and the digital force gauge were compared. It was found that they matched and when the force was removed, the readings from the force transducer went back to zero. This implied that the force transducer setup worked as expected and the differences cannot be due to drift in the force transducer.

- Further testing revealed that when the zero balancing of the instrumentation was done at the starting point of the carriage on the left end and then moved to the right end, it showed the non-zero offset, however when the carriage was then moved back to the left end the readings went back to zero. The time history plot for this is shown in Figure 4.21.

  Similarly, it was observed that when the zero balancing is done on the right end and the carriage is run to the left end, non-zero offsets are seen which disappear when the carriage is taken back to the initial position. The time history for this is shown in Figure 4.22.

  The difference in the two time history plots (Figures 4.21 and 4.22) is that the magnitude of the non-zero offsets is nearly the same however the signs get reversed.

These offsets at the ends remained the same and were unaffected when the speed or acceleration of the carriage was changed. Hence, it was theorized that accelerometer and the force transducer readings have to be corrected, and this correction was independent of speed or acceleration of the model.

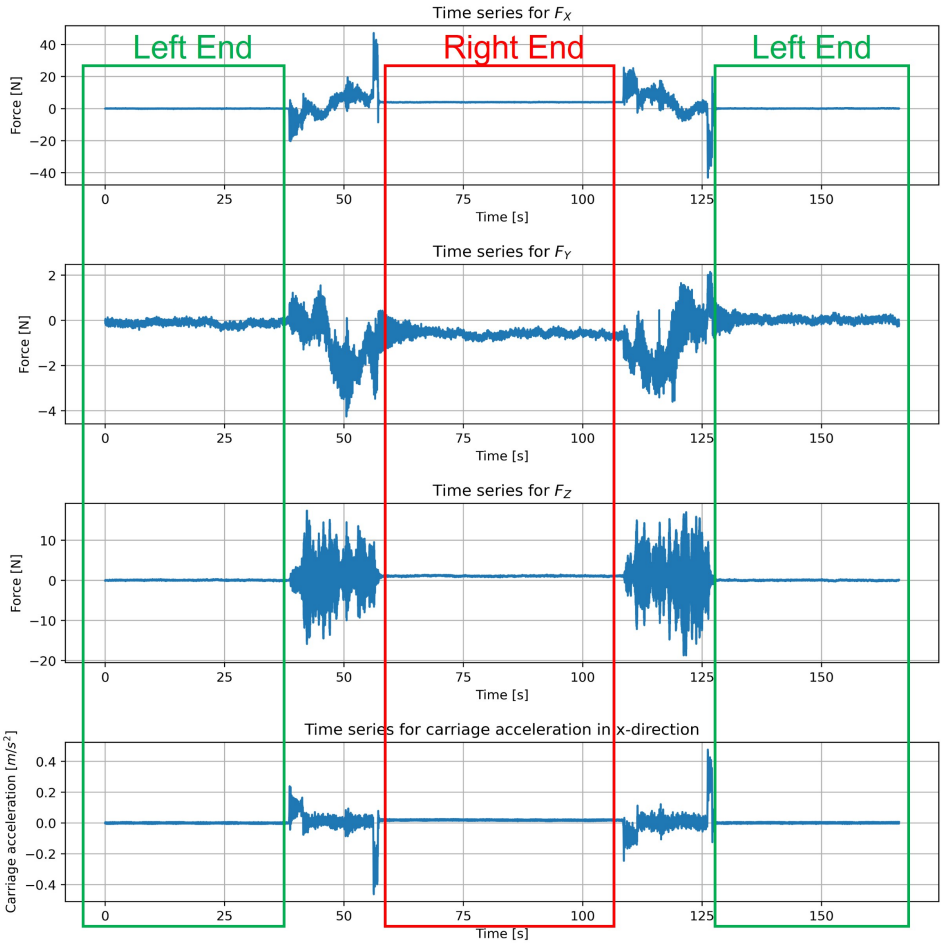

Figure 4.21: Time history of readings from the force transducers and accelerometer when zero balancing is performed when the carriage is on the left end of the carriage rails and then the carriage is run to the right end. After the disturbances die out the carriage is then moved back to the left end (Model A, wet run)

Rational explanation for correction on accelerometer readings

A change in the orientation of the accelerometer resulting in a component of acceleration due to gravity acting in the x-direction of the accelerometer is most rational possibility for the above observation. The reason for the change in orientation is possibly connected with slight changes in the alignment of rails resulting in small deformation of the base of the carriage.

A simplified representation is shown in Figure 4.23. It is assumed that the accel-

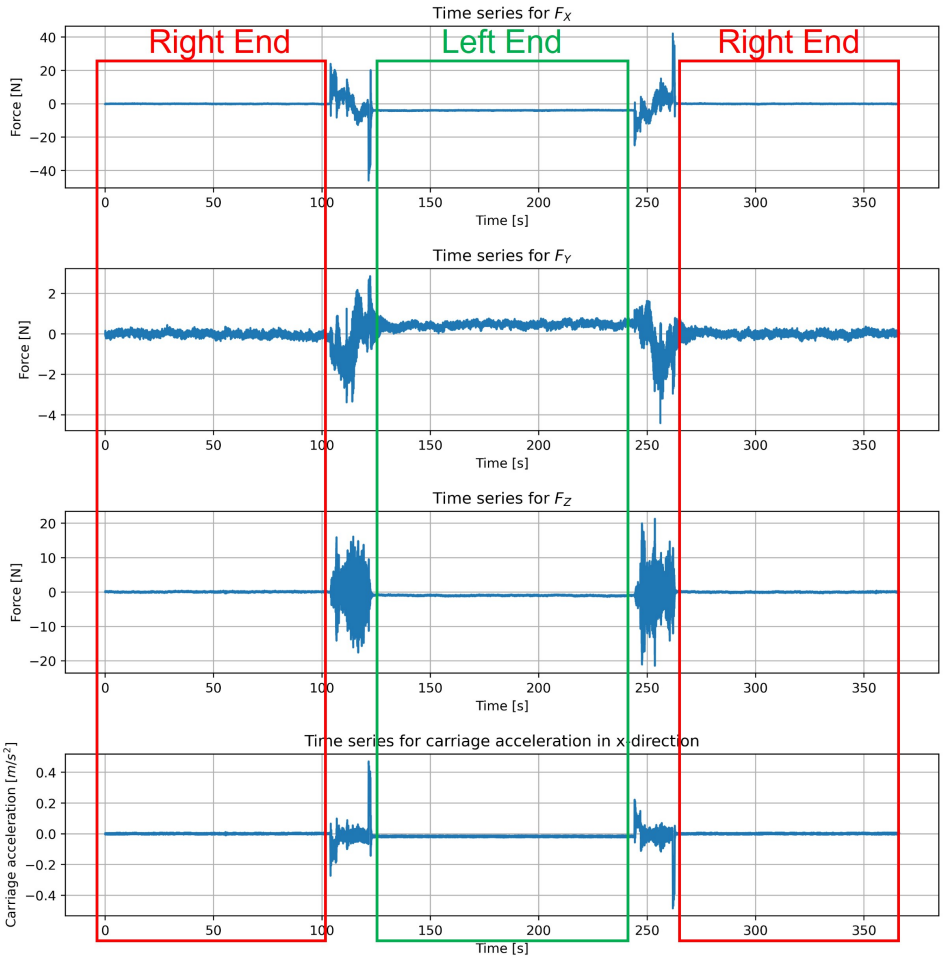

Figure 4.22: Time history of readings from the force transducers and accelerometer when zero balancing is performed when the carriage is on the right end of the rails and then it is run to the left end. After the disturbances die out the carriage is then moved back to the right end (Model A, wet run)

erometer turns by an angle θ when it goes from the left end to the right end of the carriage rails. This results in a component $g \cdot sin\theta$ to act in the x-direction of the accelerometer as shown in Figure 4.23(b), relative to the zero-balancing position shown in Figure 4.23(a). This can lead to the observations seen in Figure 4.21 with a positive offset on the right end. This situation is reversed if zero-balancing is done on the right end of the carriage rails.

However it is noted that no visible change in orientation of the accelerometer was

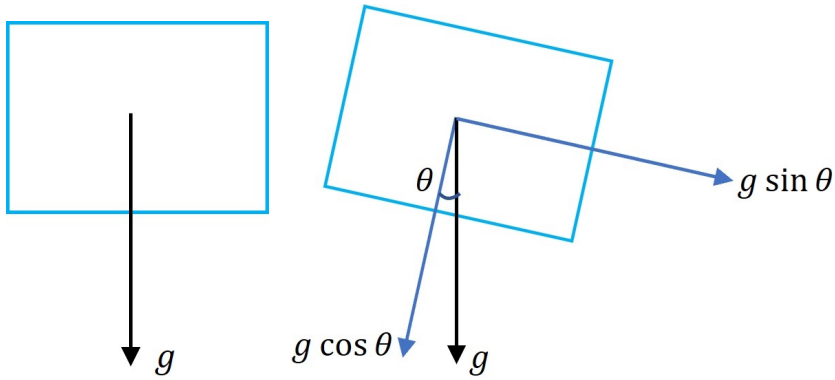

(a) Accelerometer at the zero balancing position (Left end)

(b) Accelerometer at the carriage stopping position (Right end).

Figure 4.23: Explanation for offset in accelerometer reading once the carriage stops on the right end of the rails when the zero balancing is done on the left end based on change in orientation of the x-direction of the accelerometer

seen during the experiment. Based on the offset value in accelerometer at the right end readings seen in Figure 4.20 ($\approx 0.0188\ m/s^2$) and assuming that the additional component in x-direction of the accelerometer is $g \cdot sin\theta$, the relative change in the orientation angle θ can be computed as 0.11 deg., which cannot be detected visually.

Even though this offset was detected only at the end of the run, it can be reasonably assumed that there is variation of the orientation angle through out the length of run. This change in orientation angle results in a correction which will be dependent on the absolute position of the carriage on the rails.

Further it was also reasonable to assume that the variation in the measured acceleration as a result of deformation of the carriage will have a slowly varying nature when compared to the high frequency oscillations of the model. Hence, the time history from the accelerometer was passed through a low-pass filter and the result is presented in Figure 4.24. Ignoring the peaks during the initial acceleration and during deceleration, it can be observed that, the acceleration has a slowly varying component.

Rational explanation for correction on force transducer readings

Using the same argument in case of the correction force as on accelerometer i.e a change in the orientation of the directions of the force transducer resulting in offsets in forces due to a component of weight is not logically consistent because

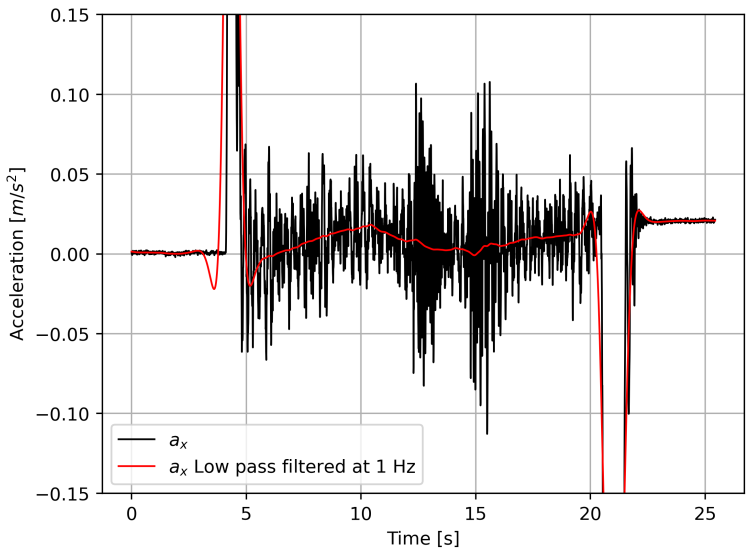

Figure 4.24: Time history of carriage acceleration. The red curve shows the result when low pass filter is applied on the time history of acceleration at 1 Hz (model A, run 1, speed 0.3 m/s, forward direction, wet run, high acceleration run)

as explained in Section 4.3.3, the models were ballasted to be neutrally buoyant.

To investigate this a dry run was done by emptying the tank and running the carriage with Model A. Dry run was also done after detaching Model A and fixing Model B. As indicated in Table 4.1, the mass of Model B is nearly half of Model A. The results are shown in Figure 4.25. As expected from Equation (4.2), the added mass and drag term is small in air, hence for dry run a lower overall value for F_x is seen.

From Figure 4.25 the following conclusions are drawn based on noting the offset in F_x at the end of the runs :

- The Offset at the end of the run in F_x for Model A in wet run seems to be slowly converging to the the offset seen in the dry run.
- The offset in F_x for dry run in model A and model B seems to be close with a very small difference (< 0.6 N).

Based on these observations it was theorised that the deformation of carriage has a different effect on the force transducers as compared to the accelerometer. The net force is obtained as the sum of the outputs from 3 force transducers as shown in

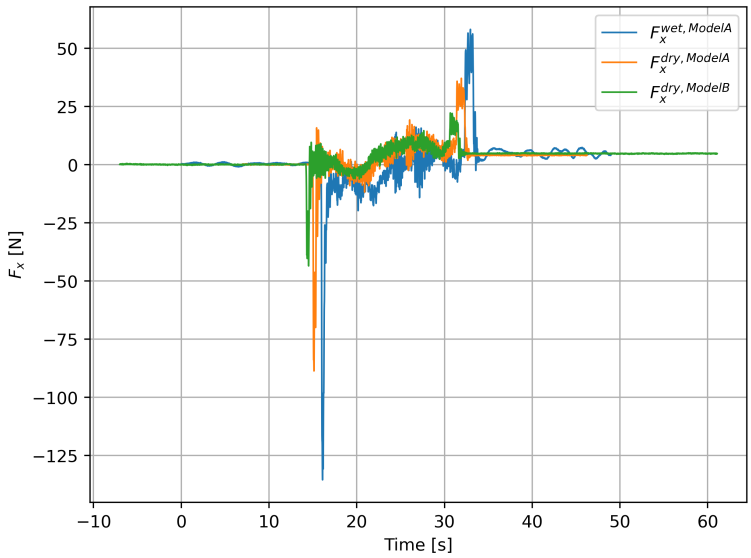

Figure 4.25: Time history of F_x for wet run of model A (run 1, speed 0.3 m/s, forward direction, high acceleration run), dry run for Model A (run 1, speed 0.3 m/s, forward direction, high acceleration run) and dry run for model B (run 1, speed 0.3 m/s, forward direction, high acceleration run). Shift of the plots in time axis does not have any significance as the carriage is started at different time for different runs

Figure 4.11(b). If the base of the carriage twists due to the difference in alignment of the rails, then this deformation can be transferred to the top aluminium plate holding the force transducers. Relative deformation of this plate with respect to the condition at zero-balancing position can potentially set off internal reactions or stresses which can cause the offsets in forces. The magnitude of these forces will then depend on the pattern of deformation which will be the same for a given absolute position on the carriage rails. Hence, this force will be independent of the weight of the model but depends only on the absolute position of the carriage. The slight different seen between Model A and Model B could be due to the fact that the lower aluminium plate (see Figure 4.10) is different for Model B due to the difference in the number of connection bolts.

Similar to the accelerometer, even though this offset was detected only at the end of the run, it can be assumed that the extent of deformation varies through out the length of run, hence a correction on the force has to be applied along the entire run.

4.4.3 Correction determination

Correction for accelerometer

Evaluating the change in the accelerometer orientation to determine the correction is very challenging. The approach taken here was to obtain the carriage acceleration from the carriage speed time history.

As mentioned in Section 4.3.6, the sampling frequency of the carriage controller is only 50 Hz i.e one data point every 0.02 s. This is up-sampled to 200 Hz (one data point every 0.005 s) by the data acquisition system by reading the nearly same value from the carriage controller 4 times. Hence, when the acceleration is calculated by applying a numerical scheme such as central difference, it will result in approximately zero acceleration periodically. This effect can be seen in Figure 4.27.

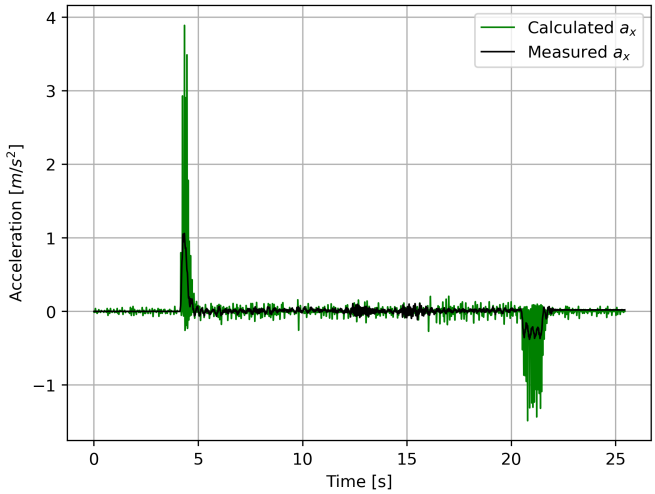

Figure 4.26: Time history of measured carriage acceleration compared against the acceleration calculated from the carriage speed (model A, run 1, speed 0.3 m/s, forward direction, wet run, high acceleration run)

From Figure 4.27 it can be observed that there are large oscillations in the acceleration calculated numerically. For the calculation of the acceleration, central difference scheme is used for all time steps except the first and last time step. Forward and backward difference is applied to calculate the acceleration at the first and last time step respectively.

However, when the numerically calculated acceleration time history is passed through a low-pass filter at 10 Hz, a reasonable representation of the measured

acceleration is obtained. This can be seen in Figure 4.27.

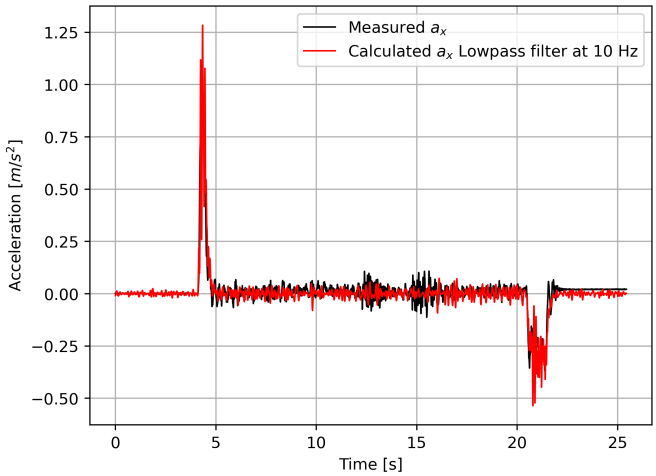

Figure 4.27: Time history of measured carriage acceleration compared against the acceleration calculated from the carriage speed and low-pass filtered at 10 Hz (model A, run 1, speed 0.3 m/s, forward direction, wet run, high acceleration run)

The acceleration calculated by this method will not require to be corrected however it will be less accurate as the high frequency features of the acceleration are lost due to the low sampling frequency used by carriage controller.

Correction for Force transducer

The theoretical expression presented in Equation (4.2) is modified in the following way to account for the correction force :

$$F_x = F_x^{wet} - F_c = -(m + m_a) \cdot a_x^{wet} + F_{drag} \tag{4.4}$$

where,

F_x	Force on the model in x - direction
F_x^{wet}	Force on the model as recorded by the force transducer when the model is towed in water
F_c	Correction force to be applied on the force recorded by the force transducer
m	mass of the model
m_a	added mass of the model

a_x^{wet} acceleration in x-direction calculated from the carriage speed

F_{drag} drag force in the x-direction

Hence the correction force can be determined as :

$$F_c = F_x^{wet} + (m + m_a) \cdot a_x^{wet} - F_{drag} \tag{4.5}$$

Equation (4.5) has 2 unknowns m_a and F_{drag}. Under the assumption that F_c is purely dependent on the deformation of the carriage base, it is reasonable to assume that this will remain the same at a given position for a dry run. However, the advantage in dry runs is that both the added mass and drag in air is negligible. Hence for dry runs, Equation (4.5) gets modified as :

$$F_c = F_x^{dry} + m \cdot a_x^{dry} \tag{4.6}$$

where,

F_x^{dry} Force on the model as recorded by the force transducer when the model is towed with the tank empty

F_c Correction force to be applied on the force recorded by the force transducer

m mass of the model

a_x^{dry} acceleration in x-direction calculated from the carriage speed

In Figure 4.28, the time history for dry run of Model A is indicated along with the inertia force calculated using the measured acceleration and the acceleration calculated from the carriage speed.It can be noted that, in principle in a dry run, the force recorded by the force transducer should be the inertial force. Hence, the difference between them is the correction force F_c. Visually from the figure it can be seen that when the carriage moves from left to right (forward direction), F_c is negative initially and then it becomes positive. Also it can be noted that at the end of the run, the inertial force calculated from the measured acceleration does not go to zero however the inertial force calculated from the calculated acceleration oscillates around zero.

In Figure 4.29, time history of correction force F_C is plotted. F_C is computed both by using the measured acceleration and the calculated acceleration. Based on the assumption that the correction force associated with deformation of the plates will be a slowly varying force, a low pass filter at 1 Hz is applied.

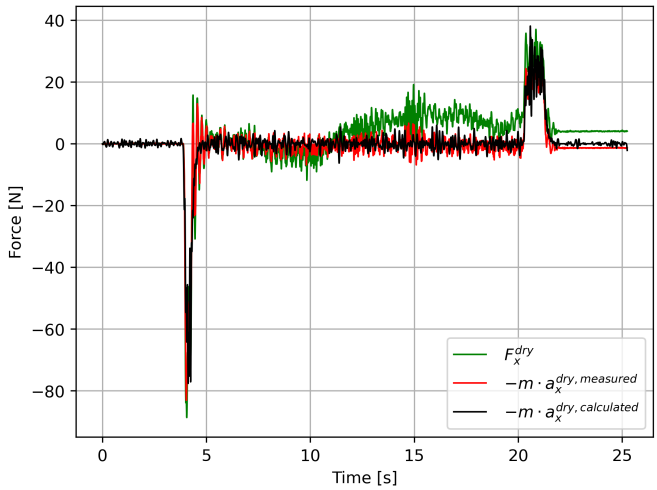

Figure 4.28: Time history of measured tow force and inertia force for dry run. Inertia force is calculated using two methods - one by using the measured acceleration and the other by using the acceleration calculated by using the carriage speed and low-pass filtered at 10 Hz (model A, run 1, speed 0.3 m/s, forward direction, dry run, high acceleration run)

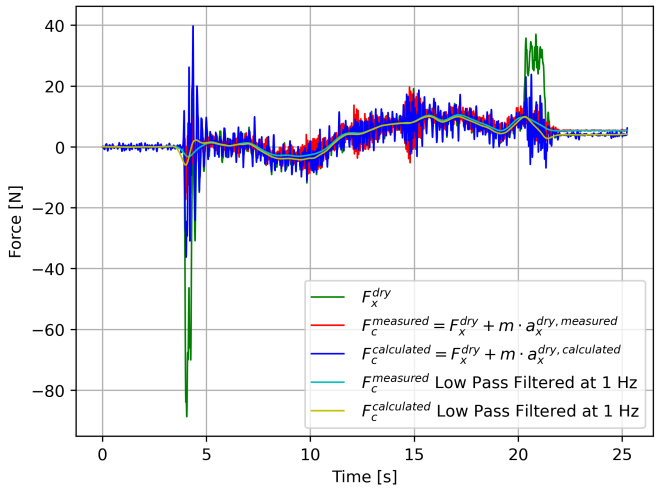

Figure 4.29: Time history of measured tow force and the correction force F_c. Calculation of F_c is done both by using the measured acceleration and by using the acceleration calculated by using the carriage speed and low-pass filtered at 10 Hz. The correction force F_c low-pass filtered at 1 Hz is also indicated (model A, run 1, speed 0.3 m/s, forward direction, dry run, high acceleration run)

The following observations are made from Figure 4.29 :

- The maximum value of F_c is approximately 10.5 N. This is in the order of estimated value of the drag force on the model. Hence, it can be concluded that the results are expected to be sensitive to the correction force and it cannot be ignored.
- The maximum difference between F_c obtained by using the measured acceleration and calculated acceleration is close to 1 N which occurs around 10s.
- At the beginning and at the ends of the run, F_c obtained by using the measured acceleration and calculated acceleration differ significantly. This is because the calculated acceleration is based on speed data at 50 Hz and at these time there is significant variations in accelerations.
- After the carriage stops, the F_c obtained by using the calculated acceleration converges with the F_x since the inertial force goes to zero. This does not happen with F_c obtained by using the measured acceleration.

Since the correction force has a magnitude which is in the order of the estimated drag force, it was essential to check the sensitivity of the correction force to different test parameters such test speed and acceleration, run direction, model etc. Dry runs were conducted for Models A and B for all the 4 speeds, both at high acceleration and low acceleration settings were used. Model C and Model D are expected to give the same results as Model A as they use the same model but with bilge keels. The resulting time series of the measured quantities are presented in Chapters B and C. The procedure used to obtain the correction curve is described below :

- A minimum of 2 repeat runs have been conducted for each case. There are slight differences between the runs. Hence, it was decided to obtain an average time series over the repeat runs because if it is assumed that the noise and disturbances are Gaussian distributed, then it is expected that averaging will reduce this noise. This effect can be seen, for instance in the tow force time series in Figure B.13. The average curve (shown in black in the plot) has a reduced oscillation amplitude as compared to the 5 repeat runs (plotted in different colours in the plot). Time duration between the instant at which the measurement recording was started and time instant at which the carriage was started, was different for different runs. Hence to obtain an average time series, all the repeat runs have to be aligned in such a way

that the duration between the time instant at which the carriage is started and the time instant at which the time series record starts, is same for all repeat runs. This was done by calculating the cross-cross relation between the time series signals of tow-force for the repeat runs using the python function `scipy.signal.correlate`. The function can calculate the time lag between two nearly same signals and this time lag has been used to align the repeat runs for all cases.

- For each repeat run the acceleration is calculated from the carriage speed measurement. Central difference scheme is used for all time steps except the first and last time step, forward and backward difference is applied to calculate the acceleration at the first and last time step respectively.Then a low pass filter at 10 Hz is applied over the calculated acceleration. Finally an averaging is done over the repeat runs. The average calculated acceleration (plotted in red) is plotted against the average measured acceleration (plotted in black) for all the dry runs presented in Chapters B and C. Significant differences are seen between the two curves especially with respect to the high frequency features, for instance see Figure B.2. Since the correction force is slowly varying, the high frequency features are expected to be filtered out. However, the differences seen during the acceleration and deceleration phase are expected to have an impact on the quality of the obtained correction force curve.

- For each repeat run Equation (4.6) is used to calculated the correction force. On the calculated force a low pass filter at 1 Hz is applied. Hence, time series of the correction force is obtained. To apply this correction on the wet runs, the time series has to be converted to a correction based on the position of the carriage. This is consistent with the assumption that the correction force will be in principle depend on the position of the carriage.

- For each repeat run, the obtained position time history is passed through a low pass filter at Hz. This is done in order to remove the high frequency oscillations seen in the position time history of the carriage about the mean position. The position time history for the dry runs are also presented in Chapters B and C. The calculated correction force is then plotted against the position of the carriage, finally an averaging over the repeat runs is performed to obtain the final correction curve.

The force correction curves obtained by using this procedure is presented in Figures 4.30 and 4.31 for model A and Figures 4.32 and 4.33 for model B.

Theoretically if we assumed that the origin of the correction force is from the deformation of the carriage base, it is expected that F_c curve obtained from the runs in forward and backward direction will be the same but they will be translated by the correction force value obtained at the end of the run. This is because zero-balancing is done at the start of the run, hence the value of correction force is expected to be zero at $x = 0$ for forward direction and at $x = 5$ in backward direction. The measurements are made relative to the zero-balanced position, hence the actual values measured will be translated. From the plots there is a general agreement in the curves in the forward and backward direction if we ignore the acceleration and deceleration phase, hence the existence of a predominately position dependent correction force is proved. Further since the forward and backward runs are completely independent, the general agreement in the nature of variation of the correction force is also proves the methodology used in obtaining these curves. Further, features of the correction curve which are in disagreement between the forward and backward direction curves have very low confidence.

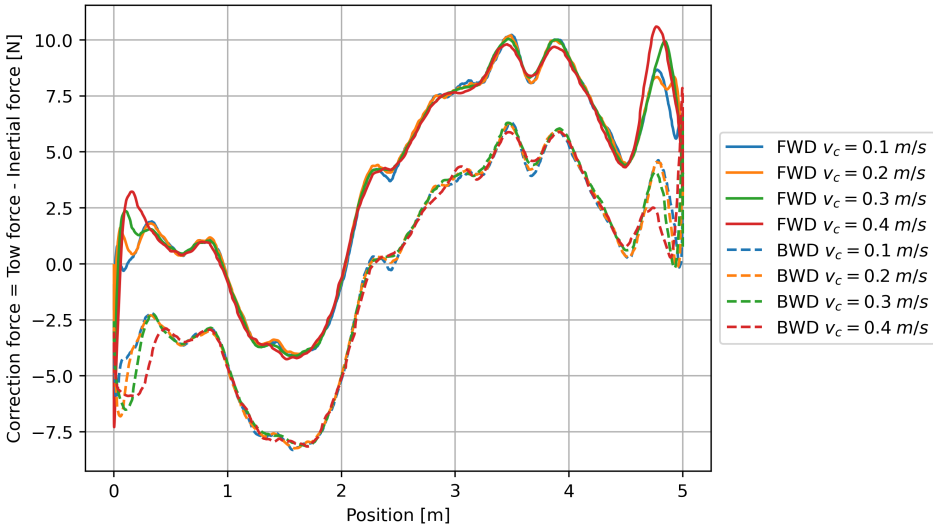

Figure 4.30: Correction force curve for Model A with high acceleration settings. Color of the lines are used to indicate the speed. Solid line indicates the correction force curve which is obtained when the carriage is run in the forward direction (FWD) and the dashed line indicates the result from the runs in backward direction (BWD).

The following observations and conclusions are noted from the plots :

- **At x = 0 and x = 5** The correction force for forward run and backward run must zero at $x = 0$ and $x = 5$ respectively, since both tow force and

acceleration is zero here in the respective cases. However the exact value obtained has deviations as this value is obtained by interpolating position time history which has small oscillations around the mean position. The exact value at the start is not very important however error in obtaining this value as exactly zero results in the slight shift the corrected time series in wet runs. This effect is clearly seen in the time series of tow force for instance in Figures B.19 and B.20 - the average corrected force (shown in red) indicates a small non-zero tow force initially when the carriage is at rest. Similarly the value of the correction force in the backward run at $x = 0$ must be exactly same but opposite in sign to the value of forward run at $x = 5$. In terms of magnitude this be same as the offset in force seen in Figure 4.25. The inaccuracy in this has resulted in a similar shift at the end of the corrected time series for instance see Figure B.19 - the the average corrected force (shown in red) value does not go to zero exactly at the end of the run.

- $\approx$ **0.25 m < x < $\approx$ 4.75 m** In this area the carriage reaches steady speed zone and the correction curves obtained in the forward and backward direction show good agreement as expected. A small speed dependence is also shown by the correction force curve based on the deviations seen for different speeds. The speed dependence possibly arises from the fact that the time available for the deformation to occur at a given position would be lower as the speed of the carriage increases.

- **0 < x < $\approx$ 0.25 m** This zone is linked with acceleration for forward runs and deceleration for backward runs. Focusing on correction force curve for model A with high acceleration setting (Figure 4.30): There is a general disagreement between the forward and backward runs in this zone and this is probably linked with the inaccuracy in the numerically determined acceleration. Hence, there is uncertainty linked with the correction force determined in this zone. The possibility of acceleration dependence of the correction force also cannot be ignored because a possible speed dependence which has already been established would also imply an acceleration dependence. Hence runs were done for both high acceleration setting as well as low acceleration setting. The resulting correction force curve for model A for high and low acceleration setting are shown in Figures 4.30 and 4.31 respectively. Comparing these two plots and as expected similarity is seen in $\approx$ 0.25 m < x < $\approx$ 4.75 m i.e. the steady speed area as this area remains unaffected by the initial acceleration. Further in 0 < x < $\approx$ 0.25 m, a similarity is seen that is the corresponding parts of the curves in the two plots will match for the deceleration phase because for all the runs (high acceleration or low acceleration) the deceleration magnitude is set to the same value. Hence in 0 < x

< ≈ 0.25 m, backward run shows the same behaviour in the two plots. But differences are seen in the forward run cases which is expected if the force has an acceleration dependence.

- **4.75 < x < ≈ 5 m** Similar observation hold in this area also as noted in 0 < x < ≈ 0.25 m. Differences arew seen in the correction force curve for forward and backward run for a given acceleration setting whereas similar behaviour is seen in forward runs in this area between the high acceleration and low acceleration run due to the same value of deceleration used.

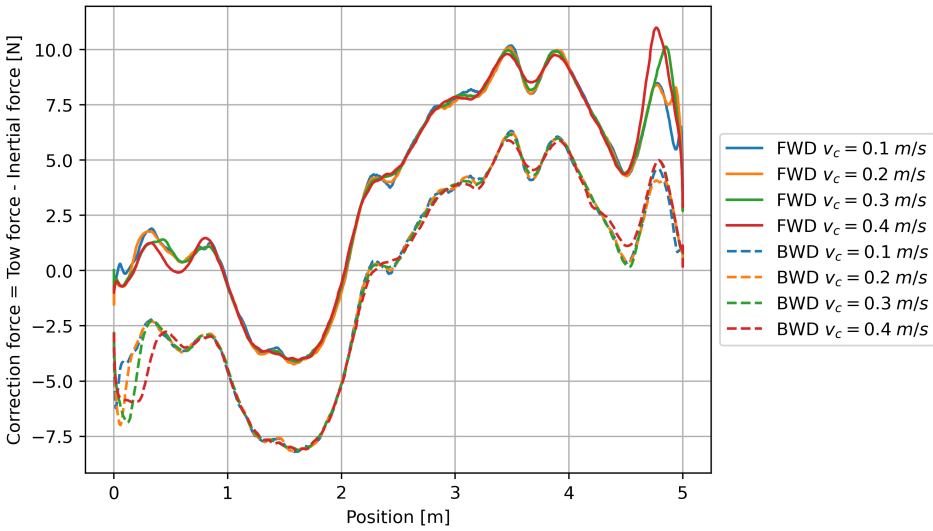

Figure 4.31: Correction force curve for Model A with low acceleration settings. Color of the lines are used to indicate the speed. Solid line indicates the correction force curve which is obtained when the carriage is run in the forward direction (FWD) and the dashed line indicates the result from the runs in backward direction (BWD).

Following the same approach the correction curves obtained for model B are presented in Figures 4.32 and 4.33 for high and low acceleration cases respectively. Comparing the plots of correction force for Model A and Model B, it can be noted that in the region ≈ 0.25 m < x < ≈ 4.75 m, there is a general agreement between the plots.

It is noted that that maximum acceleration wet runs for model A has been corrected by using the the correction curve obtained from the high acceleration runs as dry runs with maximum acceleration setting was not conducted.

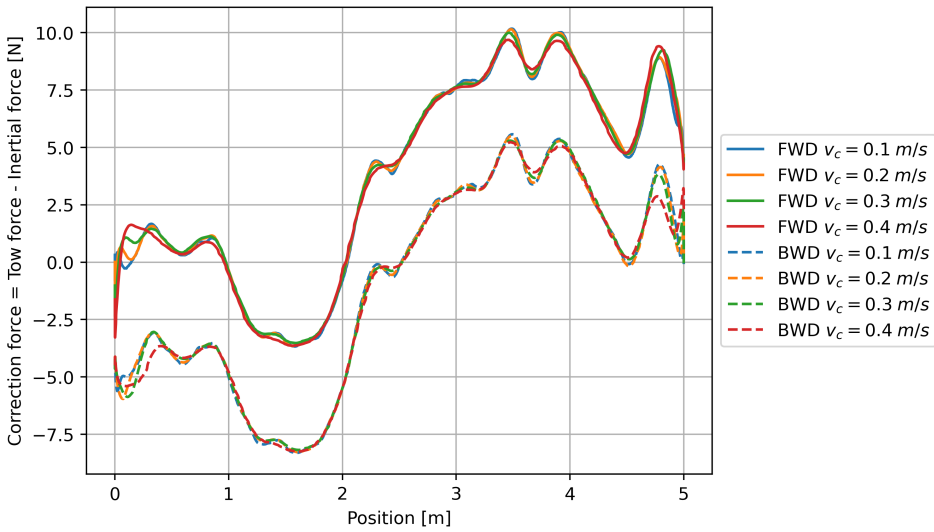

Figure 4.32: Correction force curve for Model B with high acceleration settings. Color of the lines are used to indicate the speed. Solid line indicates the correction force curve which is obtained when the carriage is run in the forward direction (FWD) and the dashed line indicates the result from the runs in backward direction (BWD)

Corrected force in wet runs

The final corrected force in wet runs is obtained by the follow-wing procedure :

- Determine the correction force to be applied for the current position of the carriage from the correction force curve for the corresponding acceleration, speed and carriage direction as the wet run. The current position of the carriage is obtained from the time history of carriage position.
- The correction force is then subtracted from the force measured in the wet runs at a given position on the carriage rail (see Equation (4.4)) to obtain the final corrected force F_x for the particular wet run.
- Finally an averaging over the repeat runs is performed using a similar procedure as done for dry runs to obtain the average corrected force.

This process can be seen in Figure 4.34 for the selected test case.

From Figure 4.34, the following observations are made :

- The corrected force F_x is not zero at start of the time series and towards the end when carriage has stopped. As already explained this is due to the error

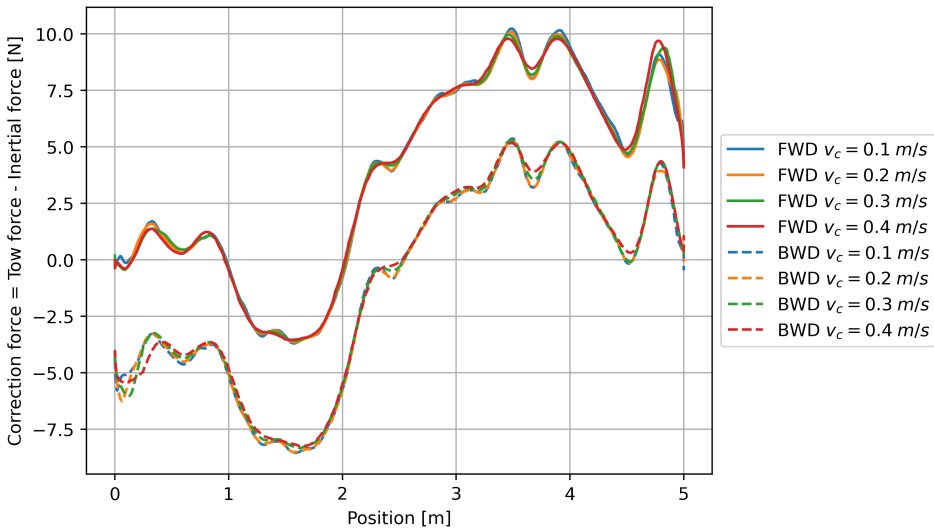

Figure 4.33: Correction force curve for Model B with low acceleration settings. Color of the lines are used to indicate the speed. Solid line indicates the correction force curve which is obtained when the carriage is run in the forward direction (FWD) and the dashed line indicates the result from the runs in backward direction (BWD).

in obtaining the correction force at $x = 0$ and $x = 5$ exactly. However this is not expected to have a significant influence on the rest of the time series.

- The similarity between the correction force curve F_c and the corresponding curve in Figure 4.30 can be noted because time history of F_c is obtained from Figure 4.30 using the carriage position time history.
- Comparing the relative values of the correction force F_c and corrected force F_x at steady-state, it is noted that they are of the same order of magnitude, implying the results will be very sensitive to the accuracy of the determined correction force curve.
- The corrected force curve oscillates with a mean value which is negative. This is physically consistent however significant high frequency oscillations are seen in the correction force curve.

The resulting corrected force curve for each acceleration and speed for each model is presented in Chapters B–E for model A, B, C and D respectively. An important general observation from the time series is that in wet runs at lower speeds runs (0.1 m/s and 0.2 m/s), comparatively large variations are seen in the accelerations and the tow force recorded between the repeat runs (for instance see the difference

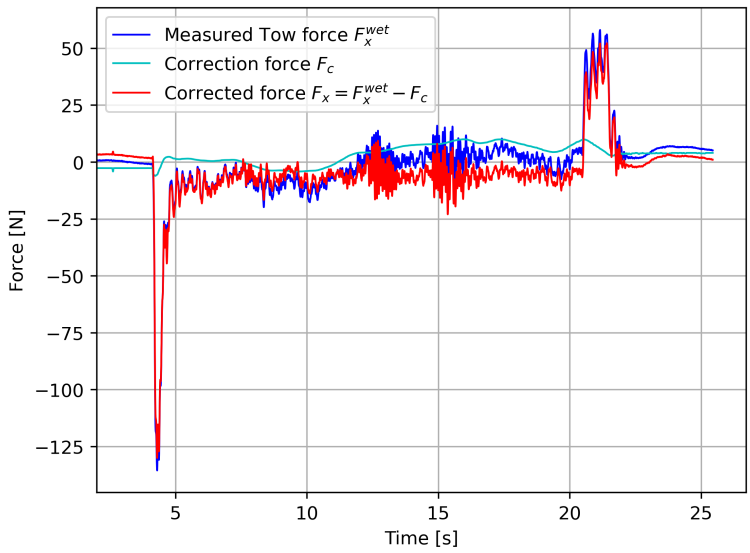

Figure 4.34: Time history for the measured tow force, correction force and the corrected force for model A, run 1, speed 0.3 m/s, forward direction, wet run, high acceleration run

between the average curve and curve for individual runs in Figures B.17 and B.18). Such differences between repeat runs are lower for runs at 0.3 m/s and 0.4 m/s (for instance see the difference between the average curve and curve for individual runs in Figures B.19 and B.20). Hence it is expected that the results from lower speeds will not be very accurate.

4.4.4 Determination of drag force

Added mass calculation

The corrected force curve F_x includes the drag force as well as the inertial force. Since the objective is to determine the drag force, the inertial loads have to be removed which requires determination of the added mass of the model.

From Equation (4.4), the added mass of the model can be obtained as :

$$m_a = \frac{F_{drag} - (F_x^{wet} - F_c) - m \cdot a_x^{wet}}{a_x^{wet}} \tag{4.7}$$

To determine the added mass the following approximations are applied :

- Considering only the initial startup-acceleration phase, the contribution from drag can be assumed to be negligible as during the startup it can be assumed

that there is no flow separation. Hence in Equation (4.7), F_{drag} is set to 0. It is noted that this is an important limitation in the current approach as this assumption may not be valid in case of the models with bilge keel, based on the size of the bilge keel, the flow separation can be instantaneous and F_{drag} may not be 0 in the start-up phase. Hence this approach is only a first approximation.

- a_x^{wet} is the acceleration in x-direction calculated from the carriage speed time history. However, the accuracy of the calculated acceleration will be significantly lower, especially in the startup phase, due to the lower sampling frequency of the carriage controller. In the startup phase the output from the accelerometer can be directly used as the correction on accelerometer readings is expected to be theoretically zero as during the start-up phase the carriage has not moved significantly compared to the zero-balancing position in case of high acceleration runs. The same argument is also applied for the force transducer readings as the correction force F_c derived is uncertain in this zone. Hence, F_c is also set to 0 in the startup phase.

- Free surface disturbance during the startup phase is assumed to be negligible

Hence Equation (4.7) can be modified for the startup phase as :

$$m_a = \frac{-F_x^{wet} - m \cdot a_x^{acc}}{a_x^{acc}} \tag{4.8}$$

where F_x^{wet} and a_x^{acc} are the tow force and acceleration directly obtained directly from the force transducer and accelerometer without any corrections. Applying Equation (4.8) on the selected test case, the result is presented in Figure 4.35. In the plot the different between F_x^{wet} and $-m \cdot a_x^{acc}$ is the contribution from the added mass force during the startup phase. The difference is used to calculate the added mass. Then the inertial force and F_x^{wet} is plotted which will match during the startup phase and will diverge subsequently due to the appearance of drag force and the corrections on acceleration and tow force.

Applying Equation (4.8) on the high acceleration runs of the 4 models, the added mass calculated is presented in Table 4.2.

From Table 4.2 it can be noted that :

- Model B is a semi-circular section with radius T = 0.145 m. The low frequency added mass for 2D semi-circular section in sway can be obtained from O. M. Faltinsen (1990, p. 50) as $\rho\pi T^2/2$. Hence the estimated added

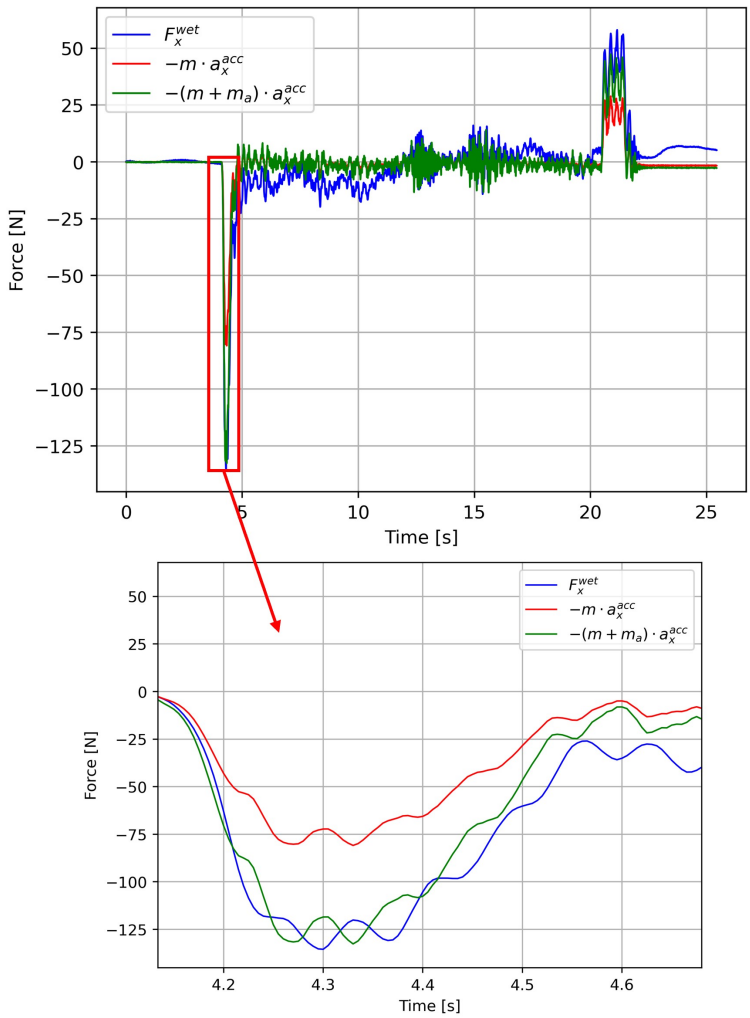

Figure 4.35: Time history for the measured tow force F_x^{wet}, inertial force component $-m \cdot a_x^{acc}$ and the inertial force $-(m + m_a) \cdot a_x^{acc}$ where added mass is as shown in Table 4.2 . A zoomed in view of the startup phase is also shown. Good agreement is seen between F_x^{wet} and $-(m + m_a) \cdot a_x^{acc}$ in the startup phase for the obtained added mass. [Case : Model A, run 1, speed 0.3 m/s, forward direction, wet run, high acceleration run]

mass for the model with submerged length of 0.985 m is 32.53 kg which is in the order of the added mass experimentally determined for model B in Table 4.2. The small difference is probably due to the additional supporting plate, wall effect and the disturbance on the free surface.

- The added mass for model A was roughly estimated by considering a rect-

Model	Cross Section	Added Mass (kg)
A	DTC midship section	48.81
B	Semi-circular section with radius 145 mm	31.65
C	DTC midship section with bilge keel of height 8 mm	52.31*
D	DTC midship section with bilge keel of height 16 mm	54.41*

Table 4.2: Estimated added mass for the model determined from the startup phase of the experiment using Equation (4.8). * The added mass for the models with bilge keel is approximate as flow separation can occur at the startup phase itself.

angular section in Section 4.4.1 as 30.9 kg. Experimentally obtained value is higher, probably due to similar reasons as above.

Drag force calculation

Finally the drag force is computed by rearranging Equation (4.4) as :

$$F_{drag} = F_x^{wet} - F_c + (m + m_a) \cdot a_x^{wet} = F_x + (m + m_a) \cdot a_x^{wet} \tag{4.9}$$

For the test case the time history of F_{drag} is shown in Figure 4.36.

In Figure 4.36, again the non-zero offset at the beginning and end of the time series are ignored as they are caused due to inaccurate estimation of F_c. As expected a significant difference between F_x and F_{drag} only appears in the acceleration and deceleration phase. To confirm repeatability of the drag time series, 15 repeat runs were conducted. The time series for the important parameters for all the runs are plotted together in Figure B.19 along with the ensemble average time series. Further the computed drag force from the different runs

From Figure 4.37, it can be observed that F_{drag} is repeatable in a low frequency sense i.e ignoring the high frequency components. An ensemble averaged time series is obtained by averaging (F_{drag}^{avg}) over all the repeat runs. It is expected that the variation of the drag force will have a slowly varying nature, hence the high frequency components can be filtered out.

Drag force filtering

A low pass filtering at 1 Hz is applied on F_{drag}^{avg} of the test case and the result is shown in Figure 4.38.

From Figure 4.38, a small resemblance can be seen in the nature of the curve with the curves for circular cylinder available in literature (Figure 4.1). The drag

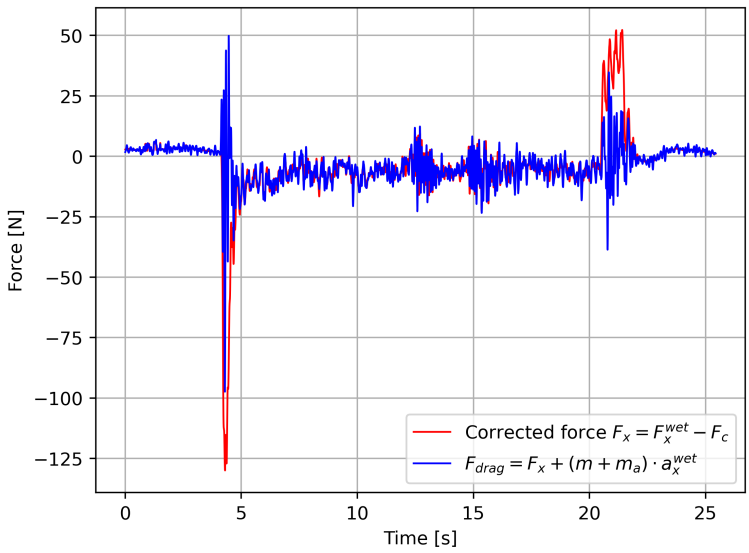

Figure 4.36: Time history for drag force F_{drag} obtained from the corrected force F_x using Equation (4.9) [Case : Model A, run 1, speed 0.3 m/s, forward direction, wet run, high acceleration run]

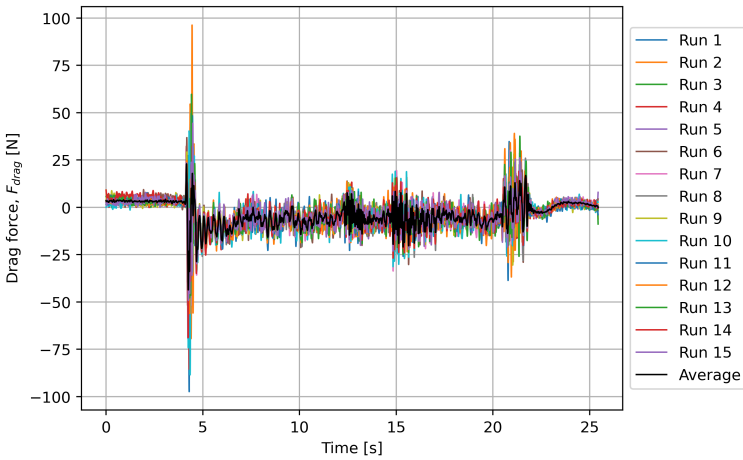

Figure 4.37: Time history for drag force F_{drag} obtained from the repeat runs along with the ensemble average time series [Case : Model A, run 1-15, speed 0.3 m/s, forward direction, wet run, high acceleration run]

force initially peaks at $\approx 5 - 6s$ and then reduces and then reduces to a steady value beyond $\approx 7s$. The peak occurs after the end of the acceleration phase of the

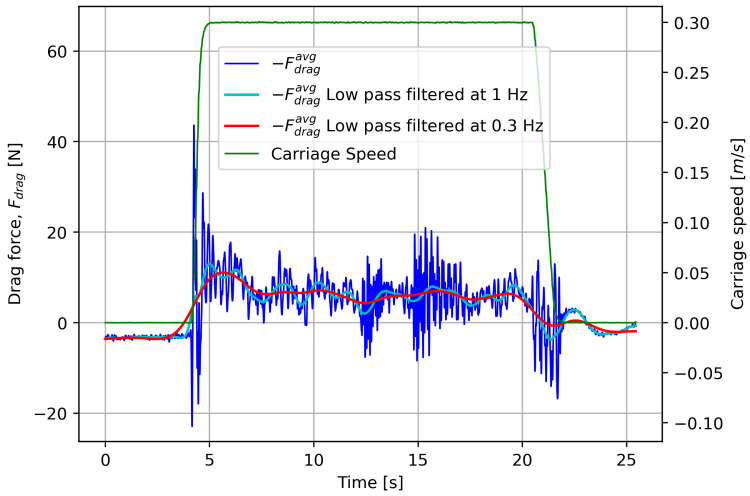

Figure 4.38: Time history for $-F_{drag}^{avg}$ obtained by averaging over the repeat runs along with the low pass filtered $-F_{drag}^{avg}$ at 1 Hz and 0.3 Hz. The ensemble averaged carriage speed is also presented. [Case : Model A, run 1-15, speed 0.3 m/s, forward direction, wet run, high acceleration run]

carriage. However, the drag force shows considerable oscillations and using a very low cut off frequency for the low pass filter can result in the loss of the initial peak in the drag curve. Hence, the low pass filter frequency was kept as 1 Hz.

The nature of the ensemble averaged unfiltered drag force signal (F_{drag}^{avg}) was studied using Empirical Mode Decomposition (EMD). The strength of EMD is in its ability to process non-linear and non-stationary data and was pioneered by Huang et al. (1998). This ability of EMD comes from the fact that there is no prescribed basis system for EMD, but the basis system is dictated by the data itself or in other words EMD has an adaptive basis system generated based on the data to be processed (Zeiler et al. 2010). This is in contrast to decomposition techniques such as Fourier transform or wavelet transform in which the basis system is made up of sine and cosine functions. Also EMD can extract physically meaningful modes because the modes are adaptive biased towards frequencies and scales which are dominant locally. The objective of the study was to check if the drag force signal contains any inherent features which can be identified, isolated and filtered out.

The mode functions obtained by using EMD are called Intrinsic Mode Functions (IMFs). The process used to obtain the IMFs from the data is called “sifting” which involves determining all the local maximas and minimas in the data and generating envelopes of maxima, minima and and a mean value envelop. Subsequently

an iterative algorithm[1] is then used to obtain the IMFs. The python library `emd` [2] is used to generate the IMFs for F_{drag}^{avg} obtained for the test case as shown in Figure 4.38. There are 7 IMFs in the signal and they are plotted in Figure 4.39.

The IMFs have the following properties :

- All the IMFs, except the the last one (also called as residual) are such that the mean value envelope of the IMF is zero. The mean value envelope is defined as an envelope passing through the mean of local maximas and minimas.
- The sum of all the IMFs gives back the original signal meaning that the decomposition is complete.
- The lower is the mode number of the IMF, the higher is the frequency content.

To de-noise F_{drag}^{avg}, it is necessary to know the IMF which corresponds to the noise to be removed. A number of attempts were made to identify the modes corresponding to the noise, however, the best result obtained gave the same output as that obtained from applying a low pass filter at 1 Hz on the data. Hence, further processing was done using low pass filter.

[1] https://www.clear.rice.edu/elec301/Projects02/empiricalMode/process.html

[2] https://emd.readthedocs.io/en/stable/

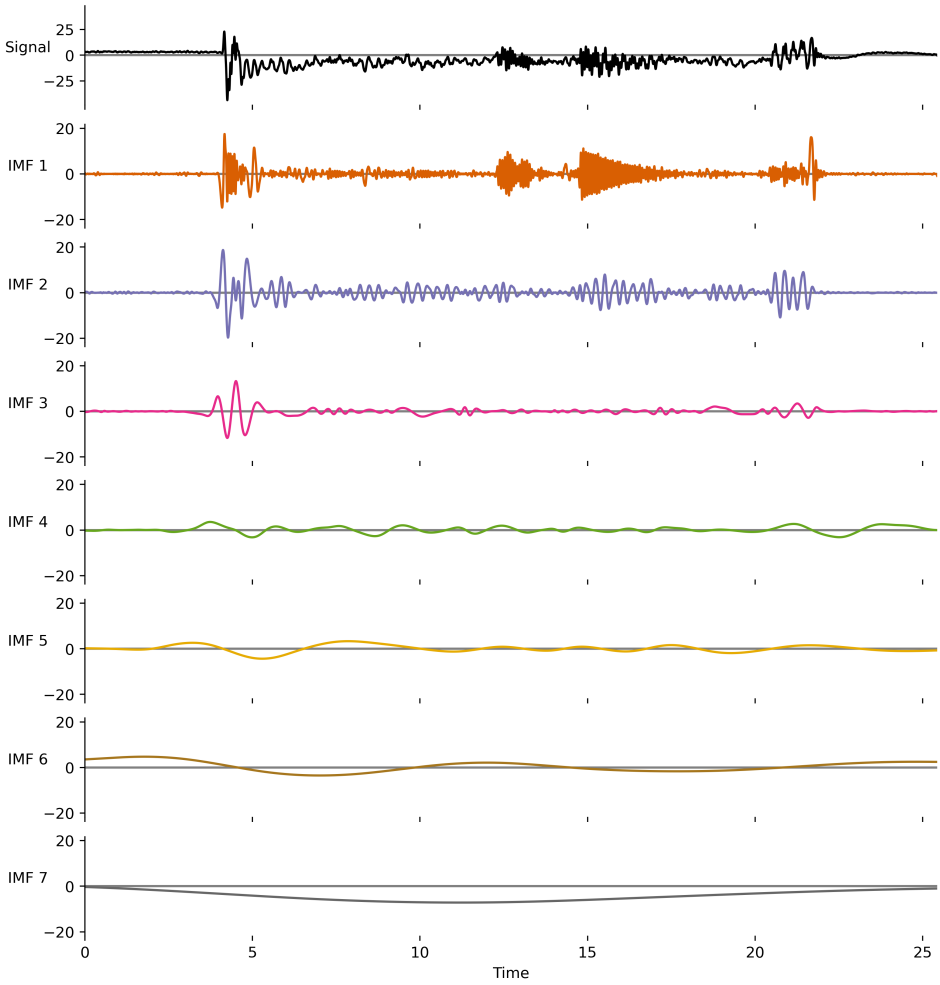

Figure 4.39: The first subplot shows the time history of the original signal F_{drag}^{avg} obtained for the test case (Note Figure 4.38 shows $-F_{drag}^{avg}$). The subsequent subplots shows the time history of the 7 IMFs which were obtained from the original signal through the process of "sifting". [Case : Model A, run 1-15, speed 0.3 m/s, forward direction, wet run, high acceleration run]

4.5 Results

The non-dimensional time can be calculated as :

$$t^* = \frac{\int v dt}{T} \tag{4.10}$$

where,

- v flow speed. In the experiment this was taken as the carriage speed corrected for the blockage effect
- $\int v dt$ the distance travelled by the flow. The integral sign is included because the flow speed v is not a constant. The carriage position readings is $\int v_c dt$ where v_c is the carriage speed. The relation between v_c and v has been established in Equation (4.1). Using this relation $\int v dt$ can be calculated as $1.312 \int v_c dt$.
- T characteristic length of the model. For ship shaped cross section models (Model A, C and D) this was taken as the ship draft whereas for the circular cross section model (Model B) this was taken as the radius.

The magnitude of the corrected tow force for different run types are passed through a low pass filter at 1Hz and then the results are plotted against the non-dimensional time for Model A in Figure 4.40(a).

A general observation from the plots is that the drag coefficient value obtained for low speeds (0.1 and 0.2 m/s) has large variations and they are likely not correct. Hence, an additional plot showing only the drag coefficient for 0.3 and 0.4 m/s is included.

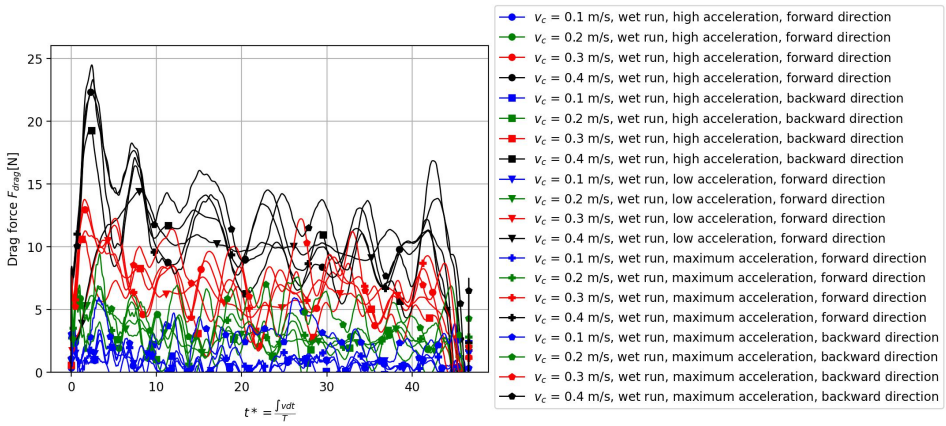

(a) Drag force on the model is plotted against non-dimensional time for carriage speeds v_c of 0.1, 0.2, 0.3 and 0.4 m/s for different run types

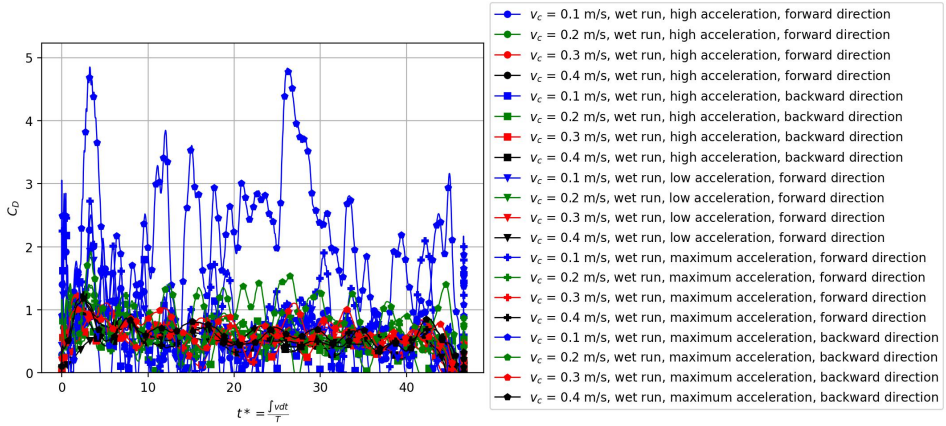

(b) Drag force coefficient is plotted against non-dimensional time for carriage speeds v_c of 0.1, 0.2, 0.3 and 0.4 m/s for different run types

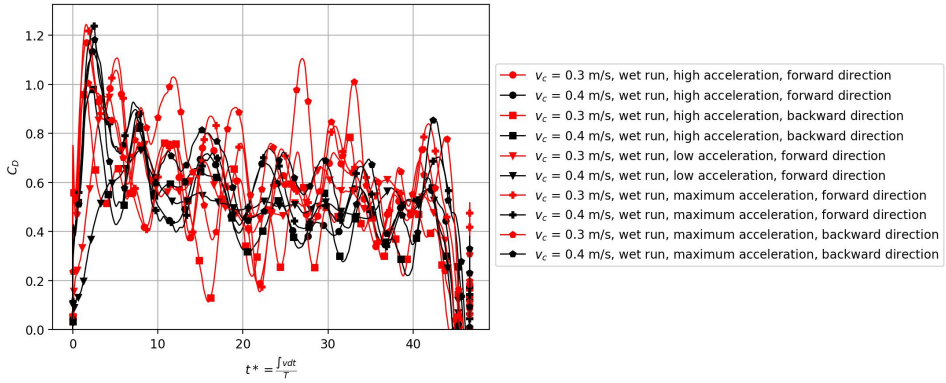

(c) Drag force coefficient is plotted against non-dimensional time for carriage speeds v_c of 0.3 and 0.4 m/s for different run types

Figure 4.40: Results for Model A. Colors are used to indicate the speed and the markers are used to indicate the different run types.

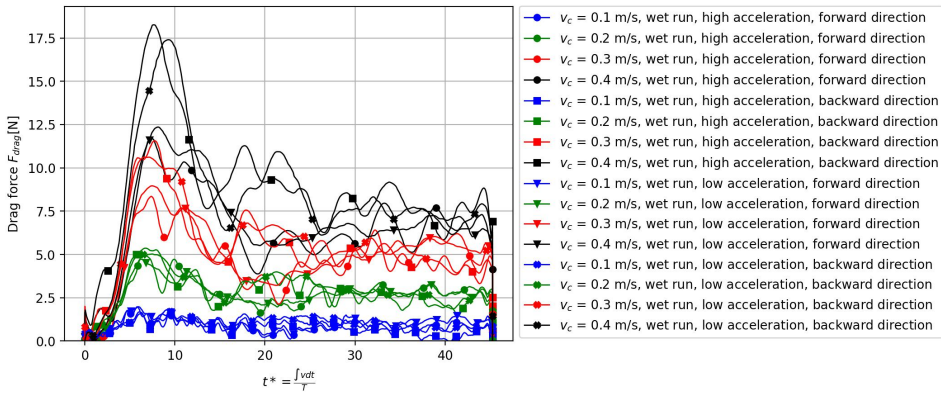

(a) Drag force on the model is plotted against non-dimensional time for carriage speeds v_c of 0.1, 0.2, 0.3 and 0.4 m/s for different run types

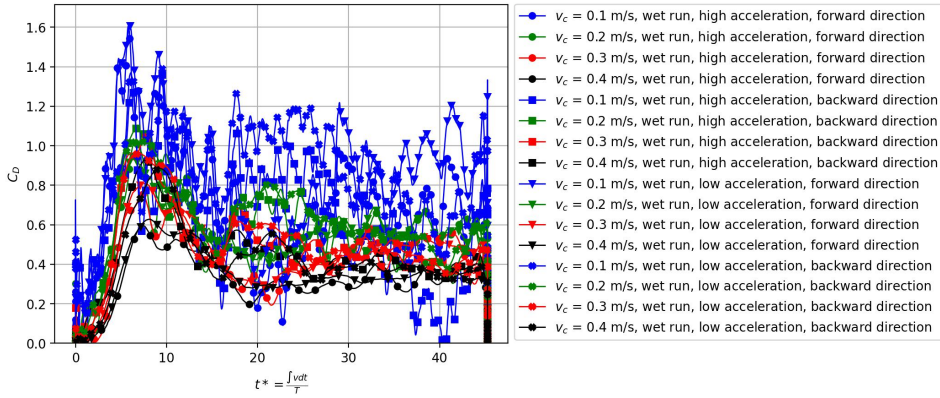

(b) Drag force coefficient is plotted against non-dimensional time for carriage speeds v_c of 0.1, 0.2, 0.3 and 0.4 m/s for different run types

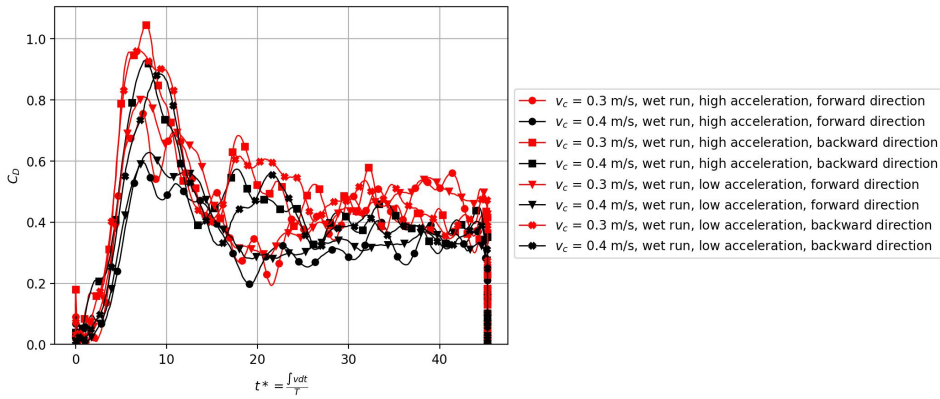

(c) Drag force coefficient is plotted against non-dimensional time for carriage speeds v_c of 0.3 and 0.4 m/s for different run types

Figure 4.41: Results for Model B. Colors are used to indicate the speed and the markers are used to indicate the different run types.

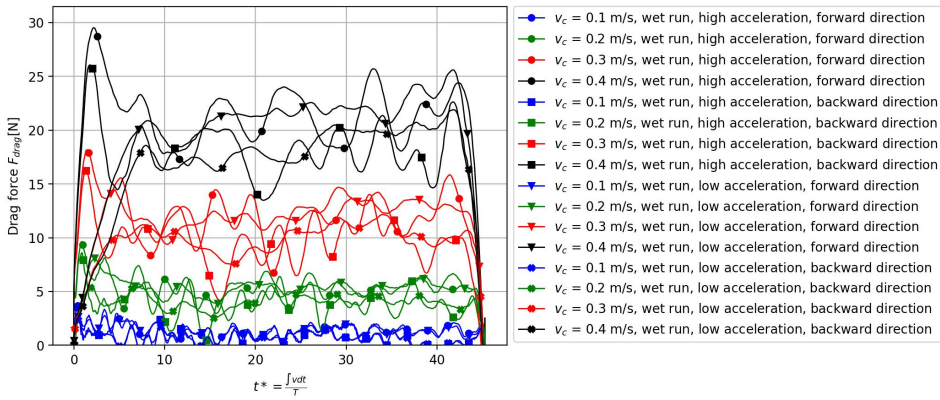

(a) Drag force on the model is plotted against non-dimensional time for carriage speeds v_c of 0.1, 0.2, 0.3 and 0.4 m/s for different run types

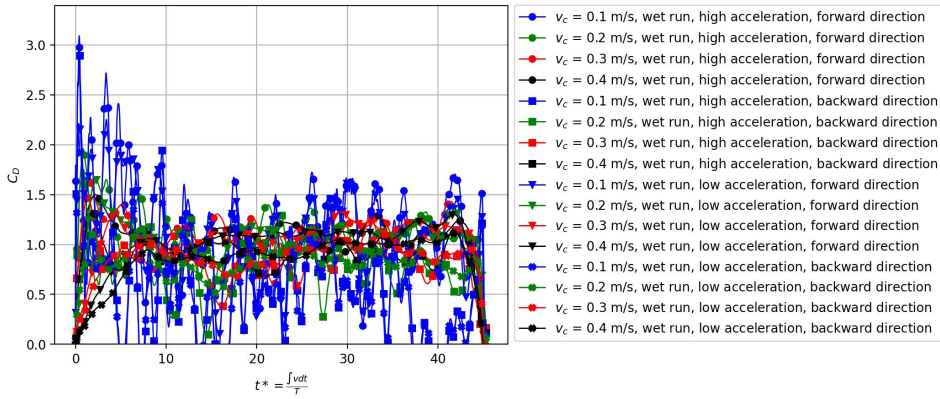

(b) Drag force coefficient is plotted against non-dimensional time for carriage speeds v_c of 0.1, 0.2, 0.3 and 0.4 m/s for different run types

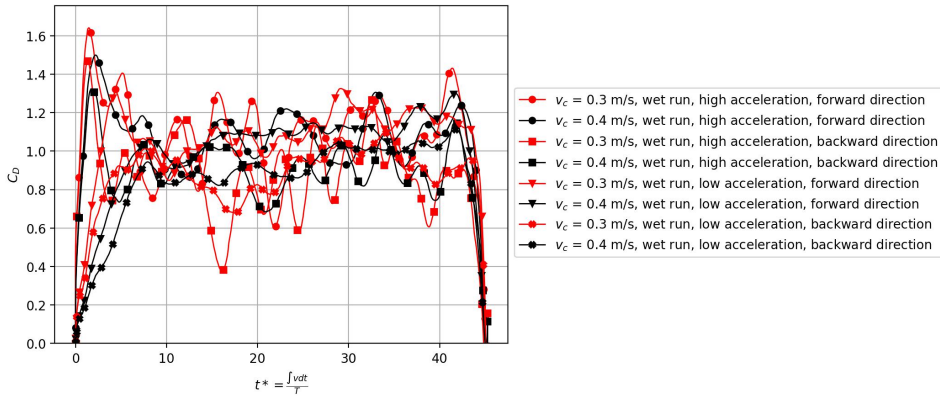

(c) Drag force coefficient is plotted against non-dimensional time for carriage speeds v_c of 0.3 and 0.4 m/s for different run types

Figure 4.42: Results for Model C. Colors are used to indicate the speed and the markers are used to indicate the different run types.

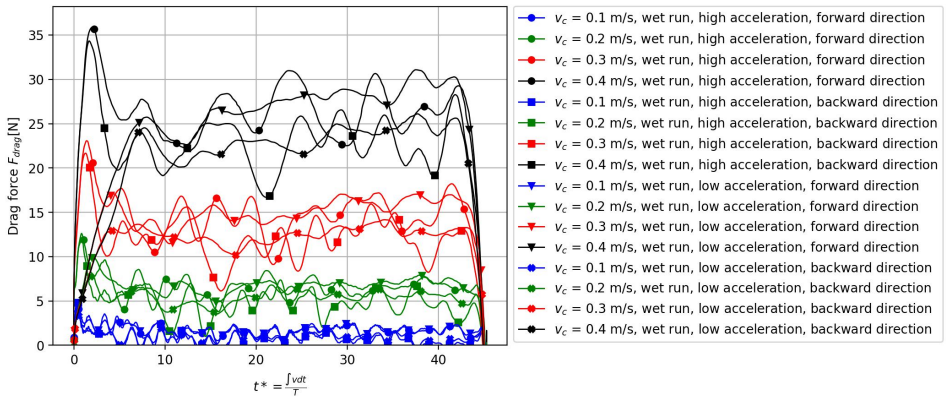

(a) Drag force on the model is plotted against non-dimensional time for carriage speeds v_c of 0.1, 0.2, 0.3 and 0.4 m/s for different run types

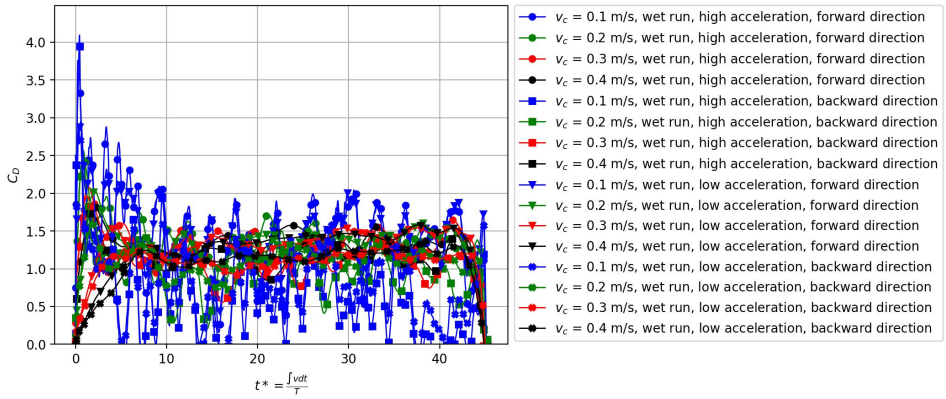

(b) Drag force coefficient is plotted against non-dimensional time for carriage speeds v_c of 0.1, 0.2, 0.3 and 0.4 m/s for different run types

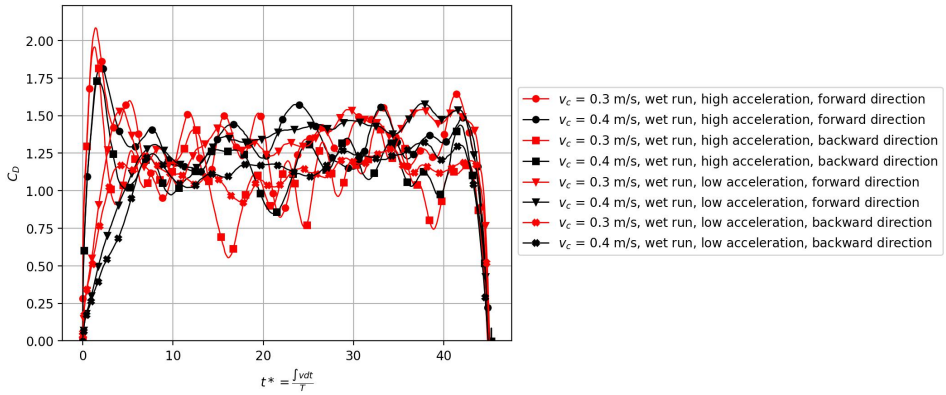

(c) Drag force coefficient is plotted against non-dimensional time for carriage speeds v_c of 0.3 and 0.4 m/s for different run types

Figure 4.43: Results for Model D. Colors are used to indicate the speed and the markers are used to indicate the different run types.

4.6 Uncertainty and Error sources

- **Model Vibration** The model was rigidly attached to the towing carriage and as detailed in Section 4.3.3, the model was stiffened internally to avoid vibration of the model when it is towed. To confirm that the model is suffieciently stiff, a hammar test was conduceted. mAormed in the dry condition for Model A to confirm that the model is sufficiently stiff. The accelerometer on the model was placed near to the base of the model and impulse was given to the model and the accelerations of the model was recorded. It was observed that :
  - The model had a natural frequency of 4.5 Hz for oscillations in y-direction as seen from the time history of acceleration in y-direction from the hammer test shown in Figure 4.44.
  - The model was very stiff and did not have any significant oscillations along x-direction.

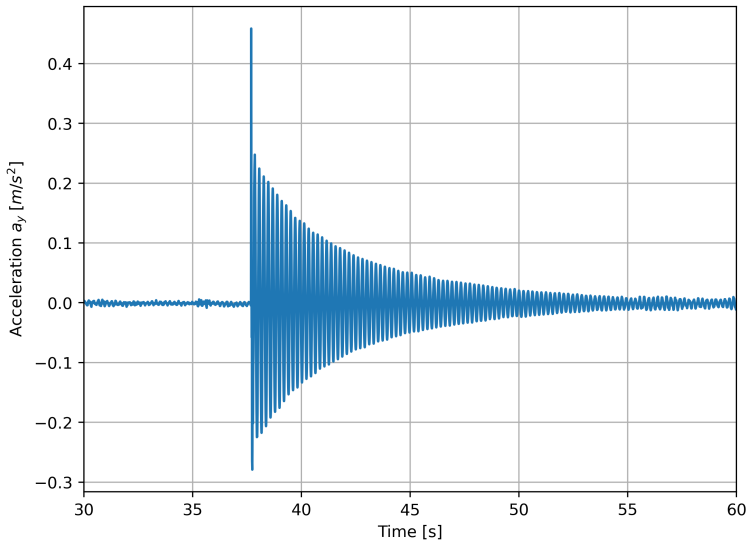

Figure 4.44: Hammer test result. The acceleration of the model is measured in y-direction

- **Free surface effects** The model was run at low Froude number, hence it was assumed that the disturbances on the free surface is minimal and there will be negligible wave making resistance.

  A simplified analysis considering only hydro-static pressure is performed to assess the sensitivity of the measured drag to an increase in water level on

the upstream side of the model. It is assumed that a water level difference of h exists between the upstream side and downstream side when the model is towed (see Figure 4.45). The force contribution in x-direction from the hydro static pressure due to the difference in water level can be obtained as :

$$F_{hyd} = 0.5\rho g T[(h_d)^2 - (h_d + h)^2] \tag{4.11}$$

where,

F_{hyd}	Force in x-direction due to difference in water level on the upstream and downstream side of the model considering only the hydro-static pressure
ρ	density = $1000 kg/m^3$
g	acceleration due to gravity = $9.81\ m/s^2$
T	draft of the model = 0.145 m
h_d	water level height from base of the model = 0.985 m
h	water height difference between the upstream and downstream side of the model

h (cm)	$F_{hyd}(N)$
0.25	-3.5
0.5	-7.0
1	-14.1
2	-28.3

Table 4.4: Variation of the force contribution due to hydro-static pressure as a result of difference in water level height for different values of h calculated using Equation (4.11).

- **Flow past top of the model**
- **Correction force** blockage effect

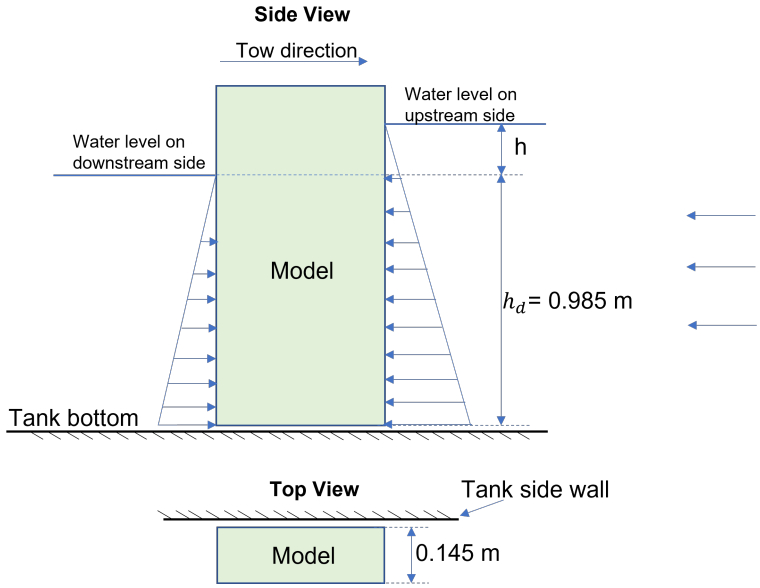

Figure 4.45: Simplified approach to calculate the load in x-direction on the model due to difference in water level height on the upstream and down stream side of the model

Chapter 5

Numerical study of non-linear viscous loads

5.1 Motivation

The experimental results presented in Chapter 4 required making a number of unexpected corrections which were derived based on observation and testing. Also, as detailed in Section 4.4.1, the test conditions do not completely conform to the theoretical expectations. Hence all the model test objectives specified in Section 4.3.1 could not be addressed completely. Therefore, a numerical study using 2D RANS was considered as an alternative approach to augment the experimental work.

The overall objective behind the numerical work are summarised below :

- To explore the physical cause for the nature of the transient drag coefficient curve
- Parametric studies to determine the design parameters which influence the transient part of the drag coefficient curve
- Comparison of the 2D CFD simulation against available experimental and numerical data and study the limitations

5.2 Governing Equations

The governing differential equations for the incompressible flow problem are :

- In-compressible Navier-Stokes Equation

$$\frac{\partial u_i}{\partial t} + u_j \frac{\partial u_i}{\partial x_j} = -\frac{1}{\rho}\frac{\partial p}{\partial x_i} + \nu \frac{\partial^2 u_i}{\partial x_j \partial x_j} \tag{5.1}$$

- Continuity equation

$$\frac{\partial u_j}{\partial x_j} = 0 \tag{5.2}$$

5.3 Solver

- PimpleFoam solver of OpenFOAM is used in the simulations. PimpleFoam is a transient solver which combines Pressure Implicit with Splitting of Operators (PISO) algorithm and Semi-Implicit Method for Pressure Linked Equations (SIMPLE) algorithms and permits transient calculation with large Courant numbers.
- 2D simulations are performed. In OpenFOAM this is implemented by providing only one cell depth in the direction perpendicular to the 2D plane.
- Turbulence model used in all the simulations is $k - \omega$ SST.
- The simulations are performed without using wall functions using wall-resolved approach.

5.4 Computational domain definition

Three computational domains are used in the simulations :

5.4.1 Domain A

The dimensions of domain A is presented in Figure 5.1.

5.4.2 Domain B

Domain B is half of domain A in the vertical direction. Domain B is used for performing simulations with rigid wall assumption for the free surface.

5.4.3 Domain C

Domain C is similar in dimensions to Domain B, however, the difference is in the grading used. In Domain B as seen in Figure 5.2(b), for a length of 14T the cells have uniform spacing. In domain C, this length is increased to 24T. This is done for simulating sections with a large B/T ratio.

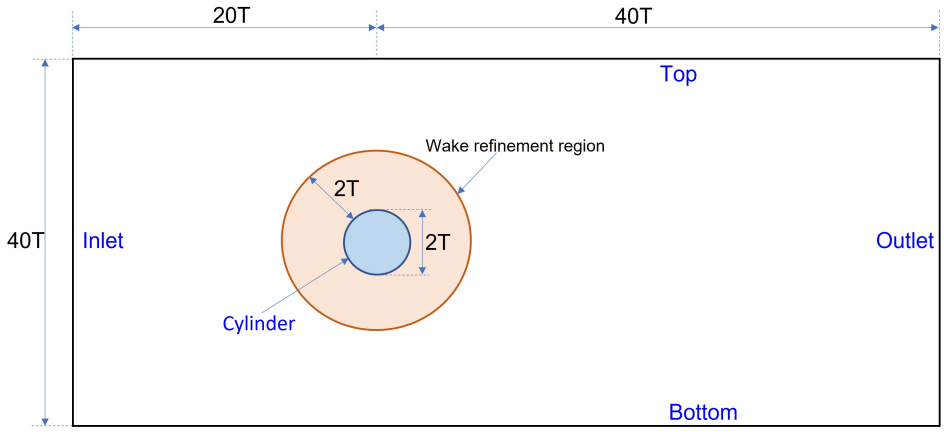

Figure 5.1: Domain size for Domain A

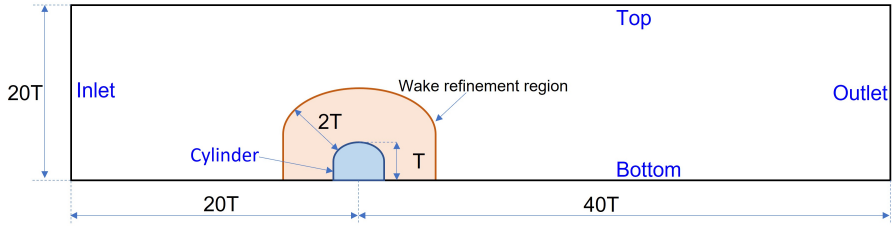

(a) Domain size for Domain B

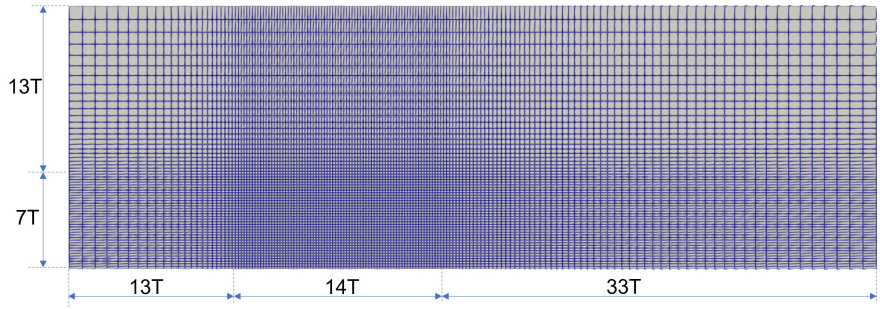

(b) View of `blockMesh` for Domain B. The dimensions indicate the limits for grading used for the cells.

Figure 5.2: Domain B description

On the background `blockMesh`, different simulations use different refinement levels for the wake refinement region and for surface refinement. The meaning of levels in mesh refinement can be inferred from Figure 5.3. Level n will divide the base cells side into 2^n equal sides.

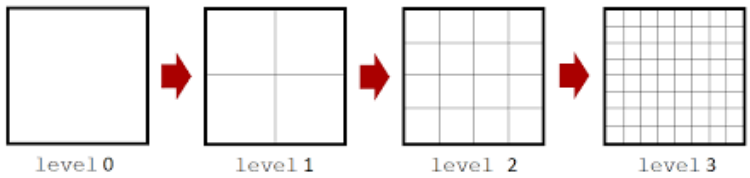

Figure 5.3: OpenFOAM description of levels in mesh refinement

These levels used for different cases are specified in the corresponding sections.

The numerical simulations are designated as SXXX where XXX numbers. This is done to easily refer to different simulations.

5.5 Boundary conditions

The boundary conditions used in all subsequent simulations are described below. For some simulations, small modifications have been made and they are described in the corresponding sections.

	Inlet	Outlet	Top/Bottom	Cylinder
u	fixedValue	zeroGradient	symmetryPlane	noSlip
p	zeroGradient	fixedValue	symmetryPlane	zeroGradient
ω	fixedValue	zeroGradient	symmetryPlane	omegaWallFunction
ν_t	calculated	calculated	symmetryPlane	nutLowReWallFunction
k	fixedValue	zeroGradient	symmetryPlane	fixedValue

Table 5.1: Boundary conditions for simulation

5.6 Circular Cylinder

Initially, test cases are run with circular cylinder as the base geometry because of the available experimental data on the nature of the transient drag coefficient curve from Sarpkaya (1966, 1978).

5.6.1 Comparison of numerically obtained drag coefficient curve with experimental data

Mesh description

The background `blockMesh` conforms to the specifications of Domain A described in Section 5.4.2 with the refinement levels set as :

Wake refinement	Level 3
Surface refinement	Level 4

The mesh used in the simulation is presented in Figure 5.4.

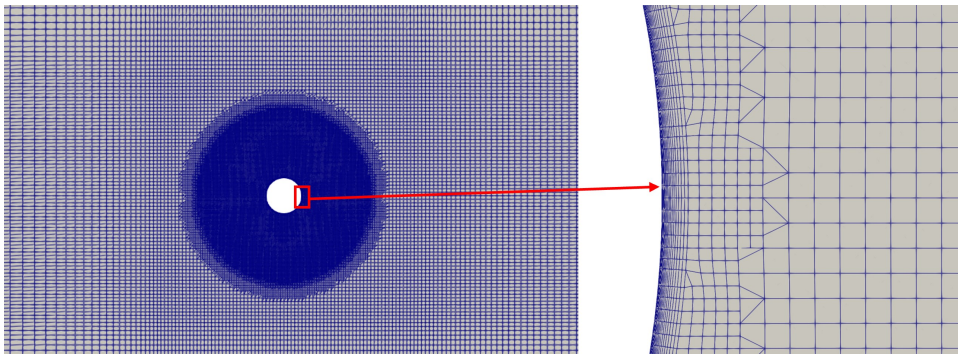

Figure 5.4: Mesh around the circular cylinder (S142, S146, S147)

Boundary conditions

The boundary conditions conform to the specifications in Section 5.5.

Simulation parameters

- The Reynolds number (calculated based on cylinder diameter) selected for the comparison is 32000.
- The time step used in the simulation must be small enough to capture the transient part of the drag coefficient curve accurately, hence a small time step has to be used. 3 different time steps were tested :
  - S142 - The time step was set as 0.0001 s
  - S146 - The time step was reduced to 0.00005 s
  - S147 - The simulation was run with variable time step with the maximum Courant number limited to 0.5.

Simulation results

The drag coefficient obtained from the simulation is plotted against non-dimensional time in Figure 5.5. The non-dimensional time t^* is calculated by as :

$$t^* = \frac{vt}{T} \tag{5.3}$$

where,

v free stream velocity
t time
T characteristic length which is taken as the cylinder radius in case of simulations with circular cylinder

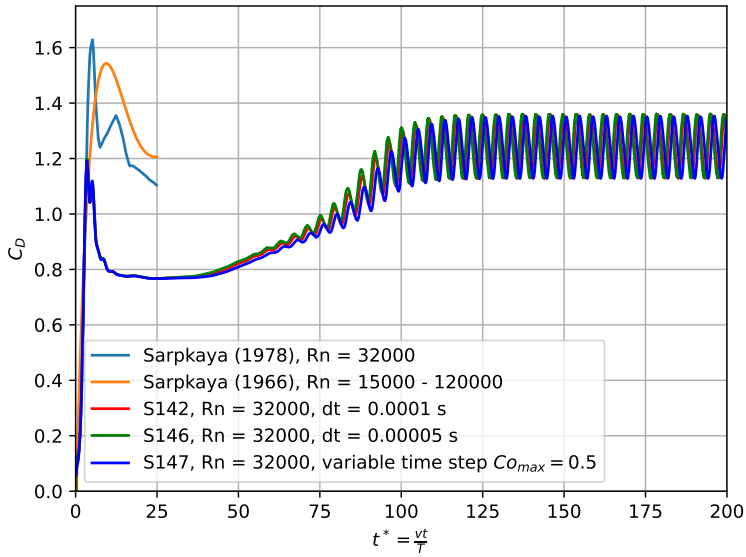

Figure 5.5: Drag coefficient plotted against non-dimensional time for simulations with different time steps. The drag coefficient curve from Sarpkaya (1966, 1978) is also indicted. The curves from the simulation and Sarpkaya (1978) are at Rn = 32000 whereas Sarpkaya (1966) provides a single curve for the Rn in the range 15000 to 120000

Comparing the simulation results presented in Figure 5.5, significant differences are not seen between the variable time step simulation with Courant number limited to 0.5 and the simulation with the smallest time step, however, the variable time step simulation was significantly faster. Hence, all the subsequent test cases are run at variable time step with Courant number limited to 0.5. Further, it is also noted that simulation results plotted are from $t^* \approx 0.2$ as the initial values of drag coefficient are large negative values which are not physical.

The steady-state phase can be defined as the period in which the drag coefficient oscillates around a constant mean value, with a constant amplitude at a frequency that is twice the vortex shedding frequency. From the simulations result presented in Figure 5.5 the steady-state phase starts from $t^* \approx 115$.

Three parameters connected with the drag coefficient can be used to characterize the steady-state phase - the mean drag coefficient ($\overline{C_D}$), the amplitude of oscillation of the drag coefficient, and Strouhal number (St) defined as :

Reference	Time step [s]	$\overline{C_D}$	St
S142	0.0001	1.247	0.240
S146	0.00005	1.248	0.240
S147	variable timestep (Co$\leq$0.5)	1.241	0.244
Experimental value	-	1.21	0.2

Table 5.2: Comparison of $\overline{C_D}$ and St obtained from the simulations and experiment, Co means Courant number

$$St = \frac{2Tf_v}{v} \tag{5.4}$$

where f_v is the vortex shedding frequency, T is the cylinder radius and v is the free stream velocity.

The comparison between $\overline{C_D}$ and St obtained from the simulations and experiment in shown in Table 5.2. The experimental values for $\overline{C_D}$ and St at Rn = 32000 is obtained from the plots presented in Anderson (2016, p. 295) and Sumer and Fredsøe (2006, p. 10) respectively.

From Table 5.2 it can be concluded that there is a fair agreement between the experimental value and the simulation value at the steady-state phase, which validates the mesh and simulation parameters. However, the transient part of simulated drag coefficient curve is significantly different from the experimental results of Sarpkaya (1966, 1978). A zoomed-in view of the of Figure 5.5 is presented in Figure 5.6. The differences can be summarised in terms of two aspects :

- **Maximum value of the transient drag coefficient** In the experimental curves, the maximum value of drag coefficient in the transient phase is ≈ 1.54 and ≈ 1.62 respectively from Sarpkaya (1966, 1978) which is higher than the mean value at steady-state. However, in the numerical simulations, the maximum value of drag coefficient is ≈ 1.19 which is significantly lower than the experimental values and is nearly the same as the mean value at steady-state.
- **Time scale of evolution of drag coefficient curve** The experimental drag coefficient curve from Sarpkaya (1966, 1978) does not indicate the oscillation in drag coefficient which is connected with alternate vortex shedding when the steady-state is attained. However, the flow description and the flow visualization presented in Sarpkaya (1966) clearly indicate the beginning of alternate vortex shedding starting from the capture of the first vortex

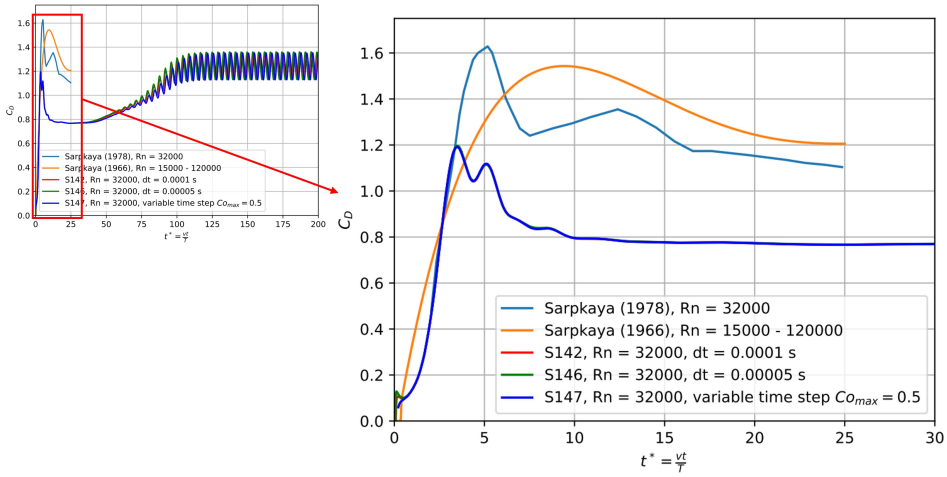

Figure 5.6: Zoomed in view of drag coefficient plotted against non-dimensional time for simulations with different time steps and experimental results from Sarpkaya (1966, 1978). No difference is seen between the results from the 3 simulations.

at $t^* \approx 17$. Further the value of C_D towards the end of experimental data at $t^* \approx 25$ is 1.2 and 1.1 from Sarpkaya (1966, 1978) respectively which is close to the value of $\overline{C_D}$ of 1.21 obtained from other experiments presented in Anderson (2016, p. 295). Hence, it was concluded that the experimental curve of Sarpkaya (1966, 1978) also includes the steady-state phase and the curve most likely presents only the mean drag coefficient value. Hence, the non-dimensional timescale in which the experimental curve evolves and reaches a steady-state can be assumed to < 25 however the non-dimensional time scale at which a steady-state is achieved in numerical simulation is at $t^* \approx 115$. Further, the numerical simulations seem to reach a "pseudo" steady-state between $t^* \approx 10$ and $t^* \approx 40$ which is probably not physically consistent.

Both the maximum value of the drag coefficient attained and the time scale of evolution of the drag coefficient curve has a significant impact on the 2D+t methods. Hence, it is essential that these two aspects are captured accurately by the CFD simulations.

5.6.2 Study of the evolution of flow field around the cylinder (S142)

The velocity and vorticity field around the cylinder is visualized against non-dimensional time in Section G.1. Based on the visualization and additional experimental results from the literature, the physical reasoning behind the evolution

of the drag coefficient curve is presented :

- **Flow separation** According to Schlichting and Kestin (1979), the flow separation in case of laminar flow starts at $t^* = 0.351$ from the rear stagnation point. In the visualized flow the flow separation can be seen clearly at $t^* = 1.1$ and in the subsequent plots, it can be observed the separation point moves upstream rapidly and finally reaches an average steady position.

- **Symmetric wake development** Figure 5.7 presents the drag coefficient and lift coefficient against the non-dimensional time. It can be observed from the flow visualization that initially the wake is characterized by the development of symmetric vortices. This is also confirmed by the lift coefficient curve as it remains zero initially. Also, the vorticity visualizations indicate a rapid accumulation of vorticity in the vicinity of the cylinder initially. Experimental results from Sarpkaya (1966, 1978) indicate that the accumulation of vorticity causes the symmetric vortices to grow to proportions that can be larger than the vortices which occur during the alternate vortex shedding phase. These large symmetric vortices cause a reduction in the pressure at the rear resulting in the peak drag coefficient. Shortly after this, since the symmetric wake is unstable (Odd M. Faltinsen 2006), small disturbances in the flow cause one of the vortices to move away from the cylinder resulting in asymmetry and hence lift begins to develop and the drag coefficient drops to the steady-state value. Therefore in the experimental results of Sarpkaya (1978) the peak drag coefficient coincides with the occurrence of the first asymmetry in the wake. However, the CFD flow visualization shows symmetric vortices up to $t^* \approx 15$. This can also be observed from the lift coefficient curve (see Figure 5.7), which remains zero. Hence in the CFD results, the occurrence of the first asymmetry in the wake (or start of oscillation in the lift coefficient curve) does not coincide with the peak in the drag coefficient curve (see Figure 5.7).

- **Alternate vortex shedding** The occurrence of the first asymmetry is then followed by the vortex closer to the cylinder growing larger and a reduction in the intensity of the other vortex. Subsequently, this process is reversed. Finally, a stage is reached where the larger vortex grows to be so large that it is captured by the flow, and alternate vortex shedding starts. In experiments done by the Sarpkaya (1966), it has been reported that the time from the start of motion to the start of alternate vortex shedding is on an average 60% of the vortex shedding period. This is clearly violated in CFD results.

Based on the timescale provided by Sarpkaya (1966), it can be concluded that

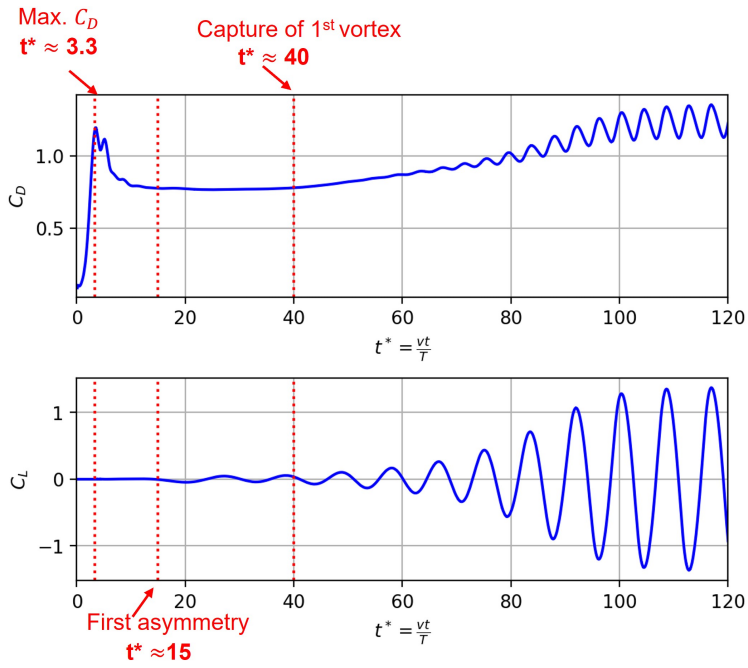

Figure 5.7: Drag and lift coefficient is plotted against non-dimensional time for circular cylinder (S142). The non-dimensional time for the occurrence of the peak drag coefficient, the first asymmetry in the wake (corresponds to the point at which the lift coefficient starts to oscillate), and capture of the first vortex is indicated.

vortex shedding is nearly instantaneous in experiments, however numerical results from CFD indicate a large delay. Vortex shedding is a flow instability that is triggered by perturbations present in the flow and the difference between experiments and CFD is likely due to the perturbation sources involved in triggering this instability. Physically in experiments, the sources of perturbation are (Laroussi et al. 2014):

- Surface irregularities on the cylinder
- Vibration of the system
- Non-uniform inlet conditions

Numerically the sources of perturbations are (Laroussi et al. 2014):

- Amplification of round-off and truncation errors

- Sweep direction used in the numerical scheme
- Errors in discretization and numerical schemes

Hence, in numerical simulations involving a perfectly symmetric flow, larger time is required in numerical simulations for the perturbations to be large enough to trigger vortex shedding compared to the case of physical experiments. Different techniques are used in CFD to reduce the time required to trigger vortex shedding and a few of them from Laroussi et al. (2014) are :

- Impulsive start initial condition for flow
- Cylinder rotation/oscillation
- Using surface roughness element
- Introducing small surface asymmetry
- Perturbation of inlet boundary condition

An important aspect to be noted while using these techniques is that it is essential to ensure that the applied perturbations do not add excess energy which will cause a change in the physics of the flow which is being simulated. In the subsequent sections, two of the above techniques are implemented to check if they can improve upon the agreement between the drag curves from CFD and Sarpkaya (1978).

5.6.3 Impulse start with smooth function for inlet boundary velocity

It was suspected that the lower value of the maximum drag coefficient attained in the numerical simulation could be due to numerical problems associated with how the impulse-started flow is simulated in OpenFOAM. The approach taken in the previous simulations (S142, S146, S147) is as described in Section 5.5, where at $t = 0$ the velocity in the entire internal domain is set to zero and the velocity at the inlet boundary is set to the desired velocity right at the beginning of the simulation. In physical experiments by Sarpkaya (1966), the inlet velocity was ramped up with a constant acceleration to the desired velocity. Hence, it was decided to mimic the same behavior by using a smooth function to ramp the inlet velocity to the desired velocity.

The simplest approach is to use a uniform acceleration to ramp the velocity from zero at the start of the simulation to desired the velocity in a short period of time. However Agromayor et al. (2017) presented an alternative approach. His objective was to numerically simulate the starting and stopping vortices of an airfoil in

OpenFOAM which required simulating both a steep acceleration in the inlet velocity from zero to the desired velocity as well as deceleration from the desired velocity to zero to obtain the starting and stopping vortex respectively. Hence this problem is similar to the current problem. He used a logistic function which is a "S" shaped curve that provides a steep jump in velocity but is also a mathematically smooth function.

The function is mathematically defined as :

$$v = \frac{v_\infty}{1 + e^{-\frac{t-t_0}{k}}} \tag{5.5}$$

where,

v	inlet velocity
v_∞	desired free stream velocity
t	time
t_0	is the midpoint of the sigmoid curve. This is set to 0.5 s in the simulation ($t^* \approx 2.77$)
$\frac{1}{k}$	is the growth rate or steepness of the curve. k is set as 0.01 s.

The fluid velocity and acceleration at the boundary is plotted against non-dimensional time in Figure 5.8.

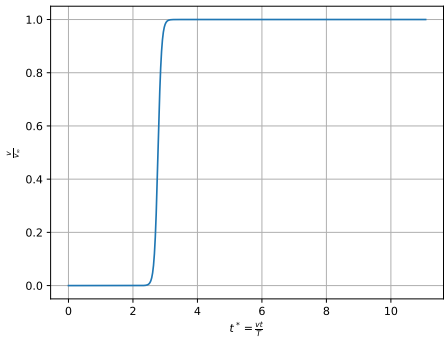

(a) Fluid velocity variation against non-dimensional time

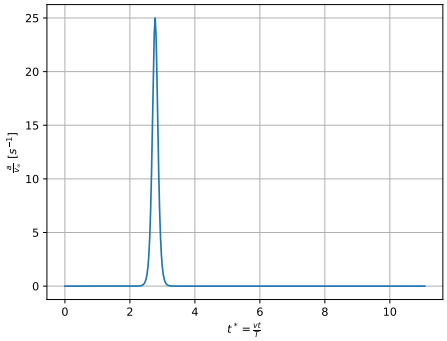

(b) Fluid acceleration variation against non-dimensional time

Figure 5.8: Fluid velocity and acceleration realised using logistic function

Compared to the simulation presented in Section 5.6.1, two differences are noted :

- OpenFOAM outputs the force on the cylinder by integrating the pressure distribution surrounding the cylinder. In this simulation the fluid is accelerated, hence the force calculated by OpenFOAM will include both the inertial

load connected with added mass and the drag force for the brief period in which acceleration is non-zero. After this period, the acceleration will be zero and the force will only include the drag force.

- Non-dimensional time in principle represents the distance moved by the fluid compared to the radius of the cylinder. Hence, t^* must be defined as $t^* = \frac{\int v dt}{T}$ in this case. However, since the interest is in the maximum value of the drag coefficient obtained, for simplicity $t^* = \frac{v_\infty t}{T}$ is used.

The mesh and Reynolds number used in the current simulation (S150) is the same as the one used in Section 5.6.1. The simulation was run with variable time step with the maximum Courant number limited to 0.5. All the boundary conditions conform to the specifications in Section 5.5 except the inlet velocity for which Equation (5.5) is implemented using the `groovyBC` library in OpenFOAM.

The obtained force coefficient curve is plotted against t^* in Figure 5.9.

From Figure 5.9 the following aspects are noted :

- As expected a peak in the force coefficient curve is seen at $t^* \approx 2.94$ which approximately coincides with the peak in acceleration seen in Figure 5.8(b) at $t^* \approx 2.78$. To check if the CFD result is physical the approximate force coefficient can be computed by assuming that initially there is no flow separation and the drag on the cylinder is caused due to the inertial load associated with added mass :

$$C_{for} = \frac{m_a \cdot a_p}{0.5 \cdot \rho \cdot 2T \cdot v_\infty^2} \tag{5.6}$$

where,

C_{for}	Force coefficient
v_∞	final free stream velocity (set to 0.3 m/s in the simulation)
m_a	added mass of cylinder. The 2D added mass for the cylinder immersed in fluid is $\pi T^2 \rho$ where T is the cylinder radius (set to 0.054 m in the simulation) and ρ is the fluid density
a_p	peak acceleration. From Figure 5.8(b) a_p/v_∞ can be obtained as 25

Substituting in Equation (5.6), the force coefficient can be obtained as ≈ 14. The peak force coefficient from CFD is ≈ 16.5 which is in general agreement, the difference is possibly because the actual acceleration in the simulation is not constant at a_p as assumed in the calculation.

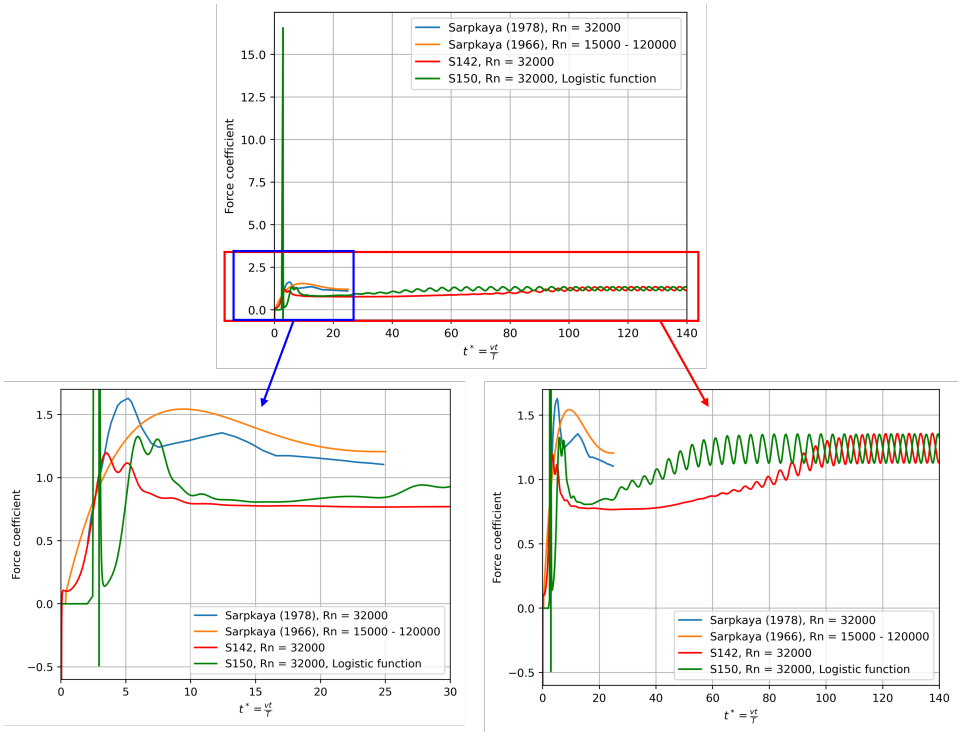

Figure 5.9: Drag coefficient plotted against non-dimensional time for simulation with the inlet velocity set using logistic function (S150). Final Rn for the simulation is 32000. The drag coefficient curve from Sarpkaya (1966, 1978) and result from simulation S142 (described in Section 5.6.1) is also indicted. Zoomed-in plot on the left indicates the shift in the peak value of the drag coefficient curve in S150 compared to S142. Zoomed-in view on the right indicates the convergence in the steady-state value between S142 and S150.

- After the peak in force coefficient at $t^* \approx 2.94$, the force coefficient has slight oscillations and briefly goes to the negative side after the acceleration stops. A shift is seen in the non-dimensional time by $t^* \approx 2.7$ between the peaks in S142 and S150, this is due to the delay in reaching the desired velocity due to the logistic ramping.

- Both the peak drag coefficient value, as well as the time scale of evolution of the drag coefficient curve, see an improvement in S150 compared to S142. The peak drag coefficient value is higher (≈ 1.3) than the value from S142. Further, the steady-state is achieved comparatively faster at $t^* \approx 73$. However, these values still do not match with the experimental data from Sarpkaya (1966, 1978).

5.6.4 Perturbation of inlet velocity

Another technique to reduce the time for triggering vortex shedding is to provide a perturbation to the inflow velocity. A time-dependent shear profile as shown in Figure 5.10 was provided for inlet velocity :

- At $t = 0$, the initial flow velocity at the bottom point of the inlet boundary patch (v_m) is reduced compared to the flow velocity at the top point of the inlet boundary patch where the velocity is the required flow speed v. The velocity at intermediate points of the patch is obtained by linear interpolation.
- As the simulation progresses, the flow velocity at the bottom point of the boundary patch is slowly ramped up at a uniform rate to the required flow speed. This ensures that there is a smooth transition between the inflow with shear and the final uniform inflow state.

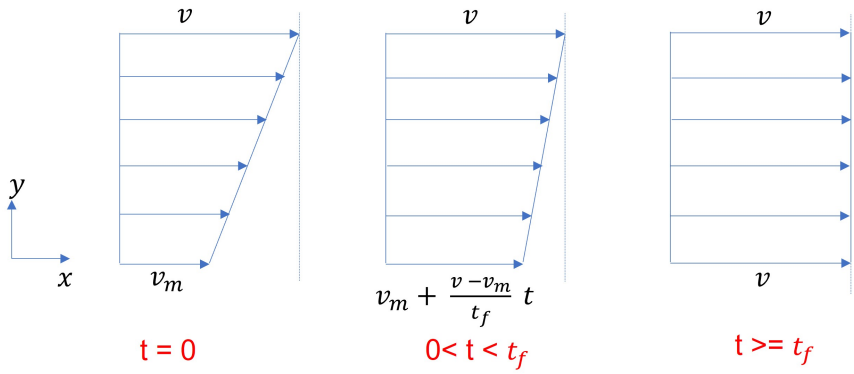

Figure 5.10: The profile for velocity at the inlet boundary is shown for three instances of time : $t = 0$, $0 < t < t_f$ and $t \geq t_f$, where t_f is the time at which velocity at the inlet at both top and bottom corner is equal to v which is the required final flow velocity and t is the simulation time.

The perturbation to the inflow is defined by using 2 parameters :

- t_f - The time at which uniform velocity is attained in the inlet boundary path
- $\frac{v_m}{v}$ - which quantifies the extent of reduction of the velocity at the bottom point of the inlet patch.

The results of 3 simulations are presented:

- S151 - $\frac{v_m}{v} = 0.9$, $t_f = 5$
- S152 - $\frac{v_m}{v} = 0.9$, $t_f = 2$
- S153 - $\frac{v_m}{v} = 0.99$, $t_f = 5$

The mesh and the final Reynolds number used in all simulations is the same as the one used in Section 5.6.1. The simulation was run with variable time step with the maximum Courant number limited to 0.5. All the boundary conditions conform to the specifications in Section 5.5 except the inlet velocity for which the velocity profile shown in Figure 5.10 was implemented using the `groovyBC` library in OpenFOAM.

The results from the simulation are shown in Figure 5.11 and the following conclusions are drawn :

- For all the 3 simulations (S151, S152, and S153), the drag coefficient at the steady-state is similar to the unperturbed case.
- The time required to reach the steady is sensitive to the parameters used to define the shear. However, still, the peak value of the drag coefficient from the experiment cannot be matched by the numerical simulation.

A possible reason for the mismatch in the peak value as well as the time scale of evolution is connected with the intensity of turbulence. This affects the rate at which the circulation is dissipated (Sarpkaya 1966). Since lower peaks are obtained in the simulations, the numerical simulations possibly encounter a higher turbulence intensity.

5.7 Semi-circular section

The simulations with semi-circular sections utilize Domain B described in Section 5.4.2. The mesh description, boundary conditions, and simulation parameters remain the same as described in Section 5.6.1.

5.7.1 Comparison of numerical results with experimental data

The simulation results for 2 Reynolds number Re = $3.2 \cdot 10^4$ (S141) and Re = $8.58 \cdot 10^4$ (S232) is shown in Figure 5.12. The following observations are made :

- The initial peak in drag coefficient occurs due to the development of symmetric vortices. Hence, the drag coefficient curve for the initial part for $Rn = 3.2 \cdot 10^4$ for the circle and semi-circular section remains the same.

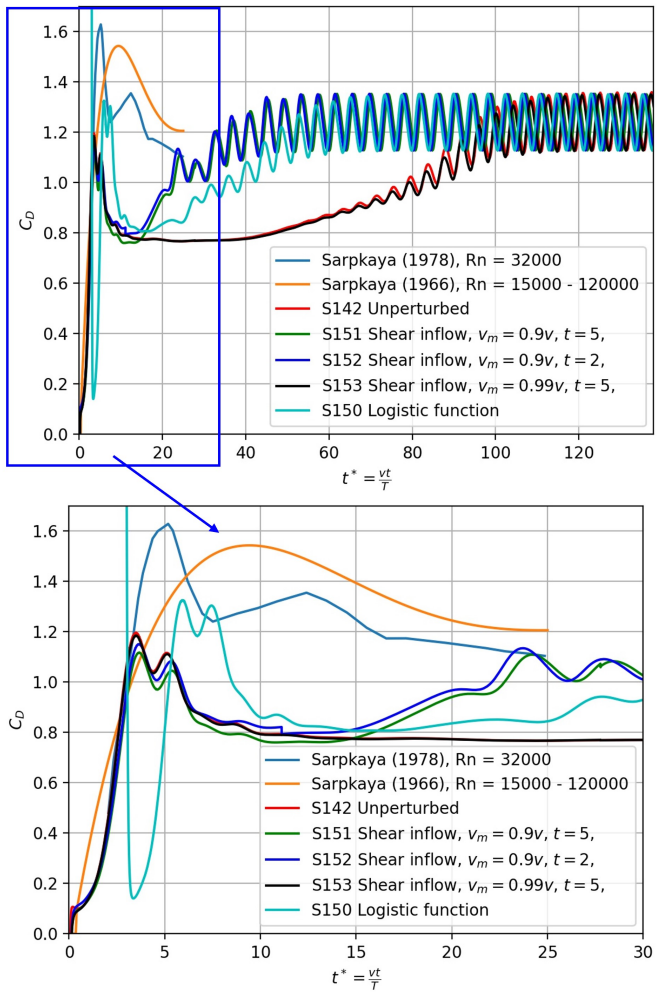

Figure 5.11: Drag coefficient plotted against non-dimensional time for simulation with the inlet velocity defined as a time dependent shear profile as shown in Figure 5.10. Three different cases are shown with different parameters used to define the profile (S151, S152, S153). For comparison the result from the simulation with impulse started flow using logistic function (S150) and the unperturbed initial case (S142) is also included. Final Rn for all the simulations is 32000. The drag coefficient curve from Sarpkaya (1966, 1978) is also indicted. A zoomed in view showing the variation up to $t^* = 30$ is also included.

- Experimentally the effect of free surface can be accounted by reducing the steady-state drag coefficient by 27.3% (Shen 2018). This level is also marked in Figure 5.12. The value obtained from numerical simulations is significantly lower.

- By comparing the curves for Re = $3.2 \cdot 10^4$ and Re = $8.58 \cdot 10^4$, it can be observed that for higher Reynolds number the peaks, as well as the Reynolds number, is lower.

The velocity and vorticity field around the cylinder is visualized against non-dimensional time in Section G.2 for $3.2 \cdot 10^4$. An important difference seen in the semi-circular section when compared to the circular cylinder case is that the shed vortices do not move away but they form a recirculating zone behind the semi-circular cylinder.

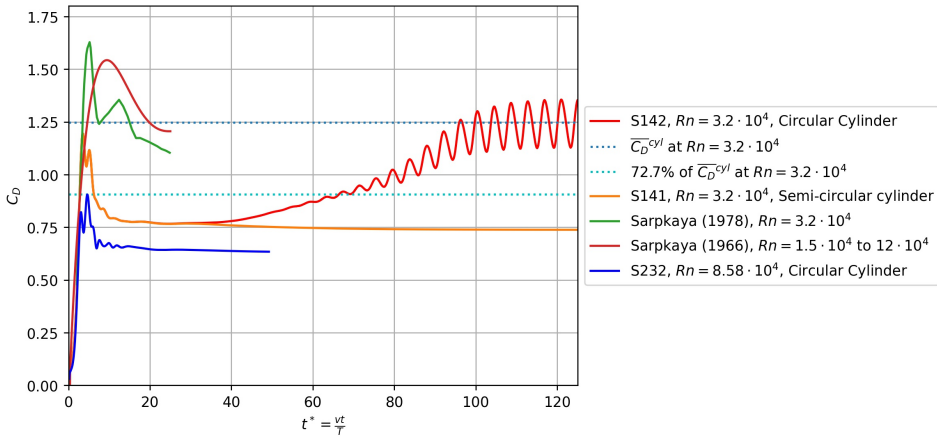

Figure 5.12: Drag coefficient plotted against non-dimensional time for simulation with semi-circular section for $Rn = 3.2 \cdot 10^4$ (S141) and $Rn = 8.58 \cdot 10^4$ (S232). For comparison the result from simulation with circular cylinder (S142) and the drag coefficient curve from Sarpkaya (1966, 1978) is included. Horizontal dotted lines are drawn at mean drag coefficient $\overline{C_D^{cyl}}$ of simulation with the circular cylinder (S142) and at $0.727 \cdot \overline{C_D^{cyl}}$.

5.7.2 Comparison with experimental results

Figure 5.13 presents a comparison between the numerical results and experimental results from Figure 4.41(c) for Model B. It is observed in the numerical simulations the peak occurs earlier than that in the case of the experiment. This may be due to the fact that the carriage takes some time to reach the required speed. The peak values are comparable between the experiment and numerical simulation, keeping in mind the uncertainties involved in the experiment.

5.8 Aarsnes ship sections

This section deals with CFD simulations to obtain the transient 2D sectional drag coefficient for the ship sections used by Aarsnes (1984). The motivation behind

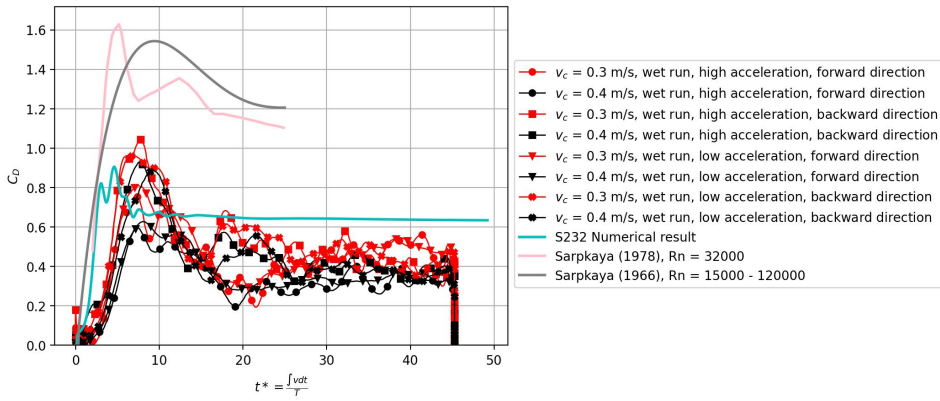

Figure 5.13: Drag coefficient obtained from numerical simulation S232 is compared against experimentally obtained result of Model B (see Figure 4.41(c))

this is to compare the transient drag coefficient curve obtained from 2D CFD simulations against the vortex tracking method used by Aarsnes (1984).

5.8.1 Comparison between the drag coefficient curve from vortex tracking method and 2D CFD

The 2D sections of the vessel is shown in Figure 5.14. The vessel has a length L_{pp} = 235 m, breadth B = 32.25 m and draft T = 12.4.

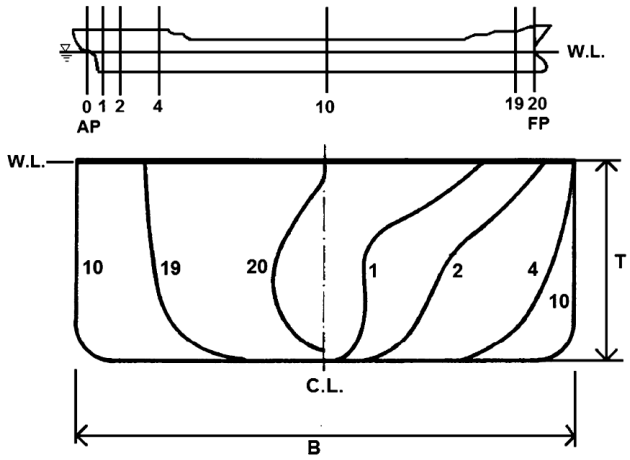

Figure 5.14: Ship sections of 60,000 dwt tanker used by Aarsnes (1984) for calculating the unsteady drag coefficient curve using vortex tracking method (from Arslan et al. 2016)

For each cross-section, Aarsnes (1984) presents the the transient drag coefficient

curve for laminar separation (sub-critical flow) with Reynolds's number $Rn = 1.5 \cdot 10^5$ and for turbulent separation (trans-critical flow) with Reynolds's number $Rn = 1.24 \cdot 10^7$. The Reynolds's number is defined based on the draft of the vessel.

Mesh description

The background `blockMesh` conforms to the specifications of Domain B described in Section 5.4.2 for all the ship sections from Aarsnes (1984) except for Section 10. For Section 10 and additional sections constructed for the parametric study on B/T ratio described in Section 5.8.3 Domain C has been used. Based on mesh sensitivity studies the refinement levels for all the cases were set as :

Wake refinement	Level 4
Surface refinement	Level 5

Using these settings, post-simulation the maximum y^+ obtained was less than 1.

Boundary conditions

The boundary conditions conform to the specifications in Section 5.5.

Simulation parameters

- The simulations were run with Reynolds's number $Rn = 1.5 \cdot 10^5$ corresponding to sub-critical flow which was used in Aarsnes (1984).
- The simulation was run in variable time step mode with a limitation on maximum Courant number as 0.5.

Results

The snapshot of the mesh and the obtained drag coefficient curves compared against the results from Aarsnes (1984) are presented in Chapter F.

Both the 2D CFD method and Aarsnes (1984) vortex tracking method used the rigid wall approximation for representing the free surface. The major challenge in the vortex tracking method is the calculation of the flow separation point. Aarsnes (1984) used "triple deck" method for calculating the separation points meaning that the flow on the surface of a solid is divided into 3 decks or layers - the innermost deck is the layer closest to the wall where viscous effects play a dominant role, then the middle deck in which the flow is rotational but inviscid and finally the outer deck which is inviscid and irrotational.

The conclusions drawn from the plots presented in Chapter F are :

- A general agreement could be seen in the timescale of evolution of the drag coefficient curve between the two methods, however, the peak drag values obtained have discrepancies.
- Section 1 and Section 20 are most similar to circular cylinder and are respectively the aft-most and forward-most sections of the vessel. Both the CFD and Aarsnes results agree that the highest peak drag coefficient occurs for Section 1 and Section 20. These sections are significant because they have the largest lever while calculating the yaw moment due to the cross-flow drag. The CFD and Aarsnes result agree well at $Rn = 1.5 \cdot 10^5$ for Section 1, however in Section 10 the CFD results appear closer to Aarsnes results at $Rn = 1.24 \cdot 10^7$, however in this case the difference in Aarsnes results for $Rn = 1.5 \cdot 10^5$ and $Rn = 1.24 \cdot 10^7$ are not as different as in case of Section 1.
- Section 2, 10, and 19 move away from the circular cylinder shape. Here the difference is that flow separation may occur both at the forward bilge as well as the aft bilge, based on the flow regime. In general for these sections the CFD results at $Rn = 1.5 \cdot 10^5$ are more in agreement with the Aarsnes results at $Rn = 1.24 \cdot 10^7$, especially for Section 2 (Figure F.4). For this section Aarsnes (1984) reported significant numerical difficulties at $Rn = 1.5 \cdot 10^5$ for establishing separation from both the forward and aft bilge. Also a significant difference is seen between the Aarsnes curves for steady-state values of drag coefficient between $Rn = 1.5 \cdot 10^5$ $Rn = 1.24 \cdot 10^7$. Further, in Aarsnes (1984, p. 334), he has presented the experimentally determined steady-state coefficient in the case of sub-critical flow to be from 0.98 to 1.09. This is not matched by his results and the reason stated for this difference is the difficulty in breaking down the formed vortex numerically to reach the steady-state at which the experimental values were obtained. The induced velocities from this vortex result in increased drag. These uncertainties could be the reason for the CFD and Aarsnes results at $Rn = 1.5 \cdot 10^5$ to be significantly different for Section 2.

Both CFD approach and vortex tracking method are numerical methods, hence it is difficult to conclude the accuracy of the obtained drag coefficient curve, however Aarsnes (1984) has used flow visualizations from model tests extensively to support his approach.

An interesting anomaly is seen in the result of Section 10 and is reproduced in Figure 5.15. Similar to the case of the cylinder (see Figure 5.5), the drag coefficient after reaching the peak goes down to a lower value and then rises back up to a value that is approximately equal to the peak value. Such a behavior is not seen in

any case presented by Aarsnes (1984). Even though a small increase in the drag coefficient is seen from the minimum point post the peak value in CFD results (for instance see CFD result of Section 20 in Figure F.10), however, such a large increase is not seen in other cases. The steady value of the drag coefficient for Section 10 has been experimentally determined and presented in Aarsnes (1984, p. 334) to range from 0.85 to 1.26, which is in general agreement with the steady-state value seen in the CFD result (see Figure 5.15).

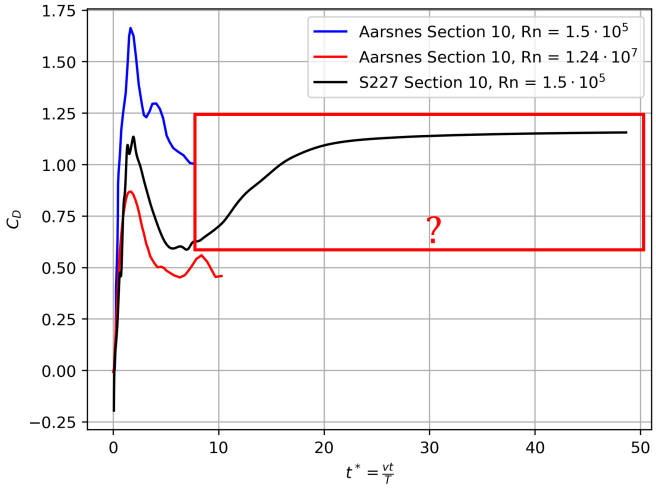

Figure 5.15: Drag coefficient from 2D CFD simulation with $Rn = 1.5 \cdot 10^5$ is plotted against non-dimensional time for Aarsnes ship section 10. Drag curves obtained using vortex tracking method from Aarsnes (1984) is also indicated for $Rn = 1.5 \cdot 10^5$ and $Rn = 1.24 \cdot 10^7$. An anomaly is seen (marked with red box) in the drag coefficient curve from CFD compared to other the Aarsnes (1984) results as well as CFD results for other ship sections.

To investigate the cause of this anomaly, two subsequent studies are performed.

5.8.2 Study on the drag contributions using a split model

To check if the result presented in Figure 5.15 is physical, the contribution to drag coefficient from different parts of the model are separately extracted. The model is split into patches as shown in Figure 5.16. The extracted contribution to the drag coefficient is shown in Figure 5.17.

The important conclusions drawn from Figure 5.17 are :

- As expected the major contribution to the drag coefficient comes from the fwd patch and it remains nearly a constant in the simulation after the initial

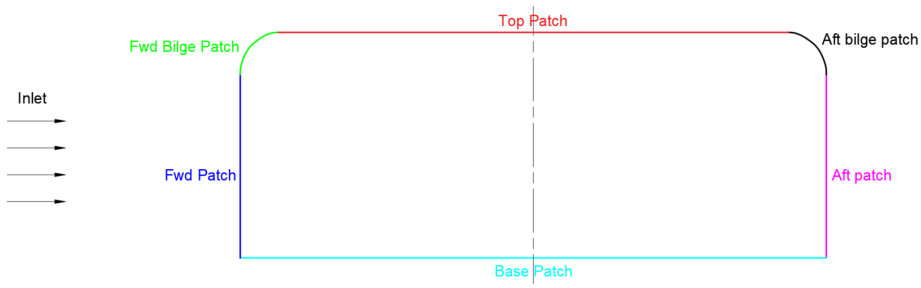

Figure 5.16: Patch names for section without bilge keel

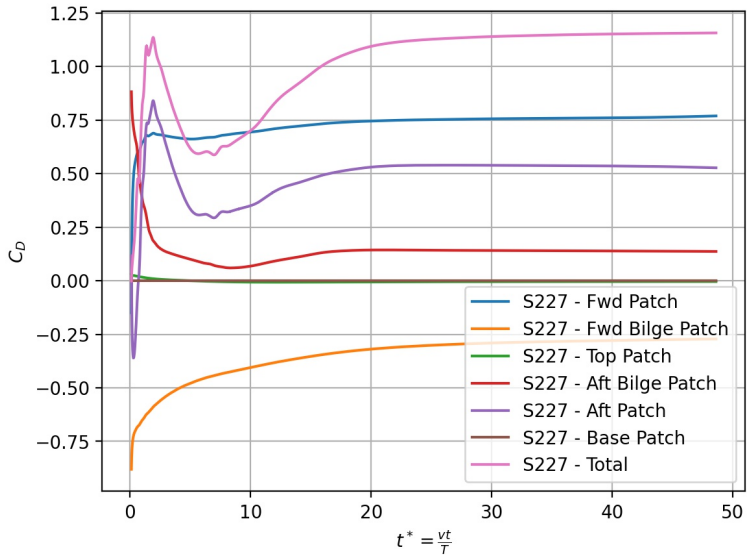

Figure 5.17: Individual contributions to the drag coefficient from the different patches in the model (see Figure 5.16) is plotted against non-dimensional time for Aarsnes Section 10. The total drag coefficient which is the sum of the individual contributions is also plotted.

startup.

- There is a speed-up of flow in the bilge sections leading to a reduction in pressure, hence the forward bilge and aft bilge patches give a negative and positive contribution to the drag coefficient respectively.
- The contribution from the top patch is almost zero as its contribution to drag is only frictional which is much smaller than the pressure drag contributions.

Further, the contribution from the base patch is also zero as it is not in contact with the fluid.

- The shape of the total drag coefficient seems to follow the shape of the drag coefficient of the aft patch.

The individual contributions do not show any major anomalies. According to O. M. Faltinsen (1990, p. 193), B/T ratio does not have a large influence on the steady drag coefficient unless the B/T ratio is very small i.e $B/T < 0.8$. Hence to check the validity of the obtained result a parametric study was performed by constructing sections that have the same bilge radius but with different B/T ratios and it is expected that they will yield nearly the same steady-state drag coefficients.

5.8.3 Parametric study on B/T ratio

Parametric studies are performed using 4 B/T ratios - 2.6, 3, 3.5, and 6. The resulting sections are shown in Figure 5.18.

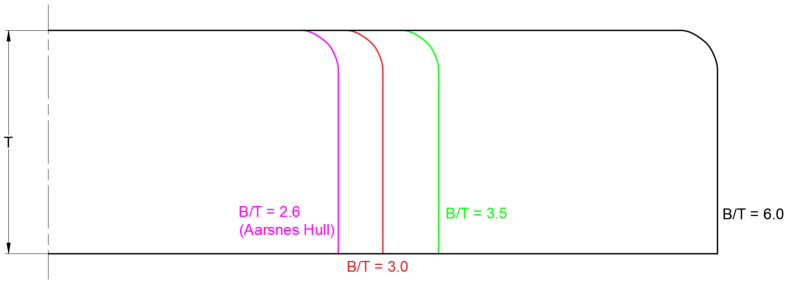

Figure 5.18: B/T ratios used in the parametric study of Aarsnes section 10. The draft and bilge radius of all the sections is the same. Only the breadth of the hull is changed to obtain the desired B/T ratio.

The resulting drag coefficient variation for different B/T ratios are plotted against the non-dimensional time in nFigure 5.19. It can be observed that for all the sections, the minimum drag coefficient which occurs post the initial peak is at nearly the same non-dimensional time $t^* \approx 6$. Further, the numerical results indicate that the B/T ratio influences the steady-state drag coefficient.

The individual contribution from different patches for B/T ratios 2.6, 3.5 and 6 is shown in Figure 5.20. It can be observed that the difference in steady-state values of drag coefficient is primarily linked to the contribution from the aft path.

A detailed comparison of the evolution of flow around the sections with B/T ratios 2.6, 3, and 6 are shown in Section G.3 against non-dimensional time. It can be

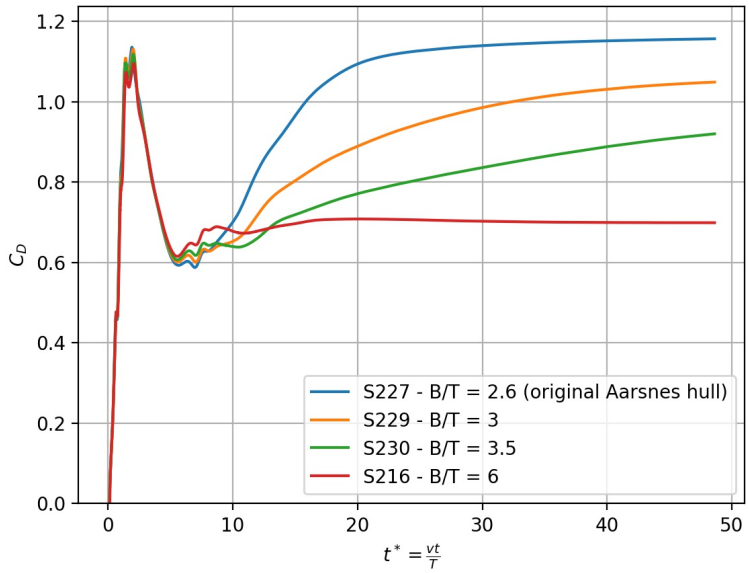

Figure 5.19: Drag coefficient is plotted against non-dimensional time for the different sections shown in Figure 5.18.

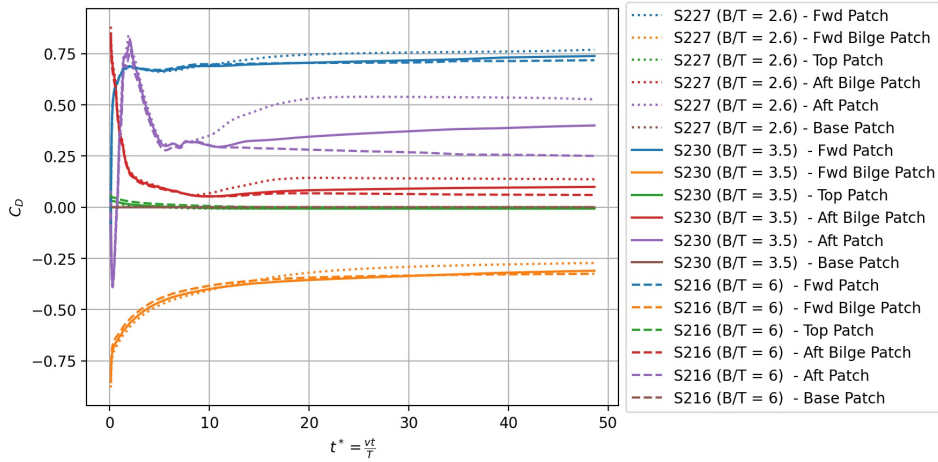

Figure 5.20: Individual contributions to the drag coefficient of sections with B/T ratio 2.6, 3.5 and 6 (see Figure 5.18) is plotted against non-dimensional time. Colors are used to indicate the patch and the line types are used to indicate the B/T ratio.

observed that two recirculating zones develop over time - one near the forward bilge and the other near the aft bilge. A rational explanation for the observed

drag coefficient curve is that for $t^* < 6$, the two re-circulating zones are small such that they would develop independently without influencing each other even for the lowest B/T ratio of 2.6 considered in the study. However, at $t^* > 6$, the recirculating zones grow into a sufficient size such that they begin to influence each other. This influence will reduce with increasing B/T ratio i.e. as the distance between the recirculating zones increases. This probably leads to a lower steady drag coefficient value as B/T ratio increases. However experimental studies are necessary to validate this theory.

5.9 DTC Hull

This section deals with CFD simulations to obtain the transient 2D sectional drag coefficient for select ship sections from DTC hull. The motivation behind this is to compare the transient drag coefficient curve obtained from 2D CFD simulations against the curves obtained by experiments described in Chapter 4 for Model A, C, and D. Also the transient drag coefficient curves are obtained for additional DTC sections as they are the input for 2D+t - 2D CFD based methods described in Section 3.2.2.

Mesh description

The background `blockMesh` conforms to the specifications of Domain B described in Section 5.4.2 for all the ship sections except for ship sections used in parametric studies. For these sections Domain C has been used. Based on mesh sensitivity studies the refinement levels for all the cases were set as :

Wake refinement	Level 3
Surface refinement	Level 4

Using these settings, post-simulation the maximum y^+ obtained was less than 1.

Boundary conditions

The boundary conditions conform to the specifications in Section 5.5.

Simulation parameters

- The simulations were run with Reynolds's number $Rn = 4.29 \cdot 10^4$. The Reynolds's number is calculated based on the ship draft.
- The simulation was run in variable time step mode with a limitation on the maximum Courant number as 0.5.

5.9.1 Drag coefficient curves for DTC sections

2D CFD simulations were run on select sections of DTC hull shown in red in Figure 5.21(b). These sections are numbered such that the corresponding sections have a close resemblance with the sections used by Aarsnes (1984).

The resulting drag coefficient curve for the different sections has been presented in Figure 3.12. Comparing the corresponding curves of DTC vessel with that of Aarsnes (1984) sections (see Chapter F) it can be observed that the peak value of drag coefficient is highest for Section 1 and section 20 which are very important for 2D+t methods as these sections may have a significant contribution to yaw moment due to transverse viscous loads for the vessel.

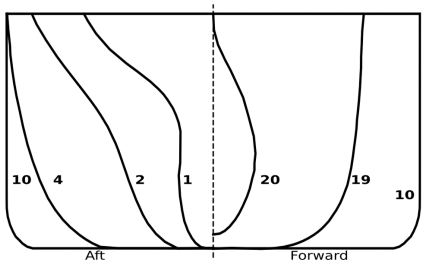

(a) Sections from Aarsnes (1984). Sec 1, 2, 10, 19 and 20 were used in 2D+t methods proposed by Rabliås and Kristiansen (2021) for simulating DTC maneuvers

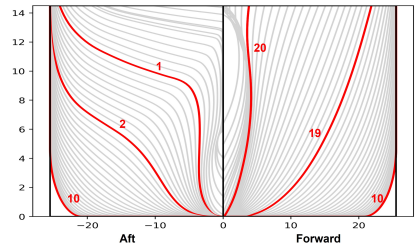

(b) A selection of sections from DTC. 2D CFD is performed to determine the transient drag coefficient for sections indicated in red

Figure 5.21: Comparison of Aarsnes sections and DTC sections. The sections selected for 2D CFD for DTC hull are given the same number as the most similar section in Aarsnes (1984).

5.9.2 Comparison of numerical and results experimental results for Model A

Figure 5.22 shows the comparison between the experimentally obtained drag coefficient of Model A and the result from numerical simulation.

From Figure 5.22 it can be observed that if the results from low acceleration runs are ignored, then a slight resemblance can be seen between the experimental curve and the curve from numerical results. However, the spread of the data in the experiment is too large to make any reasonable conclusions.

5.9.3 Effect of bilge keel

Simulations were performed with different bilge keel heights as shown in Figure 5.23.

The resulting drag coefficient curve is presented in Figure 5.24.

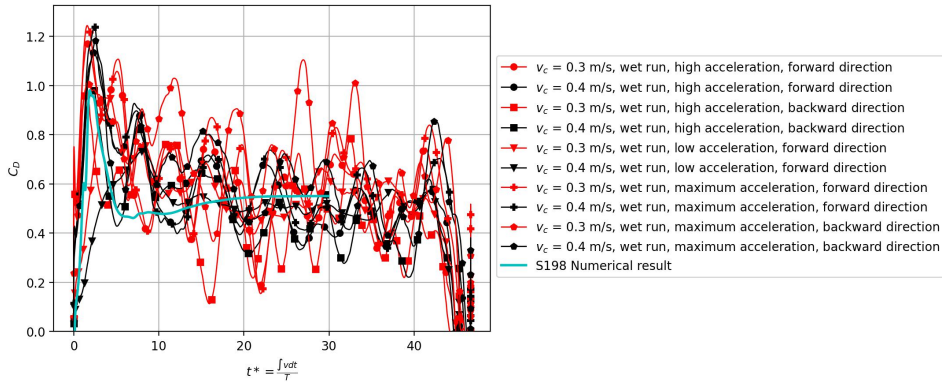

Figure 5.22: Drag coefficient obtained from numerical simulation is compared against experimentally obtained result of Model A (see Figure 4.40(c))

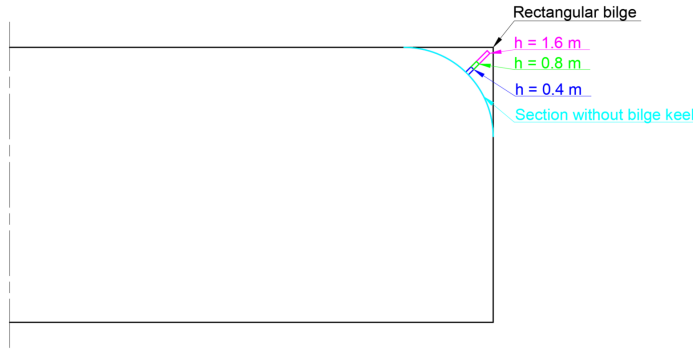

Figure 5.23: Bilge keel heights $h_{bk} = h$ used in the study. The dimensions marked are full scale values.

The following conclusions are drawn from Figure 5.24:

- As expected both the transient and steady drag coefficient increases with increasing height of the bilge keel.
- It can be noted that the peak value of drag coefficient is reached very quickly in the case of rectangular section and for bilge keel with the largest height. Further, the drag curve of the rectangular section is very close to the bilge keel section with the largest height. This can be explained by the close resemblance of the flow pattern as shown in Figure 5.25.

  For sections with bilge keel, a similar behavior as seen for Aarsnes section 10 (see Figure 5.15) is observed - the drag coefficient starts to increase after

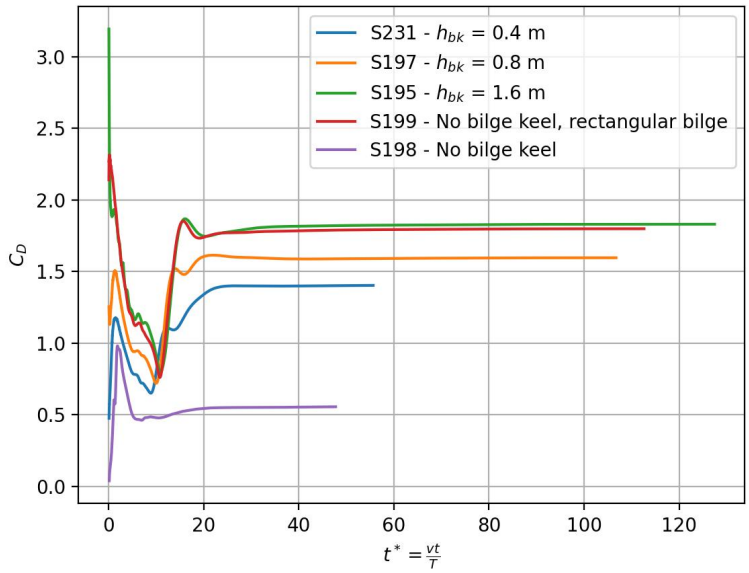

Figure 5.24: Drag coefficnts for rectangular section and sections with different bilge keel heights h_{bk}

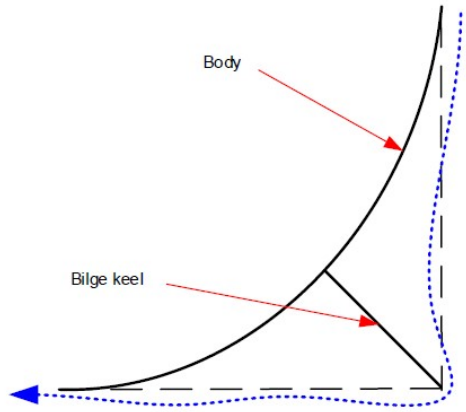

Figure 5.25: Flow around section with bilge keel and rectangular section (Shen 2018)

reaching a minimum post the initial peak.

A comparison between the experimentally obtained drag coefficient from Model C and Model D from Figures 4.42(c) and 4.43(c) respectively are shown in Figures 5.26 and 5.27 respectively.

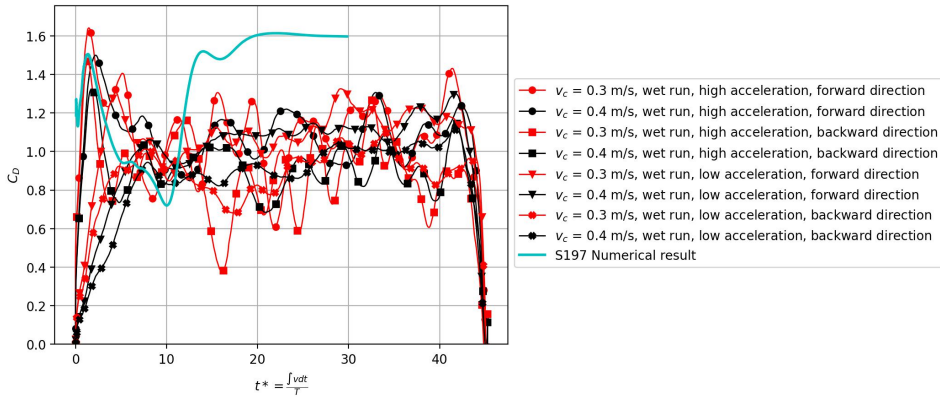

Figure 5.26: Drag coefficient obtained from numerical simulation is compared against experimentally obtained result of Model C (see Figure 4.42(c))

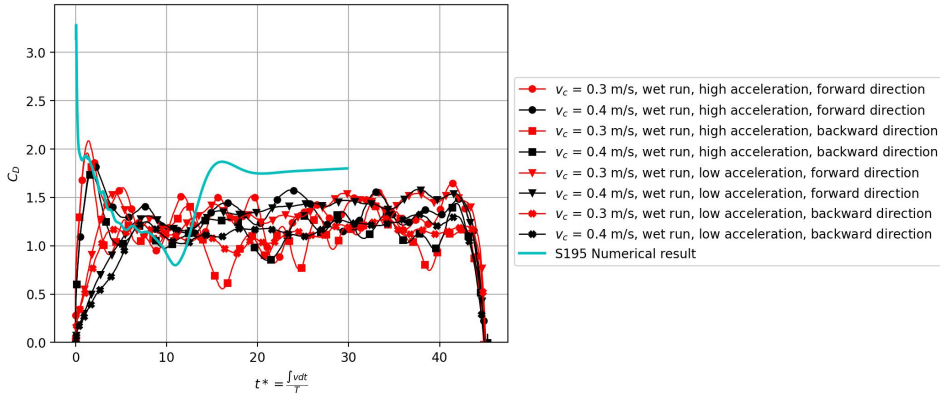

Figure 5.27: Drag coefficient obtained from numerical simulation is compared against experimentally obtained result of Model D (see Figure 4.43(c))

It can be observed that this increase in drag coefficient post the minima is not present in the experimental results. Hence, a detailed parametric study was done.

5.10 Effect of B/T ratio for sections with bilge keel

The B/T ratios used in the study are presented in Figure 5.28. The resulting drag coefficient curve is plotted in Figure 5.29. In contrast to the section without bilge keel, here it is observed that the minimum point shifts forward with an increasing B/T ratio. From the detailed flow visualization presented in Section G.4 it can be concluded that the increase in drag post the minima occurs at the point where the recirculation zone near the forward bilge reaches the recirculation zone in the aft.

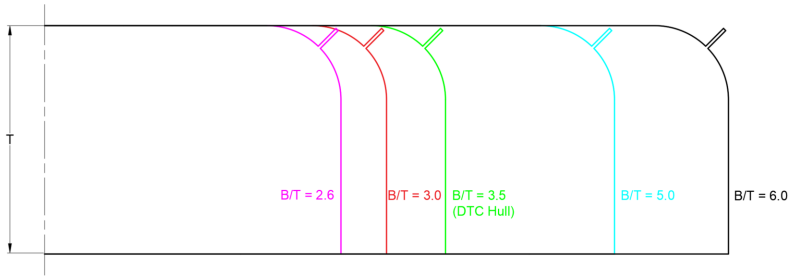

Figure 5.28: B/T ratios used in the parametric study in sections with bilge keel. The sections are based on the midship section of DTC hull. The height of bilge keel and draft of all the sections is fixed at 0.16 m and 14.5 m respectively.

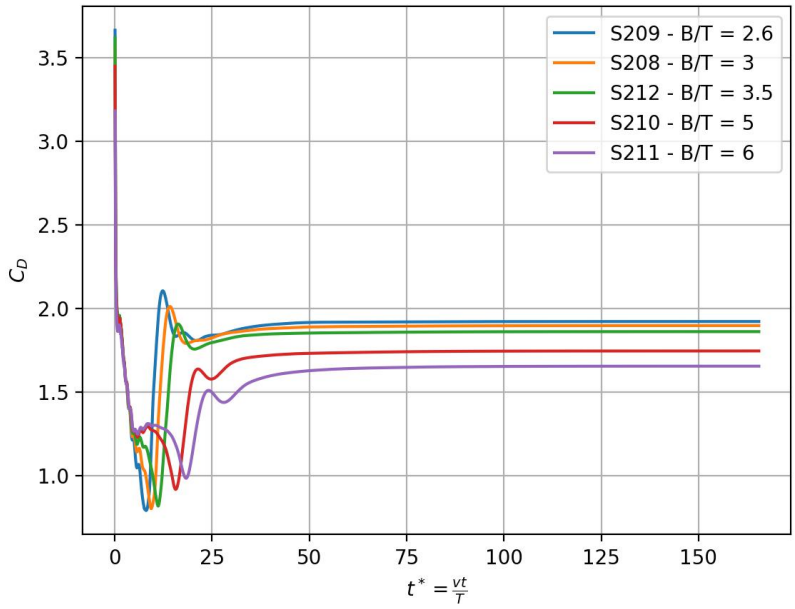

Figure 5.29: Drag coefficient for different B/T ratios for section with bilge keel

Chapter 6

Maneuvering simulations

The chapter presents the results of the turning circle maneuver of DTC and KCS vessels in calm water and in regular waves. Comparisons are made between the numerical results and available experimental results. The experimental results for DTC vessel and KCS is obtained respectively from Rabliås and Kristiansen (2021) and *SIMMAN* (2020).

6.1 Parameters of interest in calm water and maneuvering in waves

The parameters which are used to describe the turning circle test in calm water as indicated in Figure 6.1 are (ITTC 2002) :

- **Advance** ($x_{0,90}$) It is the distance moved by the vessel in the direction of approach, from the point of execution of the rudder to the point where the vessel has a heading change by 90°.
- **Transfer** ($y_{0,90}$) It is the distance moved by the vessel in the direction perpendicular to the initial approach course, from the point of execution of the rudder to the point where the vessel has a heading change by 90°.
- **Tactical diameter** ($y_{0,180}$) It is the distance moved by the vessel in the direction perpendicular to the initial approach course, from the point of execution of rudder to the point where the vessel has a heading change by 180°.
- Loss of speed on steady turn

In addition to these parameters, the steady-state in the turning circle is described

by using the steady-state turning radius, speed, yaw rate, and the drift angle. Further, the maximum roll angle and the peak yaw rates are also considered as the parameters of interest in turning circle maneuver.

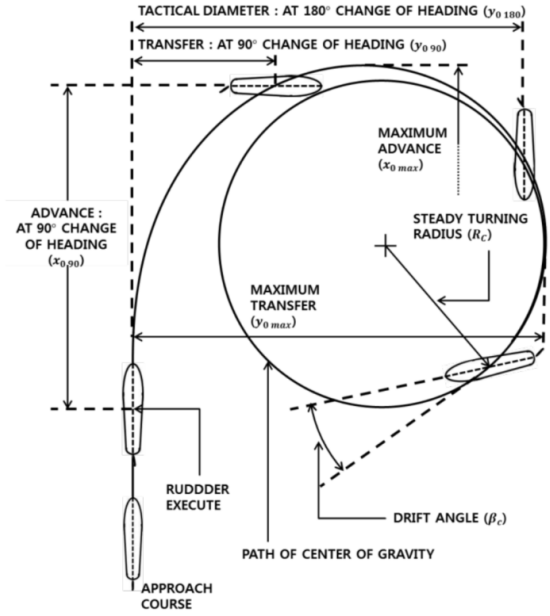

Figure 6.1: Turning circle parameters in calm water (ITTC 2002)

For turning circle in waves, two additional parameters are considered (Schoop-Zipfel 2017):

- **Drifting distance**, H_D - defined as the distance between consecutive positions of the ship at which the wave encounter angle is 90 deg.
- **Drifting angle** μ_D - The vessel generally does not drift in the direction of the wave heading. The offset angle between the wave direction and the line defined by the ship position at which the wave encounter angle is 90 deg. is defined as the drift angle.

These parameters are indicated in Figure 6.2. It is to be noted that the drifting distance and the drifting angle are nearly independent of the initial wave encounter angle, however other parameters such as the advance and transfer are strongly dependent on the initial wave encounter angle (Schoop-Zipfel 2017).

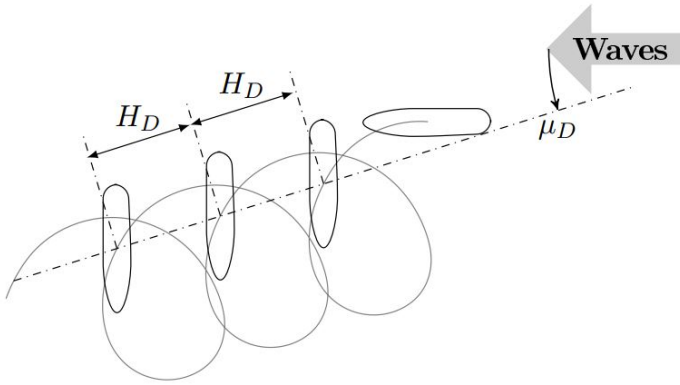

Figure 6.2: Turning circle parameters in waves (Schoop-Zipfel 2017)

6.2 Calm water test results

6.2.1 Importance of viscous transverse forces and moments

The trajectory of the center of gravity of KCS vessel for 35 deg. rudder angle turning circle test in calm water with an initial approach speed of 14.5 kn is shown in Figure 6.3. The viscous forces/moment are calculated by applying the cross-flow method. Comparing the trajectory from the experiment with the one obtained from the simulation it can be observed that the tactical diameter is comparatively small in the simulation results.

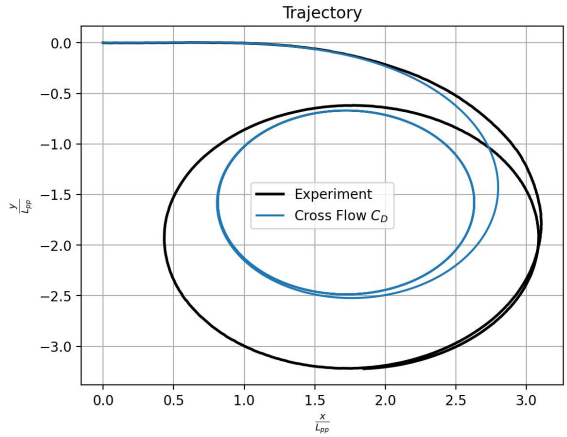

Figure 6.3: The trajectory for 35 deg. rudder angle turning circle test with 14.5 kn approach speed in calm water for KCS vessel. Transverse viscous forces are calculated using the cross-flow method. For comparison, the trajectory from experiment is also included.

The time history of the external sway forces, yaw moments and roll moments acting on KCS vessel during the turn is indicated in Figure 6.4. Figure 6.4 clearly indicates the importance of the transverse viscous forces/moments in the turning circle maneuver. The magnitude of the transverse viscous loads clearly has a magnitude that is comparable to other significant forces and moments.

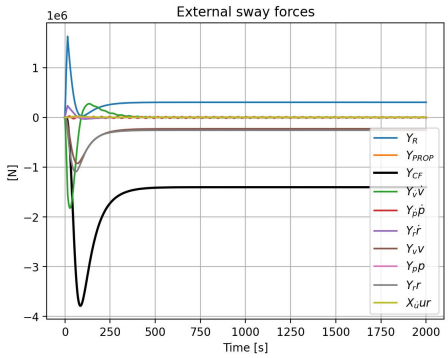

(a) External sway forces

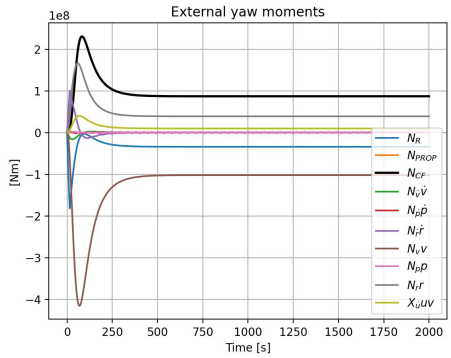

(b) External yaw moments

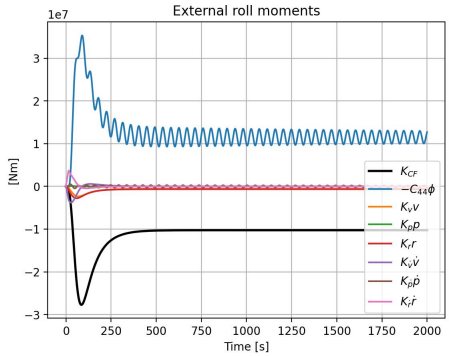

(c) External roll moments

Figure 6.4: External sway forces, yaw moments, and roll moments in 35 deg. rudder angle turning circle test with 14.5 kn approach speed in calm water for KCS vessel. Transverse viscous loads are calculated using the cross-flow method.

The development of the forces over time shown in Figure 6.4 is described below :

- The initial approach speed is 14.5 knots. The RPS of the propeller is calculated based on the thrust required to achieve this speed in calm water, and the RPS is kept constant in the simulation.
- The rudder turning velocity applied in the simulation is 2.32 deg/s according to the experiment data obtained from *SIMMAN* (2020), hence the rudder is deflected from 0 deg. to 35 deg in approximately 15 s. In the simulations the

rudder is applied towards the starboard, hence as indicated in Figure 6.4(a), a positive sway rudder force (Y_R) starts to develop which increases with increasing rudder angle. During this phase, the rudder forces are only counteracted by the inertial forces of the vessel as the vessel has not yet developed a drift angle. Hence during this phase we have peaks of $Y_{\dot{v}}\dot{v}$, $Y_{\dot{r}}\dot{r}$, $N_{\dot{v}}\dot{v}$, $N_{\dot{r}}\dot{r}$, $K_{\dot{v}}\dot{v}$ and $K_{\dot{r}}\dot{r}$

- Once the vessel develops a substantial drift angle and rotation velocity r, the velocity-dependent forces $Y_v v$ and $Y_r r$ develop which are directed towards the center of the turn. Here we observe a substantial contribution from the cross-flow forces which is also directed towards the center of the turning circle. Simulations with the cross-flow forces set to zero resulted in non-physical results. Hence the cross-flow forces have a significant role in this maneuver. The combined magnitude of these 3 forces exceeds the sway force towards port induced by the rudder and this ensures a starboard turn.

- From Figure 6.4(c) it can be observed that the major load contributing to the steady roll angle is the moment due to transverse viscous loads (K_{CF}) which is counteracted by the restoring force (-$C_{44}\phi$).

- Towards the end of the simulation all the acceleration-dependent forces go to zero and steady-state is achieved and the ship starts to have a steady turn radius.

6.2.2 Sensitivity of the turning circle parameters to the drag coefficient in calm water

Figure 6.5 indicates the sensitivity of the turning circle parameters to the drag coefficient in 35 deg. rudder angle turning circle test with 14.5 kn approach speed in calm water. The plot indicates the results with the drag coefficient C_D obtained from the cross-flow approach increased by 20% and 40% and decreased by 20%. A general observation from Figure 6.5 is that C_D obtained from the cross-flow approach increased by 40% leads to a turning circle with parameters that are closer to the one realized in the experiment.

From Figure 6.5 we note the following :

- From Figure 6.5(c) it can be observed that an increase in drag coefficient reduces the sway velocity i.e. the peak values and the steady-state values.

- From Figure 6.5(b) it can be observed that increasing drag coefficient leads to a lower speed loss during the turn i.e a higher steady-state surge velocity. The speed loss is associated with the coupling terms $-C_{TN}Y_{\dot{v}rv}$ and $-Mrv$.

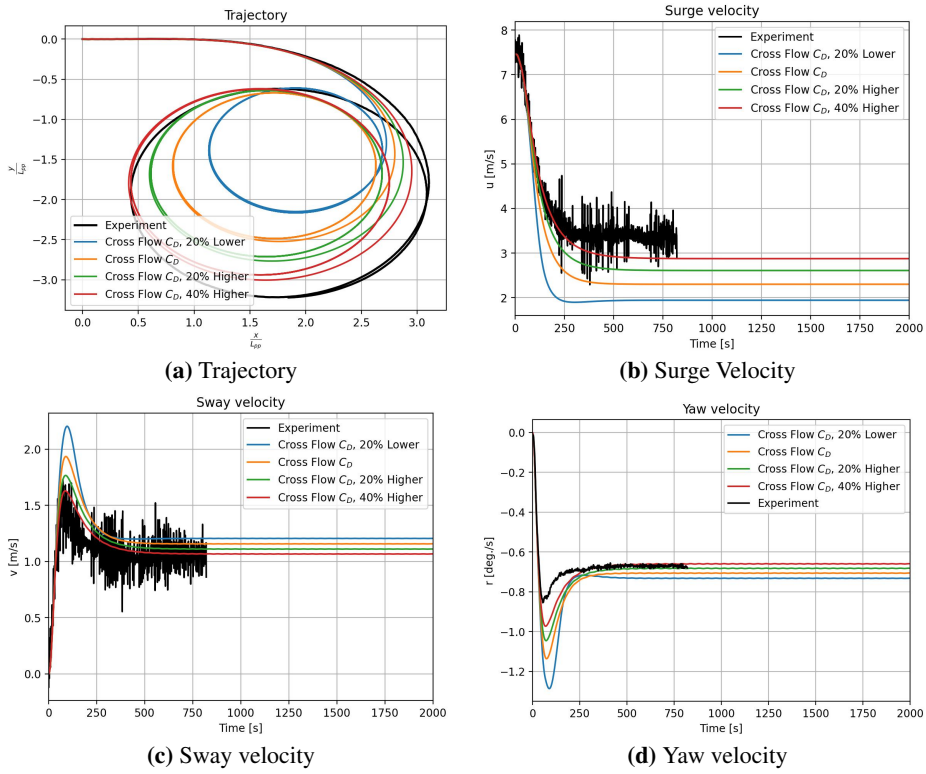

(a) Trajectory

(b) Surge Velocity

(c) Sway velocity

(d) Yaw velocity

Figure 6.5: Sensitivity of the turning circle parameters to the drag coefficient in 35 deg. rudder angle turning circle test with 14.5 kn approach speed in calm water for KCS vessel. Transverse viscous forces are calculated using cross-flow method for the base case.

- A lower speed loss with higher C_D results in a larger diameter of turn as observed from Figure 6.5(a). The opposite effect occurs when the drag coefficient is reduced.

Figure 6.5 clearly demonstrates the importance of transverse viscous loads in the turning circle test. It is noted that the experimental data for calm water resistance test of KCS from J. Kim (2021) is only available from $u = 5.16$ m/s as seen in Figure 2.8. From Figure 6.5(b), the surge velocity falls to ≈ 1.9 m/s in the steady-state, which is outside this range. Here the calm water resistance has been obtained by extrapolation and hence there is an uncertainty associated with this extrapolation. This can also be one of the reasons for the large difference between the numerical results and experiment results.

Similar findings with regards to the sensitivity of turning circle parameters for DTC vessel have been presented by Rabliås and Kristiansen (2021).

6.2.3 Turning circle parameters for different methods of drag coefficient estimation in calm water

In Section 6.2.2, the sensitivity of the turning circle parameters have only been presented by increasing and decreasing the drag coefficient value obtained by the cross-flow approach i.e. for all the presented results the distribution remained the same only the mean value was varied. In contrast to this approach, in this section, the comparison is made between different methods to estimate the drag coefficient which was elaborated in Section 3.2.

KCS vessel simulations

Figure 6.6 indicates the turning circle parameters in 35 deg. rudder angle turning circle test with 14.5 kn approach speed in calm water with the drag coefficients calculated based on different methods for KCS vessel.

From Figure 6.6 it can be observed that :

- In Figure 6.6(e) it can be observed that the amplitude of roll angle in 2D+t method goes on increasing exponentially. This is probably due to numerical instability and is explored further in Section 6.4.2.
- The trajectories presented in Figure 6.6(a) are significantly different for the different methods used to estimate the drag coefficient. Figure 6.6(b) indicates that the speed loss is the least for 2D+t method which in turn leads to the largest turning circle diameter compared to other methods.
- From Figure 6.6(a), it can be observed that in the initial part of the turn 2D+t^0 matches the most with the experiment data, however, the final turning diameter is underpredicted by the method.
- From Figure 6.6(a), the trajectory obtained from cross-flow approach and 2D+t^{cyl} heavily underpredicts the turning diameter. From Figure 6.6(d) it can be observed that during the turning, these two methods cause a large negative peak in the yaw velocity compared to the experimental value. This is probably due to the fact that the distribution of C_D seen in Figure 3.10(a) shows higher drag values concentrated towards the aft of the vessel. This is especially true for the 2D+t^{cyl} method. This probably leads to a large yaw velocity initially.
- From Figure 6.6(d) it can be observed that there are oscillations in yaw velocity which extends into the steady-state. This can be explained by the yaw-roll coupling terms. The vessel has a low GM of 0.6 m resulting in roll

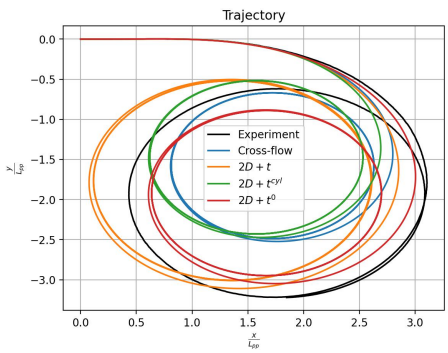

(a) Trajectory

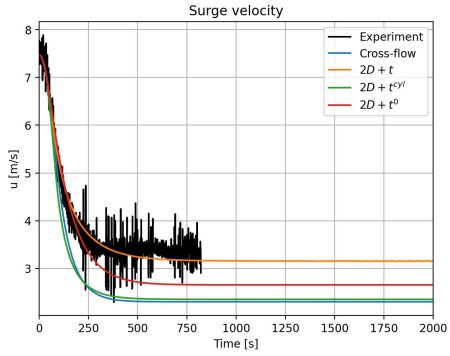

(b) Surge Velocity

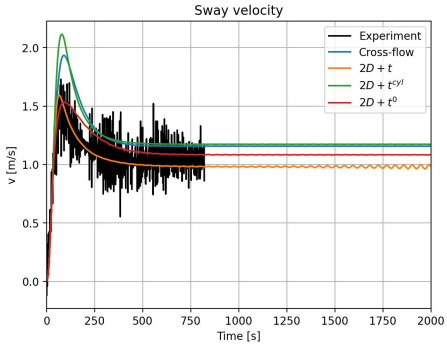

(c) Sway velocity

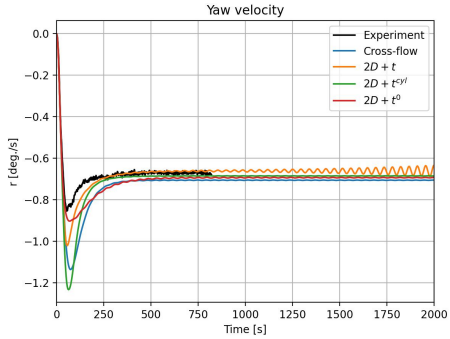

(d) Yaw velocity

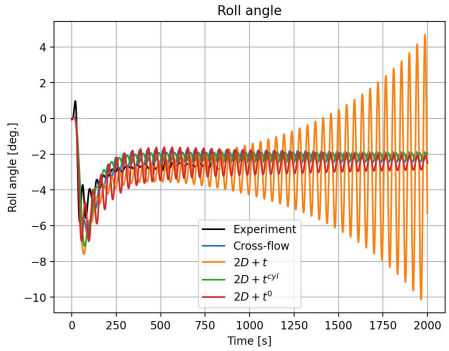

(e) Roll angle

Figure 6.6: Comparison of turning circle parameters with the drag coefficient estimated by different methods in 35 deg. rudder angle turning circle test with 14.5 kn approach speed in calm water for KCS vessel.

oscillations as indicated in Figure 6.6(e). The peak roll angle from the experiment is approximately $-5.8°$. The simulation overpredicts the roll angle in all cases. One of the reasons could be the uncertainty associated with re-

spect to the lever at which the resultant cross-flow drag force is assumed to act which in the simulation was taken as 0.65T from baseline where T is the draft of the vessel.

DTC vessel simulations

Figure 6.7 indicates the turning circle parameters in 35 deg. rudder angle turning circle test with 16 kn approach speed in calm water with the drag coefficients calculated based on different methods for DTC vessel.

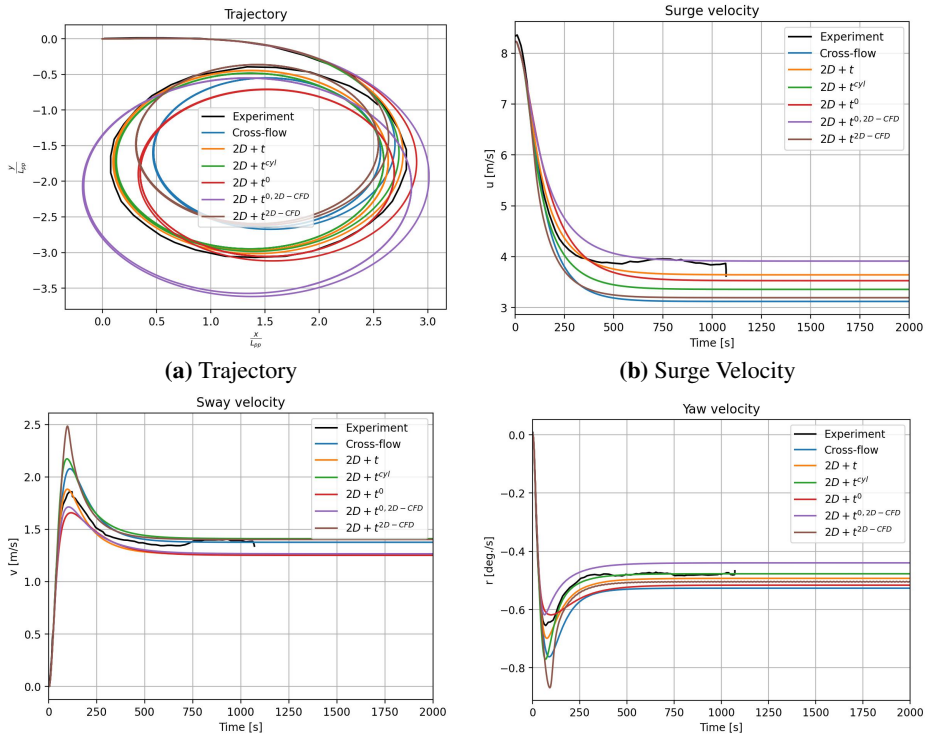

(a) Trajectory **(b)** Surge Velocity

(c) Sway velocity **(d)** Yaw velocity

Figure 6.7: Comparison of turning circle parameters with the drag coefficient estimated by different methods in 35 deg. rudder angle turning circle test with 16 kn approach speed in calm water for DTC vessel.

From Figure 6.7 it can be observed that :

- Figure 6.7(a) The best agreement in the trajectory obtained between the experiment and simulation is seen in 2D+t method in the case of DTC vessel, however as seen in Figure 6.7(b) it over predicts the speed reduction.

- From Figure 6.7(b) it can be observed that the best agreement in the steady-state surge velocity is seen with the 2D+t$^{0,2D\text{-}CFD}$ method, however from Figure 6.7(a) it overpredicts the turning diameter heavily.
- In general it can be concluded that the 2D-CFD based methods do not offer any overall improvement in the results from the original methods proposed by Rabliås and Kristiansen (2021). This is probably due to the uncertainties linked with the 2D CFD simulations. Also, an improvement may be seen by increasing the number of sections selected for 2D CFD simulations.

A sensitivity study is performed on the DTC vessel to identify the parameters which have the largest influence on the turning circle maneuver. 27 parameters and 7 maneuvering indices have been identified which describe a turning circle maneuver. The 7 maneuvering indices are :

- Advance
- Transfer
- Tactical diameter
- Steady turning diameter
- Steady turning speed
- Steady yaw velocity
- Steady drift angle

The original values of parameters in the maneuvering model were decreased by 20% separately and its influence on the above maneuvering indices was calculated. The sensitivity index S is defined as (Sukas et al. 2019) :

$$S = \frac{(R - R^*)/R^*}{(H - H^*)/H^*} \tag{6.1}$$

where,

S	Sensitivity index
R	Value of the maneuvering index after 20% reduction in the parameter
H	Value of the parameter after 20% reduction
R^*	Original value of the maneuvering index
H^*	Original value of the parameter

After computing the value of S by perturbing each parameter in the model separately, the sensitivity values are summed so that for each maneuvering index a total is obtained. Then, the sensitivity for each of the maneuvering index is divided by the summed-up value for that index and a percentage value is calculated. The obtained percentage value is presented in Figure 6.8.

Parameter	Advance	Transfer	Tactical Diameter	Steady Diameter	Steady Speed	Steady Yaw velocity	Steady drift angle
$X_{\dot{u}}$	2.948	2.000	2.755	1.778	0.667	3.468	0.719
$Y_{\dot{v}}$	0.595	1.641	0.323	2.579	6.055	3.662	2.546
$Y_{\dot{p}}$	0.000	0.000	0.000	0.000	0.000	0.000	0.000
$Y_{\dot{r}}$	0.003	0.131	0.190	0.408	0.938	0.560	0.412
$K_{\dot{v}}$	0.000	0.000	0.000	0.000	0.000	0.000	0.000
$K_{\dot{p}}$	0.000	0.000	0.000	0.000	0.000	0.000	0.000
$K_{\dot{r}}$	0.000	0.000	0.000	0.000	0.000	0.000	0.000
$N_{\dot{v}}$	**0.857**	0.115	0.021	0.000	0.000	0.000	0.000
$N_{\dot{p}}$	0.001	0.002	0.001	0.000	0.000	0.000	0.000
$N_{\dot{r}}$	4.473	0.019	0.468	0.000	0.000	0.000	0.000
Y_v	0.303	1.646	0.331	0.108	0.786	1.619	2.840
Y_p	0.000	0.000	0.000	0.000	0.000	0.000	0.000
Y_r	0.195	1.995	0.566	0.117	0.841	1.735	3.044
K_v	0.000	0.000	0.000	0.000	0.000	0.000	0.000
K_p	0.000	0.000	0.000	0.000	0.000	0.000	0.000
K_r	0.000	0.000	0.000	0.000	0.000	0.000	0.000
N_v	28.447	27.107	28.552	19.177	10.848	25.949	6.694
N_p	0.000	0.000	0.000	0.000	0.000	0.000	0.000
N_r	10.747	8.499	8.598	5.964	3.657	9.546	2.181
C_{TN}	0.628	1.424	2.001	2.578	6.054	3.661	2.546
w	6.738	4.405	3.620	2.390	0.212	5.887	2.494
t	0.997	0.767	0.861	1.623	2.489	0.097	1.614
C_q	1.767	0.639	0.673	1.344	1.784	0.389	1.362
k_m	18.349	14.893	18.072	31.343	32.928	18.591	26.458
γ_v	5.158	6.862	7.332	7.766	8.215	6.294	8.434
γ_r	7.180	8.116	8.211	9.237	9.794	7.563	10.146
C_D	10.613	19.737	17.425	13.587	14.733	10.979	28.511

Figure 6.8: Sensitivity analysis for DTC vessel for turning circle maneuver in calm water. Grading of the color is from red to green with red indicating the most important parameter and green the least

The conclusions drawn from the sensitivity studies are :

- The largest influence on the turning circle indices is from the first order hydrodynamic derivative N_v. This is followed by the hydrodynamic derivative N_r.
- The rudder parameter k_m (see Section 2.8) which was empirically determined also has a significant influence especially on the steady diameter, steady turning speed, and the steady drift angle.
- The drag coefficient C_D has the largest influence over the steady drift angle of the vessel.

6.3 Regular wave test results

Figure 6.9 presents the results for KCS vessel in 35 deg. rudder angle turning circle test with 14.5 kn approach speed and initial wave encounter angle $\eta = 180$ deg. in regular waves with $\lambda/L_{pp} = 1$, wave steepness $H/\lambda = 1/63.7$ and with the drag coefficients calculated based on different methods. The conclusions drawn are :

- As seen in the case of calm water, in 2D+t method the roll angle goes on increasing (see Figure 6.9(f)) indicating numerical instability. This is discussed in more detail in Section 6.4.2.
- Drift in the trajectories seen in Figures 6.9(a) and 6.9(b) is due to the wave drift forces and moments. It can be observed that the distortion of the circular trajectory in waves from the experiment is more gradual than that seen in the simulation. Specifically, if the trajectory from 2D+t is observed in Figure 6.9(b), it can be seen that initially up to $\psi \approx 270°$, there is a good between the experimental and simulated result, however, beyond this, a sudden deviation is observed from the experimental trajectory. The poor agreement between the experimental plots and simulations is likely due to the inaccurate estimation of the wave drift forces and moments.
- High-frequency oscillations are observed in the surge velocity, sway velocity, yaw velocity, and roll angle which have not been captured in the simulation. These are associated with the linear wave-induced motion of the vessel which is not explicitly accounted for in the model. However, it is essential that the linear wave motions are accurately captured by the model as they are the input for the wave drift force calculation.
- From Figure 6.9(c), it can be observed that the speed reduction is heavily overpredicted in all the methods. This is likely due to the overestimation of added resistance in waves.

The time history of external sway forces, yaw moments and roll moments in the maneuver are presented in Figure 6.9. It clearly represents the importance of the transverse viscous loads and drift loads on the regular wave test simulations.

6.4 Limitation of the implemented model

6.4.1 Physical nature of drag coefficient distrubution from 2D+t models

As detailed in Section 3.2.2, the 2D+t theory based methods computes the sectional drag coefficient by establishing an analogy between the time-dependent initiation

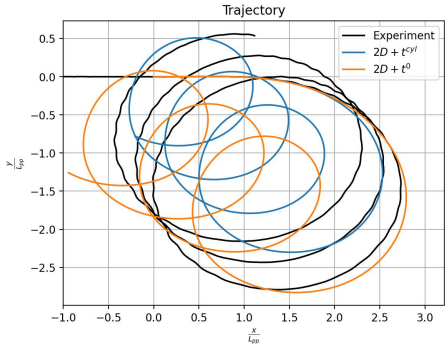

(a) Trajectory for 2D+t^{cyl} and 2D+t^0 compared against experiment

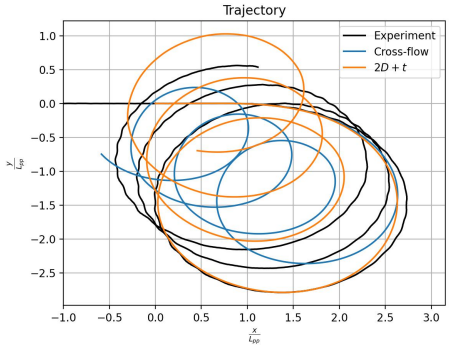

(b) Trajectory for 2D+t and cross-flow approach compared against experiment

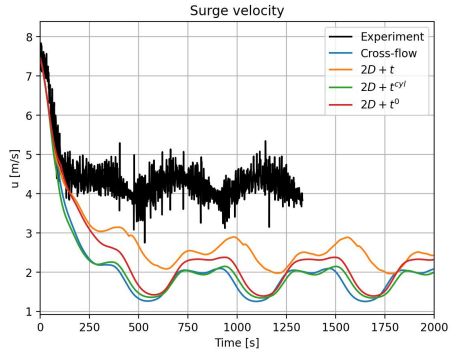

(c) Surge Velocity

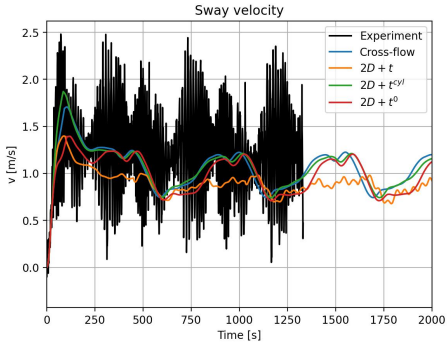

(d) Sway velocity

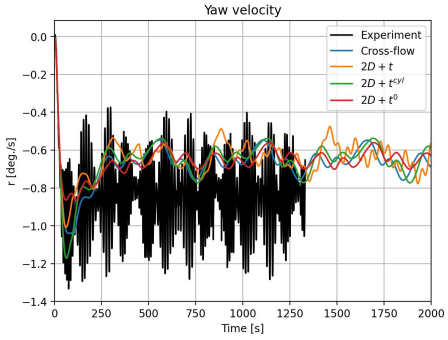

(e) Yaw velocity

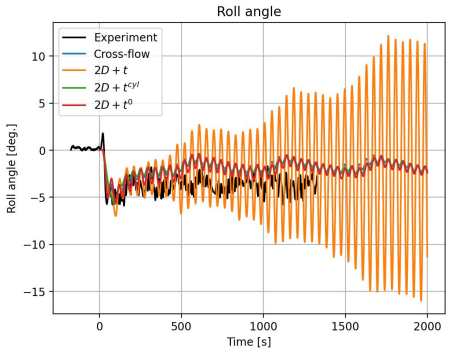

(f) Roll angle

Figure 6.9: Comparison of turning circle parameters with the drag coefficient estimated by different methods in 35 deg. rudder angle turning circle test with 14.5 kn approach speed in regular waves for KCS vessel. $\lambda/L_{pp} = 1$, wave steepness $H/\lambda = 1/63.7$ and initial wave encounter angle $\eta = 180$ deg.

and development of vortex for a cross-section with the space-dependent initiation

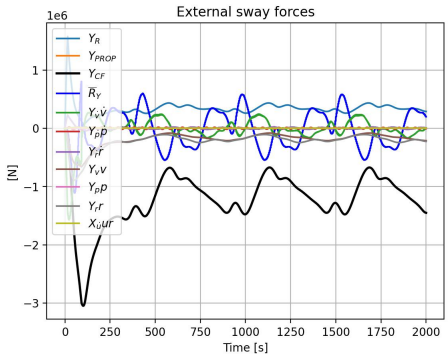

(a) External sway forces

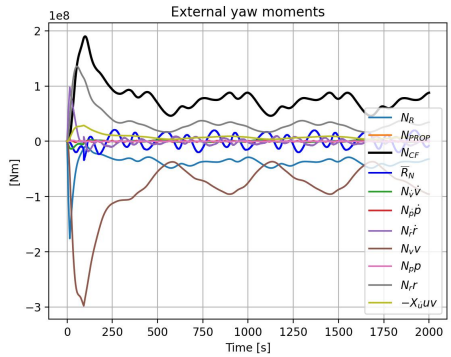

(b) External yaw moments

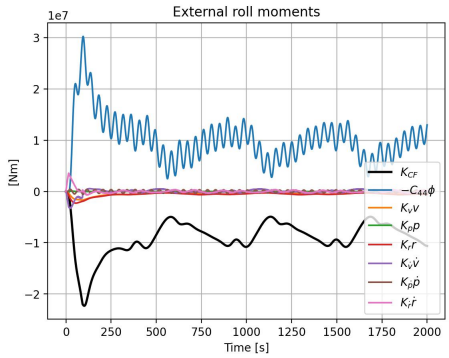

(c) External roll moments

Figure 6.10: External sway forces, yaw moments, and roll moments in 35 deg. rudder angle turning circle test with 14.5 kn approach speed in regular waves for KCS vessel. $\lambda/L_{pp} = 1$, wave steepness $H/\lambda = 1/63.7$ and initial wave encounter angle $\eta = 180$ deg.

and development of vortex from the bow towards the aft of the vessel. This analogy implies that the variation of non-dimensional time t^* along the length from the bow of the vessel towards the aft end of the vessel should have an increasing nature.

However, the rate at which t^* increases along the length of the vessel will depend on the drift angle and the ratio $\frac{r}{u}$ (see Equation (3.5)). For instance, if $r = 0$, as the drift angle increases it can be observed that the development of the vortex along the length of the vessel will be faster and hence the peak of the drag coefficient curve will move towards the bow and a large portion of the length of the vessel will have the steady-state drag coefficient. This effect was observed both experimentally (see Figure 4.4) and numerically in the 2D+t$^{\text{cyl}}$ method (see Figure 3.10). This effect is less apparent in other 2D+t methods due to the jumps in the C_D curve which occur when different time-dependent drag curves are used along the length of the vessel to account for the changing geometry. Finally, for high drift angles

(for instance α>30-45°), the development of the vortex will be so quick that most of the length of the vessel will see the steady-state drag coefficient value or the drag coefficient from 2D+t theory will tend towards the result from the cross-flow approach.

Equation (3.5) was used to calculate the transverse distance moved by the ship section in the π plane which is the basis for the calculation of non-dimensional time t^*. For t^* to be increasing, it is necessary that $|s_y|$ also have an increasing nature (see Equation (3.6)) assuming the draft T remains constant. However, for cases where $r \neq 0$, the variation of s_y with the distance from the bow $x_b - x_p$ has a quadratic nature implying there may be cases in which t^* may not be increasing with increasing distance from the bow.

To exemplify this and check if such cases arise during the simulation, two calm water simulation results from DTC vessel is used :

- Approach speed 16 kn, rudder angle $\delta = 35°$
- Approach speed 16 kn, rudder angle $\delta = 30°$

For both the simulations, transverse viscous loads are calculated using 2D+t^{cyl} method. The results from these two simulations are plotted in Figure 6.11.

Specifically, at time instant $t = 73$ s for the case with $\delta = 35°$, the drag coefficient variation along the length of the vessel is presented in Figure 6.12. It is observed that the drag coefficient remains nearly zero from $x/L_{pp} \approx 0.27$ towards the bow of the vessel. A zoomed-in view shows small increase then decrease in C_D around $x/L_{pp} \approx 0.43$ moving towards aft.

The variation of s_y and non-dimensional time t^* along the length is shown in Figures 6.13(a) and 6.13(b) respectively. It can be observed that s_y initially decreases then reaches a minimum value and subsequently increases, and therefore t^* increases reach a maximum then decreases, and then subsequently starts to increase towards the aft of the vessel. This variation of t^* is not consistent with the 2D+t theory.

Physically this occurs because the transverse velocity calculated as $v + xr$ does not have the same sign along the entire length of the vessel, and hence the 2D section in the π plane as described in Section 3.2.2 does not move in one direction alone.

The variation of $v + xr$ along the length of the vessel at $t = 73$ for the case with $\delta = 35°$ is shown in Figure 6.14. The change in sign near the bow of the vessel can be observed.

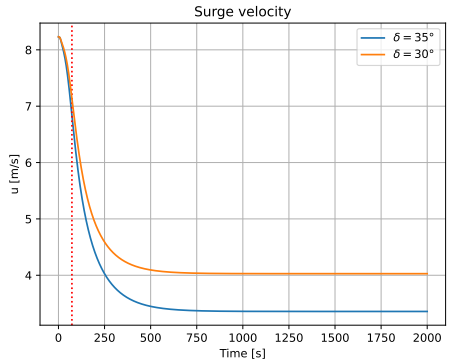

(a) Time history for surge velocity

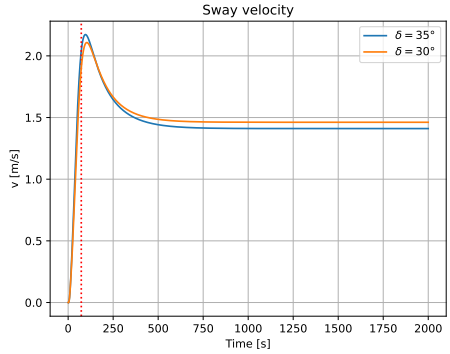

(b) Time history for sway velocity

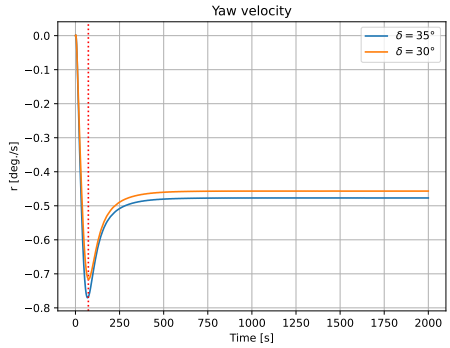

(c) Time history for yaw velocity

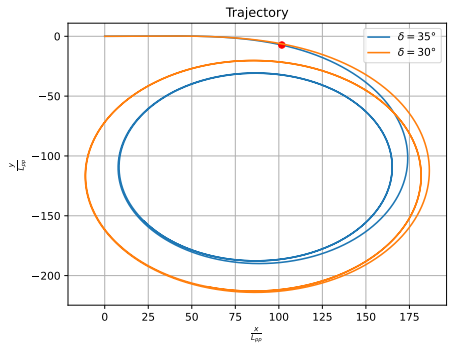

(d) Trajectory for turning circle. The red dot indicates the position of the vessel at t = 73 s for the simulation with rudder angle $\delta = 35°$

Figure 6.11: Results for turning circle of DTC vessel with rudder angles $\delta = 35°$ and $30°$. 16 kn is the approach speed. Transverse viscous loads is calculated by using 2D+t^{cyl} method. The red dotted line indicates a particular time instant t = 73 s.

Hence, this inconsistency with 2D+t theory assumption occurs only when there is a change in sign in transverse velocity occurs. Since the variation of transverse velocity along the length of the vessel is linear, the criteria to check the occurrence of this inconsistency is that the transverse velocity at the fore and aft-most sections of the vessel will have opposite signs.

The time history of $v + xr$ at these two sections for DTC simulations with $\delta = 35°$ and $\delta = 30°$ is plotted in Figure 6.15. It can be observed that this inconsistency occurs almost throughout the turn for both the rudder angles however the effect is less severe for the lower rudder angle.

Even though in the case presented, the effect appears to be less severe, however with different combinations of vessels and turn radius, this can have a significant

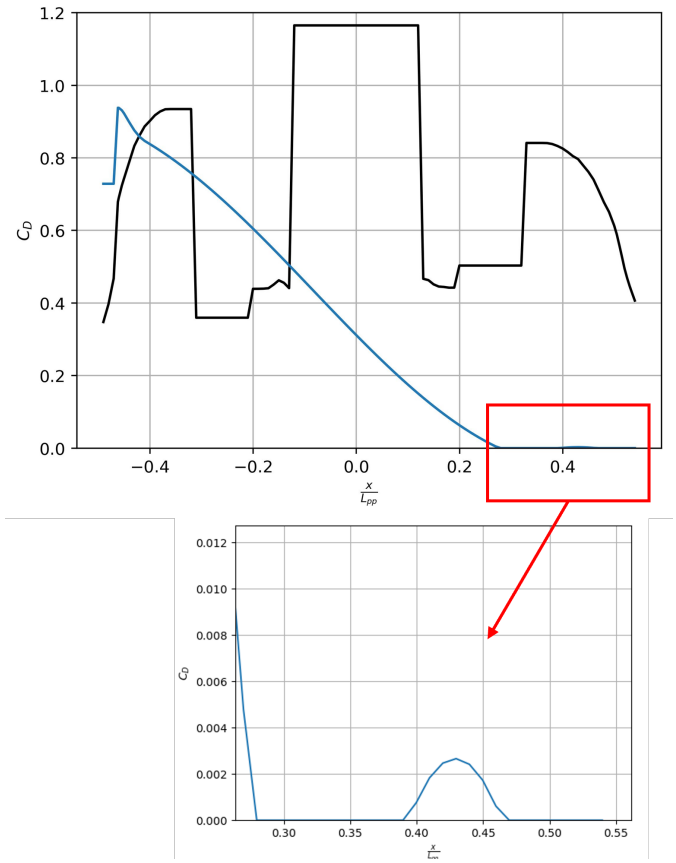

Figure 6.12: Variation of C_D along the length of the vessel at t = 73 s for turning circle of DTC vessel with rudder angles $\delta = 35°$. 16 kn is the approach speed. Transverse viscous loads are calculated by using 2D+t^{cyl} method (blue). For reference the C_D curve from cross flow approach is shown in black. A zoomed in view of the drag coefficient in the bow region is also presented.

impact on the predicted maneuvers and therefore requires further study.

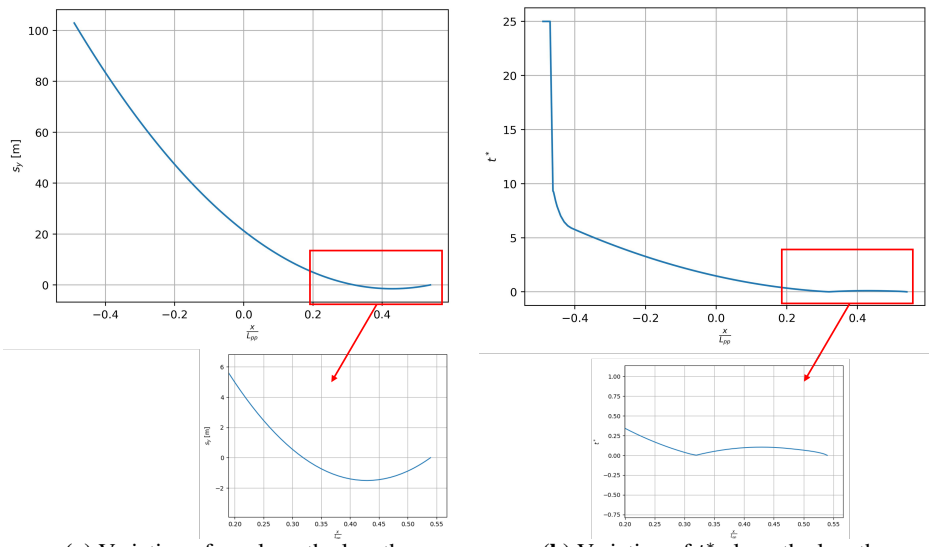

(a) Variation of s_y along the length **(b)** Variation of t^* along the length

Figure 6.13: Variation of s_y and t^* along the vessel at t = 73 s for turning circle of DTC vessel with rudder angles $\delta = 35°$. 16 kn is the approach speed. Transverse viscous loads is calculated by using 2D+t^{cyl} method. A zoomed-in view of the variation in bow part of the vessel is also presented.

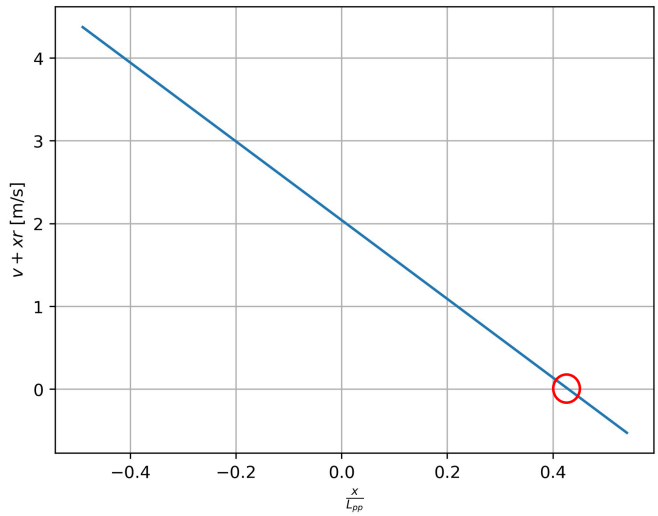

Figure 6.14: Variation of trasverse velocity $v + xr$ along the vessel at t = 73 s for turning circle of DTC vessel with rudder angles $\delta = 35°$. 16 kn is the approach speed. Transverse viscous loads is calculated by using 2D+t^{cyl} method. The red circle indicates the point at which the transverse velocity changes its sign along the length of the vessel.

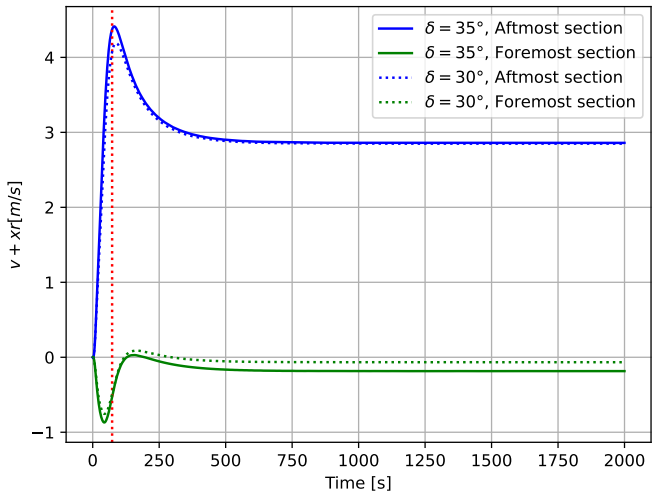

Figure 6.15: Time history of trasverse velocity $v + xr$ at the forward and aft tip of the vessel for turning circle of DTC vessel with rudder angles $\delta = 35°$ and $\delta = 30°$. 16 kn is the approach speed. Transverse viscous loads is calculated by using 2D+t^{cyl} method. The red dotted line indicates a particular time instant t = 73 s.The red dotted line indicates a particular time instant t = 73 s.

6.4.2 Numerical instability in KCS simulations

The equation for roll degree of freedom in the 4-dof maneuvering model is (refer Equation (2.1)) in calm water :

$$\begin{aligned} I_{44}\dot{p} - I_{46}\dot{r} = K_{\dot{v}}\dot{v} + K_{\dot{p}}\dot{p} + K_{\dot{r}}\dot{r} + K_v v + K_p p + \\ K_r r - C_{44}\phi + K_R + K_{PROP} + K_{CF} \end{aligned} \tag{6.2}$$

In the simulations, the inertial coupling term between roll and yaw (I_{46}) and the contribution to roll moment from rudder (K_R) and propeller (K_{PROP}) was set to zero. Hence Equation (6.2) can be modified as :

$$\begin{aligned} (I_{44} - K_{\dot{p}})\dot{p} + (-K_p)p + C_{44}\phi = K_{\dot{v}}\dot{v} + K_{\dot{r}}\dot{r} + K_v v + \\ K_r r + K_{CF} \end{aligned} \tag{6.3}$$

In 4-dof system of equations shown in Equation (2.1), restoring force only exists in roll degree of freedom, hence the system is expected to have only one natural period. The natural period can be calculated as :

$$T_4 = 2\pi\sqrt{\frac{I_{44} - K\dot{p}}{C_{44}}} \tag{6.4}$$

For KCS vessel T_4 was calculated to be 43.8 s. The comparatively large natural period is due to the low GM of the vessel. The calculated roll period agrees with the roll decay test results of KCS obtained from *SIMMAN* (2020) shown in Figure 6.16. The period obtained from the roll decay test is 40.7 s. The difference is probably due to the difference in the added mass term. The oscillations seen in roll angle in Figure 6.6(e) are at the calculated natural period.

The exponential increase seen in the roll angle in Figure 6.6(e) is likely due to numerical instability connected with galloping phenomenon resulting in negative damping. A preliminary indication of this can be seen from Figure 6.17. It can be observed that the moment associated with transverse viscous loads (K_{CF}) is nearly in-phase with the roll velocity. Hence it is possible to express K_{CF} as :

$$K_{CF} = a + b \cdot p \tag{6.5}$$

where a and b are two factors and b>0. In other words K_{CF} is linearized with respect to p.

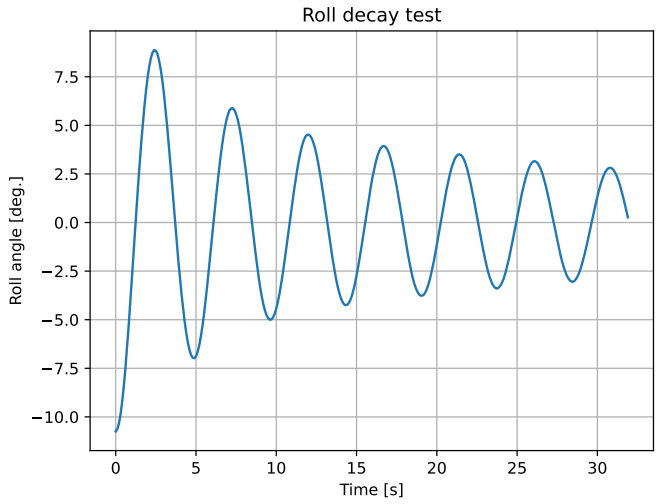

Figure 6.16: Result from roll decay test of KCS from *SIMMAN* (2020). The model scale used for the test is 1:75.24. The natural period for the model is $\approx$ 4.7 s. Hence, in full scale the natural period is 40.7 s.

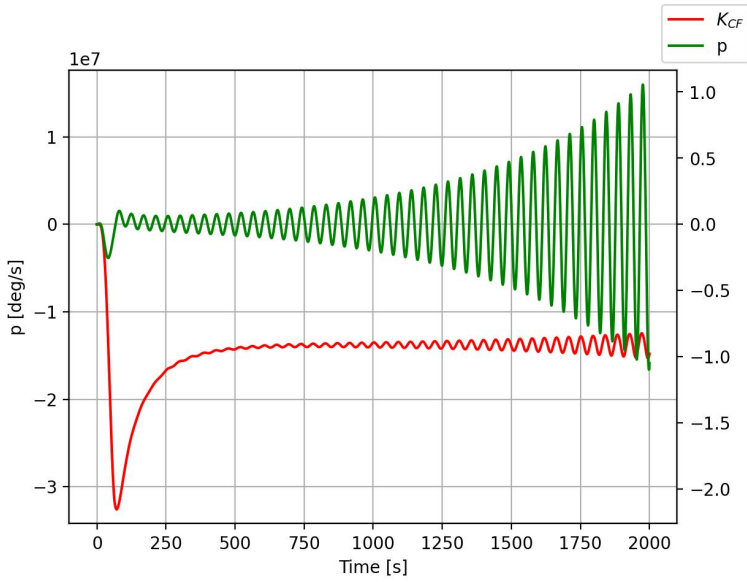

Figure 6.17: Roll velocity and the roll moment due to the transverse viscous loads in 35 deg. rudder angle turning circle test with 14.5 kn approach speed in calm water for KCS vessel. Transverse viscous loads is calculated by 2D+t ,method.

Substituting for K_{CF} in Equation (6.3) and rearranging :

$$(I_{44} - K_{\dot{p}})\dot{p} + (-K_p - b)p + C_{44}\phi = K_{\dot{v}}\dot{v} + K_{\dot{r}}\dot{r} + K_v v + K_r r + a \tag{6.6}$$

In Equation (6.6), it can be noted that $-K_p$ is positive whereas $-b$ is a negative quantity. Hence if K_{CF} has a large enough amplitude of oscillation, the damping becomes negative and this can result in an exponentially increasing roll angle. However, it is noted that this is a very crude analysis as the equation is fully coupled - for instance the value of K_p is not a constant but depends on the surge velocity. Hence, in order to arrive at definitive criteria for the occurrence of this phenomenon, the system has to be linearised about p. It can also be noted that this instability occurs only in the case of 2D+t theory because as seen in Figure 6.6(e), this method results in the largest peak roll angle, hence it can be reasonably assumed that the threshold is exceeded only in this method.

Chapter 7

Recommendations for future work

- Improve the design of the experimental approach to determine the transient drag coefficient such as by using screw driven carriage for towing, flexible attachment to the carriage etc.
- The weaknesses identified in Section 6.4 require further work to identify their significance.
- Experimental results using segmented model tests as presented in can be used to assess different methods for predicting the drag coefficient.
- Comparison of the drag coefficient curve for different drift angles presented in Section 3.2 against data extracted from CFD simulations of turning circle tests will be valuable in assessing the best method for estimation of the drag coefficient.
- Accurate estimation of the mean second-order loads is essential for the tests in regular waves. Implementation and comparison of different methods for computing the second-order mean drift loads is essential.
- Conduct simulation in irregular waves and also include results from zig-zag maneuvers.

Bibliography

Aarsnes, J.V. (1984). "Current forces on ships, In: Rapport (Norges tekniske høgskole Marinteknisk avdeling) (trykt utg.), vol. UR-84-39". Doctoral Thesis. Division of Marine Hydrodynamics, Norwegian Institute of Technology, University of Trondheim.

Abkowitz, M A (1964). *Lectures on ship hydrodynamics—steering and manoeuvrability*. Tech. rep. Hy-5. Hydro- and Aerodynamics Laboratory, Hydrodynamics Section, Lyngby, Denmark. URL: http://resolver.tudelft.nl/uuid:d511bd6b-ca2e-4f10-ad9f-6c881eb1e9f8 (visited on 7th Nov. 2021).

Agromayor, Roberto, Jairo Rua Pazos and Reidar Kristoffersen (2017). "Simulation of Starting and Stopping Vortices of an Airfoil". In: Proceedings of the 58th SIMS, September 25 - 27, Reykjavik, Iceland.

Alsos, Hagbart S. and Odd M. Faltinsen (2018). "3D motion dynamics of axisymmetric bodies falling through water". In: *Ocean Engineering* 169, pp. 442–456. ISSN: 0029-8018. DOI: https://doi.org/10.1016/j.oceaneng.2018.08.033.

Anderson, J.D. (2016). *Fundamentals of Aerodynamics*. McGraw-Hill series in aeronautical and aerospace engineering. McGraw-Hill Education.

Arslan, Tufan, Bjornar Pettersen and Helge Andersson (Jan. 2016). "Large-eddy simulation of cross-flow around ship sections". In: *Journal of Marine Science and Technology* 21. DOI: 10.1007/s00773-015-0366-6.

Bertram, Volker (2012). "Chapter 2 - Propellers". In: *Practical Ship Hydrodynamics (Second Edition)*. Ed. by Volker Bertram. Second Edition. Oxford: Butterworth-Heinemann. ISBN: 978-0-08-097150-6. DOI: https://doi.org/10.1016/B978-0-08-097150-6.10002-8. URL: https://www.sciencedirect.com/science/article/pii/B9780080971506100028.

Beukeinian, W (1989). *Cross flow drag on a segmented model*. Tech. rep. Ship Hydromechanics Laboratory Delft University of. Technology.

Clarke, D. (1972). "Paper 8. A Two-Dimensional Strip Method for Surface Ship Hull Derivatives: Comparison of theory with Experiments on a Segmented Tanker Model". In: *Journal of Mechanical Engineering Science* 14.7, pp. 53–61. DOI: 10.1243/JMES_JOUR_1972_014_063_02. URL: https://doi.org/10.1243/JMES_JOUR_1972_014_063_02.

Cura-Hochbaum, Andrés (Nov. 2006). "Virtual PMM Tests for Manoeuvring Prediction". In.

DNV-RP-H103 (2011). *Modelling and Analysis of Marine Operations*. DET NORSKE VERITAS.

Faltinsen, O. M. (1990). *Sea Loads on Ships and Offshore Structures*. Cambridge University Press.

Faltinsen, O.M., K.J. Minsaas and S.O Liapis N.and Skjørdal (1980). "Ship motions and sealoads". In: Proceedings of the 13th Symposium on Naval Hydrodynamics, Tokyo,

Faltinsen, Odd M. (2006). *Hydrodynamics of High-Speed Marine Vehicles*. Cambridge University Press. DOI: 10.1017/CBO9780511546068.

Fossen, Thor (Sept. 2005). "A Nonlinear Unified State-Space Model for Ship Maneuvering and Control in a Seaway." In: *I. J. Bifurcation and Chaos* 15, pp. 2717–2746. DOI: 10.1142/S0218127405013691.

Fujii, Hitoshi and Takeshi Takahashi (1975). "Experimental Study on the Resistance Increase of a Large Full Ship in Regular Oblique Waves". In: *Journal of the Society of Naval Architects of Japan* 1975.137, pp. 132–137. DOI: 10.2534/jjasnaoe1968.1975.132.

Greco, M. (2020). *TMR4217 Hydrodynamics for High-Speed Marine Vehicles. Lecture Notes*. Department of Marine Technology, NTNU, Trondheim.

Hall, Robert M (1987). *Forebody and missile side forces and the time analogy*. NASA Langley Research Center Hampton, VA, United States. URL: https://ntrs.nasa.gov/citations/19870035287.

Hoerner, S. F. (1965). *Fluid Dynamic Drag*. URL: https://ci.nii.ac.jp/naid/20000254063/en/.

Hooft, J.P (Apr. 1994). "The cross-flow drag on a manoeuvring ship". en. In: *Ocean Engineering* 21.3, pp. 329–342. ISSN: 00298018. DOI: 10.1016/0029-8018(94)90004-3. URL: https://linkinghub.elsevier.com/retrieve/pii/0029801894900043 (visited on 7th July 2021).

Huang, Norden E. et al. (1998). "The empirical mode decomposition and the Hilbert spectrum for nonlinear and non-stationary time series analysis". In: *Proceedings of the Royal Society of London. Series A: Mathematical, Physical and Engineering Sciences* 454.1971, pp. 903–995. DOI: 10.1098/rspa.1998.

0193. URL: https://royalsocietypublishing.org/doi/abs/10.1098/rspa.1998.0193.

Ikeda, Yoshiho, Yoji Himeno and Norio Tanaka (1978). "Components of Roll Damping of Ship at Forward Speed". In: *Journal of the Society of Naval Architects of Japan* 1978.143, pp. 113–125. DOI: 10.2534/jjasnaoe1968.1978.113.

ITTC (2002). *Full Scale measurements, manoeuvrability, full Scale manoeuvring trials procedure*. Tech. rep. ITTC.

ITTC (2014). *Validation of Manoeuvring Simulation Models*. Tech. rep. ITTC.

ITTC (2017). *Proposed tasks and structure of the 29th ITTC Technical Committees and Groups*. Tech. rep. ITTC.

ITTC (2021a). *Benchmark Data for Validation of Manoeuvring Predictions*. Tech. rep. ITTC.

ITTC (2021b). *The Specialist Committee on Manoeuvring in Waves - Final Report and Recommendations to the 29th ITTC*. Tech. rep. ITTC.

Jin, Yuting et al. (Aug. 2020). "System-Based Modelling of KCS Manoeuvring in Calm Water, Current and Waves". In: vol. Volume 6A: Ocean Engineering. International Conference on Offshore Mechanics and Arctic Engineering. V06AT06A050. DOI: 10.1115/OMAE2020-18625. URL: https://doi.org/10.1115/OMAE2020-18625.

Kim, Jin (Jan. 2021). "Experimental Data for KCS Resistance, Sinkage, Trim, and Self-propulsion". In: pp. 53–59. ISBN: 978-3-030-47571-0. DOI: 10.1007/978-3-030-47572-7_3.

Kinaci, Omer et al. (Oct. 2018). "On self-propulsion assessment of marine vehicles". In: *Brodogradnja* 69, pp. 29–51. DOI: 10.21278/brod69403.

Korkmaz, Kadir, Sofia Werner and Rickard Bensow (Oct. 2019). "Investigations for CFD Based Form Factor Methods". In.

Koumoutsakos, P. and A. Leonard (1995). "High-resolution simulations of the flow around an impulsively started cylinder using vortex methods". In: *Journal of Fluid Mechanics* 296, pp. 1–38. DOI: 10.1017/S0022112095002059.

Laroussi, Mouna, Mohamed Djebbi and Mahmoud Moussa (2014). "Triggering vortex shedding for flow past circular cylinder by acting on initial conditions: A numerical study". In: *Computers Fluids* 101, pp. 194–207. ISSN: 0045-7930. DOI: https://doi.org/10.1016/j.compfluid.2014.05.034.

Moctar, Ould, Vladimir Shigunov and Tobias Zorn (Aug. 2012). "Duisburg Test Case: Post-Panamax Container Ship for Benchmarking". In: *Ship Technology Research* 59, pp. 50–64. DOI: 10.1179/str.2012.59.3.004.

NMRI (2022). URL: https://www.nmri.go.jp/institutes/fluid_performance_evaluation/cfd_rd/cfdws05/Detail/KCS/container.html (visited on 1st May 2022).

Norrbin, N.H. (1970). *Theory and observations on the use of a mathematical model for ship manoeuvring in deep and confined waters*.

Papanikolaou, A. et al. (Jan. 2016). "Energy Efficient Safe SHip Operation (SHOPERA)". en. In: *Transportation Research Procedia*. Transport Research Arena TRA2016 14, pp. 820–829. ISSN: 2352-1465. DOI: 10.1016/j.trpro.2016.05.030. URL: https://www.sciencedirect.com/science/article/pii/S2352146516300308 (visited on 4th Nov. 2021).

Perez, Tristan and Thor I Fossen (2006). "Time-Domain Models of Marine Surface Vessels for Simulation and Control Design Based on Seakeeping Computations Plenary Talk". In: *Proc. of IFAC MCMC'06, Lisbon, Portugal, September 20-22 2006*.

Rabliås, Øyvind and Trygve Kristiansen (May 2021). "A 2Dt approach for the transverse viscous loads in a modular maneuvering model". In: *Ocean Engineering* 228, p. 108853. DOI: 10.1016/j.oceaneng.2021.108853. URL: https://doi.org/10.1016/j.oceaneng.2021.108853.

Rabliås, Øyvind and Trygve Kristiansen (2022). "A rational model for maneuvering in irregular waves with the effect of waves on the propeller and rudder inflow taken into account". In: *Ocean Engineering* 243, p. 110186. ISSN: 0029-8018. DOI: https://doi.org/10.1016/j.oceaneng.2021.110186.

Rumsey, C. L. (Dec. 1988). "Details of the Computed Flowfield Over a Circular Cylinder at Reynolds Number 1200". In: *Journal of Fluids Engineering* 110.4, pp. 446–452. ISSN: 0098-2202. DOI: 10.1115/1.3243576. eprint: https://asmedigitalcollection.asme.org/fluidsengineering/article-pdf/110/4/446/5577761/446_1.pdf.

Salvesen, Nils, E. O. Tuck and Odd Magnus Faltinsen (1970). "Prediction of resistance and propulsion of a ship in a seaway. In: Proceedings of the 13th Symposium on Naval Hydrodynamics, Tokyo, 1980." In: SNAME.

Sarpkaya, Turgut (Mar. 1966). "Separated flow about lifting bodies and impulsive flow about cylinders." en. In: *AIAA Journal* 4.3, pp. 414–420. ISSN: 0001-1452, 1533-385X. DOI: 10.2514/3.3453. URL: https://arc.aiaa.org/doi/10.2514/3.3453 (visited on 7th July 2021).

Sarpkaya, Turgut (1978). *Impulsive flow about a circular cylinder*. National Science Foundation, Washington, D. C. 20550. URL: http://hdl.handle.net/10945/29346.

Schlichting, H. and J. Kestin (1979). *Boundary-layer Theory*. McGraw-Hill classic textbook reissue series. McGraw-Hill.

Schoop-Zipfel, Jochen (2017). "Efficient simulation of ship maneuvers in waves". Doctoral Thesis. Technische Universität Hamburg. ISBN: 978-3-89220-700-9. DOI: 10.15480/882.1375.

Seo, Min-Guk and Yonghwan Kim (2011). "Numerical analysis on ship maneuvering coupled with ship motion in waves". In: *Ocean Engineering* 38.17, pp. 1934–1945. ISSN: 0029-8018. DOI: https://doi.org/10.1016/j.oceaneng.2011.09.023.

Shen, Yugao (Nov. 2018). "Operational limits for floating-collar fish farms in waves and current, without and with well-boat presence". PhD thesis. DOI: 10.13140/RG.2.2.17501.13288.

SIMMAN (2008). URL: http://www.simman2008.dk/ (visited on 12th Nov. 2021).

SIMMAN (2014). URL: https://simman2014.dk/ (visited on 12th Nov. 2021).

SIMMAN (2020). URL: http://www.simman2019.kr/ (visited on 12th Nov. 2021).

Skejic, Renato (2008). "Maneuvering and Seakeeping of a Single Ship and of Two Ships in Interaction". Doctoral Thesis. Fakultet for ingeniørvitenskap og teknologi, Norwegian Institute of Technology, University of Trondheim.

Skjetne, Roger, Oyvind Smogeli and Thor Fossen (Jan. 2004). "A Nonlinear Ship Manoeuvering Model: Identification and adaptive control with experiments for a model ship". In: *Modeling, Identification and Control* 25, pp. 3–27. DOI: 10.4173/mic.2004.1.1.

Söding, Heinrich (Mar. 1982). "Prediction of Ship Steering Capabilities". In: 29, pp. 3–29.

Sukas, Omer Faruk, Omer Kemal Kinaci and Sakir Bal (2019). "Theoretical background and application of MANSIM for ship maneuvering simulations". In: *Ocean Engineering* 192, p. 106239. ISSN: 0029-8018. URL: https://www.sciencedirect.com/science/article/pii/S0029801819304184.

Sumer, B Mutlu and Jørgen Fredsøe (2006). *Hydrodynamics Around Cylindrical Structures*. World Scientific. DOI: 10.1142/6248.

Sutulo, Serge and Carlos Guedes Soares (Jan. 2011). "Mathematical models for simulation of manoeuvring performance of ships". In: pp. 661–698. ISBN: 978-0-415-69808-5. DOI: 10.13140/2.1.3538.7209.

Xiang, Xu (Nov. 2012). "Maneuvering of two interacting ships in waves". Doctoral Thesis. Fakultet for ingeniørvitenskap og teknologi, Norwegian Institute of Technology, University of Trondheim.

Yasukawa, Hironori and Yasuo Yoshimura (Mar. 2014). "Introduction of MMG standard method for ship maneuvering predictions". In: *Journal of Marine Science and Technology* 20, pp. 37–52. DOI: 10.1007/s00773-014-0293-y.

Zeiler, Angela et al. (July 2010). "Empirical Mode Decomposition - an introduction". In: pp. 1–8. DOI: 10.1109/IJCNN.2010.5596829.

Appendices

Appendix A

Sensitivity study results for DTC in calm water

Appendix B

Time series plots for Model A

B.1 Dry run, model A, high acceleration, forward direction

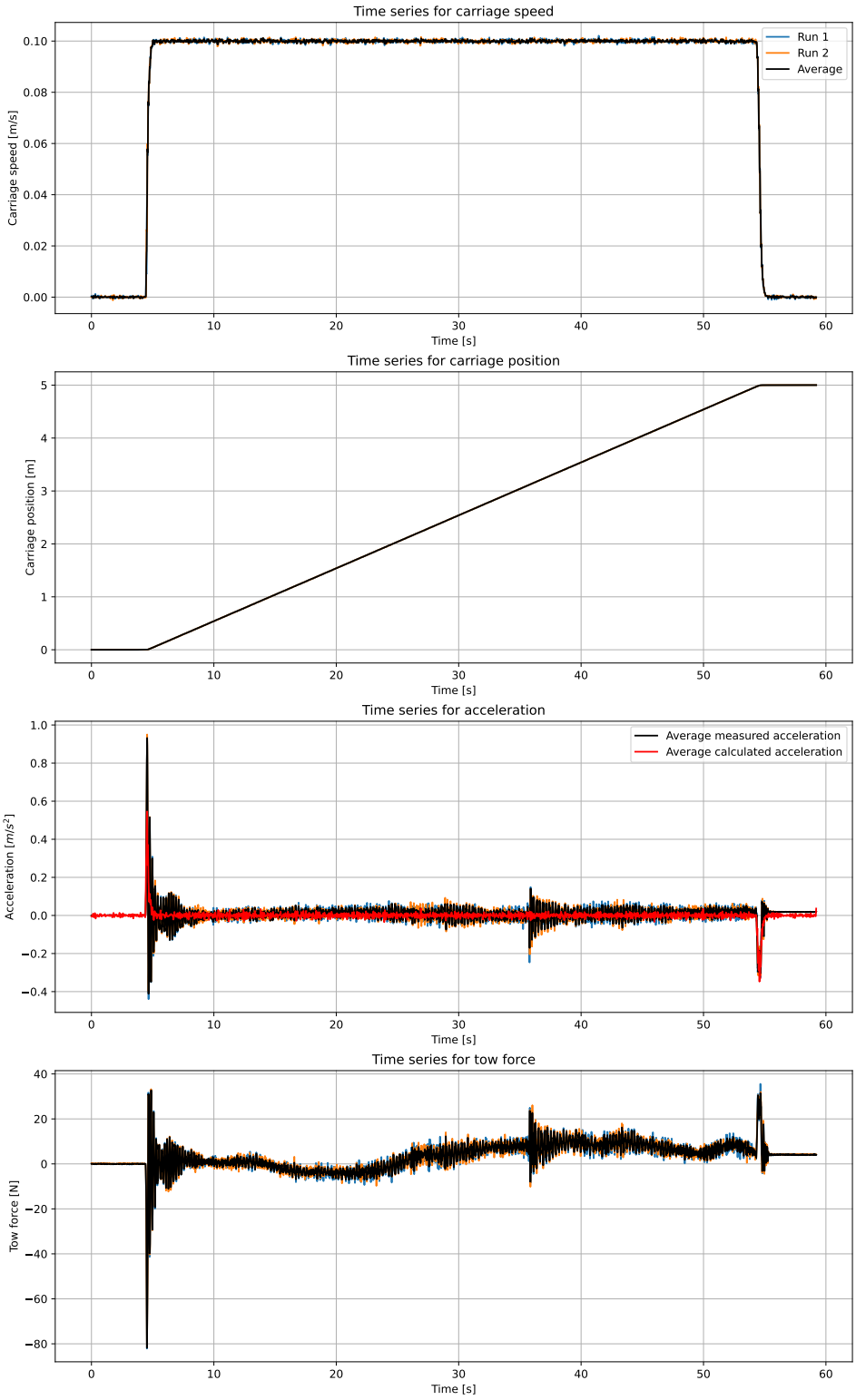

Figure B.1: Time series for model A, dry run, high acceleration, forward direction, speed 0.1 m/s

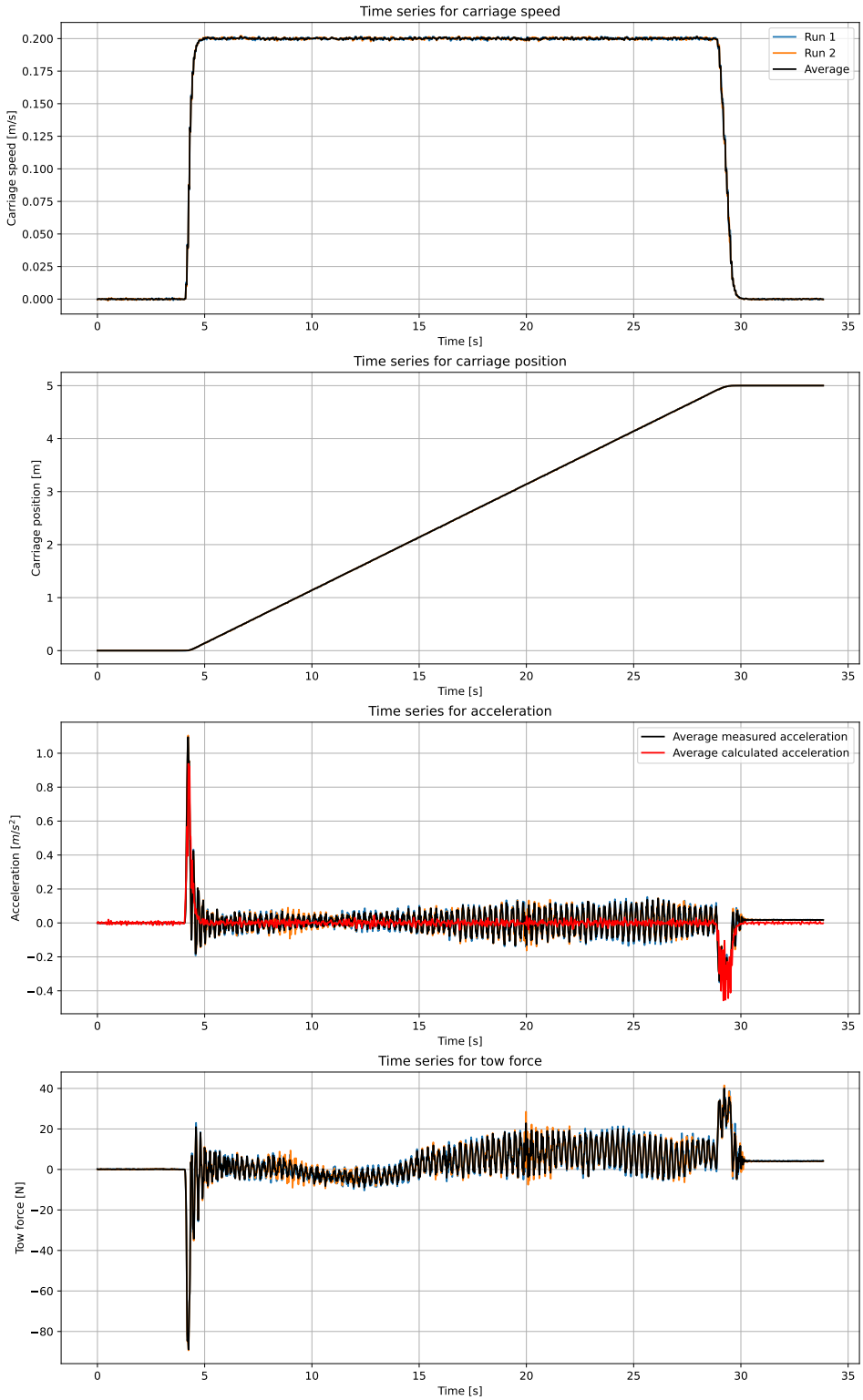

Figure B.2: Time series for model A, dry run, high acceleration, forward direction, speed 0.2 m/s

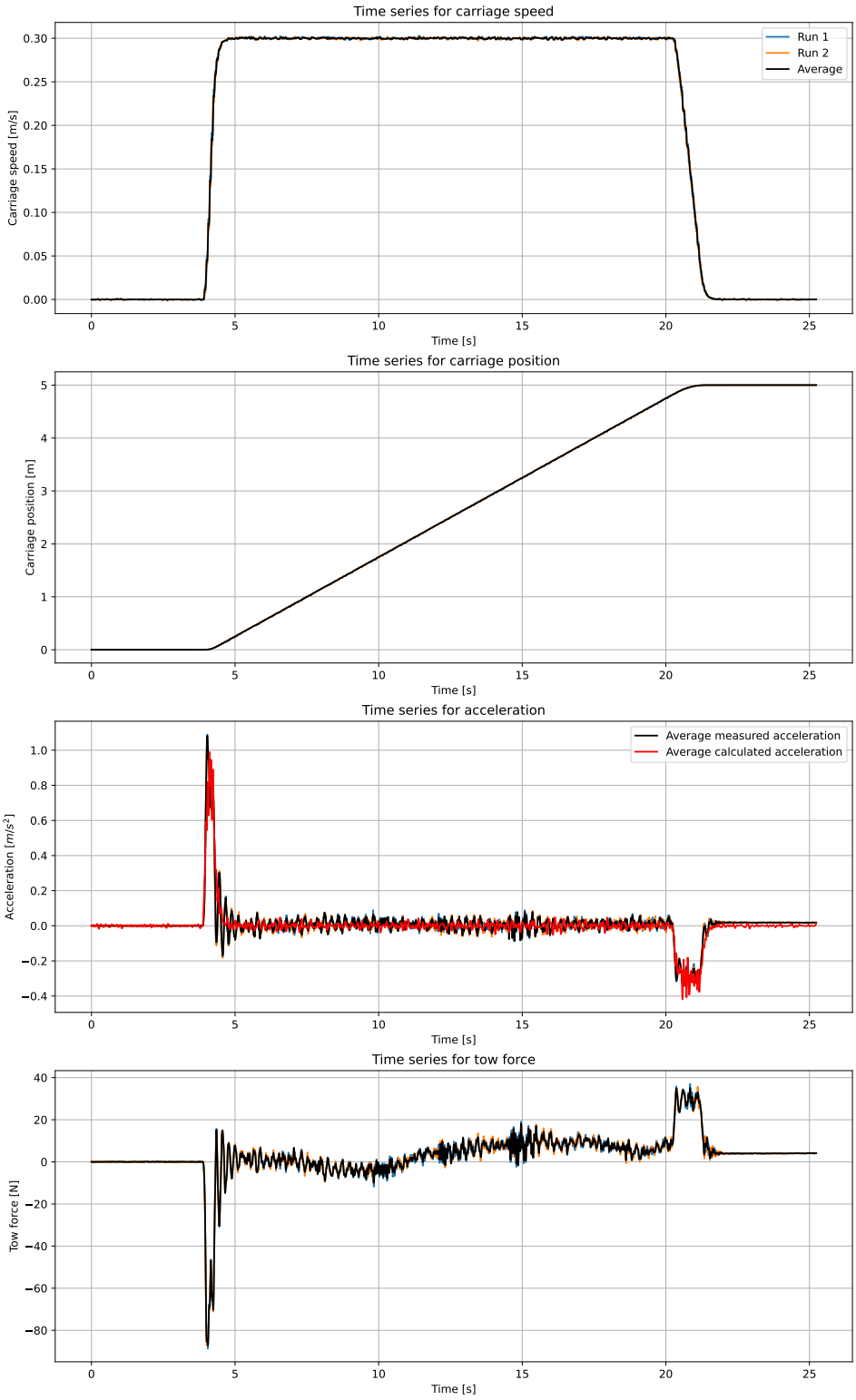

Figure B.3: Time series for model A, dry run, high acceleration, forward direction, speed 0.3 m/s

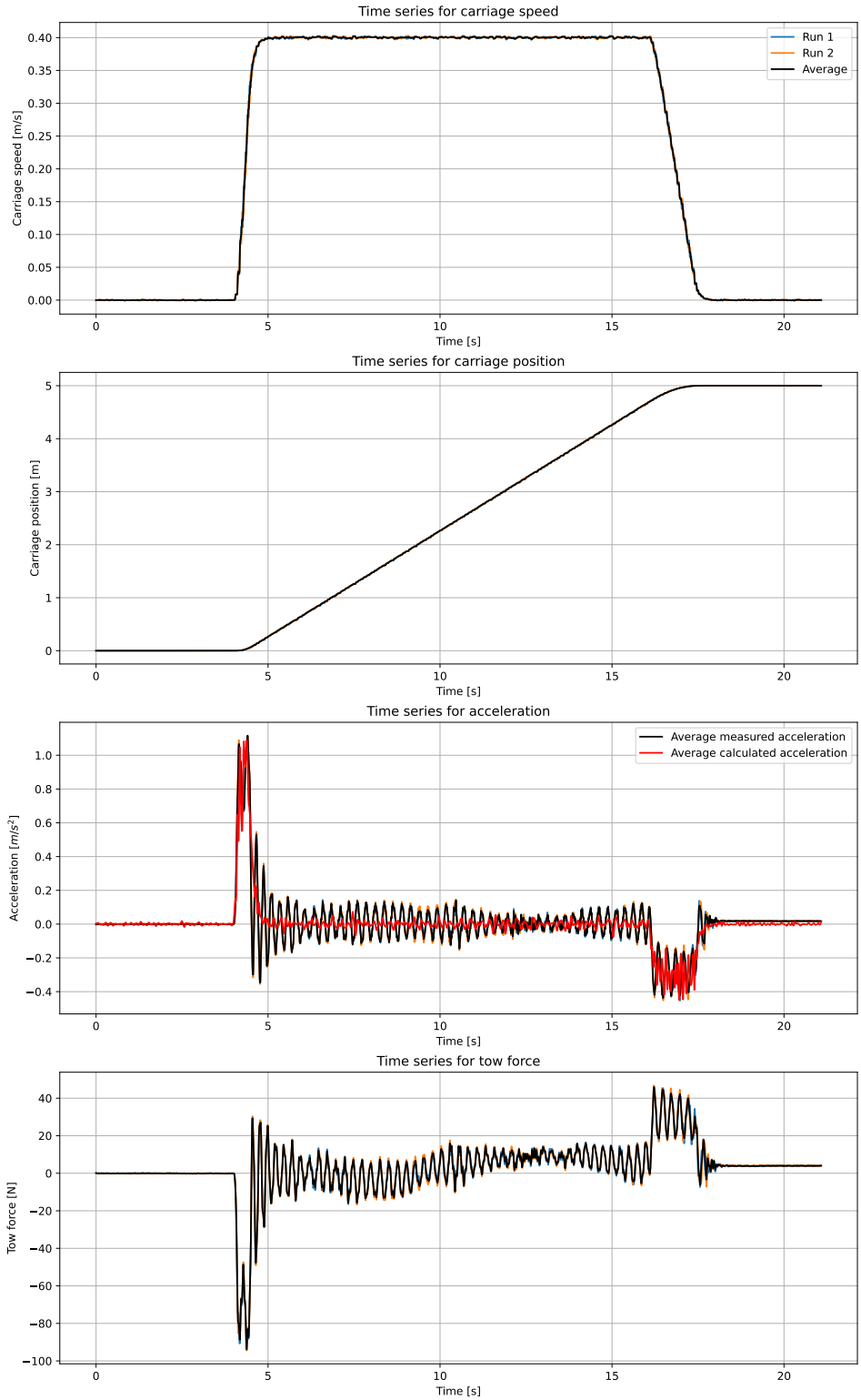

Figure B.4: Time series for model A, dry run, high acceleration, forward direction, speed 0.4 m/s

B.2 Dry run, model A, high acceleration, backward direction

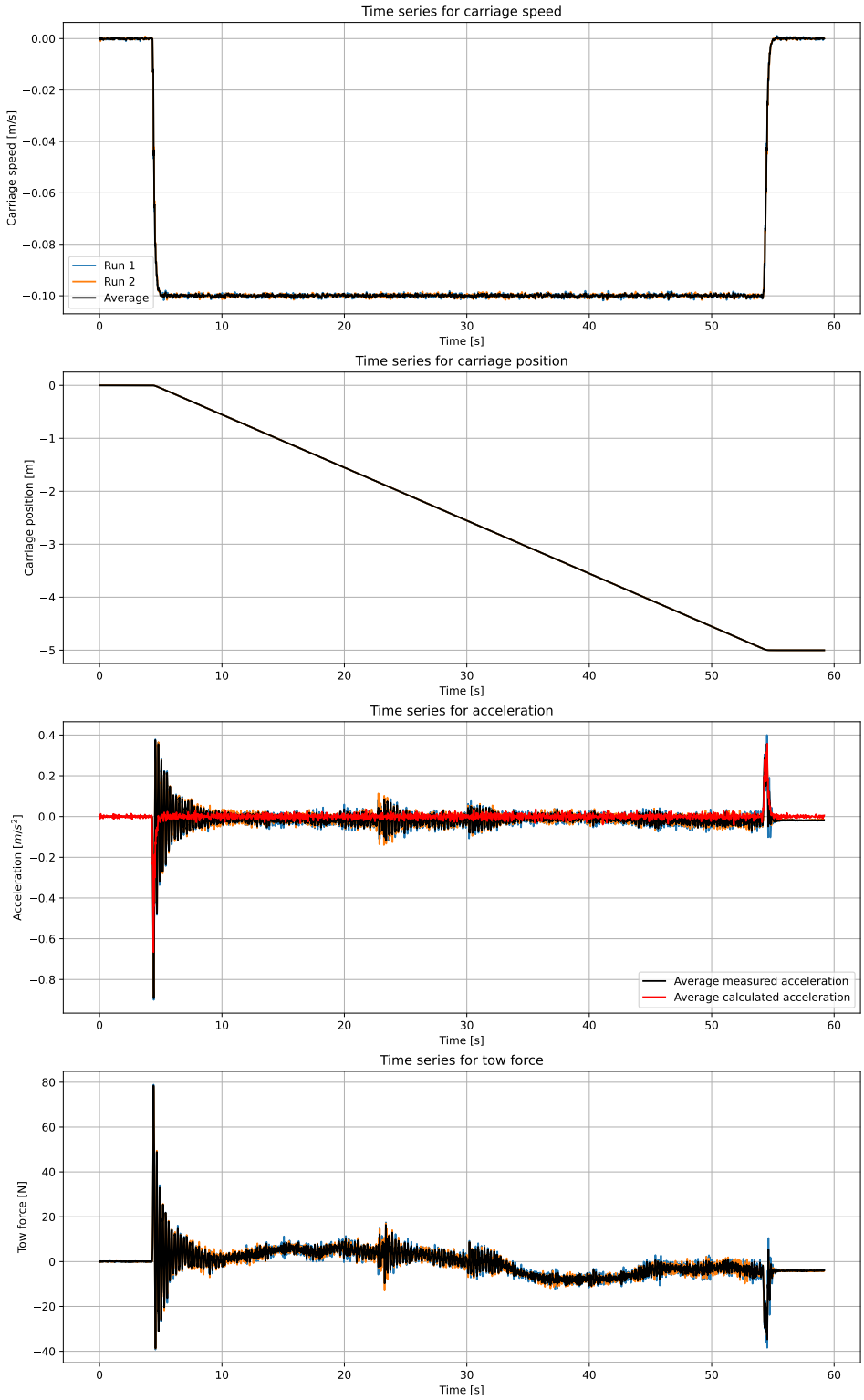

Figure B.5: Time series for model A, dry run, high acceleration, backward direction, speed 0.1 m/s

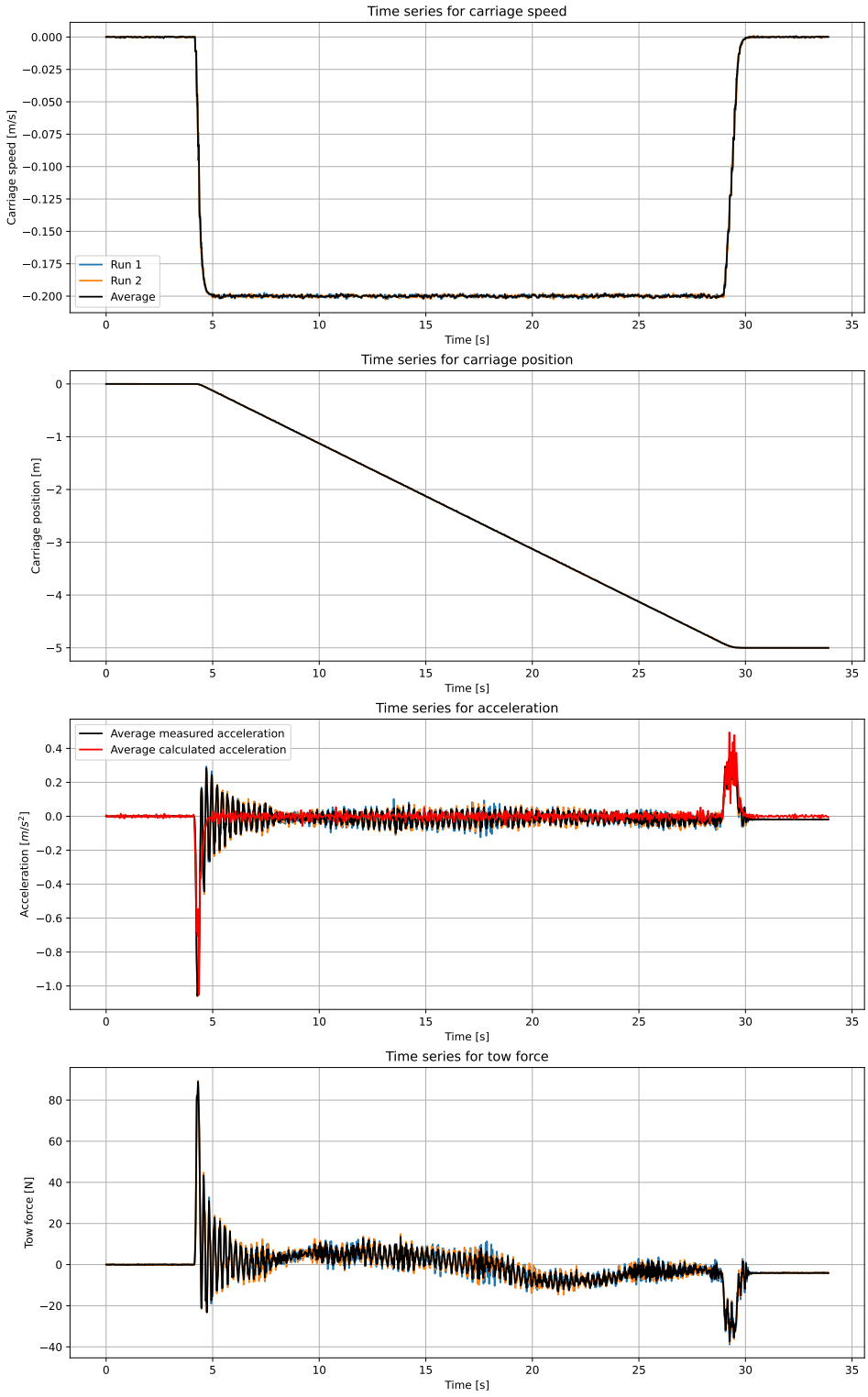

Figure B.6: Time series for model A, dry run, high acceleration, backward direction, speed 0.2 m/s

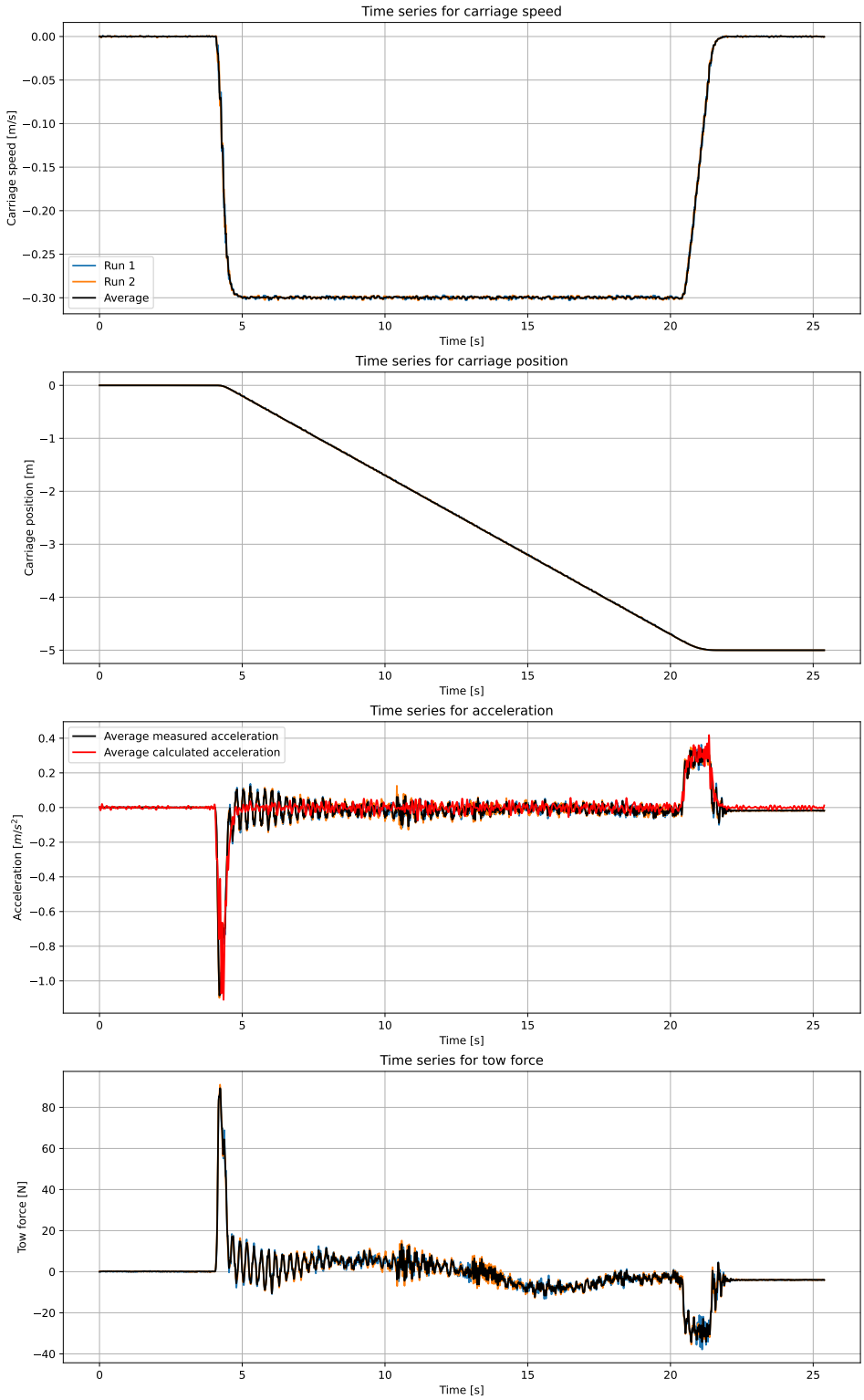

Figure B.7: Time series for model A, dry run, high acceleration, backward direction, speed 0.3 m/s

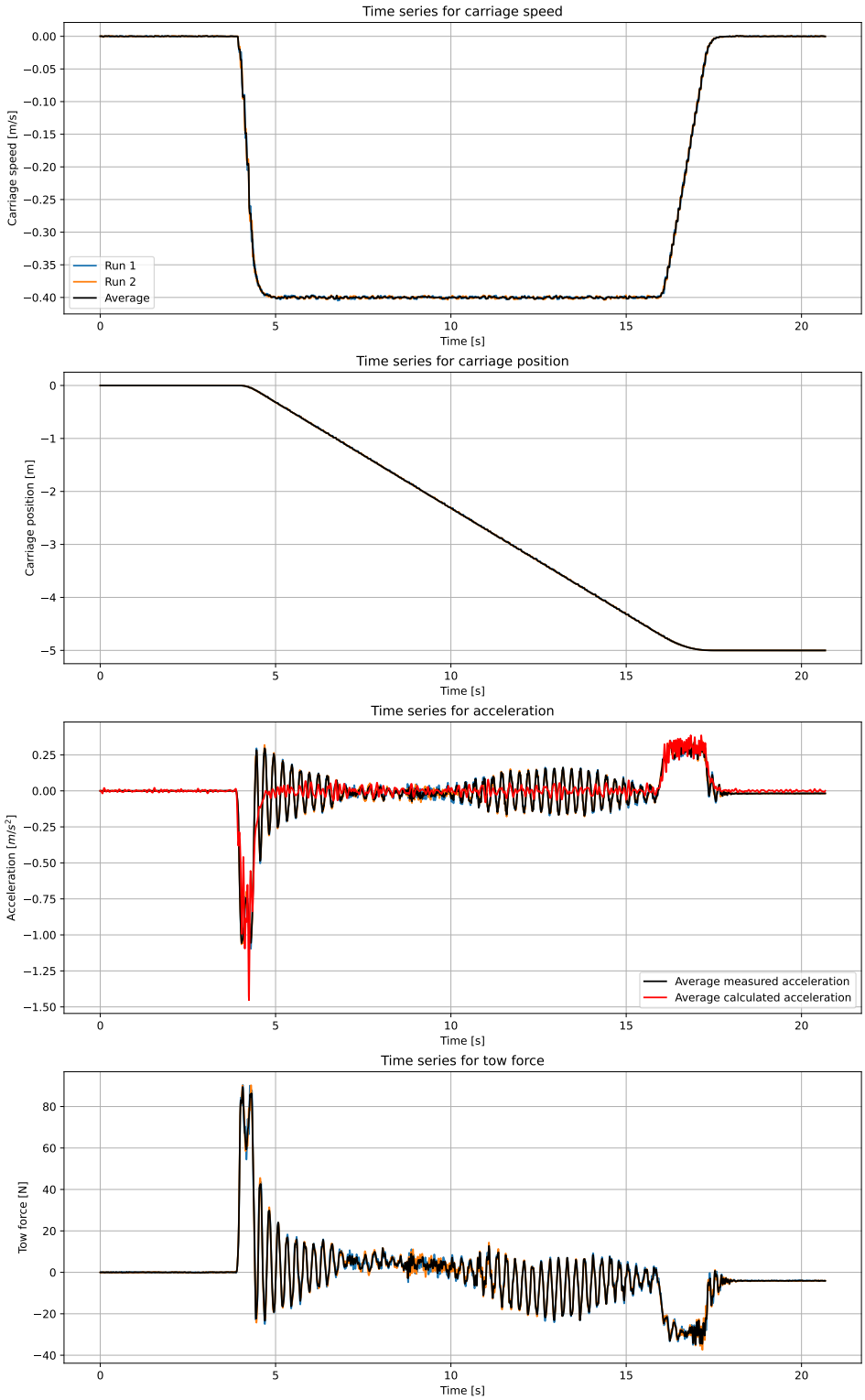

Figure B.8: Time series for model A, dry run, high acceleration, backward direction, speed 0.4 m/s

B.3 Dry run, model A, low acceleration, forward direction

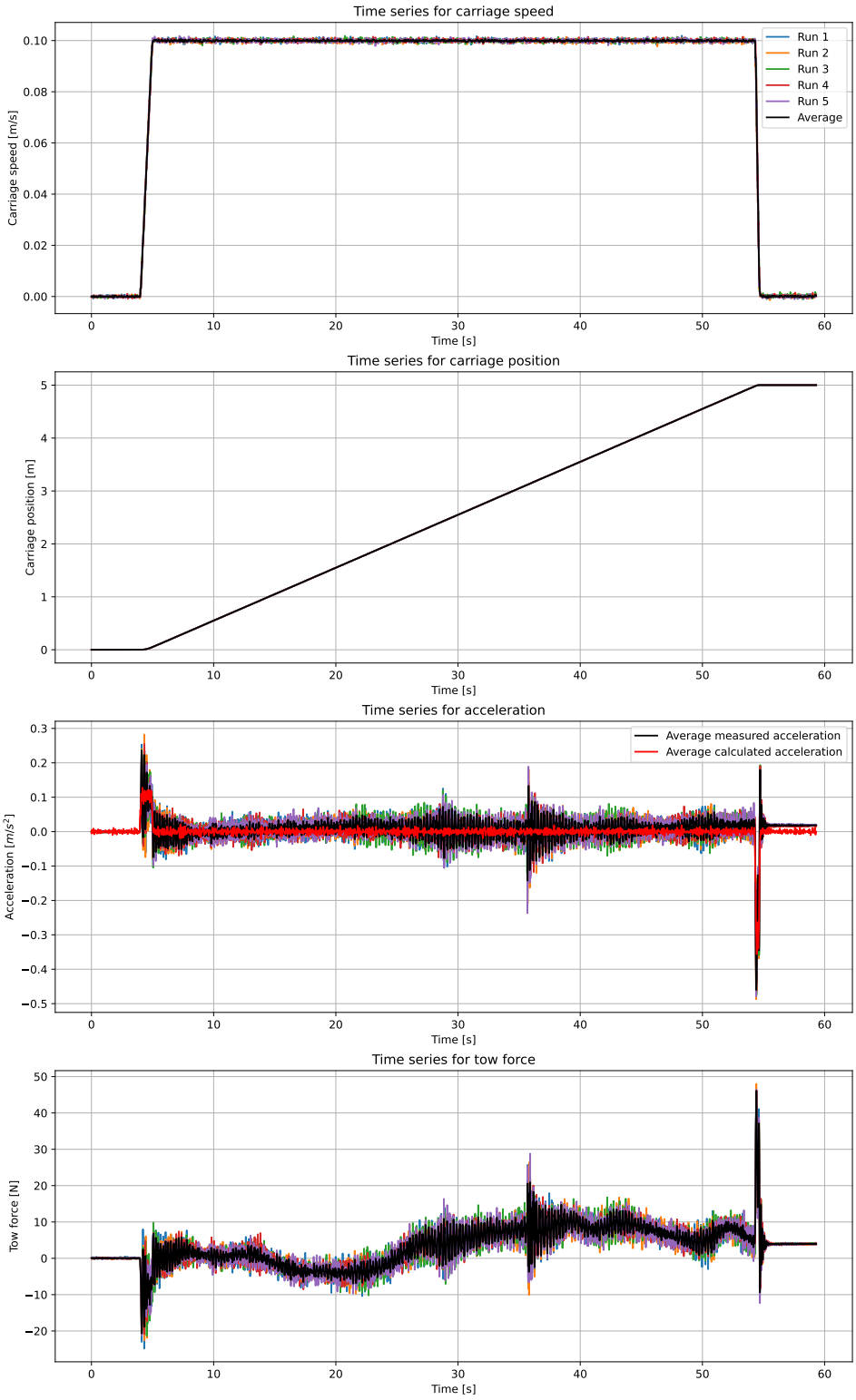

Figure B.9: Time series for model A, dry run, low acceleration, forward direction, speed 0.1 m/s

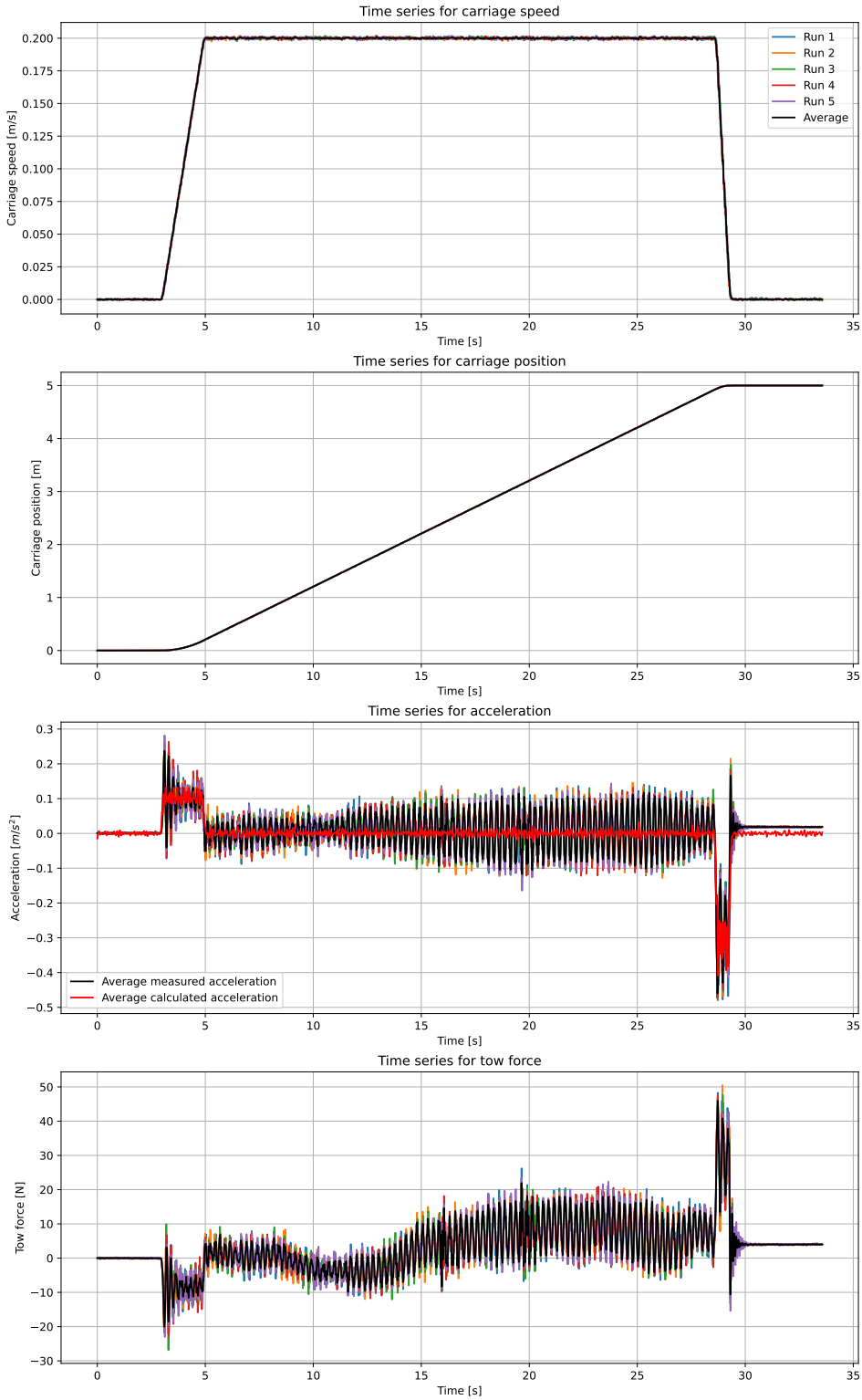

Figure B.10: Time series for model A, dry run, low acceleration, forward direction, speed 0.2 m/s

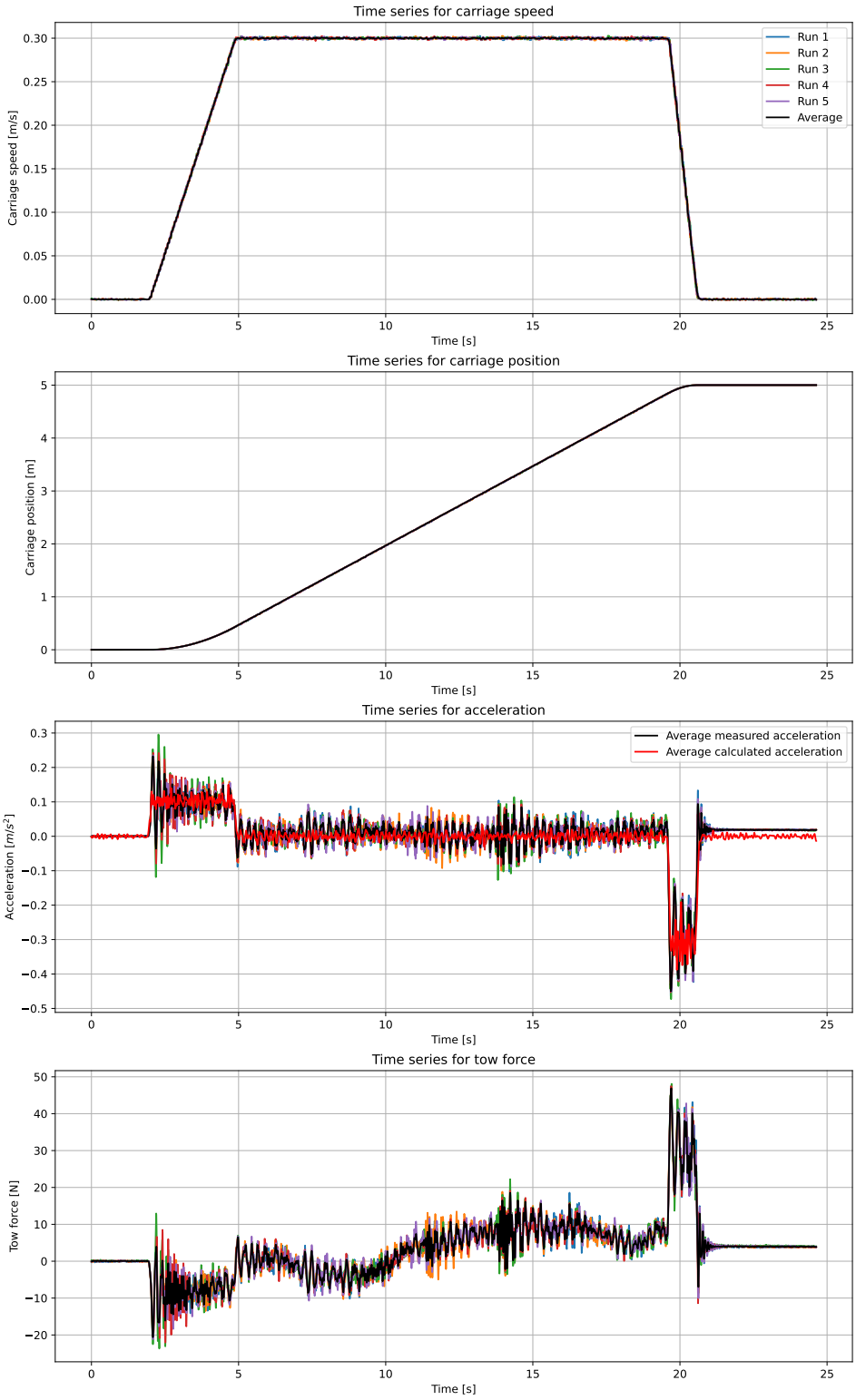

Figure B.11: Time series for model A, dry run, low acceleration, forward direction, speed 0.3 m/s

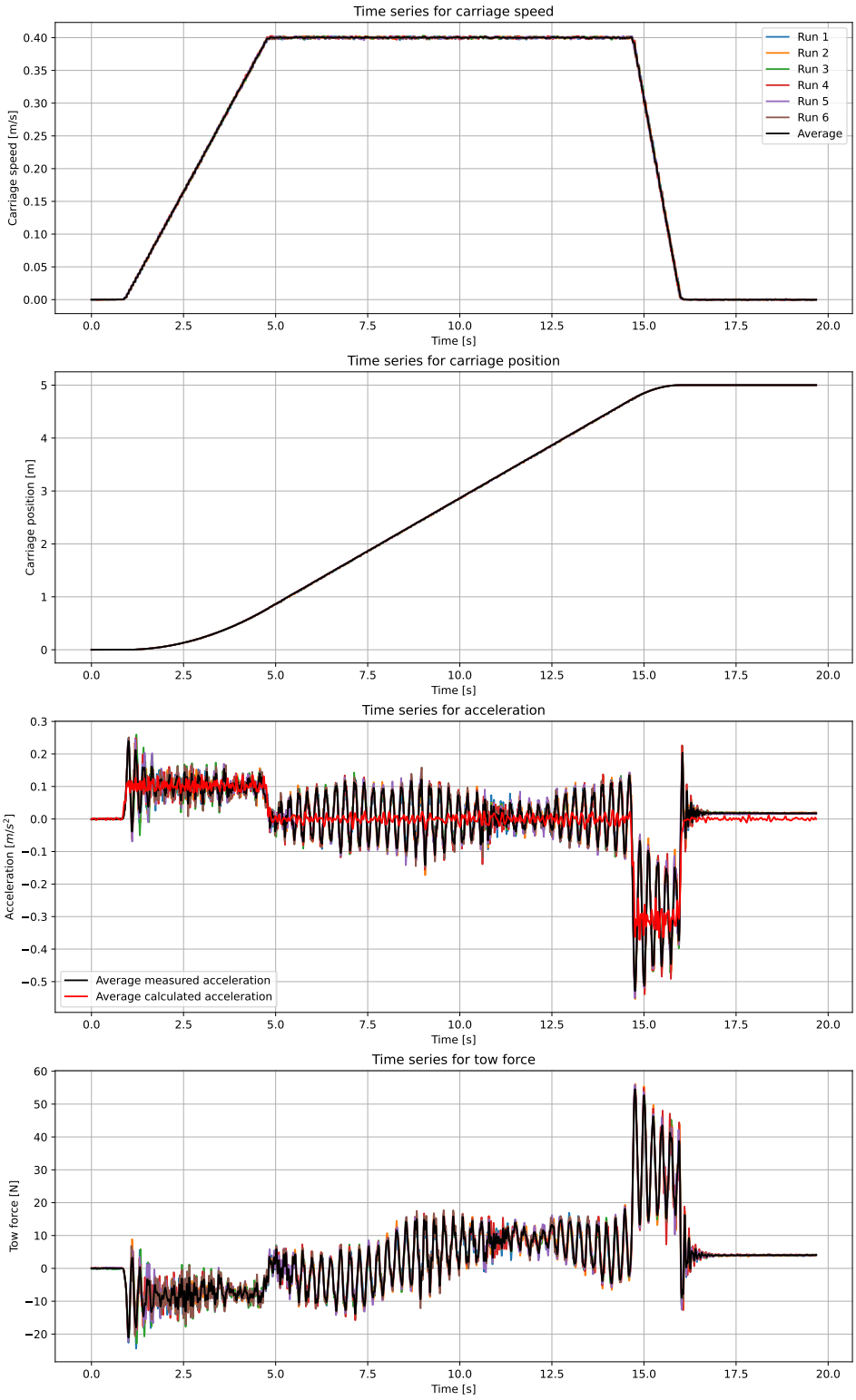

Figure B.12: Time series for model A, dry run, low acceleration, forward direction, speed 0.4 m/s

B.4 Dry run, model A, low acceleration, backward direction

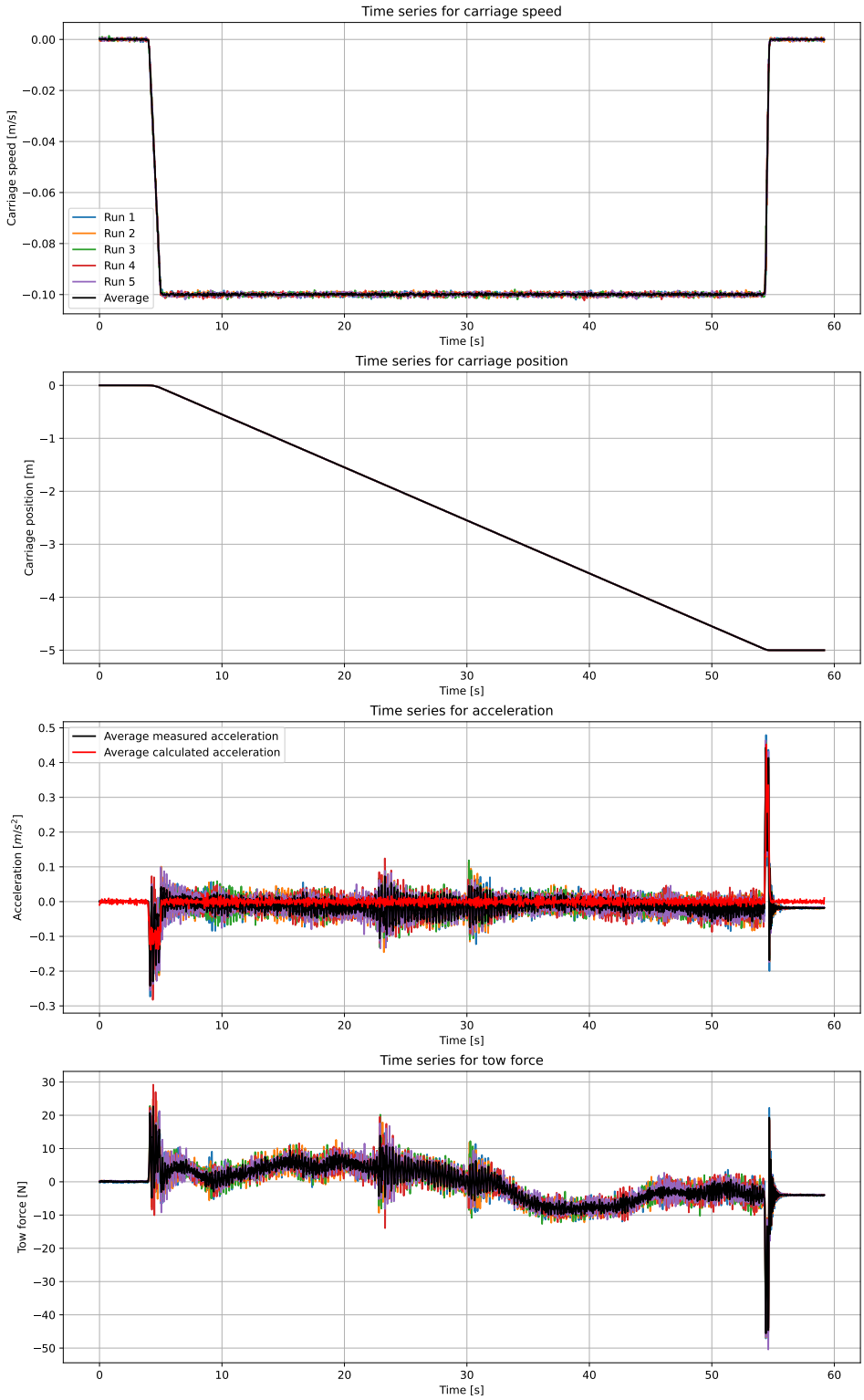

Figure B.13: Time series for model A, dry run, low acceleration, backward direction, speed 0.1 m/s

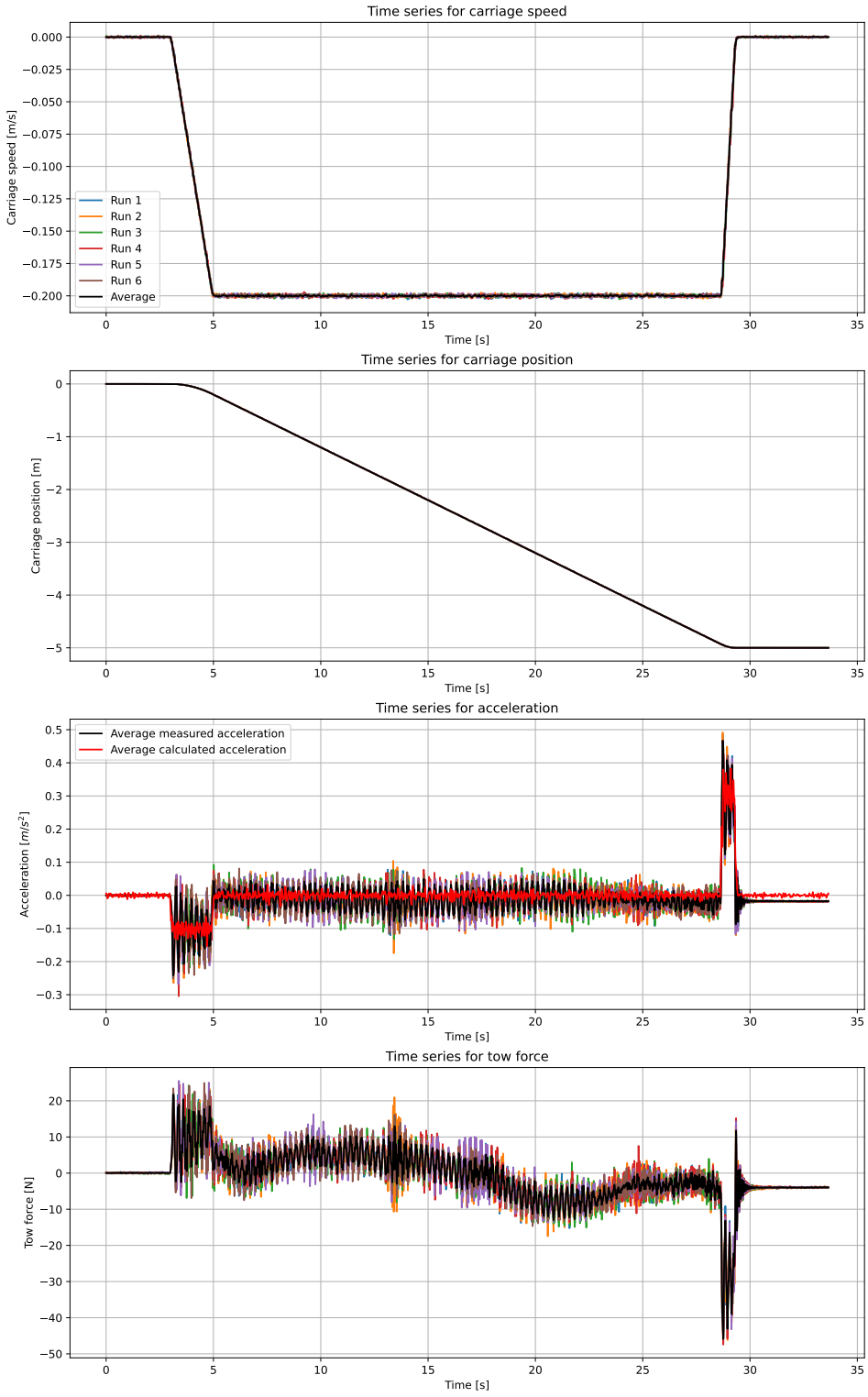

Figure B.14: Time series for model A, dry run, low acceleration, backward direction, speed 0.2 m/s

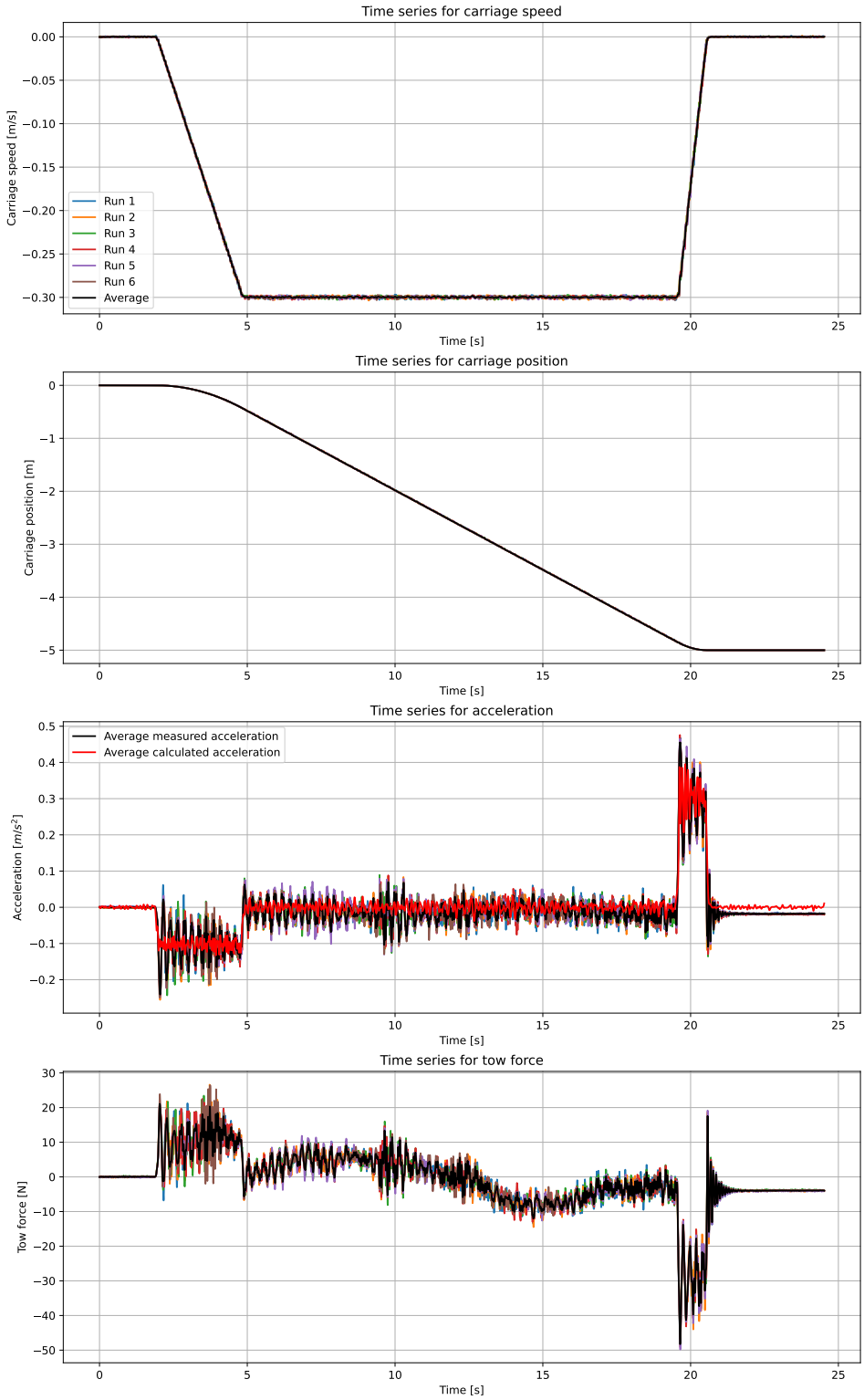

Figure B.15: Time series for model A, dry run, low acceleration, backward direction, speed 0.3 m/s

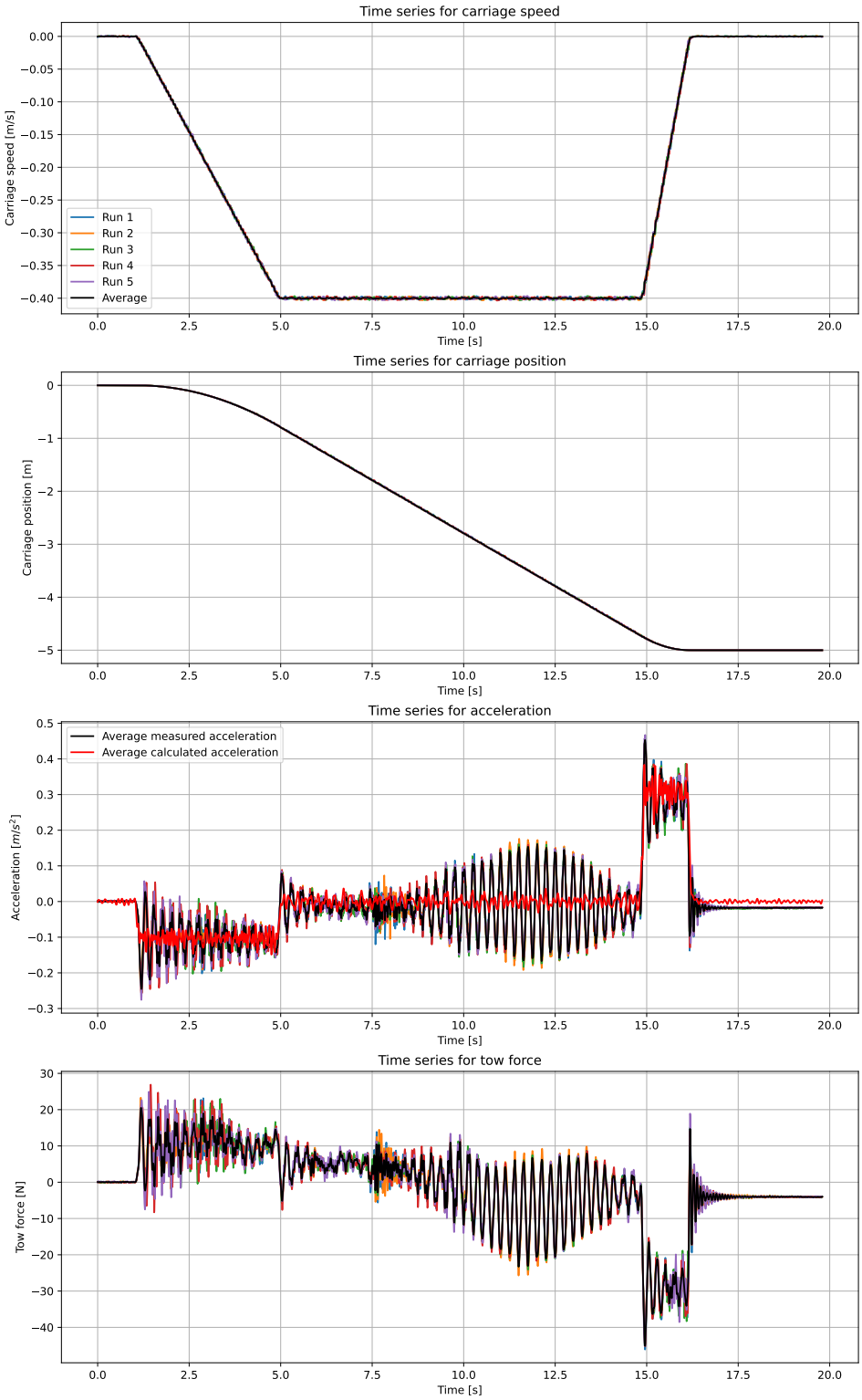

Figure B.16: Time series for model A, dry run, low acceleration, backward direction, speed 0.4 m/s

B.5 Wet run, model A, high acceleration, forward direction

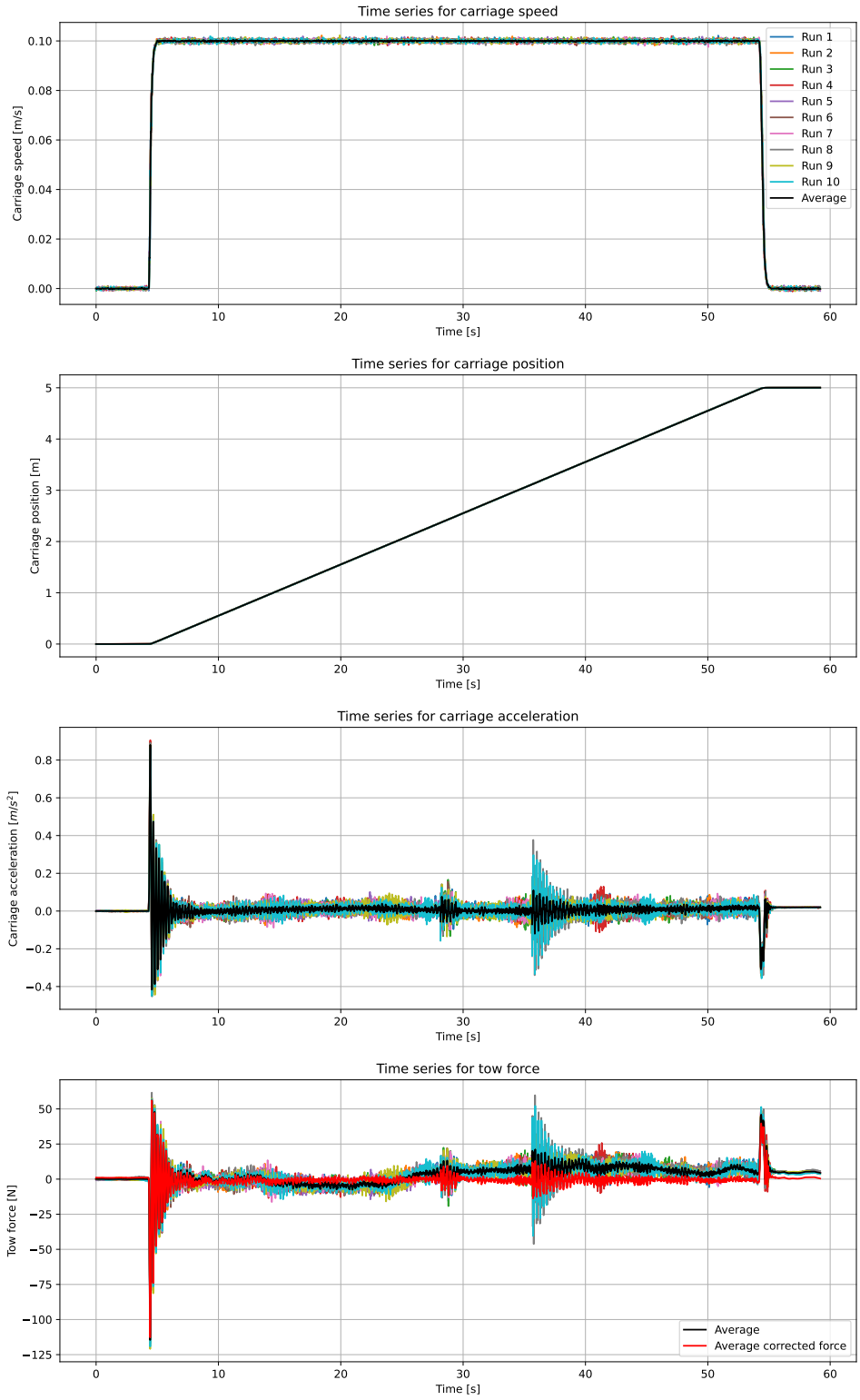

Figure B.17: Time series for model A, wet run, high acceleration, forward direction, speed 0.1 m/s

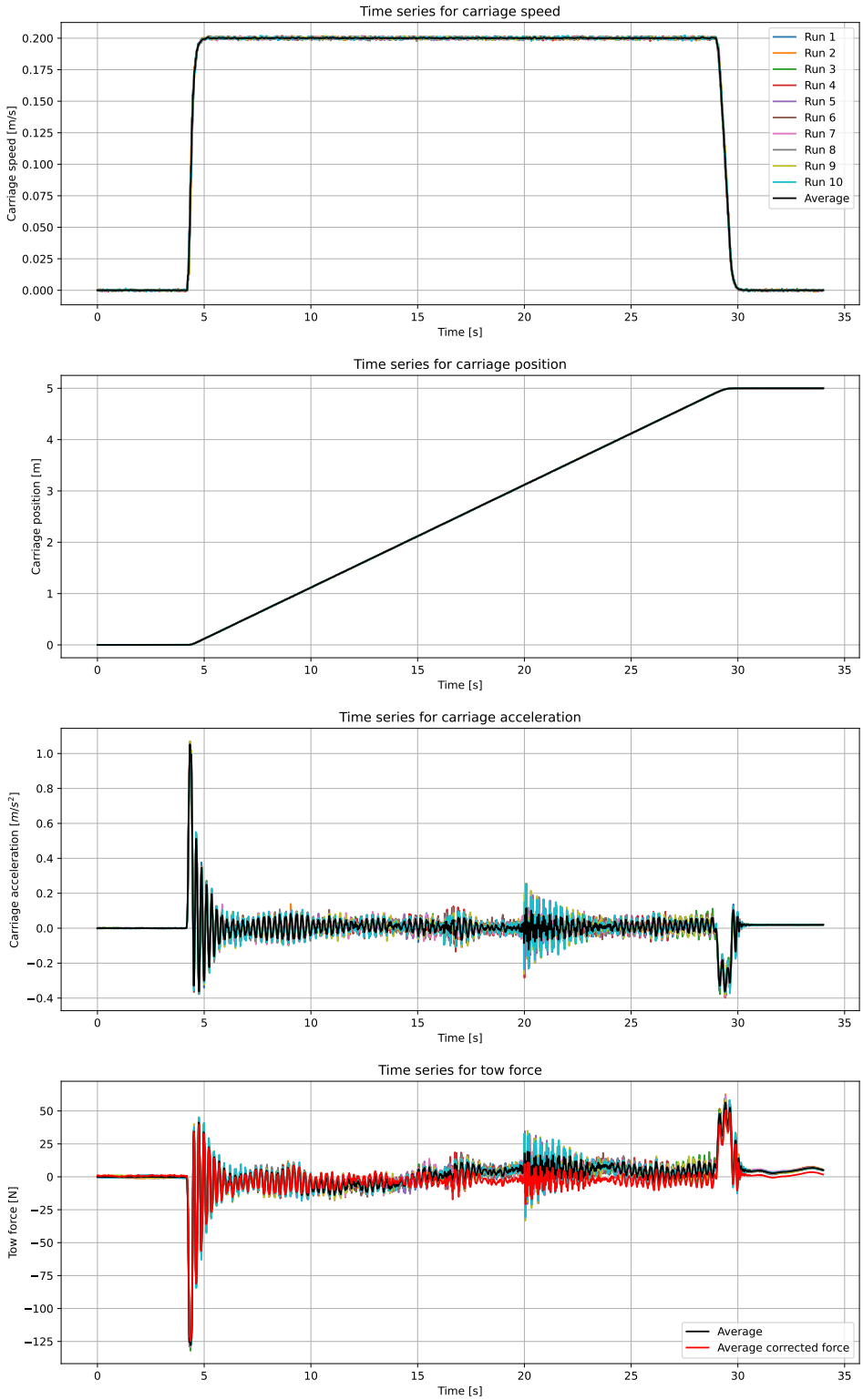

Figure B.18: Time series for model A, wet run, high acceleration, forward direction, speed 0.2 m/s

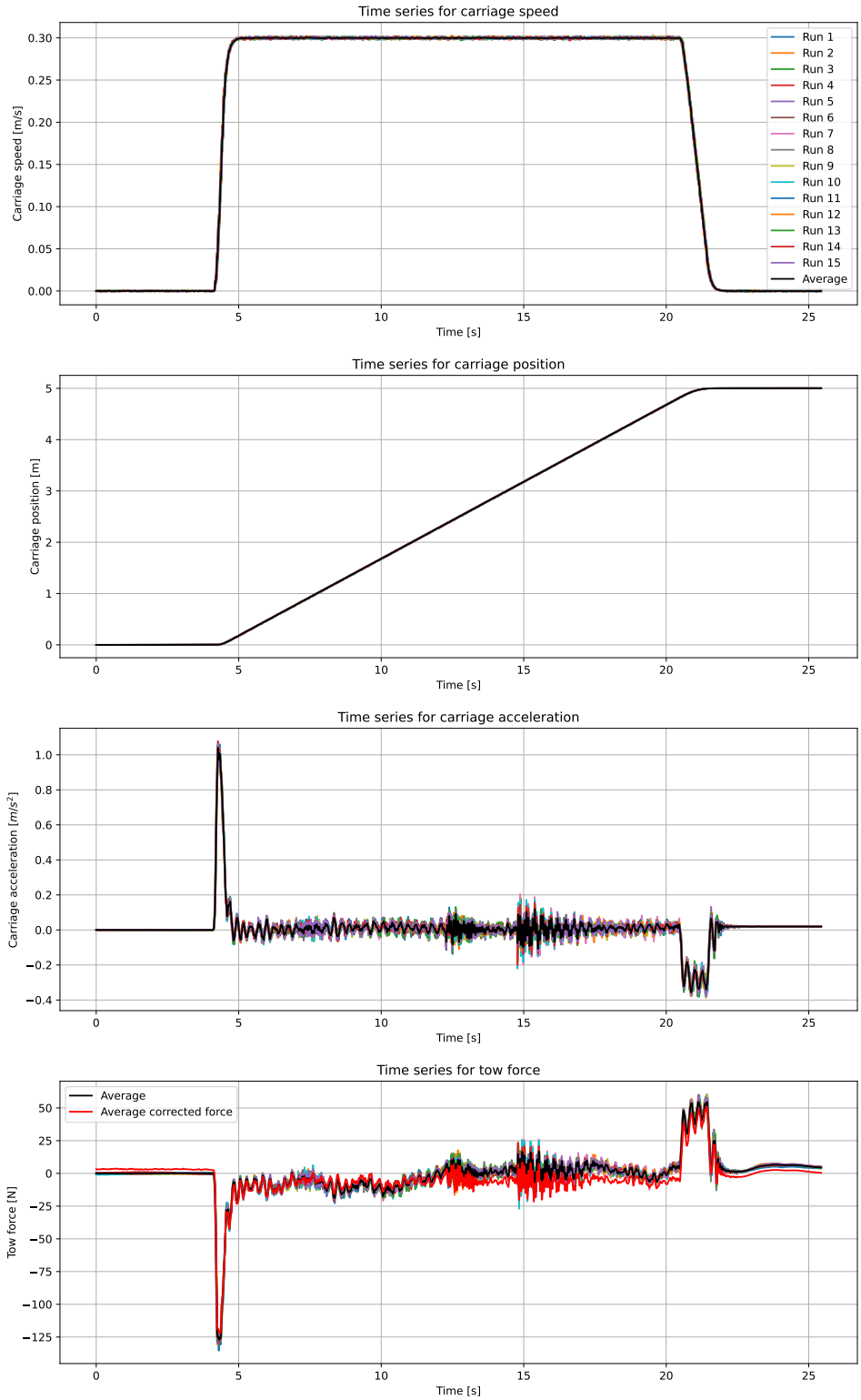

Figure B.19: Time series for model A, wet run, high acceleration, forward direction, speed 0.3 m/s

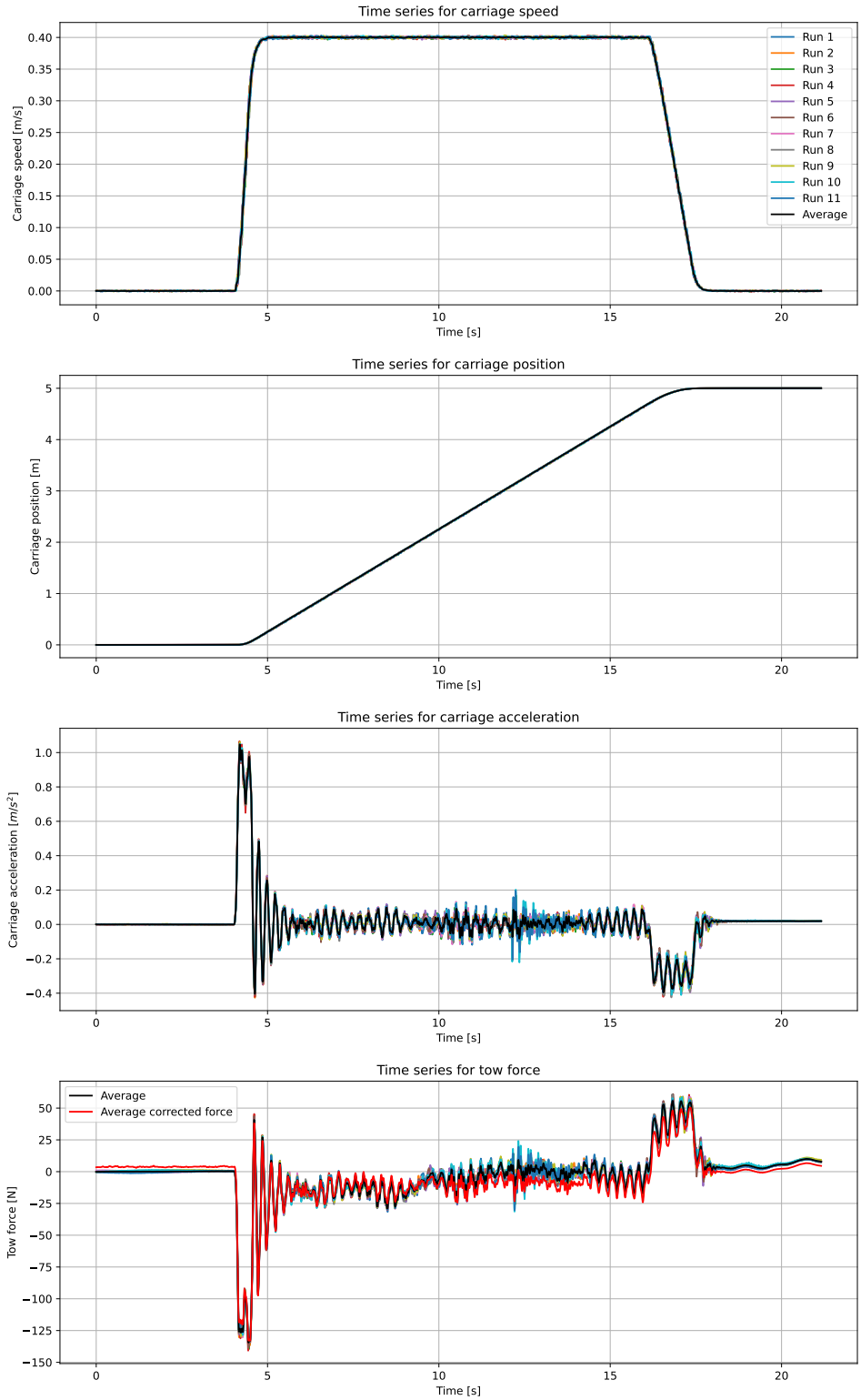

Figure B.20: Time series for model A, wet run, high acceleration, forward direction, speed 0.4 m/s

B.6 Wet run, model A, high acceleration, backward direction

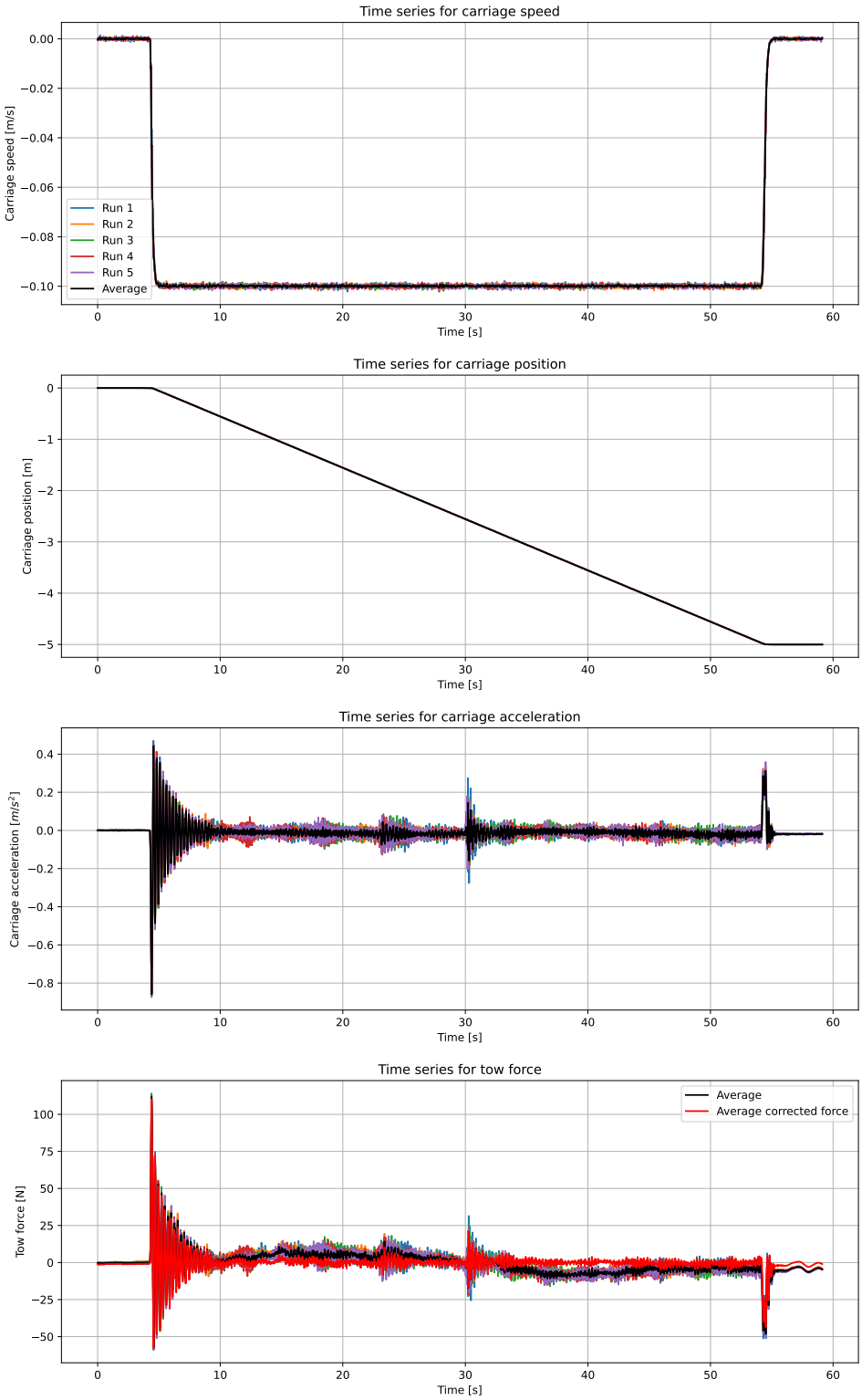

Figure B.21: Time series for model A, wet run, high acceleration, backward direction, speed 0.1 m/s

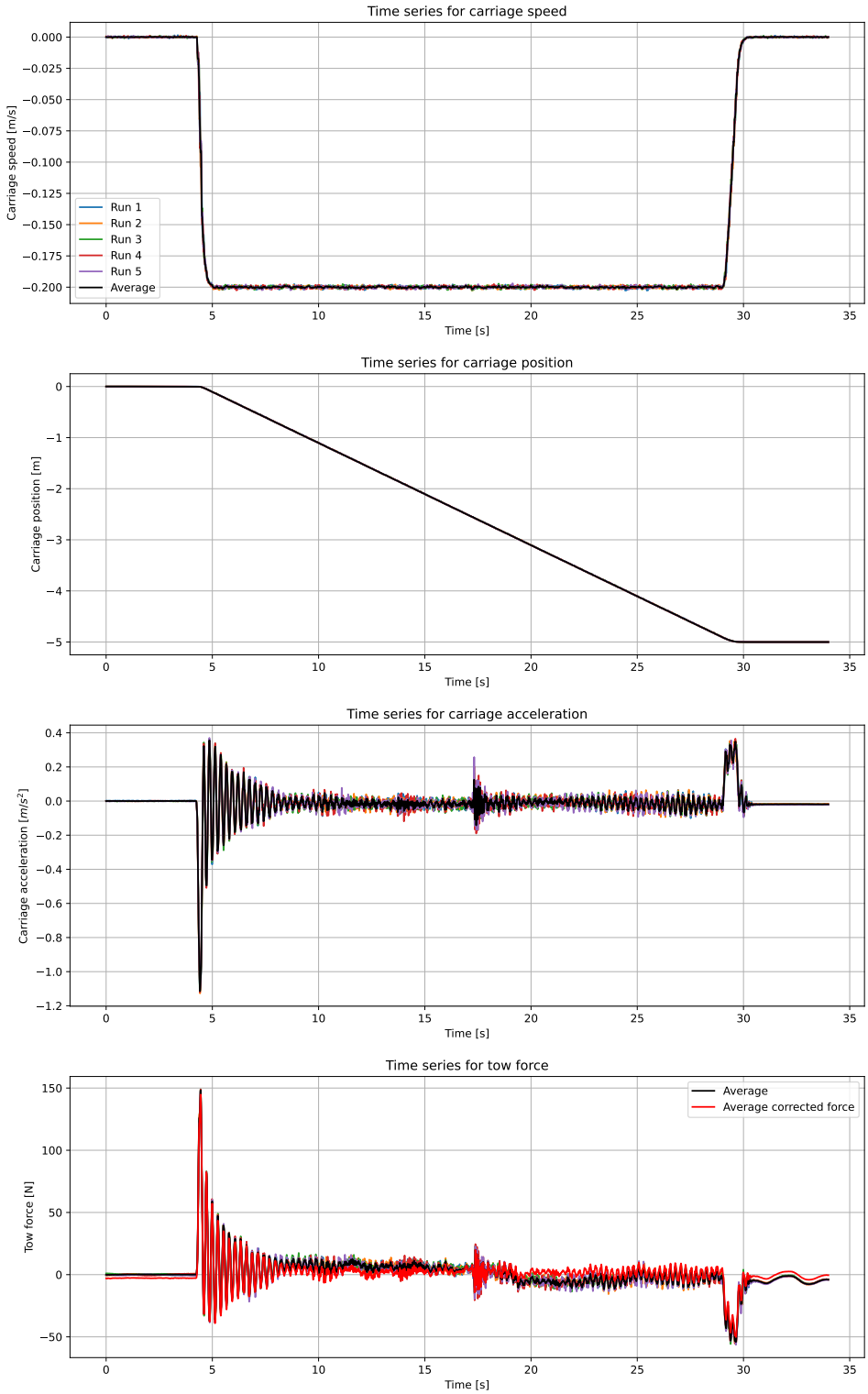

Figure B.22: Time series for model A, wet run, high acceleration, backward direction, speed 0.2 m/s

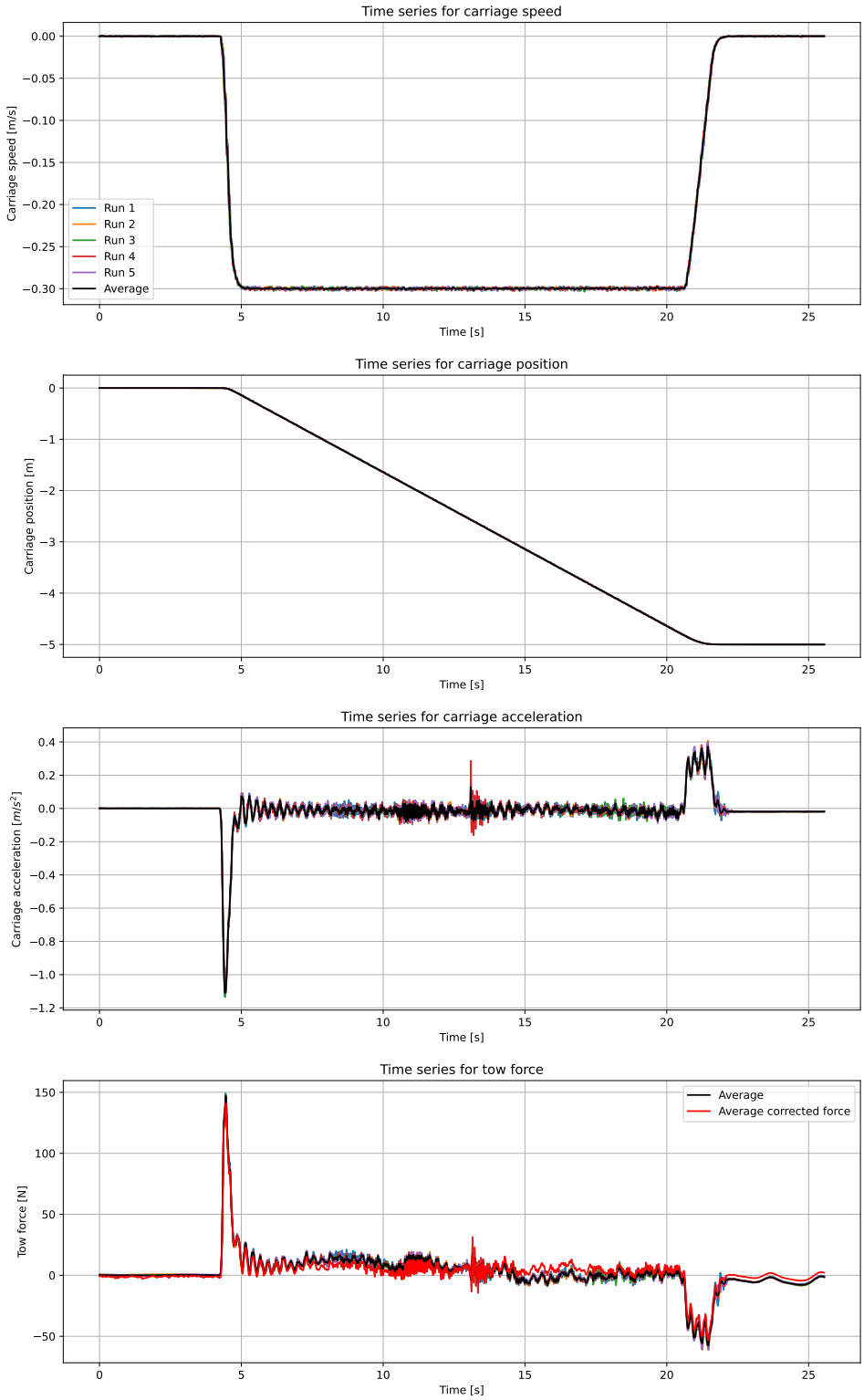

Figure B.23: Time series for model A, wet run, high acceleration, backward direction, speed 0.3 m/s

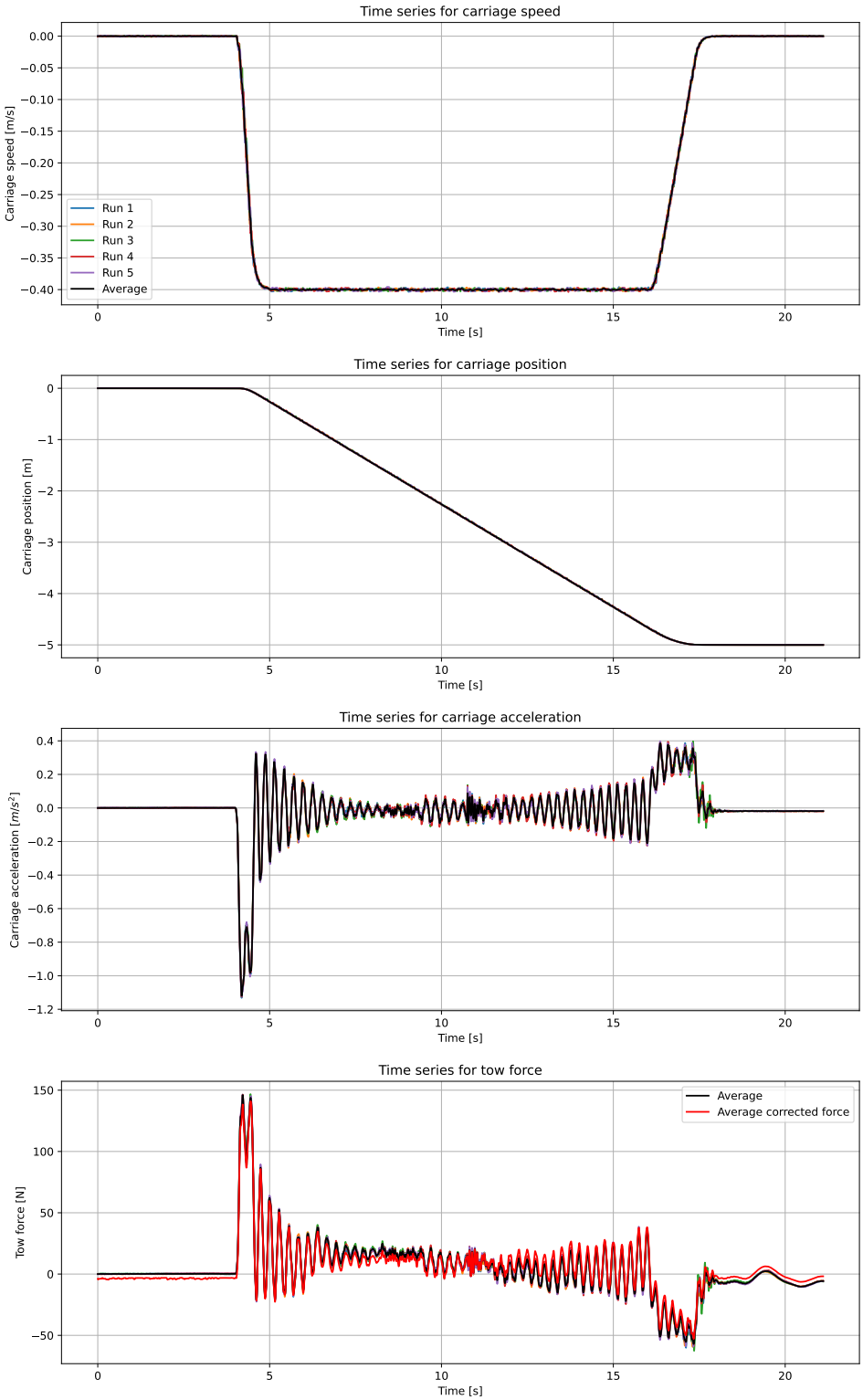

Figure B.24: Time series for model A, wet run, high acceleration, backward direction, speed 0.4 m/s

B.7 Wet run, model A, low acceleration, forward direction

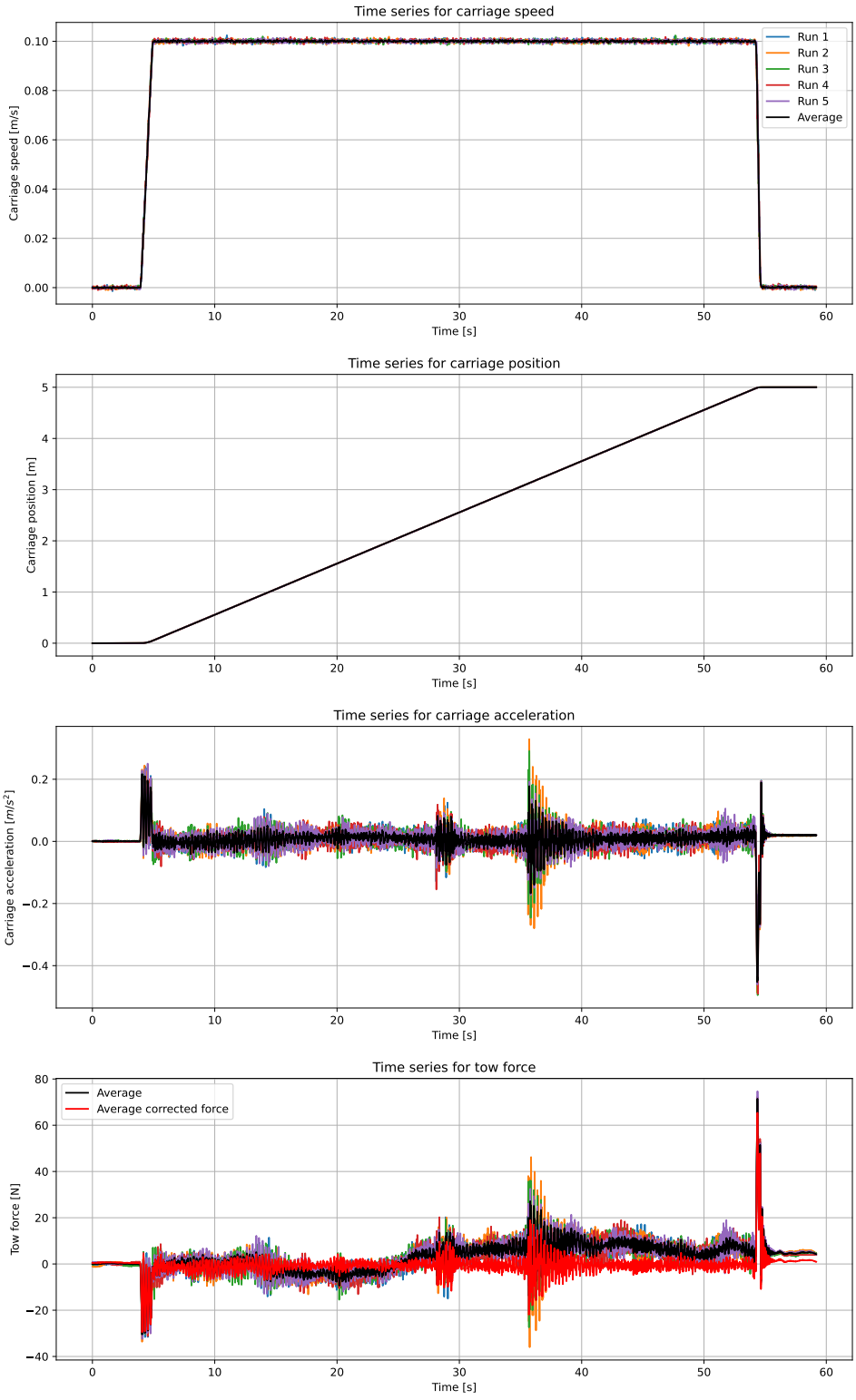

Figure B.25: Time series for model A, wet run, low acceleration, forward direction, speed 0.1 m/s

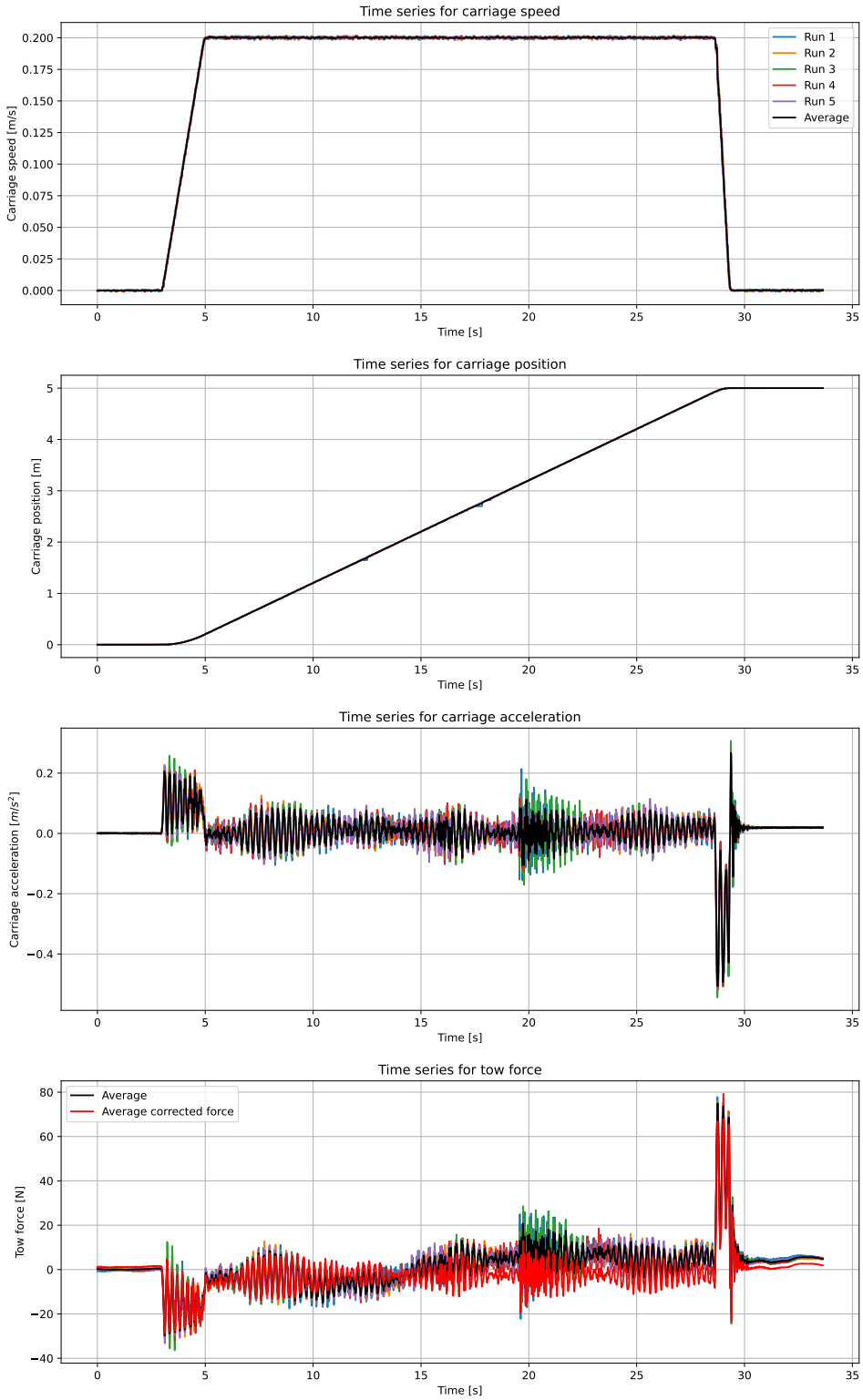

Figure B.26: Time series for model A, wet run, low acceleration, forward direction, speed 0.2 m/s

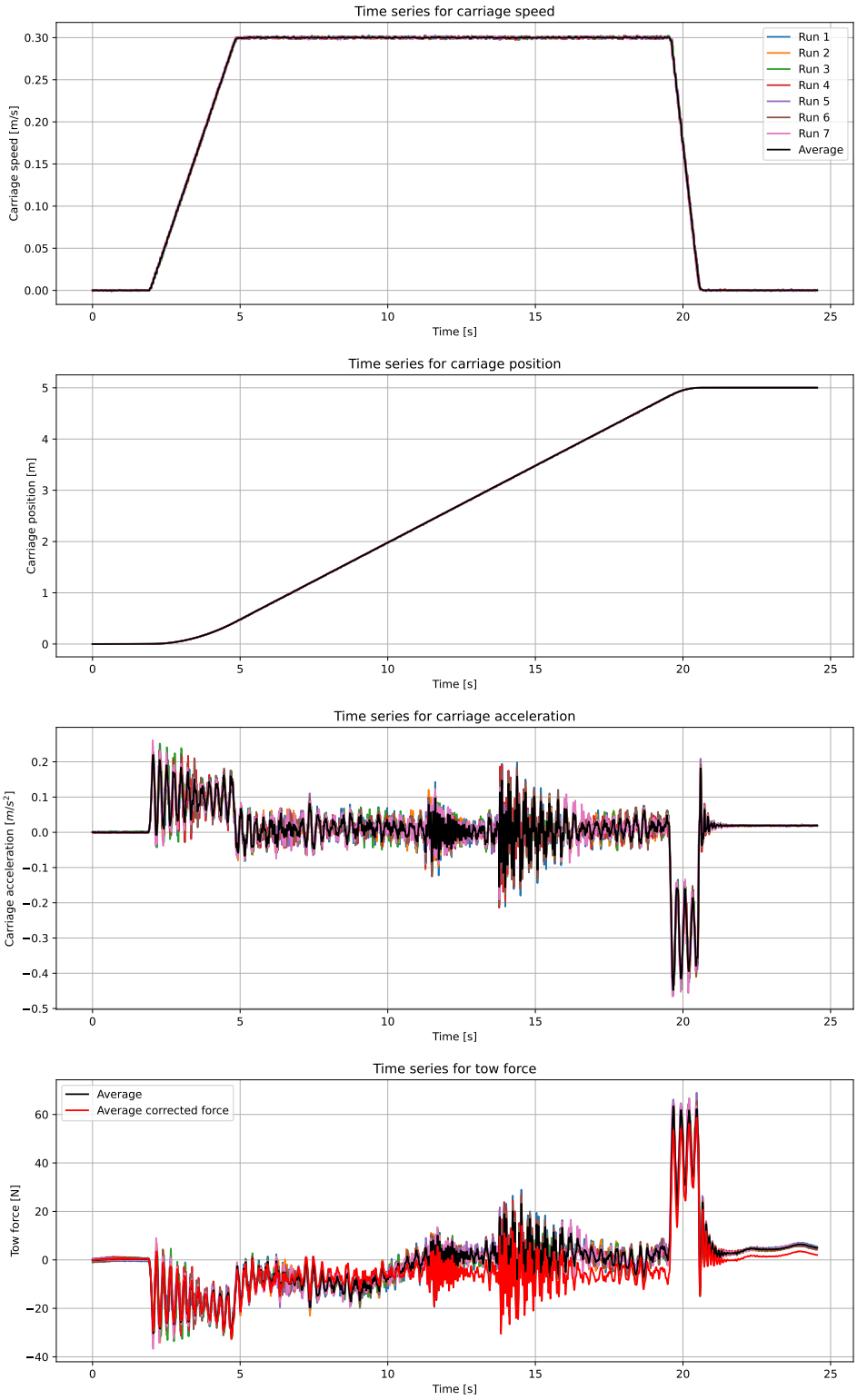

Figure B.27: Time series for model A, wet run, low acceleration, forward direction, speed 0.3 m/s

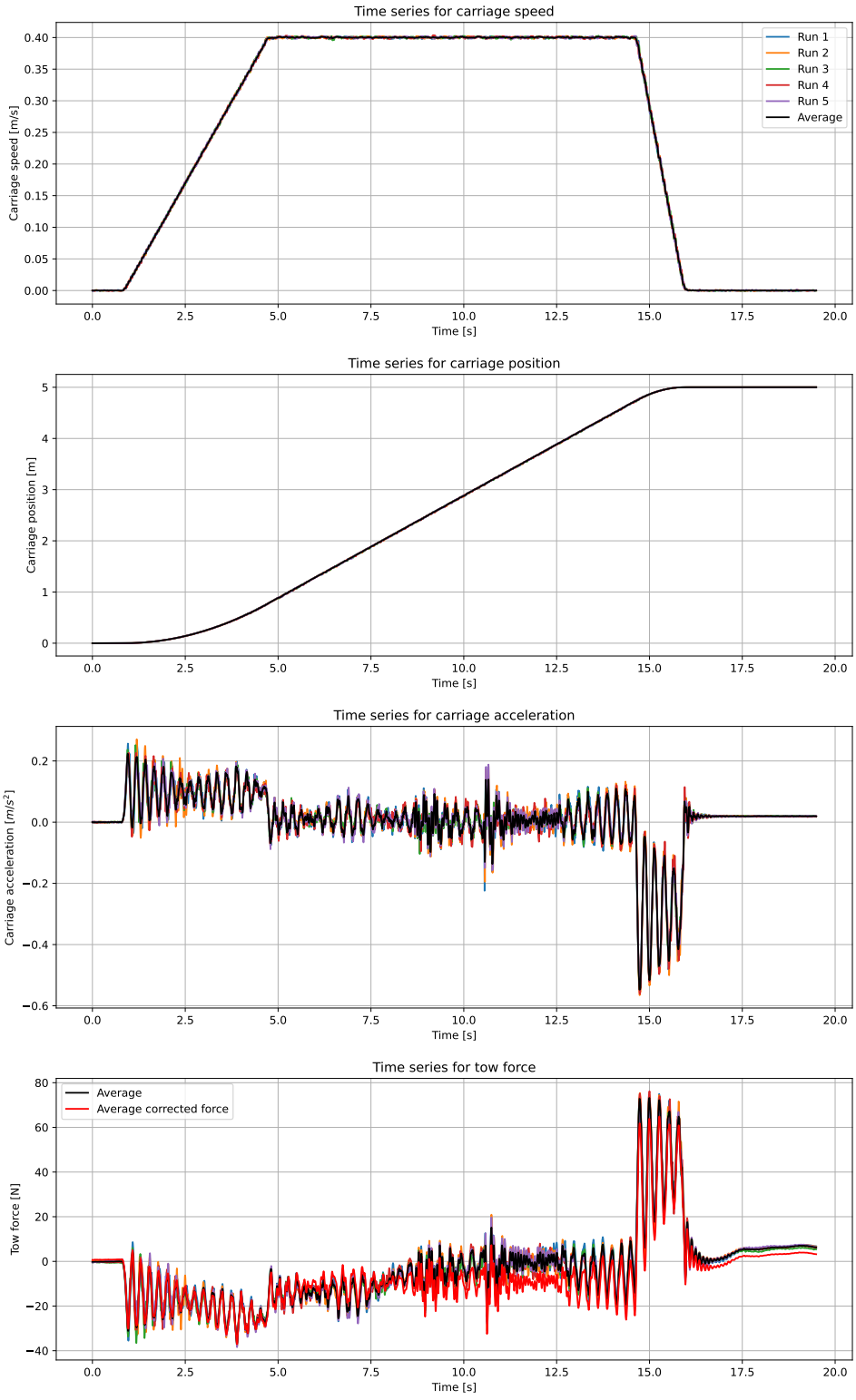

Figure B.28: Time series for model A, wet run, low acceleration, forward direction, speed 0.4 m/s

B.8 Wet run, model A, maximum acceleration, forward direction

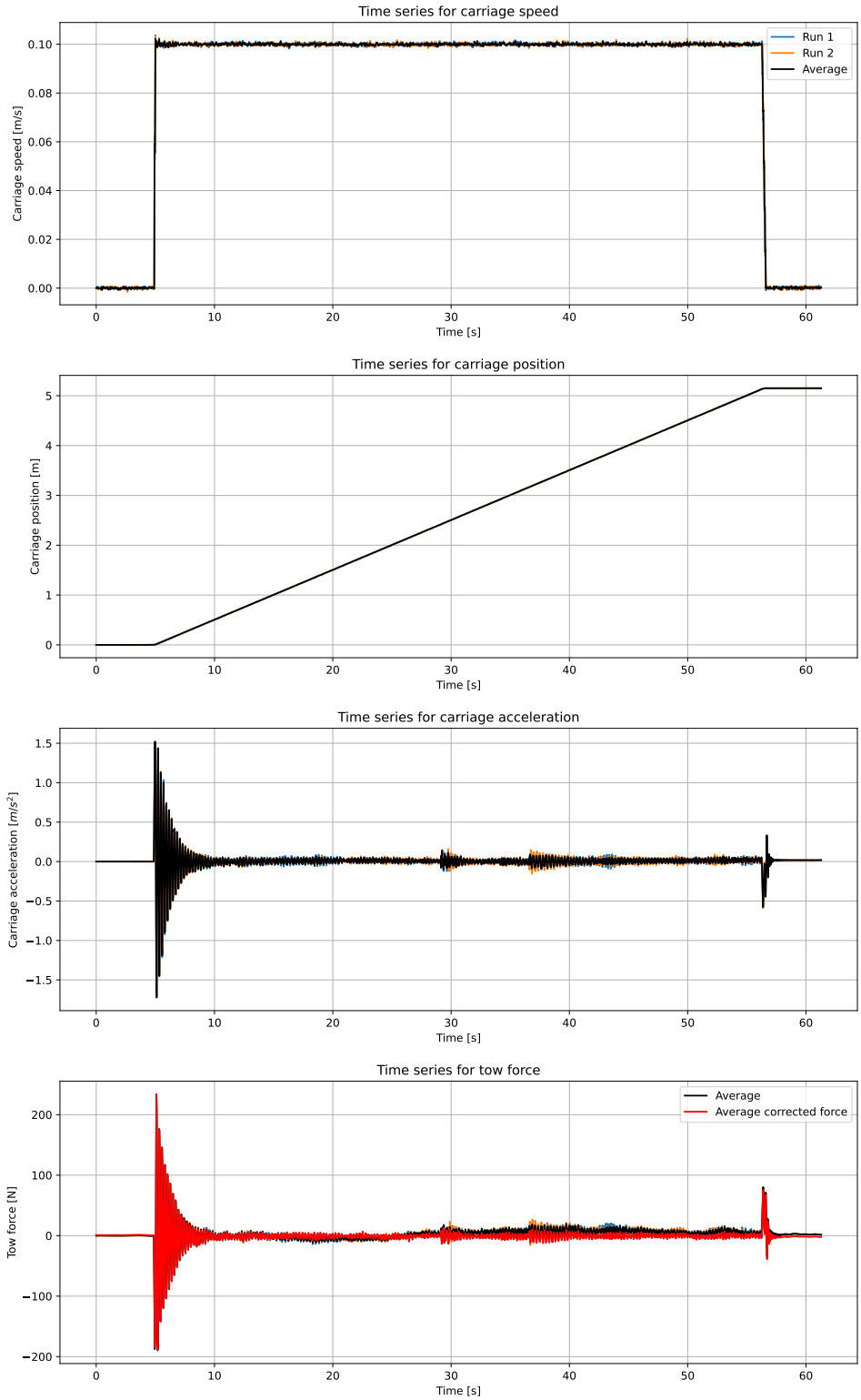

Figure B.29: Time series for model A, wet run, maximum acceleration, forward direction, speed 0.1 m/s

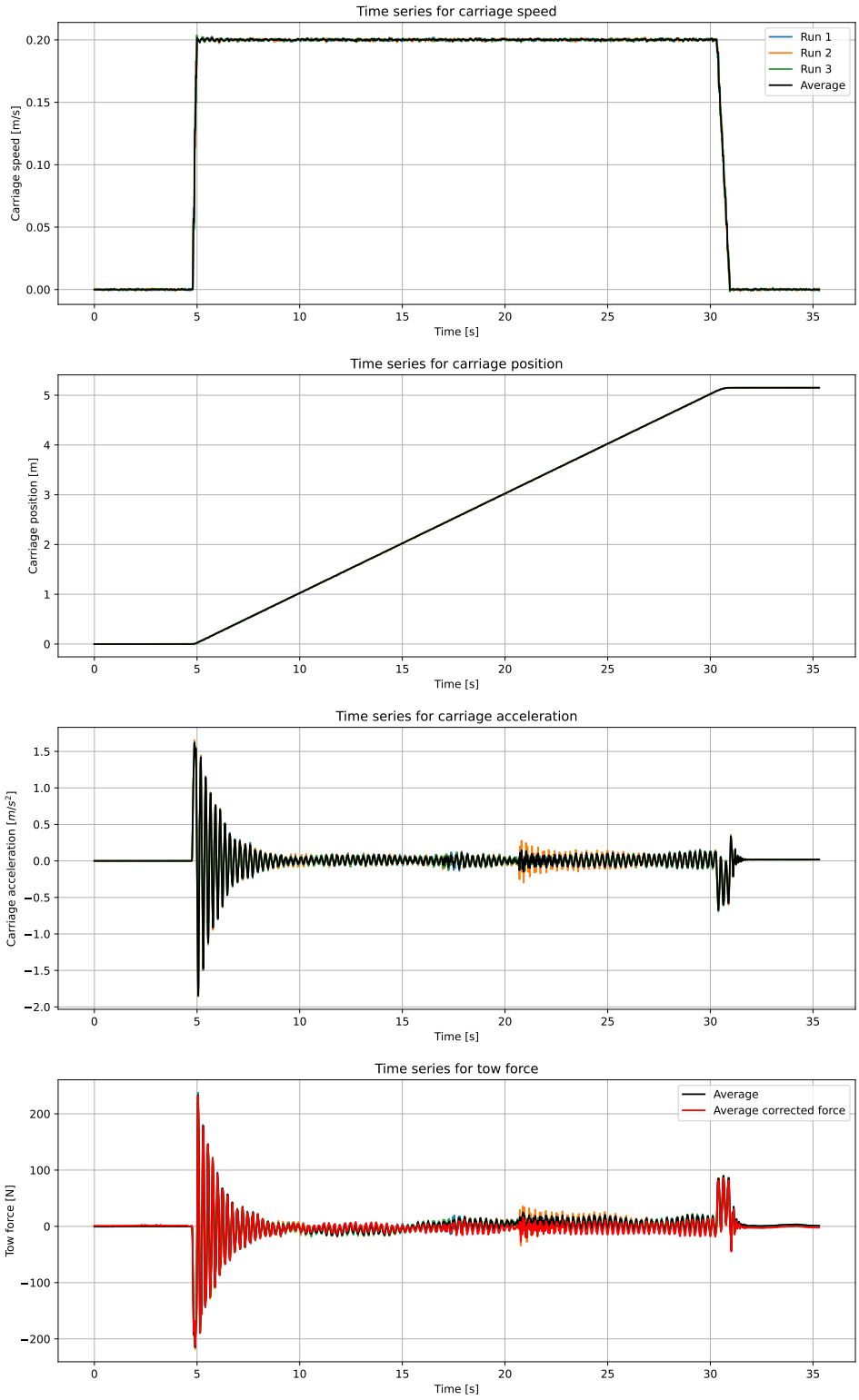

Figure B.30: Time series for model A, wet run, maximum acceleration, forward direction, speed 0.2 m/s

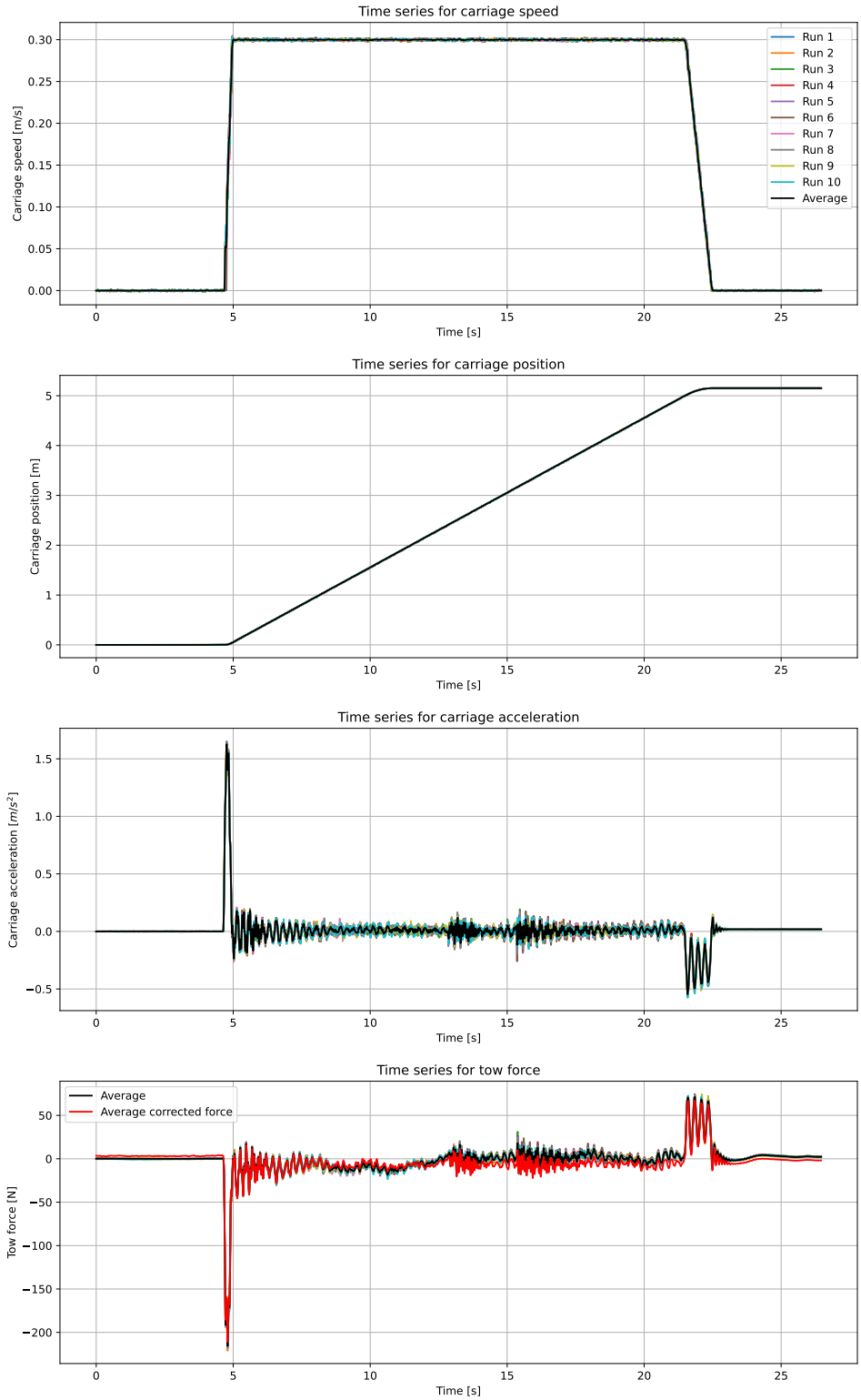

Figure B.31: Time series for model A, wet run, maximum acceleration, forward direction, speed 0.3 m/s

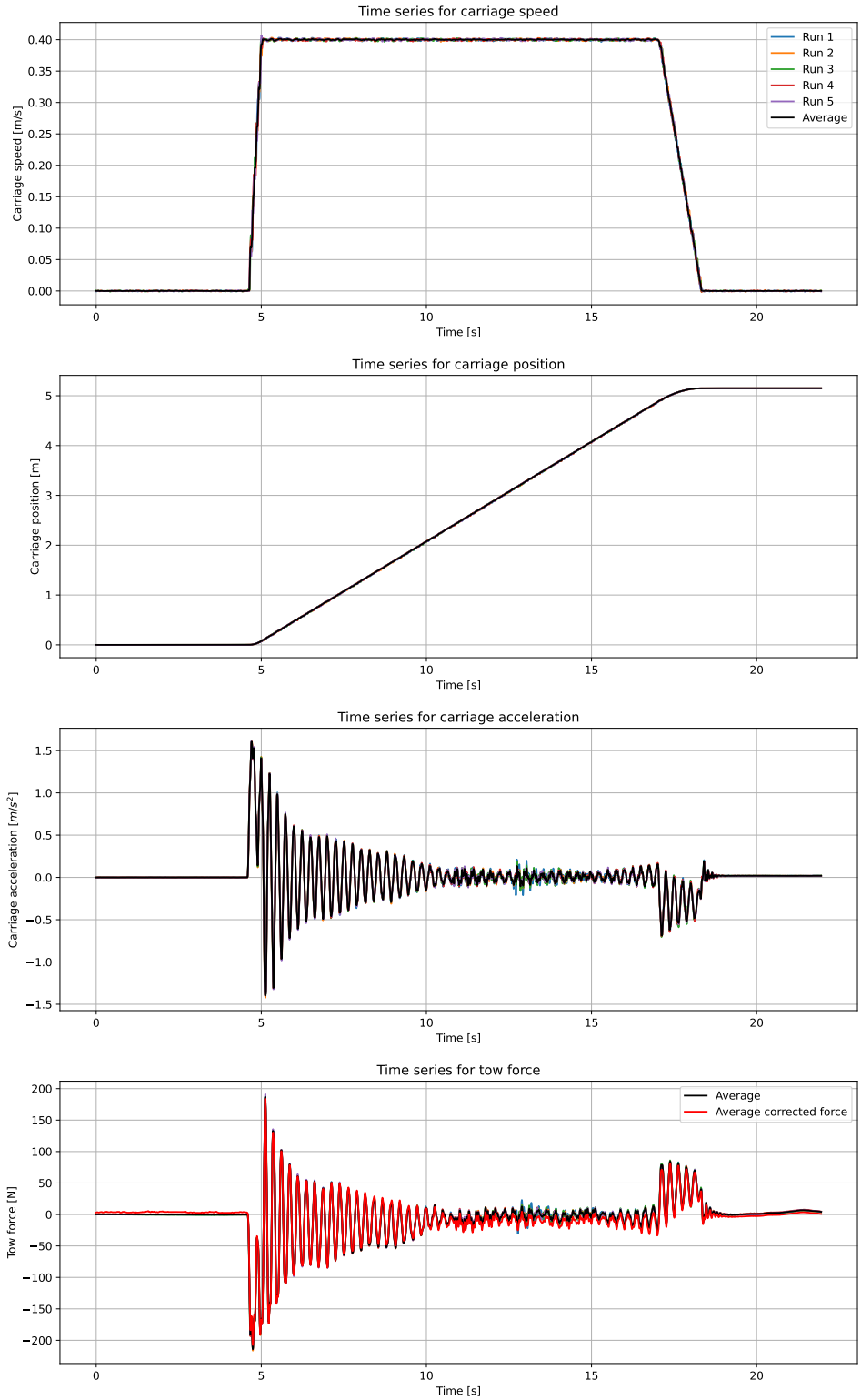

Figure B.32: Time series for model A, wet run, maximum acceleration, forward direction, speed 0.4 m/s

B.9 Wet run, model A, maximum acceleration, backward direction

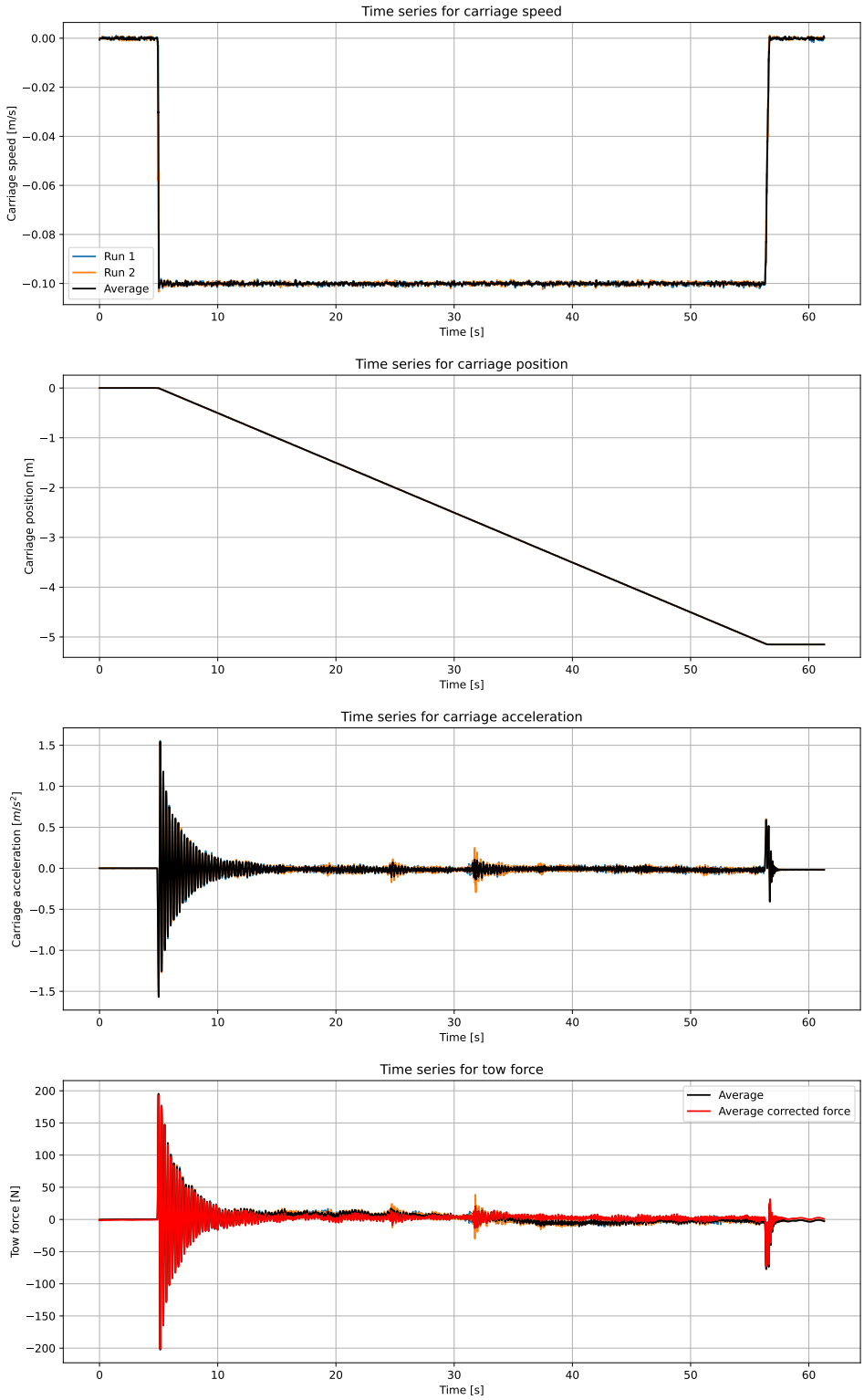

Figure B.33: Time series for model A, wet run, maximum acceleration, backward direction, speed 0.1 m/s

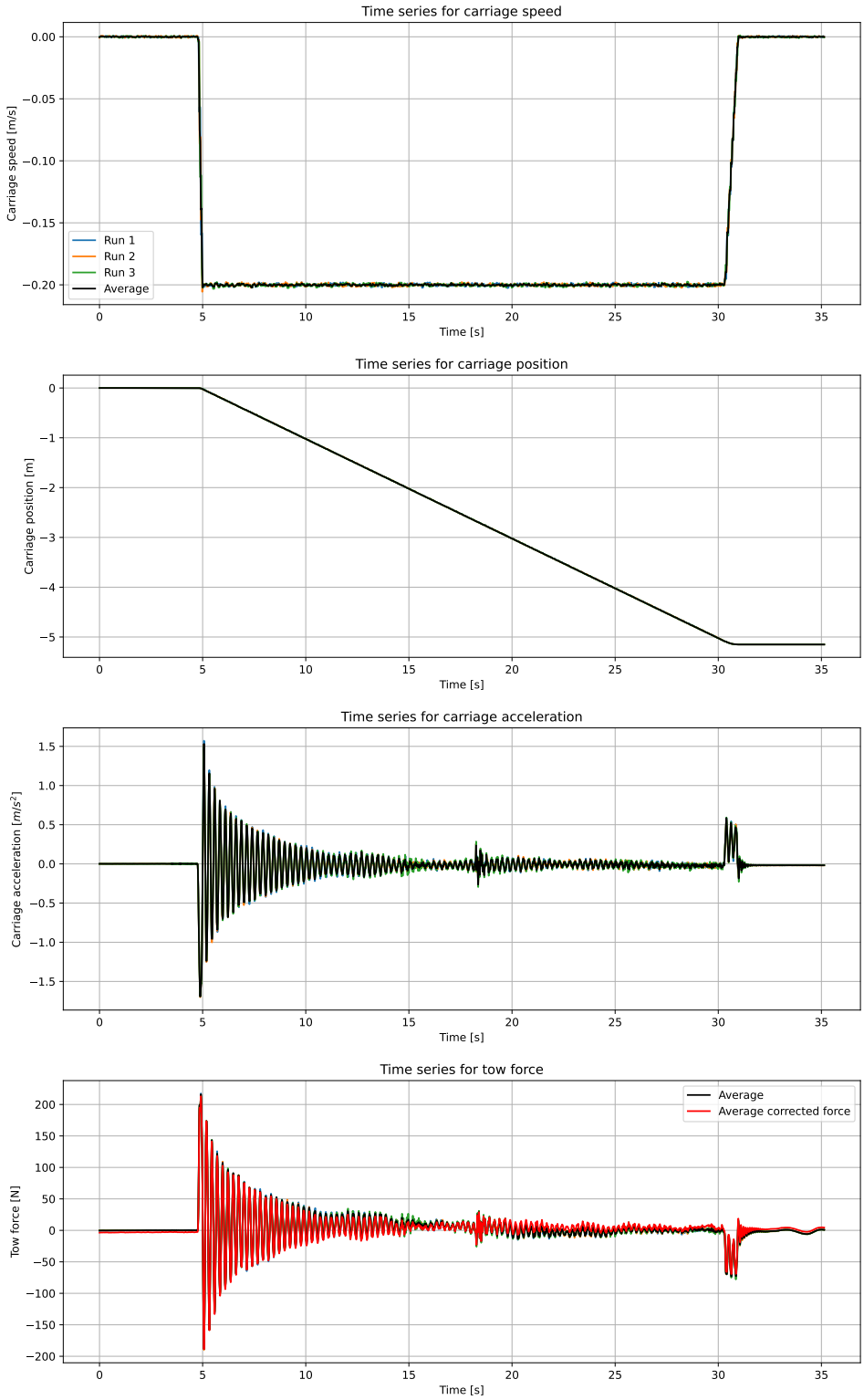

Figure B.34: Time series for model A, wet run, maximum acceleration, backward direction, speed 0.2 m/s

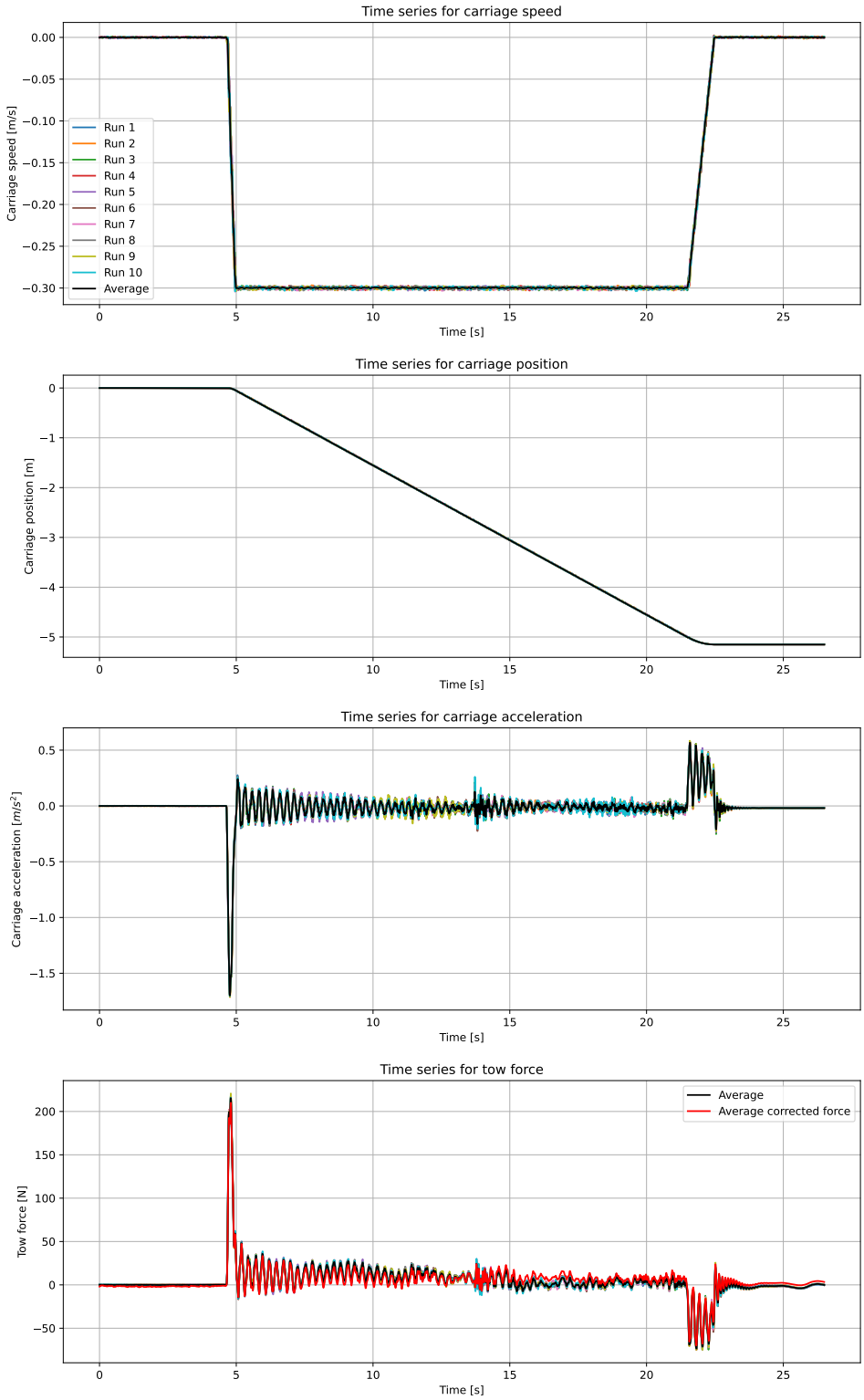

Figure B.35: Time series for model A, wet run, maximum acceleration, backward direction, speed 0.3 m/s

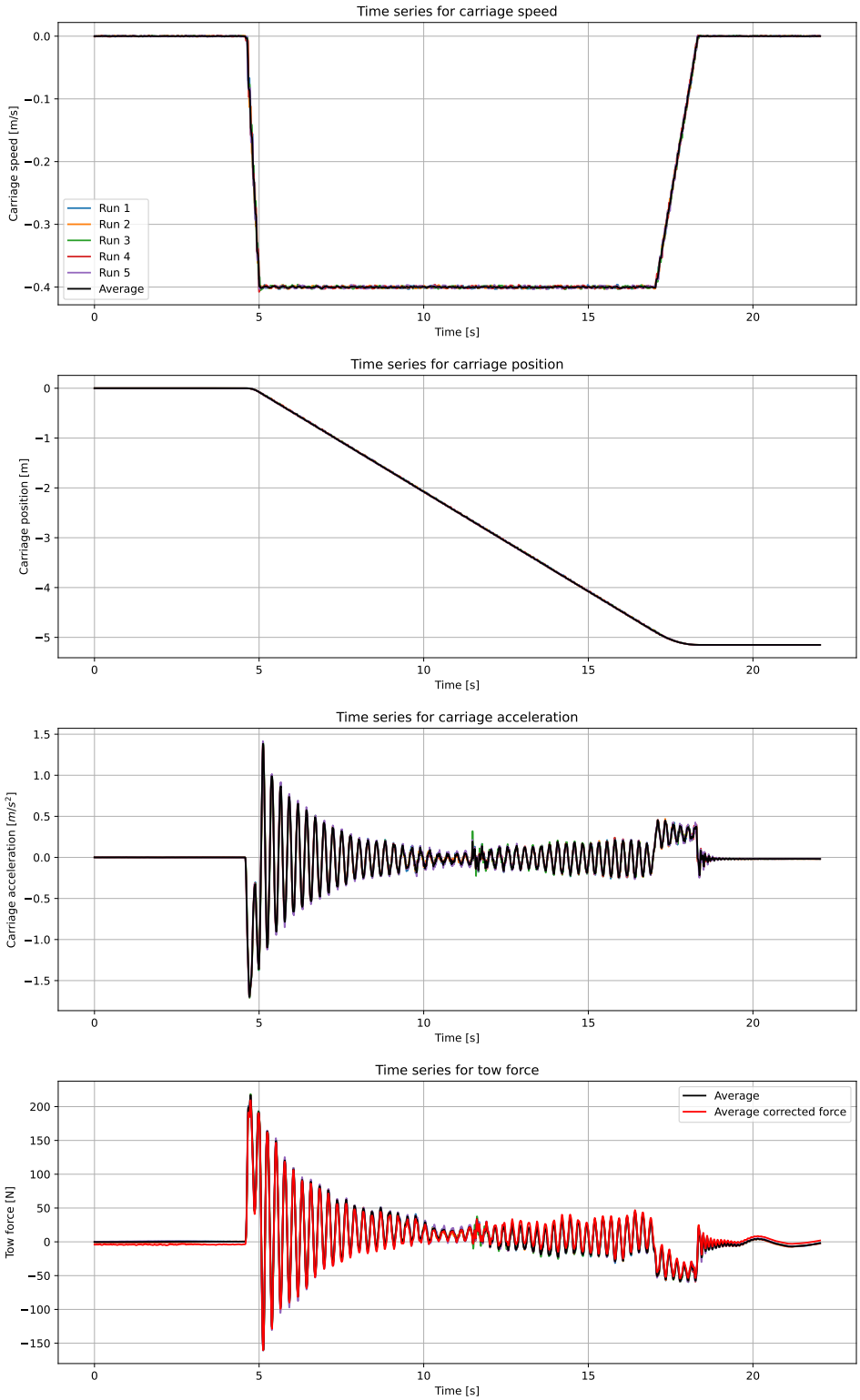

Figure B.36: Time series for model A, wet run, maximum acceleration, backward direction, speed 0.4 m/s

Appendix C

Time series plots for Model B

C.1 Dry run, model B, high acceleration, forward direction

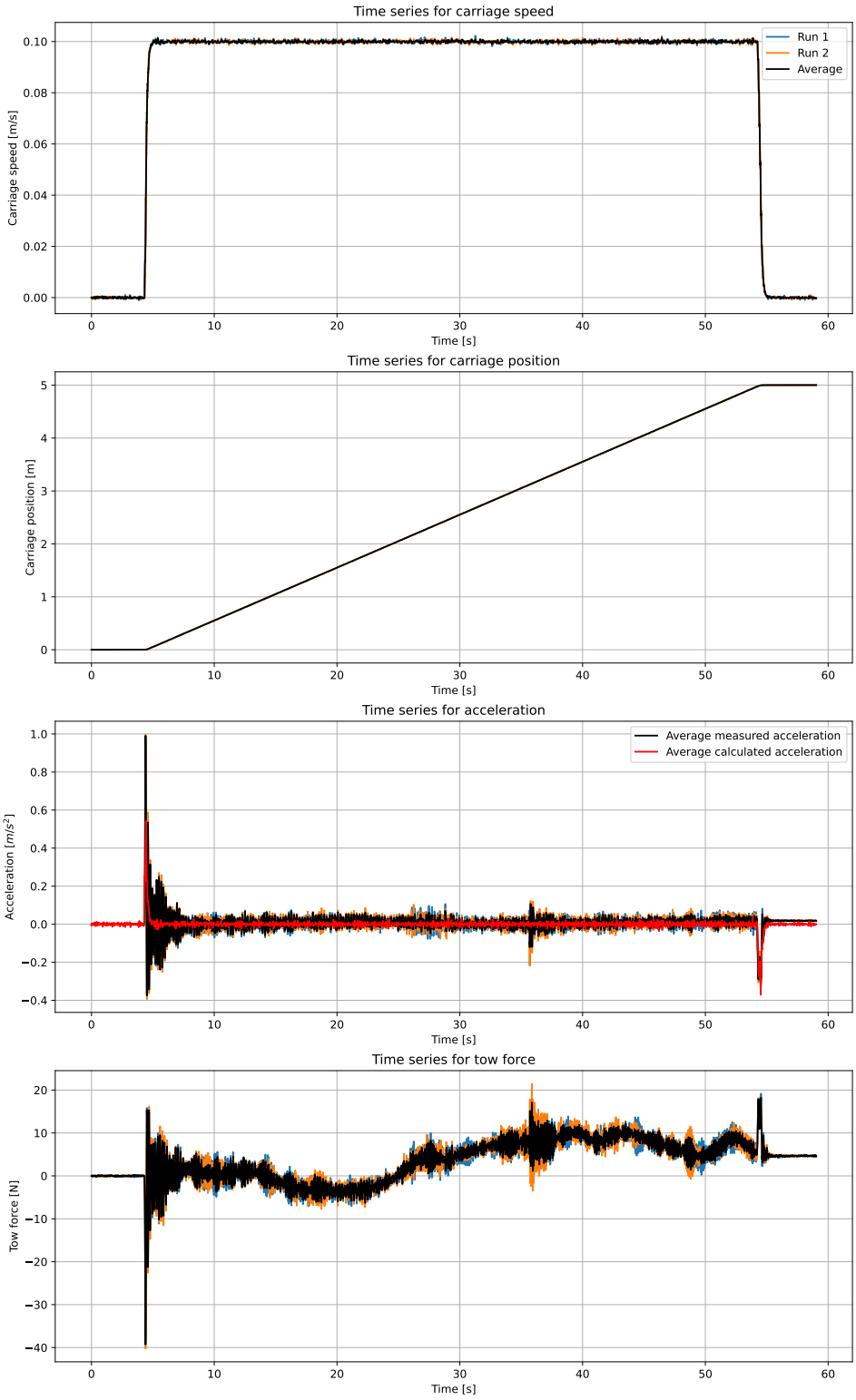

Figure C.1: Time series for model B, dry run, high acceleration, forward direction, speed 0.1 m/s

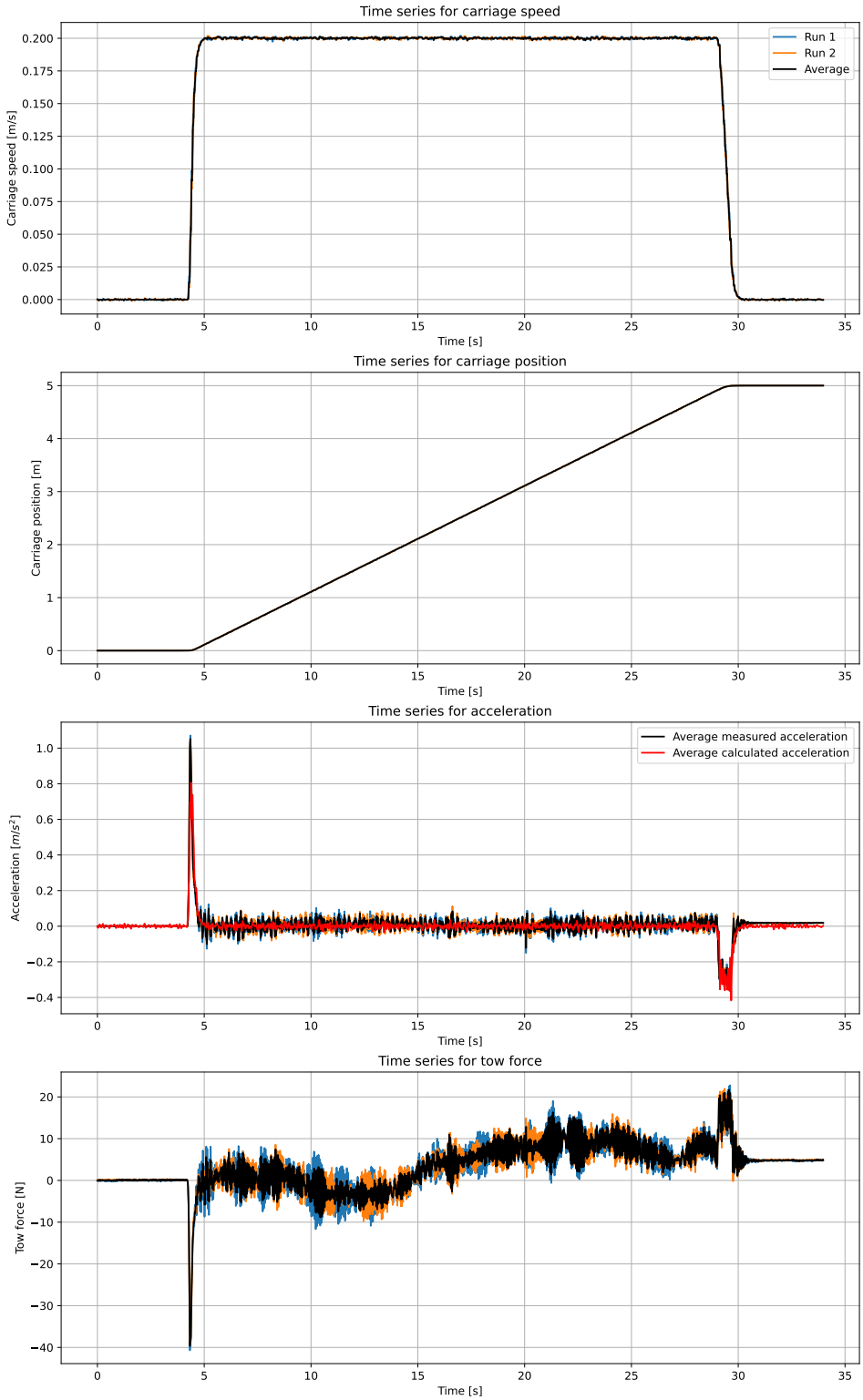

Figure C.2: Time series for model B, dry run, high acceleration, forward direction, speed 0.2 m/s

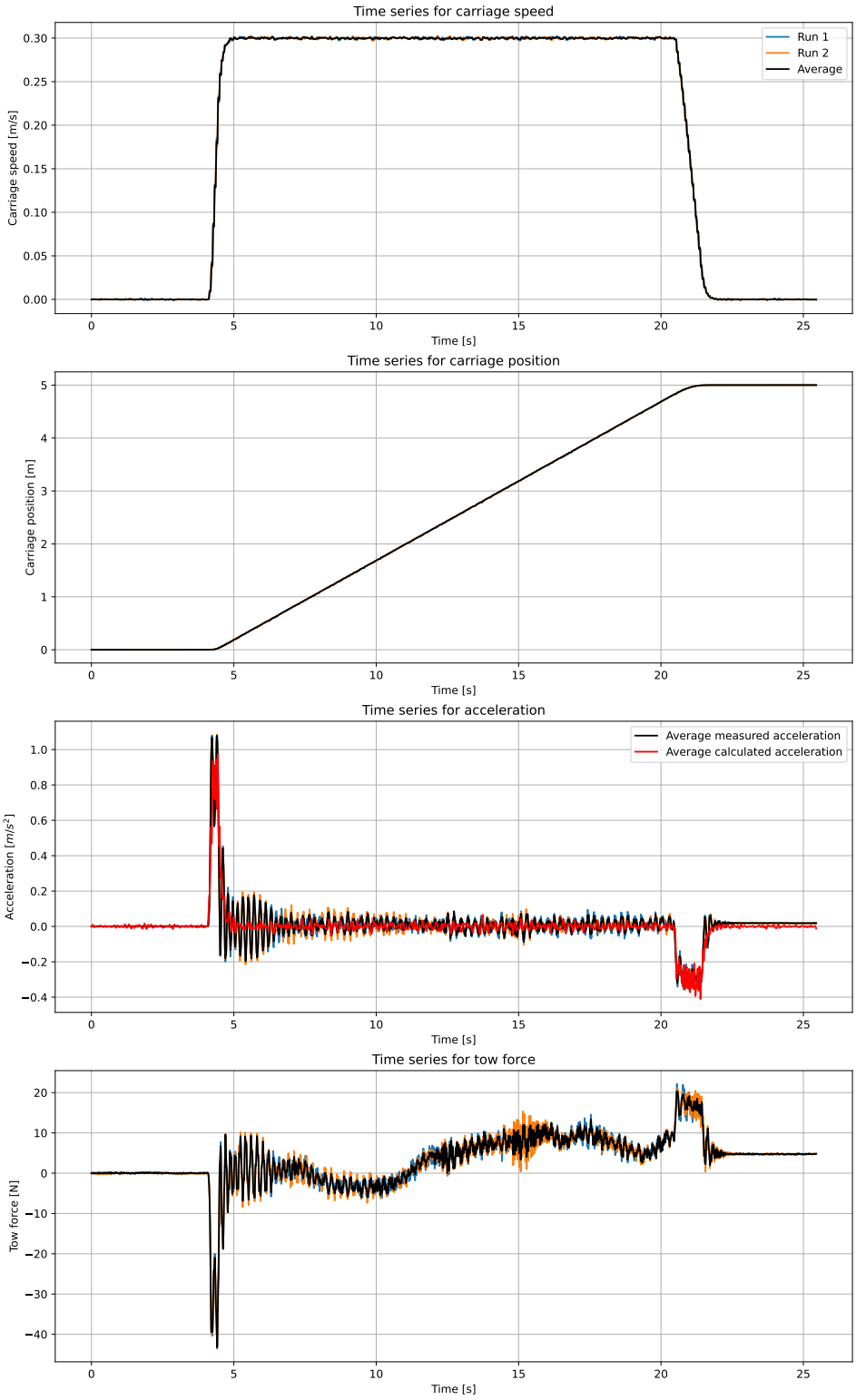

Figure C.3: Time series for model B, dry run, high acceleration, forward direction, speed 0.3 m/s

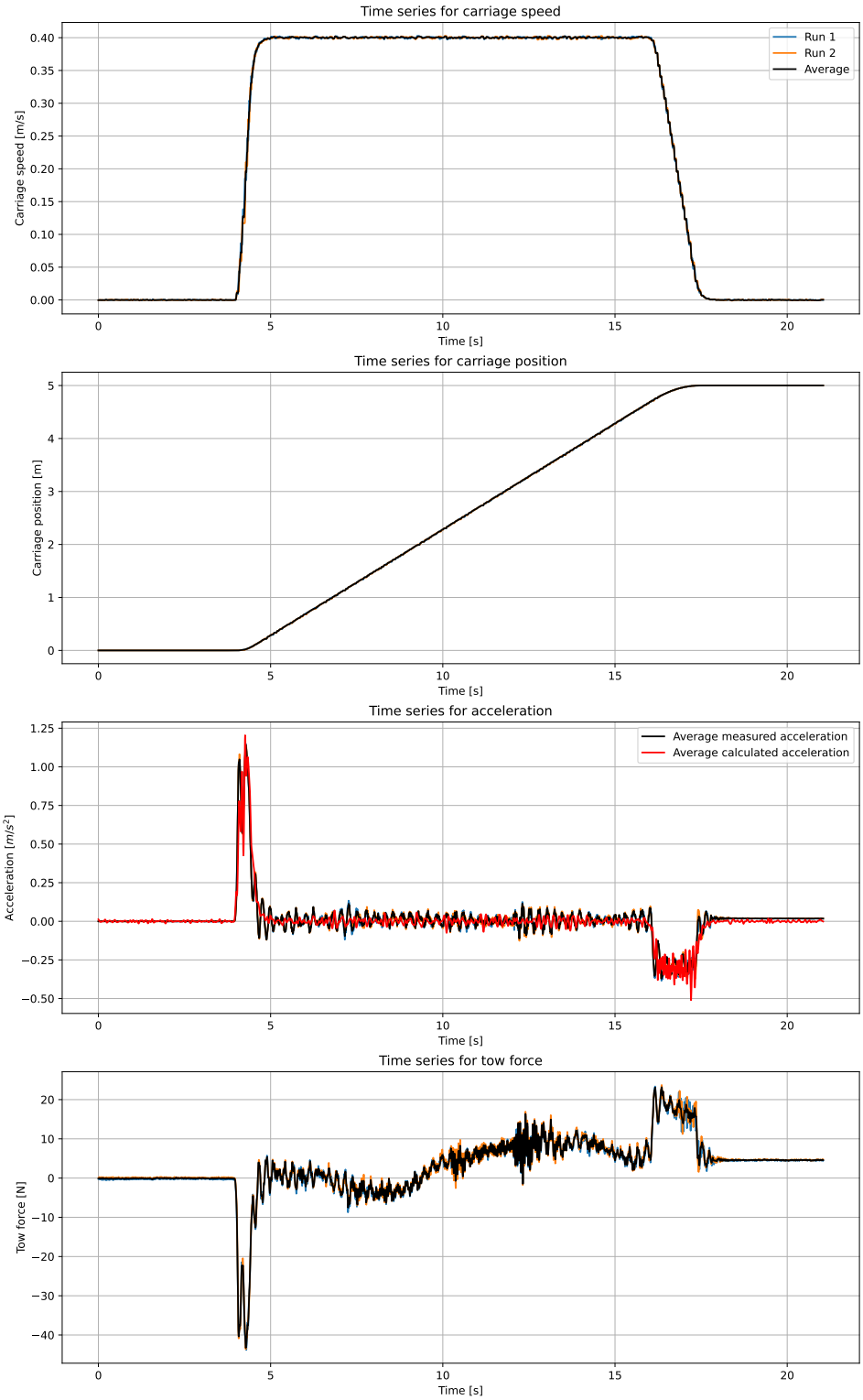

Figure C.4: Time series for model B, dry run, high acceleration, forward direction, speed 0.4 m/s

C.2 Dry run, model B, high acceleration, backward direction

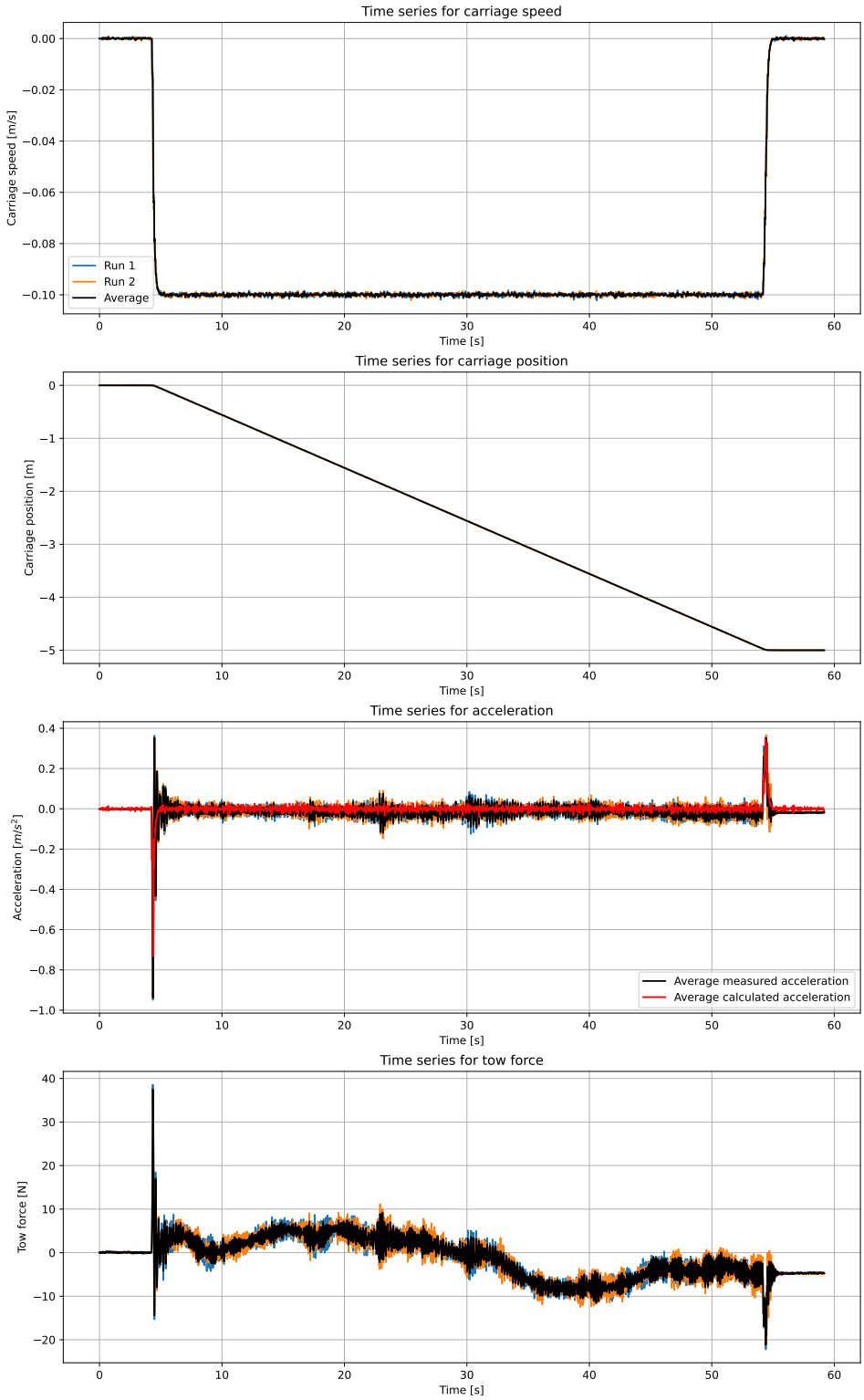

Figure C.5: Time series for model B, dry run, high acceleration, backward direction, speed 0.1 m/s

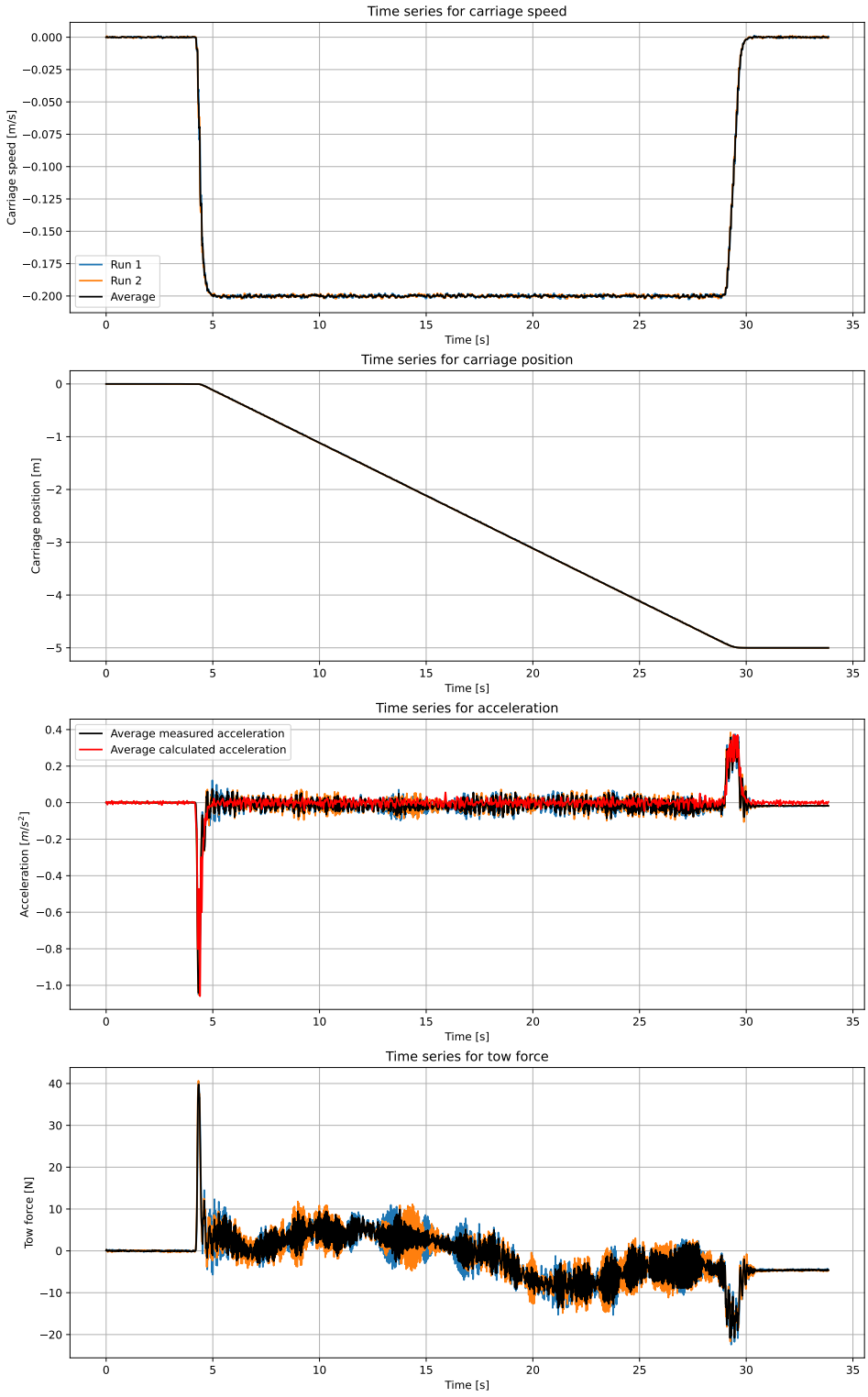

Figure C.6: Time series for model B, dry run, high acceleration, backward direction, speed 0.2 m/s

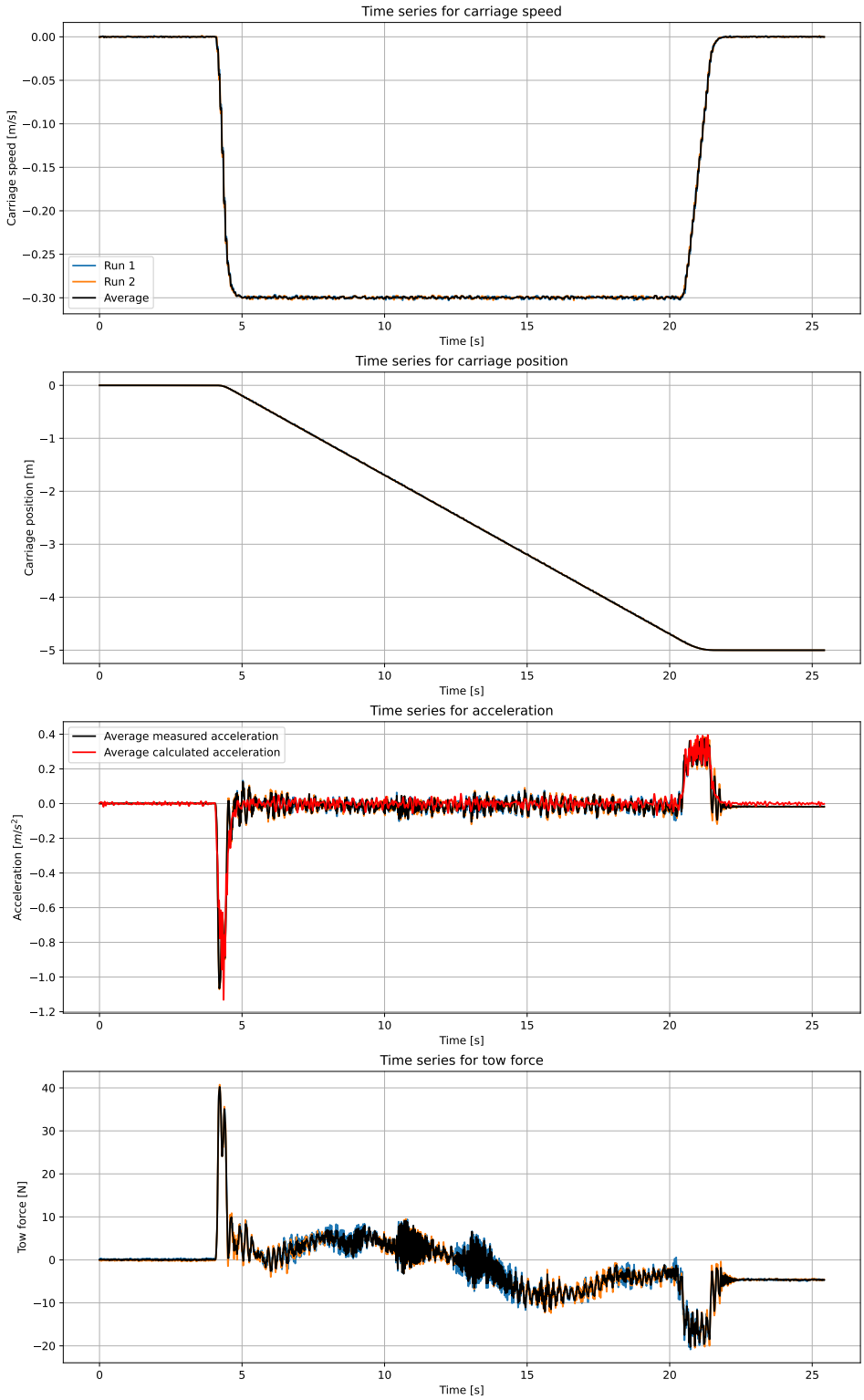

Figure C.7: Time series for model B, dry run, high acceleration, backward direction, speed 0.3 m/s

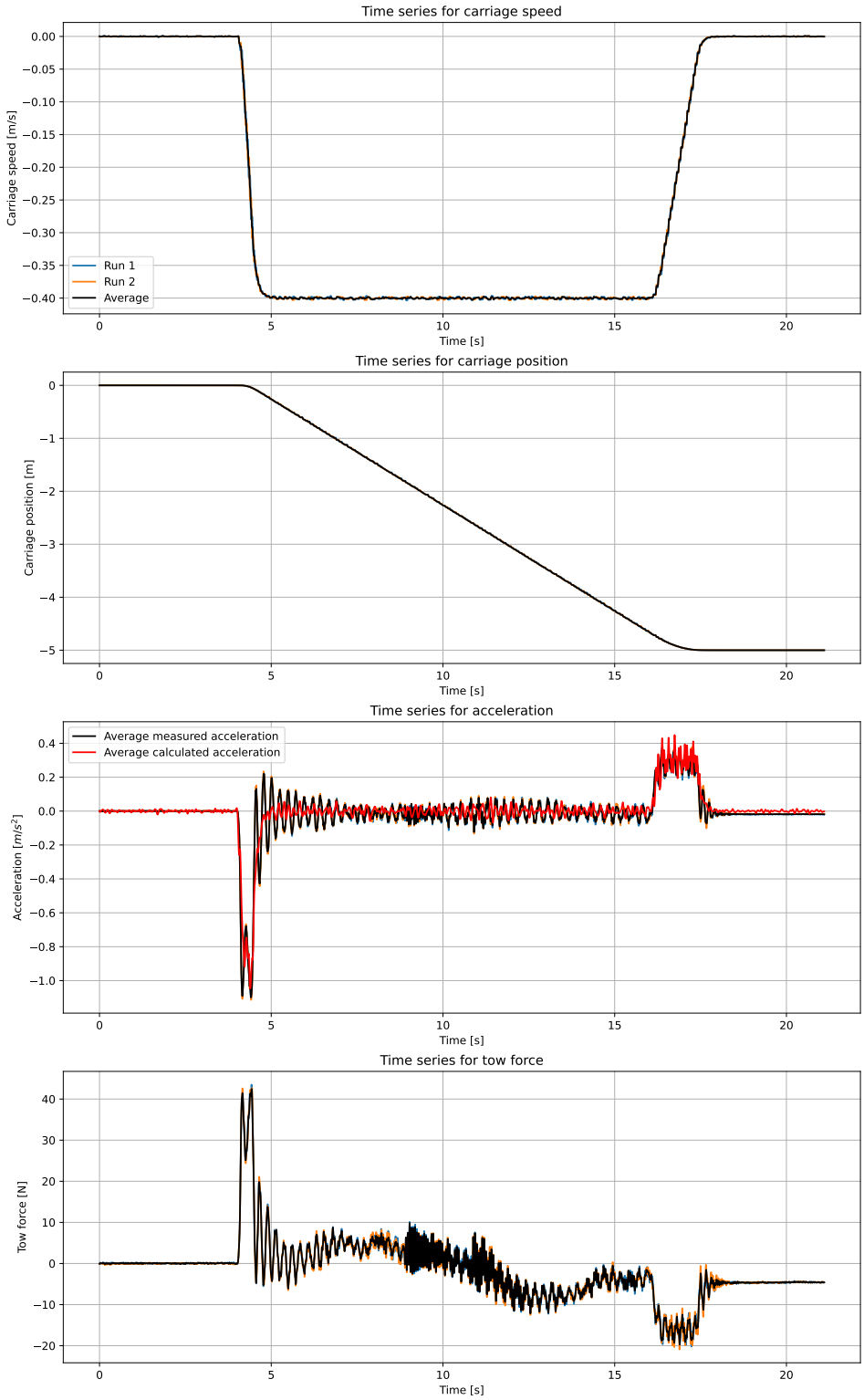

Figure C.8: Time series for model B, dry run, high acceleration, backward direction, speed 0.4 m/s

C.3 Dry run, model B, low acceleration, forward direction

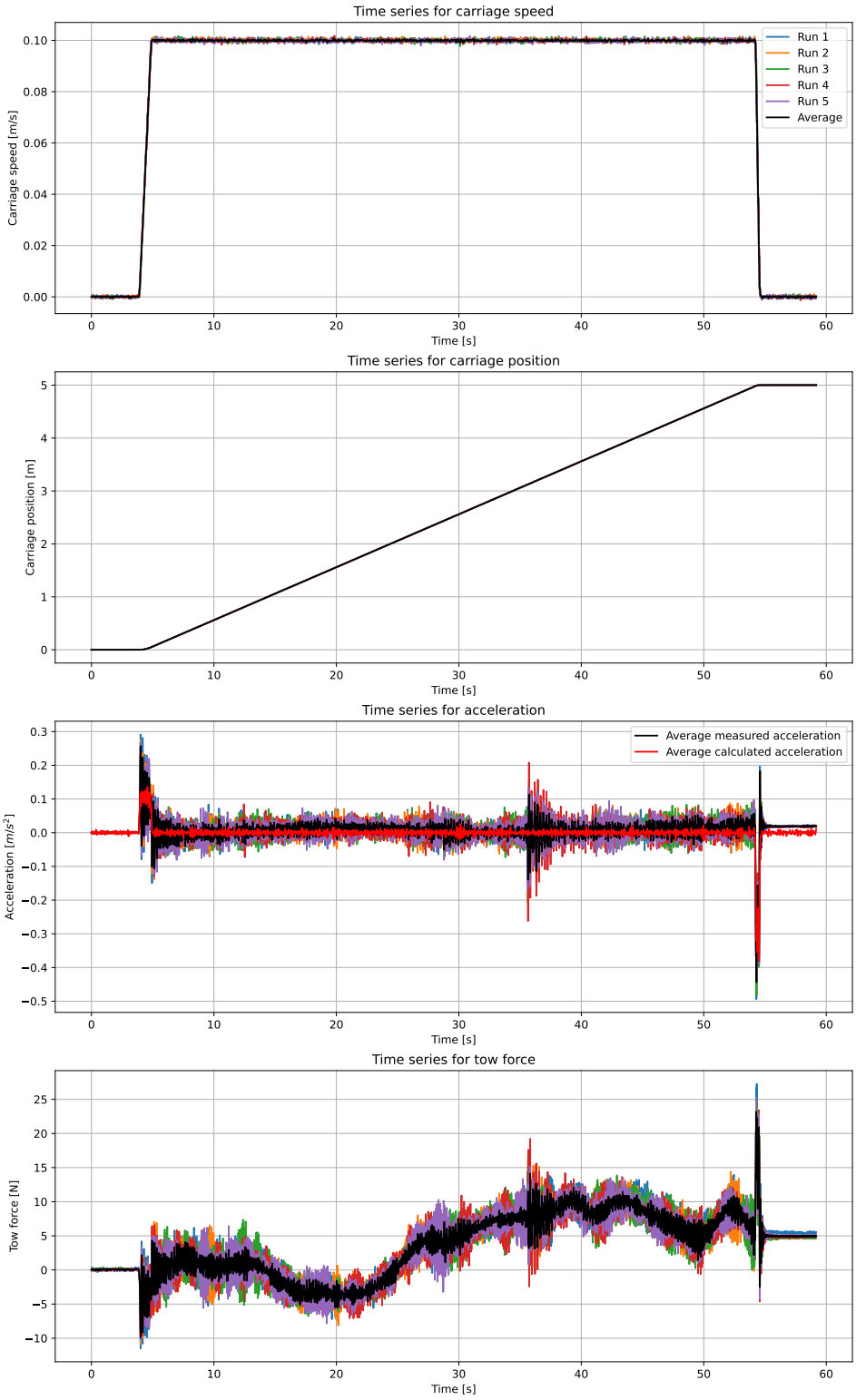

Figure C.9: Time series for model B, dry run, low acceleration, forward direction, speed 0.1 m/s

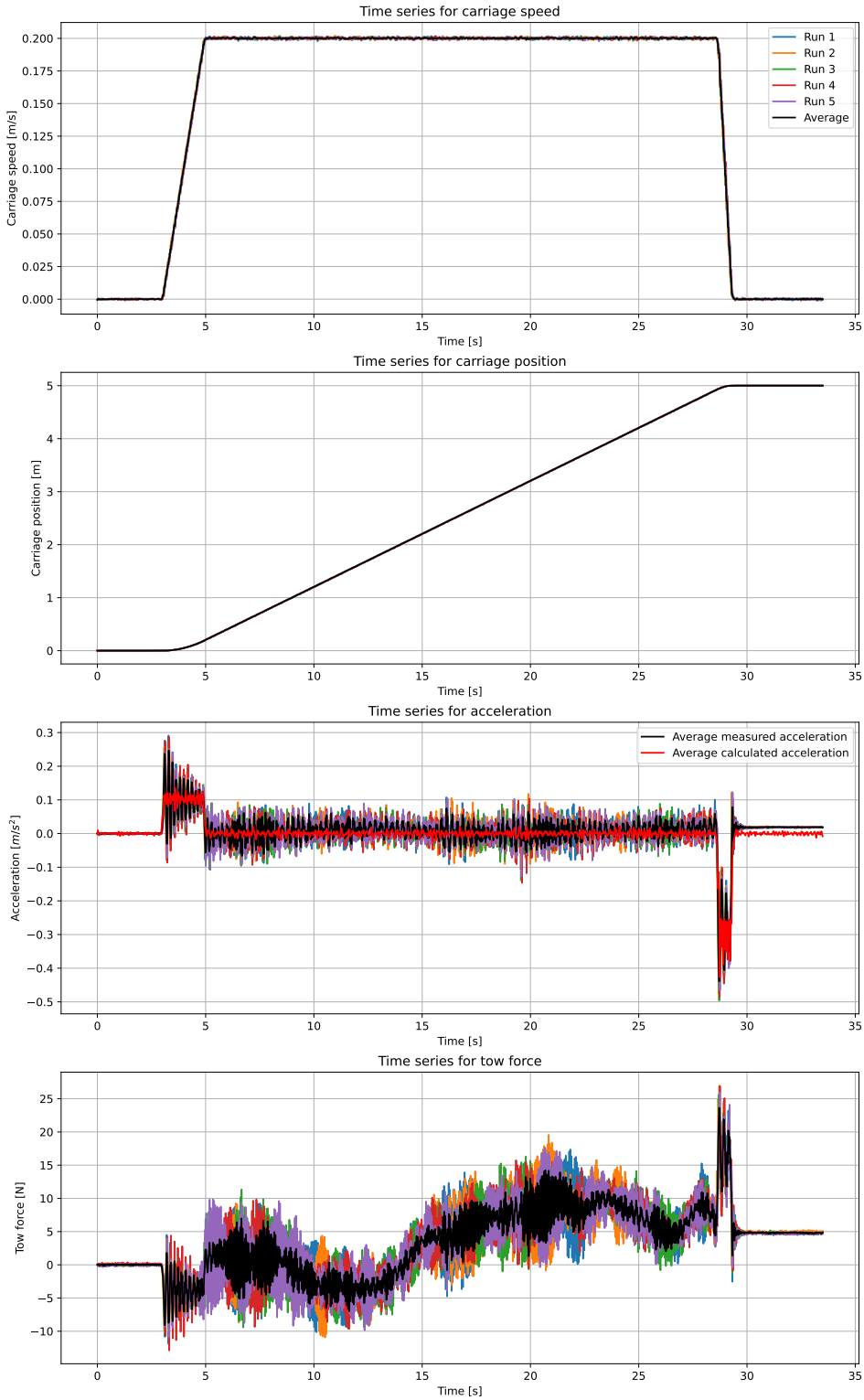

Figure C.10: Time series for model B, dry run, low acceleration, forward direction, speed 0.2 m/s

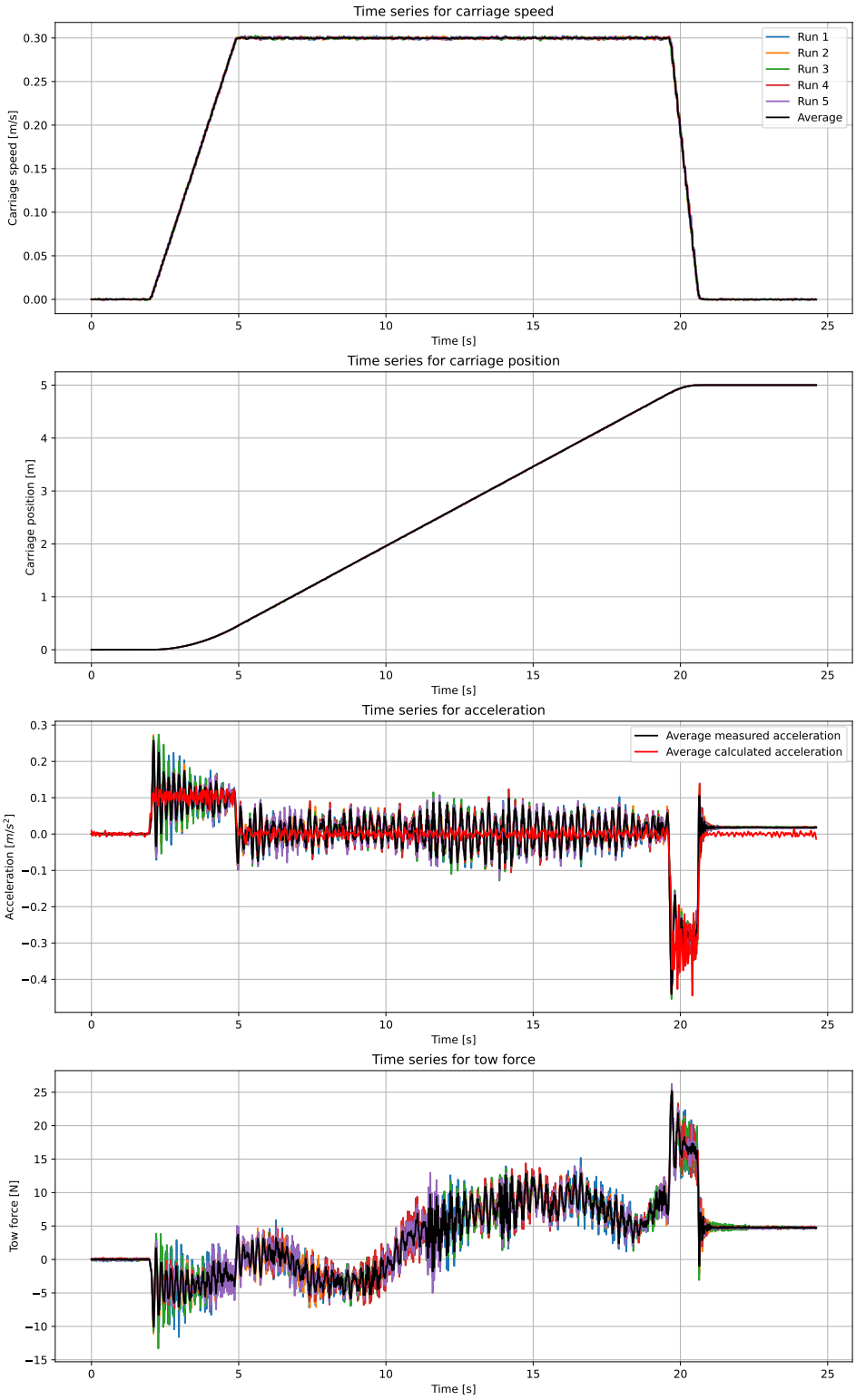

Figure C.11: Time series for model B, dry run, low acceleration, forward direction, speed 0.3 m/s

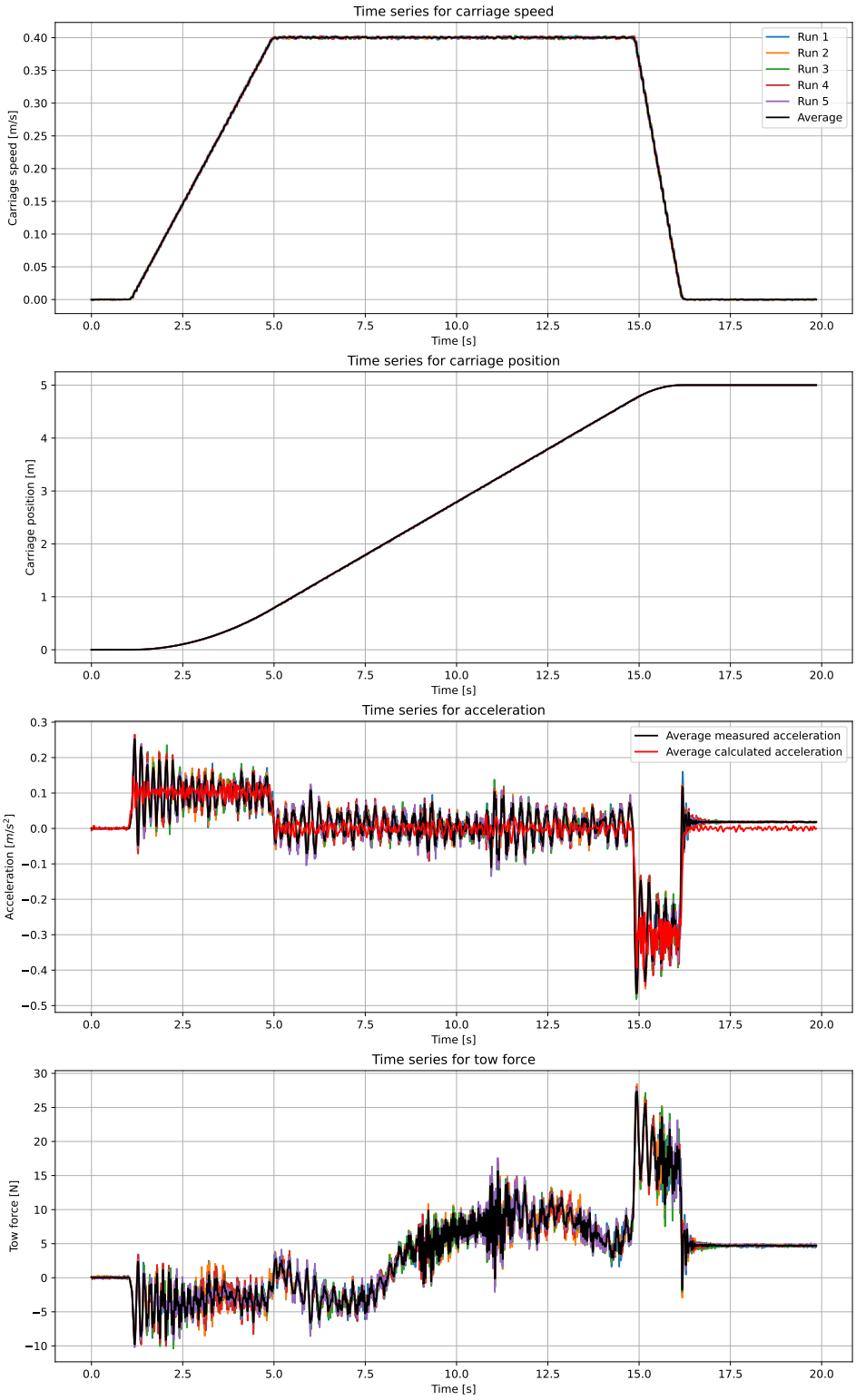

Figure C.12: Time series for model B, dry run, low acceleration, forward direction, speed 0.4 m/s

C.4 Dry run, model B, low acceleration, backward direction

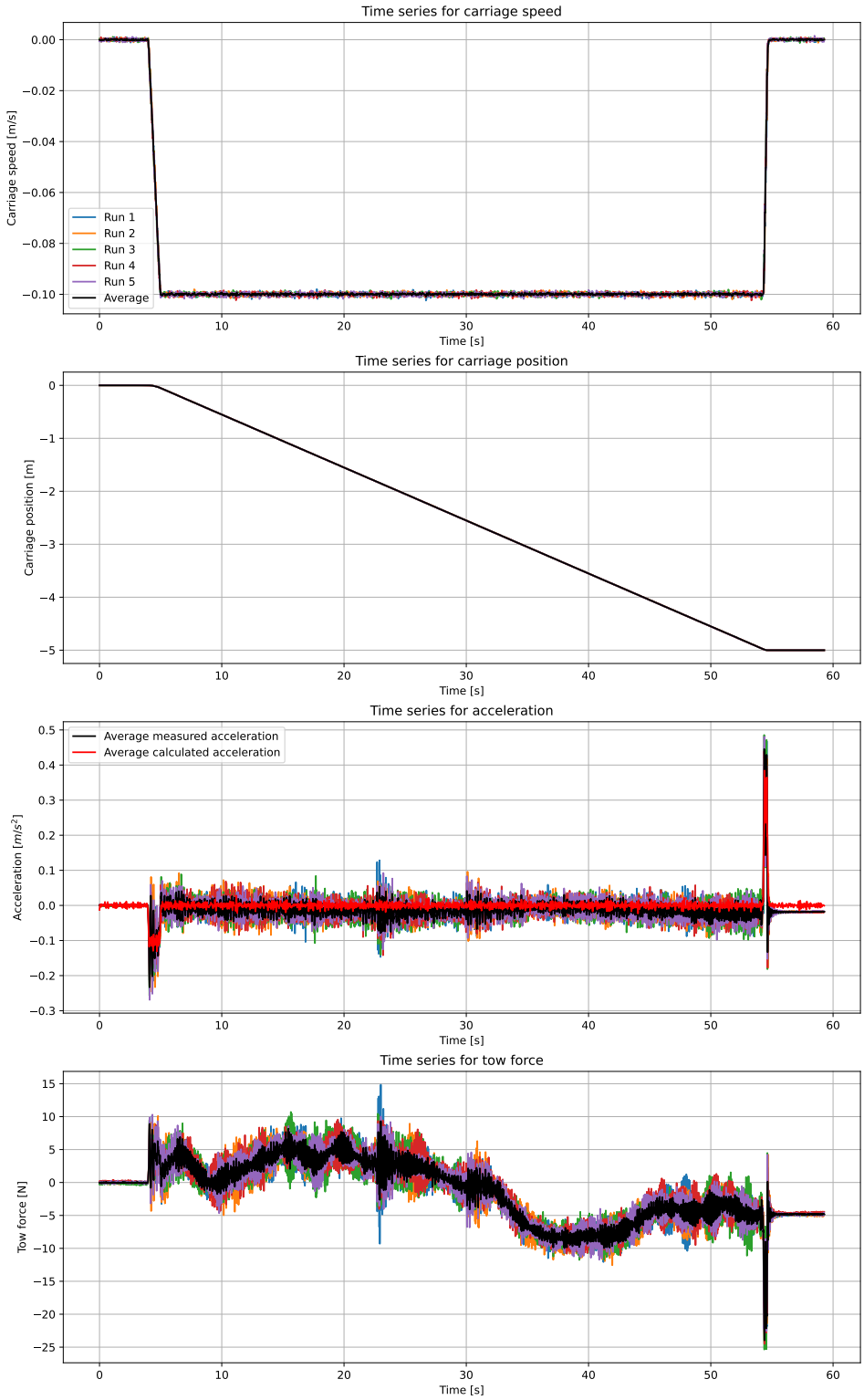

Figure C.13: Time series for model B, dry run, low acceleration, backward direction, speed 0.1 m/s

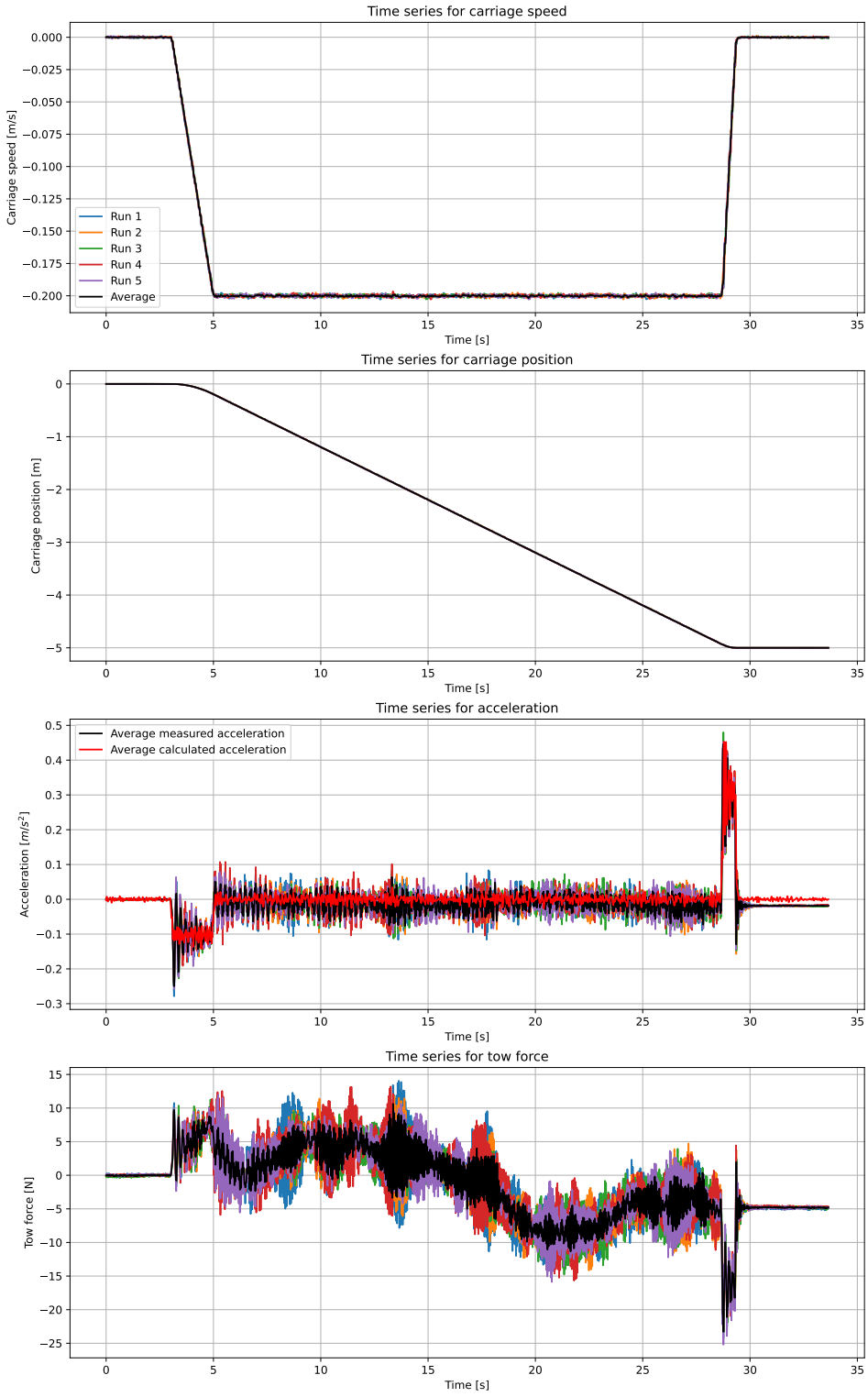

Figure C.14: Time series for model B, dry run, low acceleration, backward direction, speed 0.2 m/s

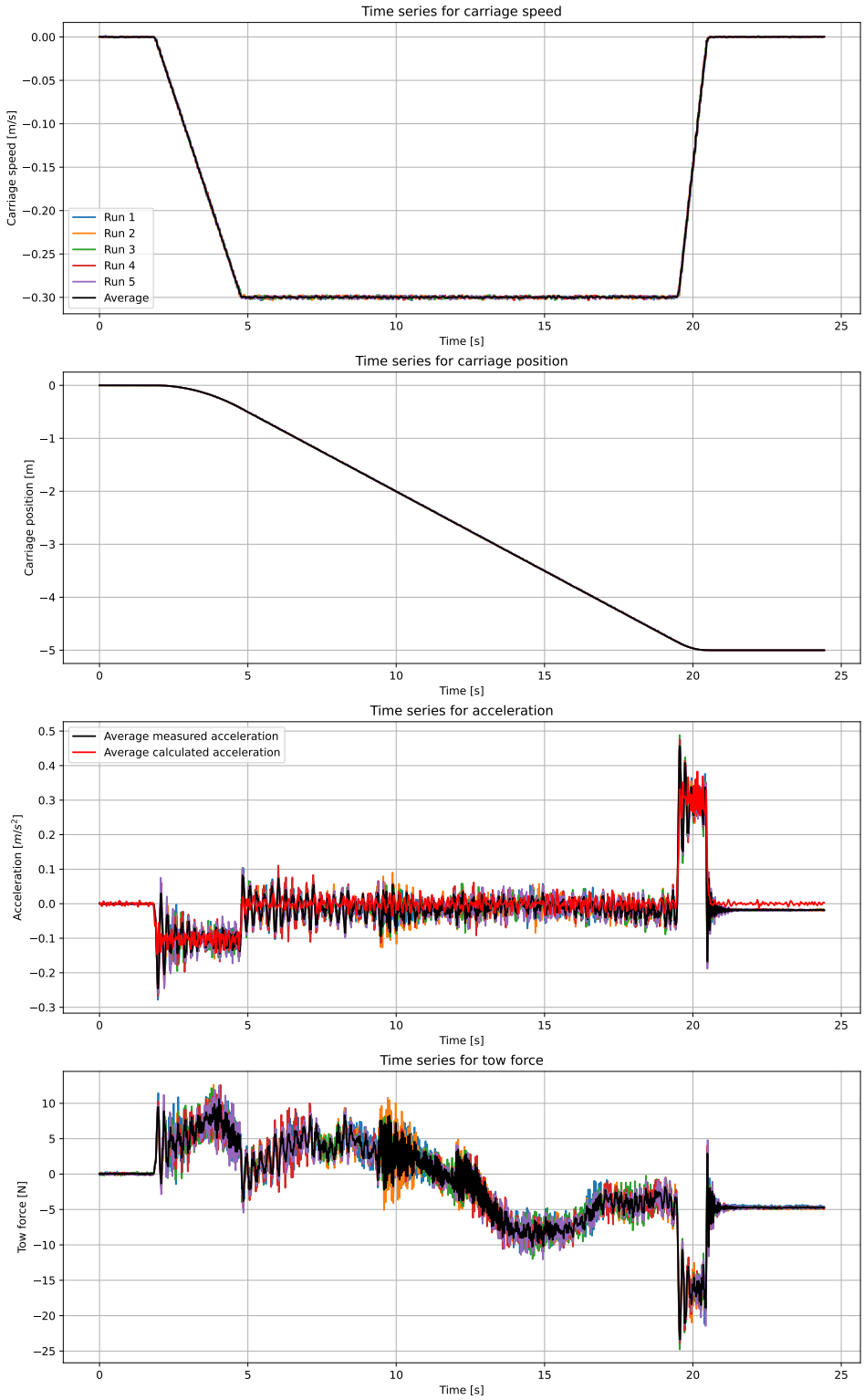

Figure C.15: Time series for model B, dry run, low acceleration, backward direction, speed 0.3 m/s

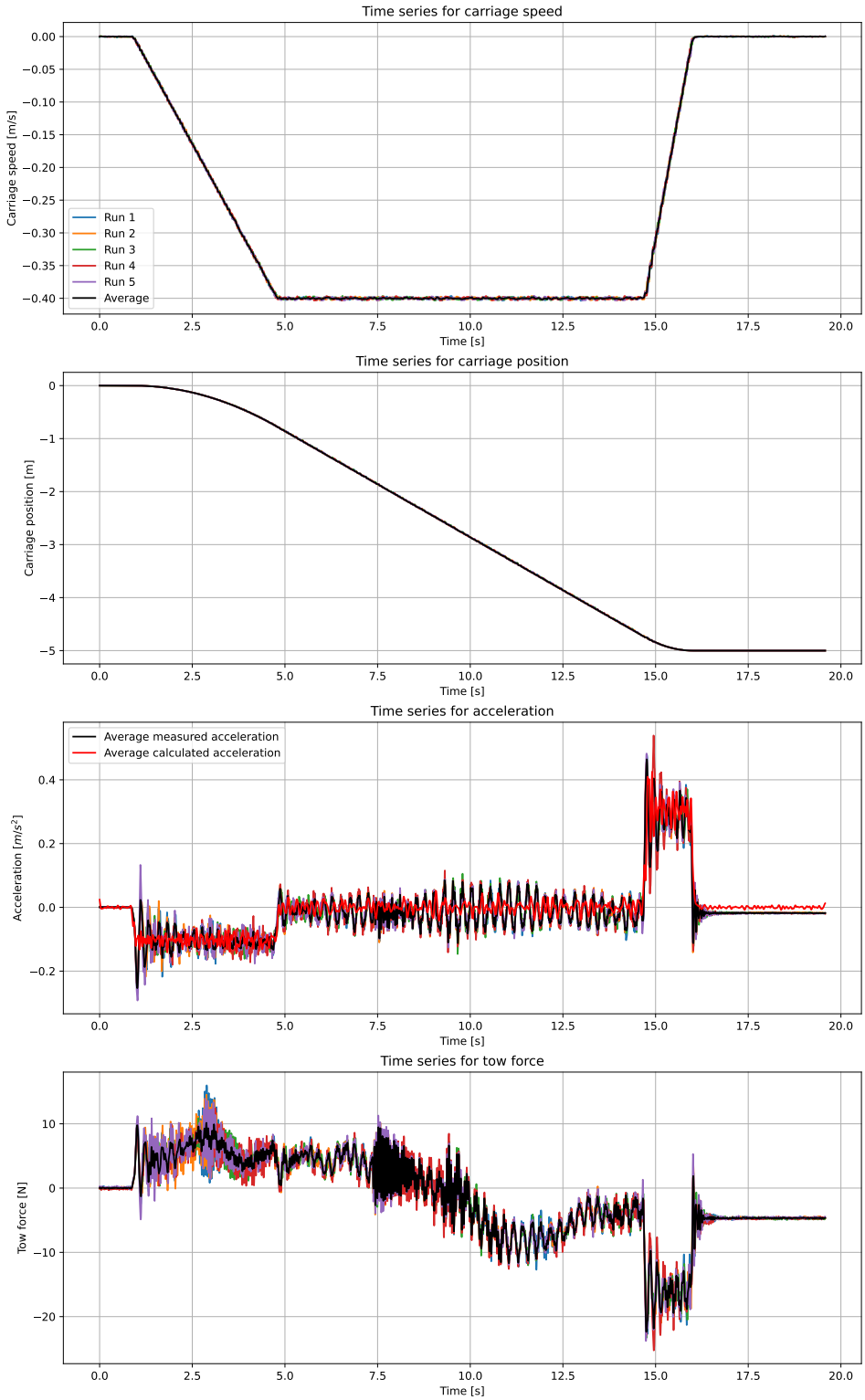

Figure C.16: Time series for model B, dry run, low acceleration, backward direction, speed 0.4 m/s

C.5 Wet run, model B, high acceleration, forward direction

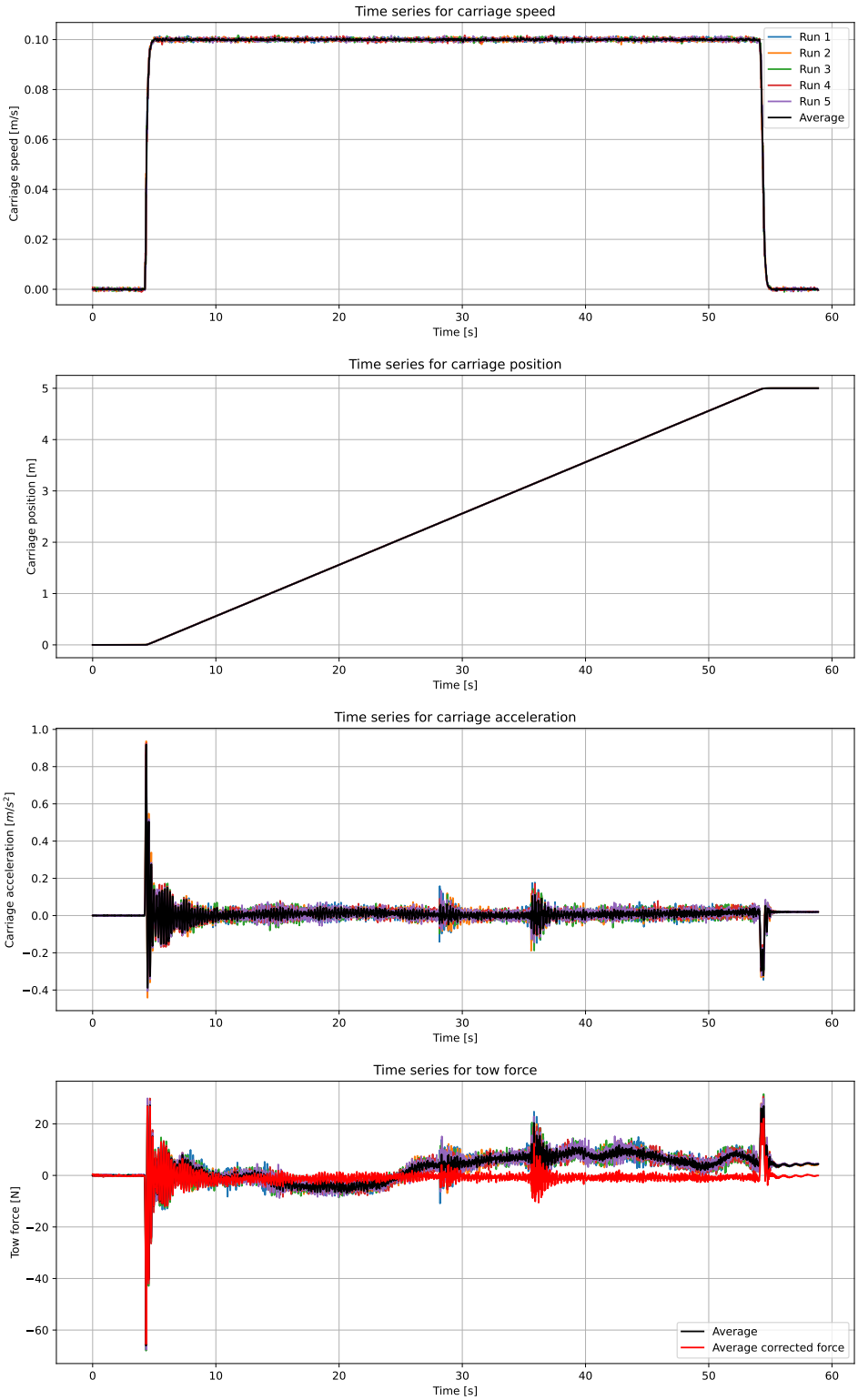

Figure C.17: Time series for model B, wet run, high acceleration, forward direction, speed 0.1 m/s

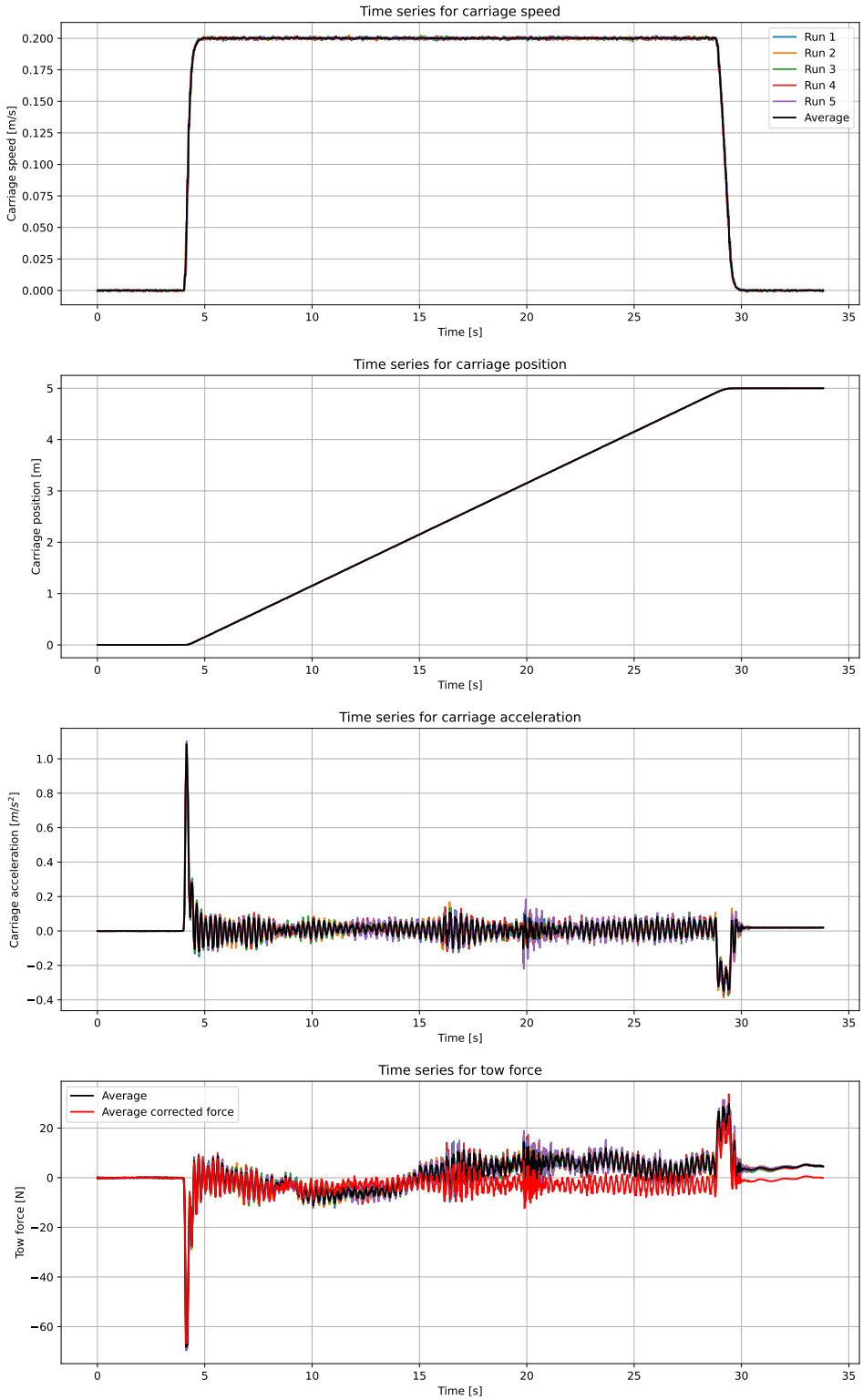

Figure C.18: Time series for model B, wet run, high acceleration, forward direction, speed 0.2 m/s

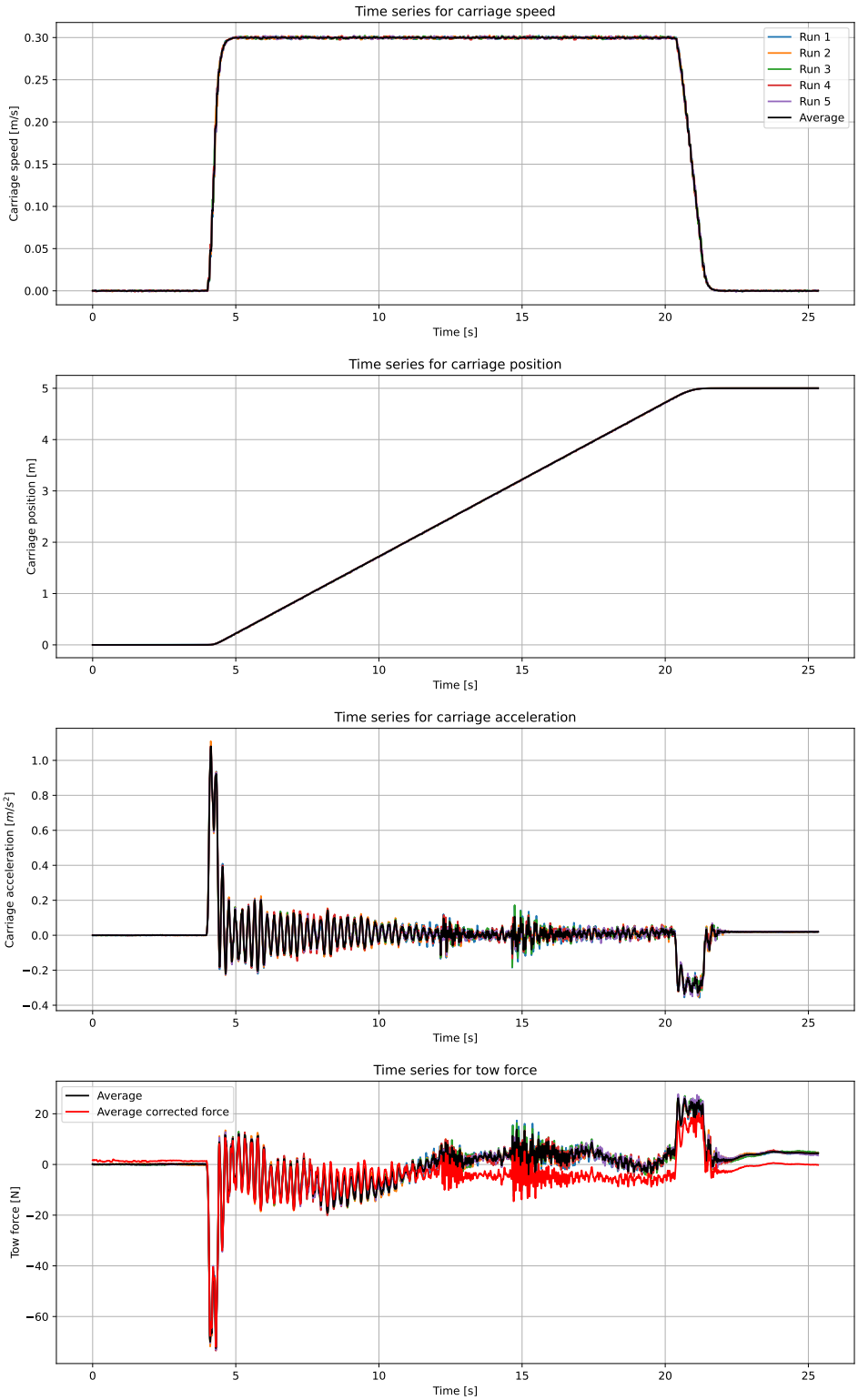

Figure C.19: Time series for model B, wet run, high acceleration, forward direction, speed 0.3 m/s

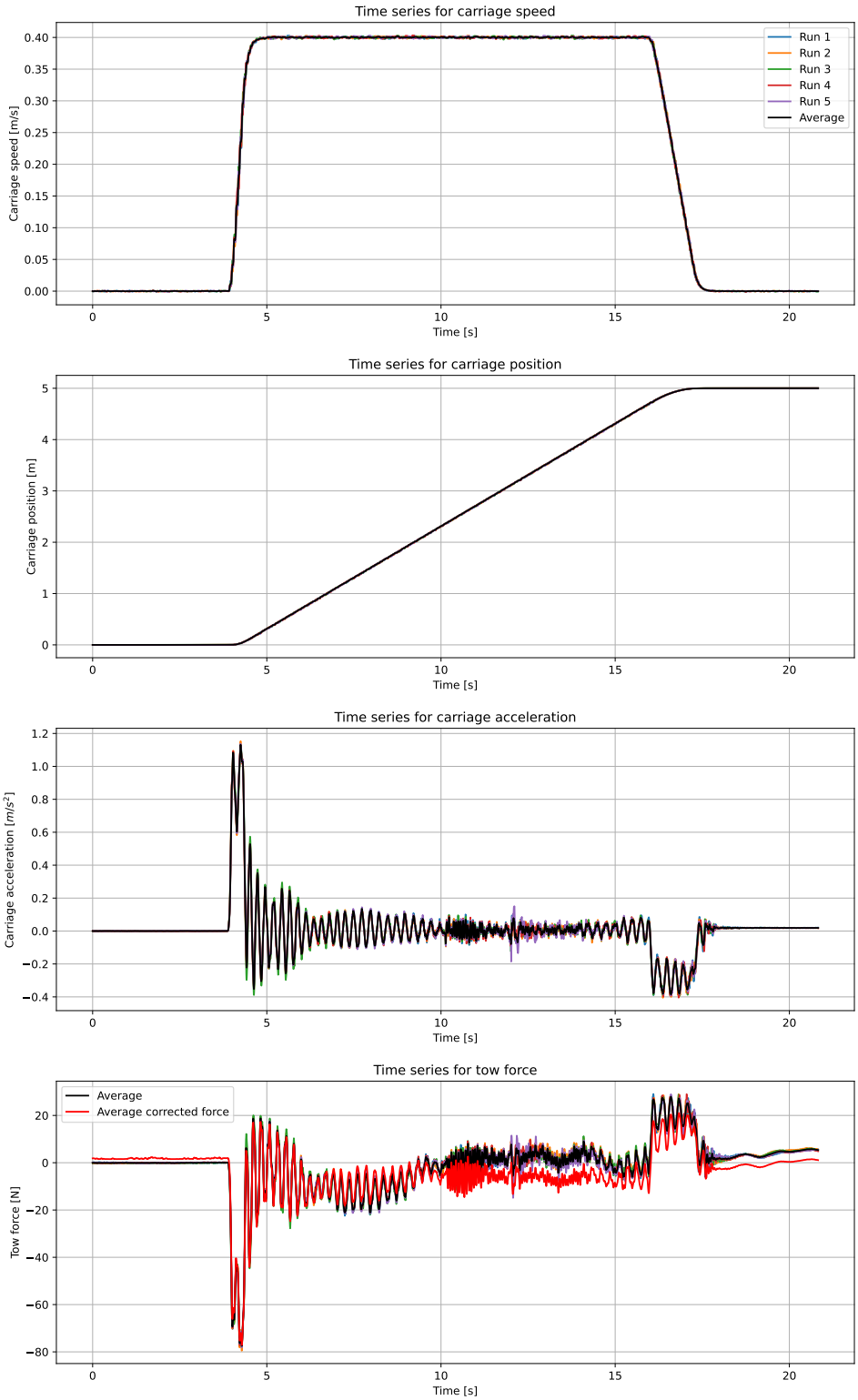

Figure C.20: Time series for model B, wet run, high acceleration, forward direction, speed 0.4 m/s

C.6 Wet run, model B, high acceleration, backward direction

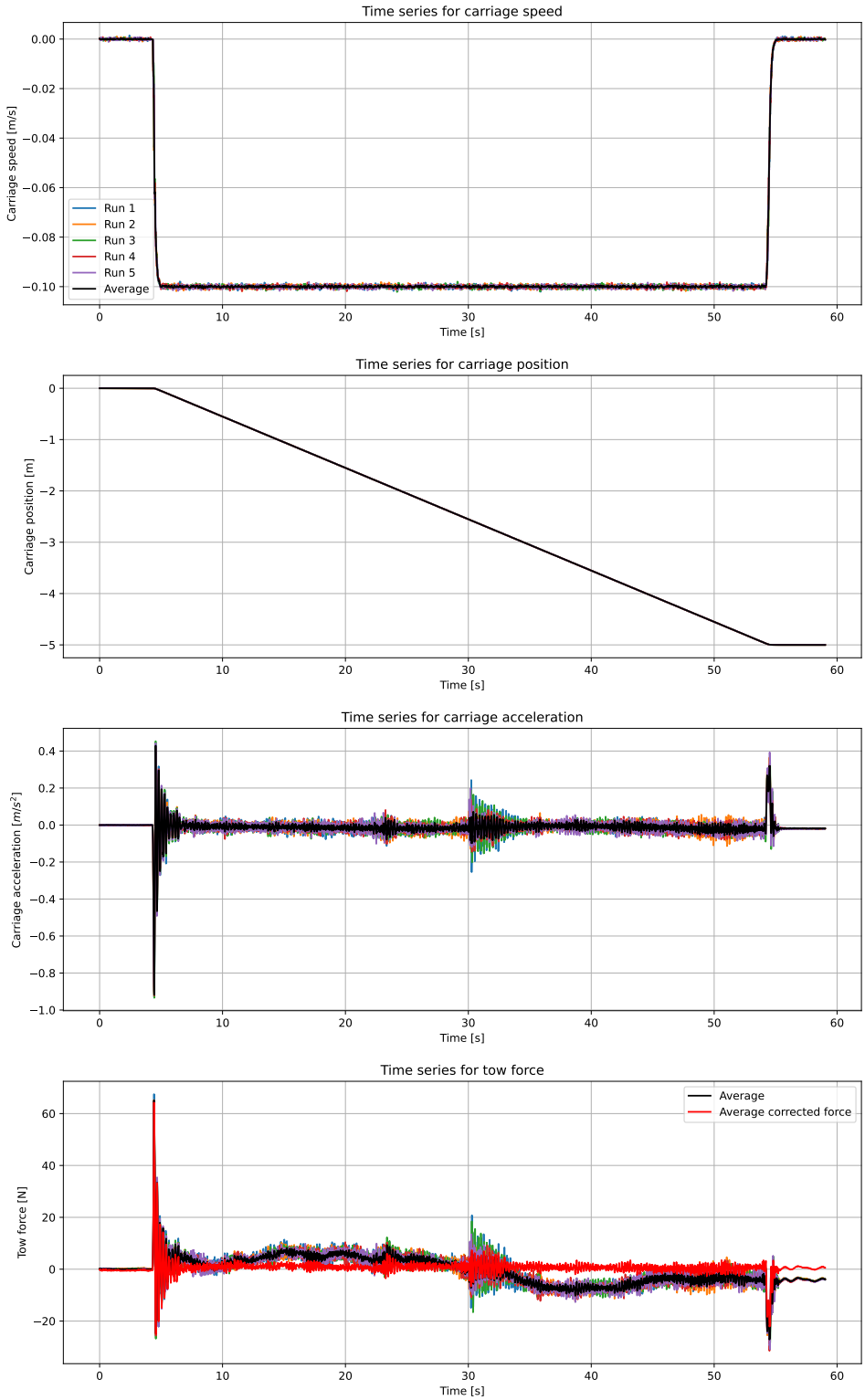

Figure C.21: Time series for model B, wet run, high acceleration, backward direction, speed 0.1 m/s

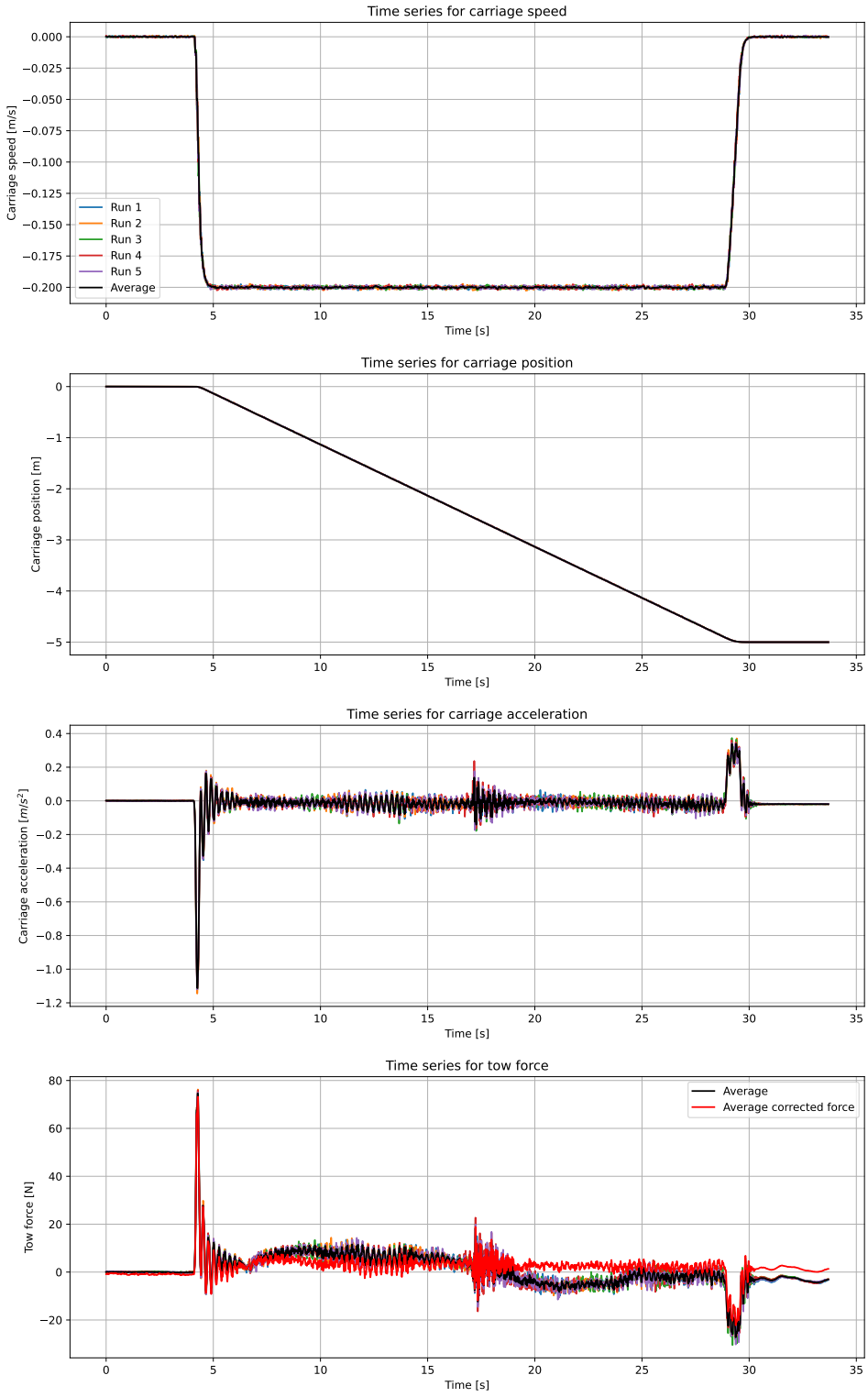

Figure C.22: Time series for model B, wet run, high acceleration, backward direction, speed 0.2 m/s

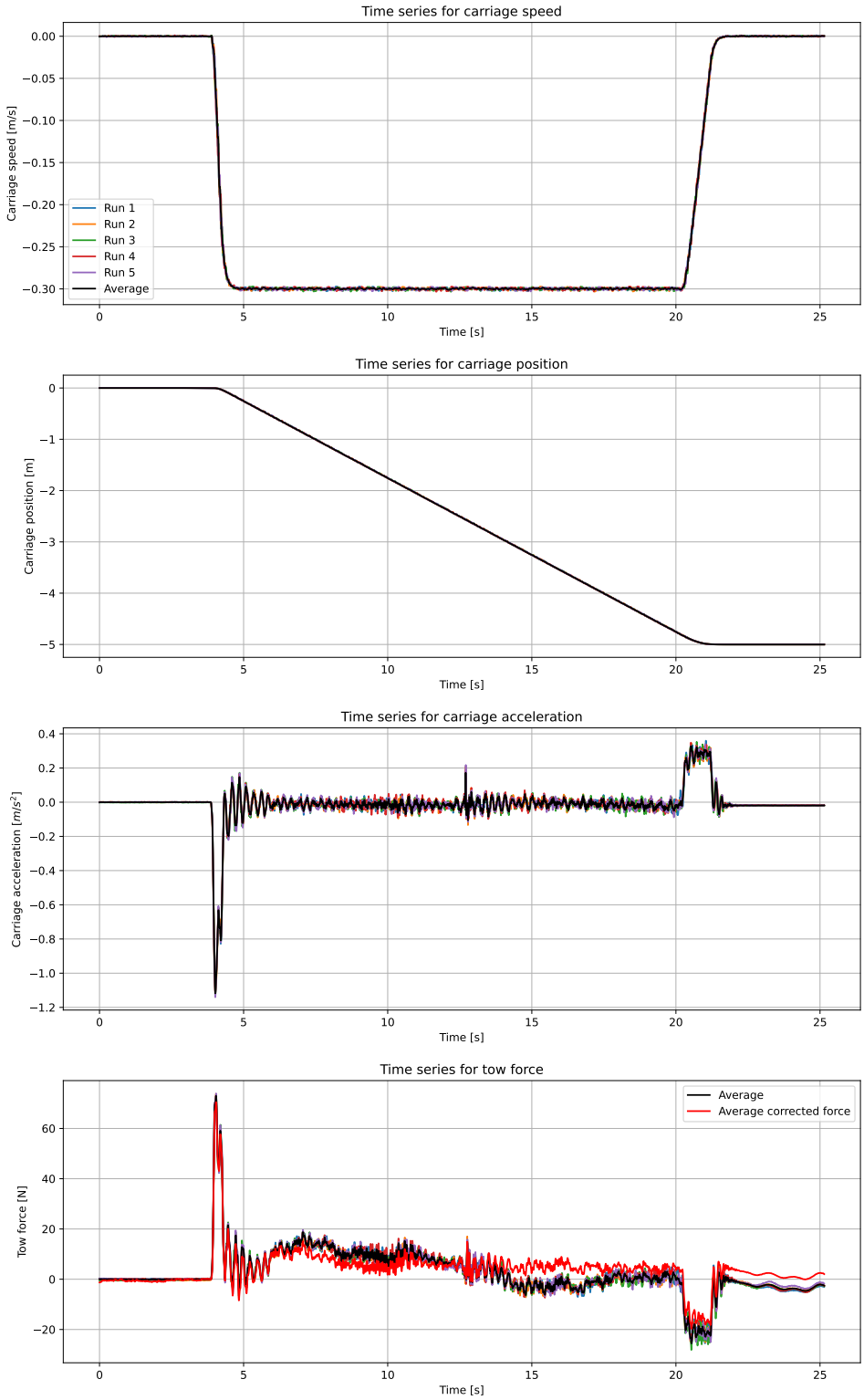

Figure C.23: Time series for model B, wet run, high acceleration, backward direction, speed 0.3 m/s

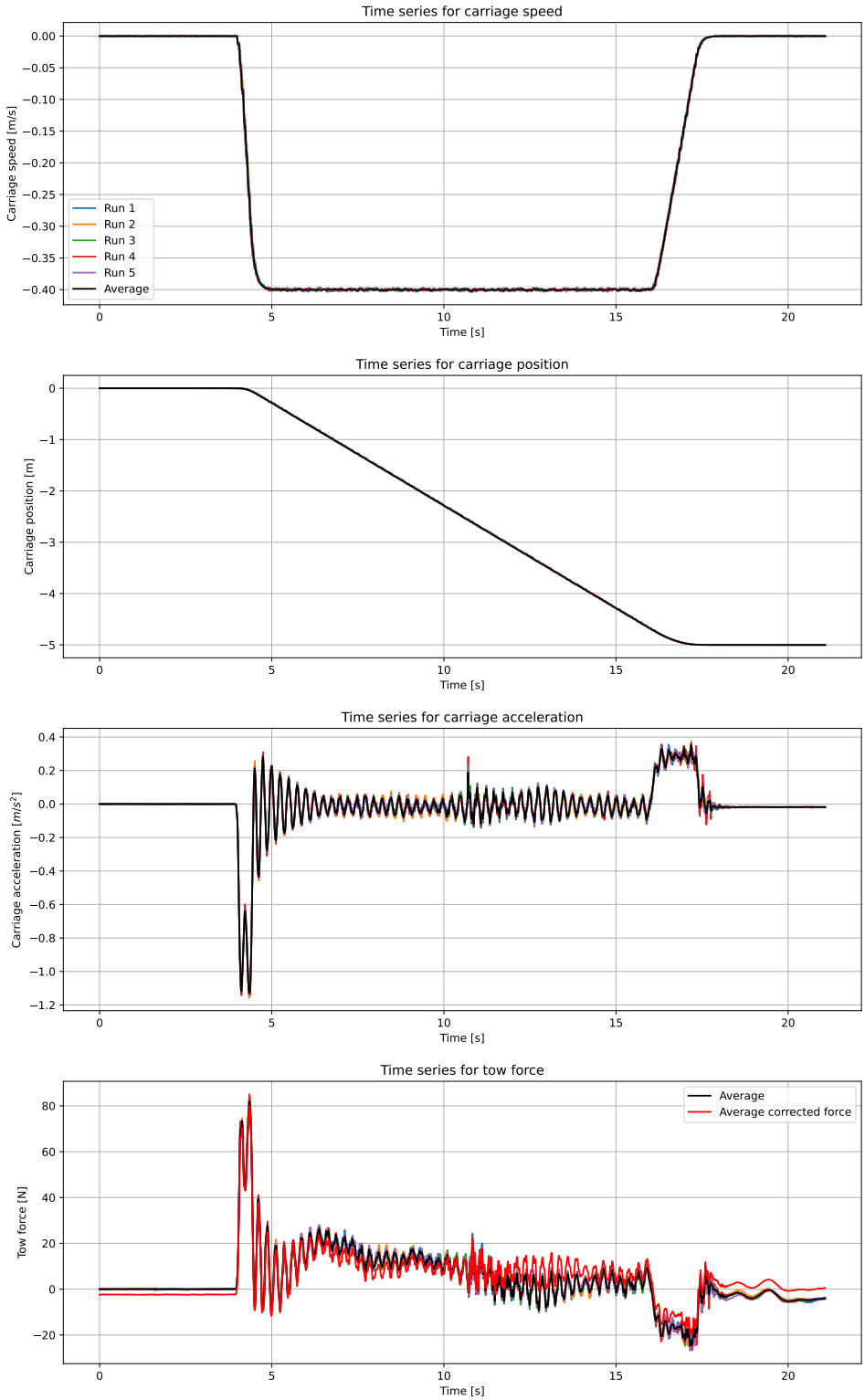

Figure C.24: Time series for model B, wet run, high acceleration, backward direction, speed 0.4 m/s

C.7 Wet run, model B, low acceleration, forward direction

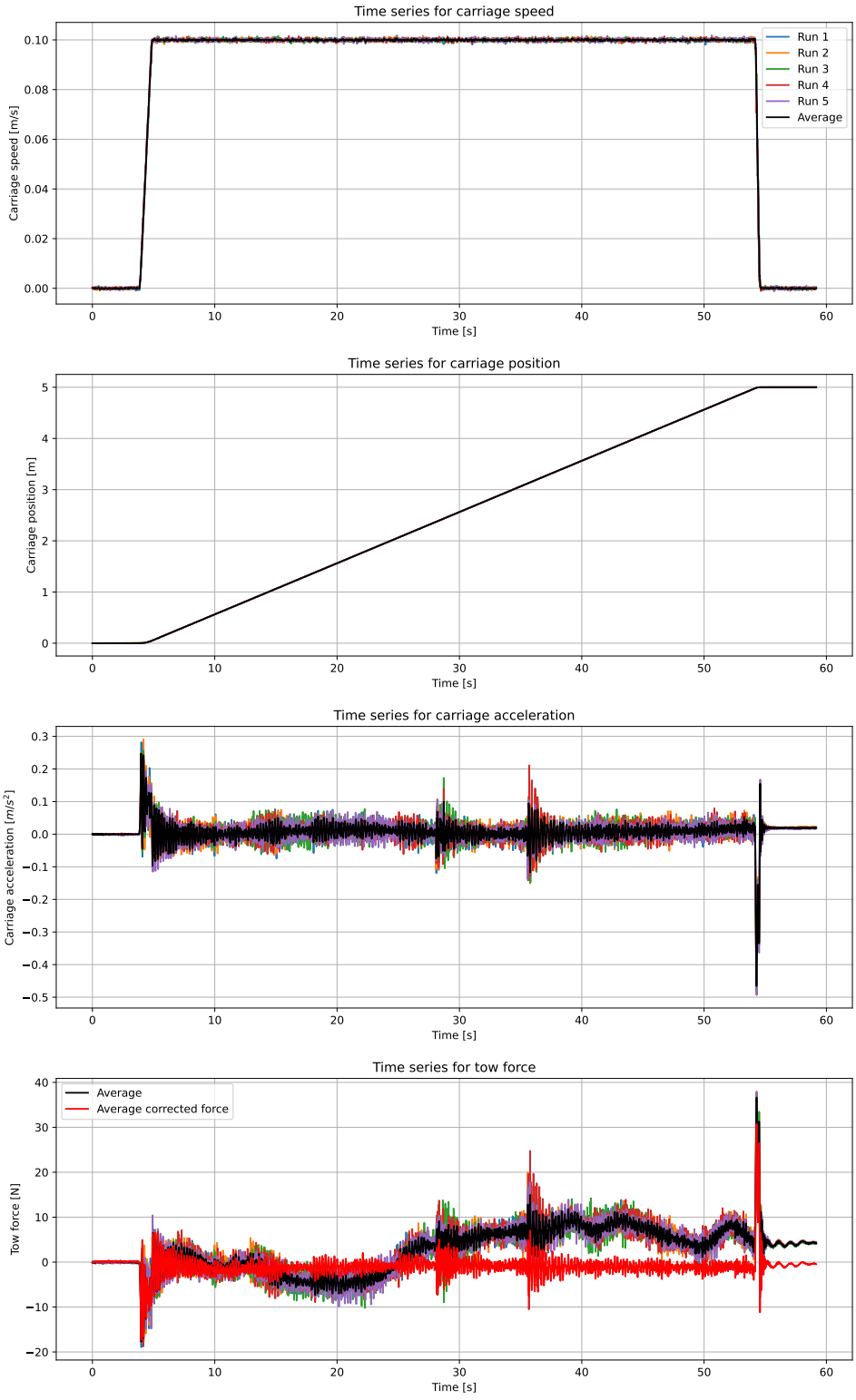

Figure C.25: Time series for model B, wet run, low acceleration, forward direction, speed 0.1 m/s

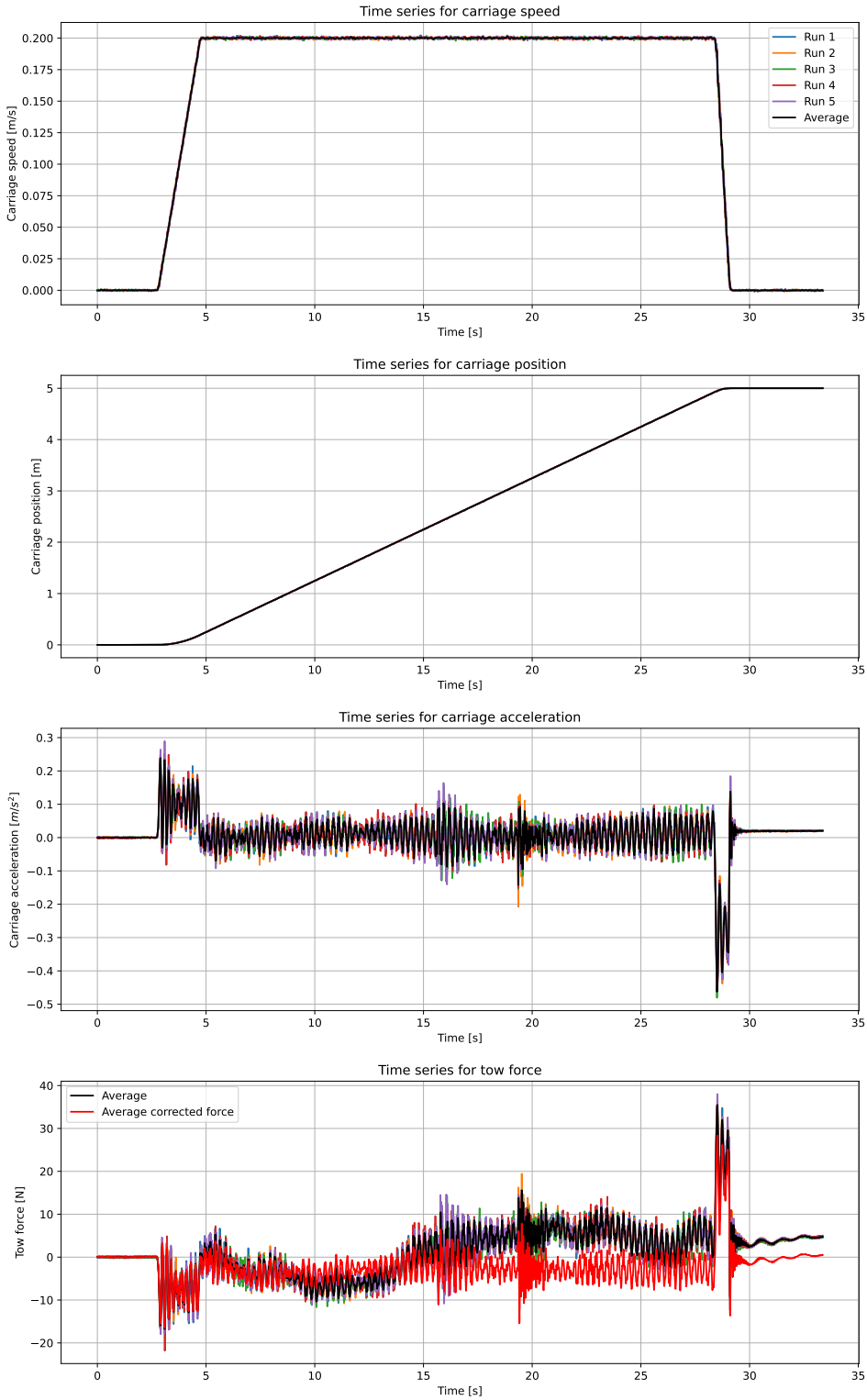

Figure C.26: Time series for model B, wet run, low acceleration, forward direction, speed 0.2 m/s

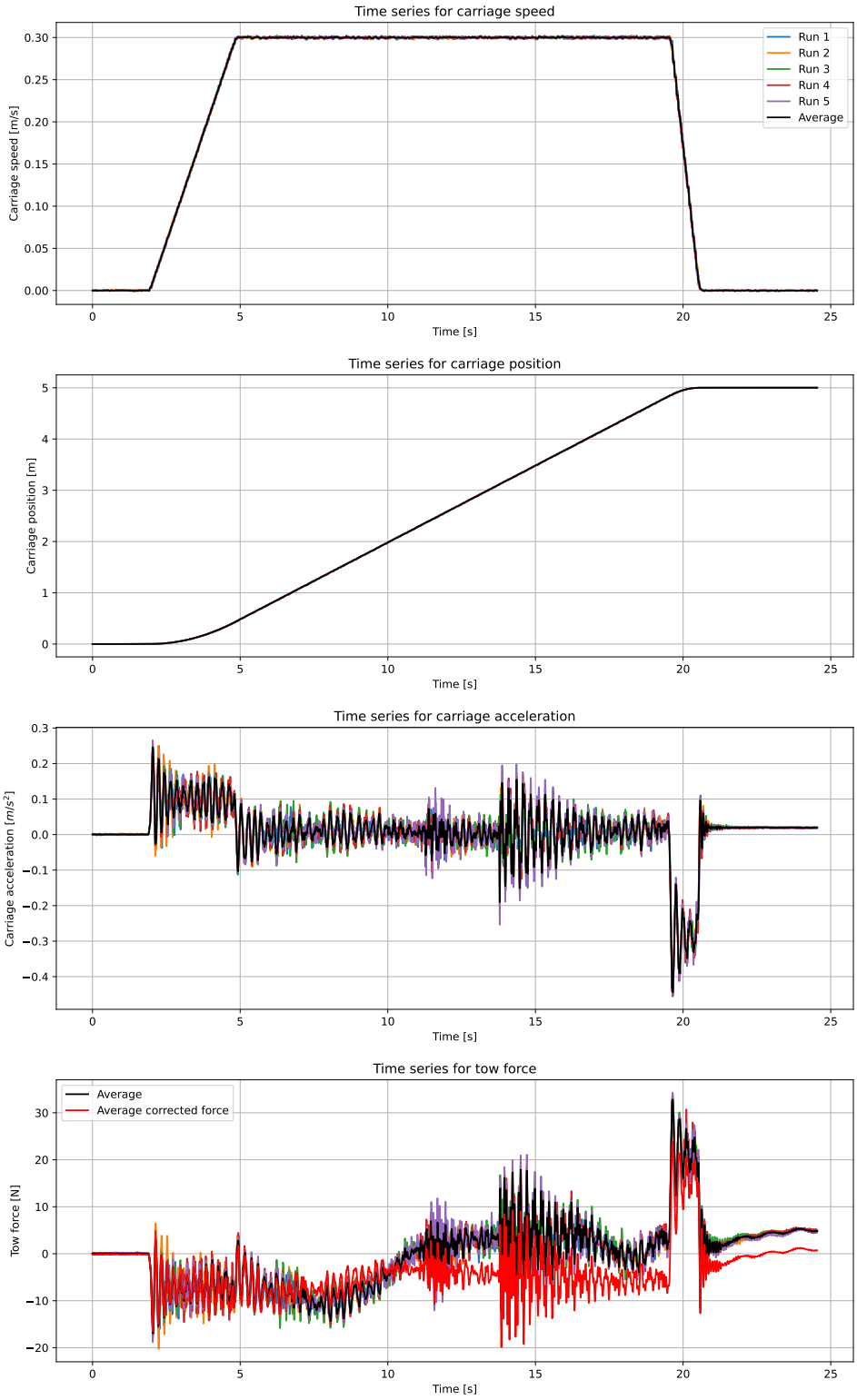

Figure C.27: Time series for model B, wet run, low acceleration, forward direction, speed 0.3 m/s

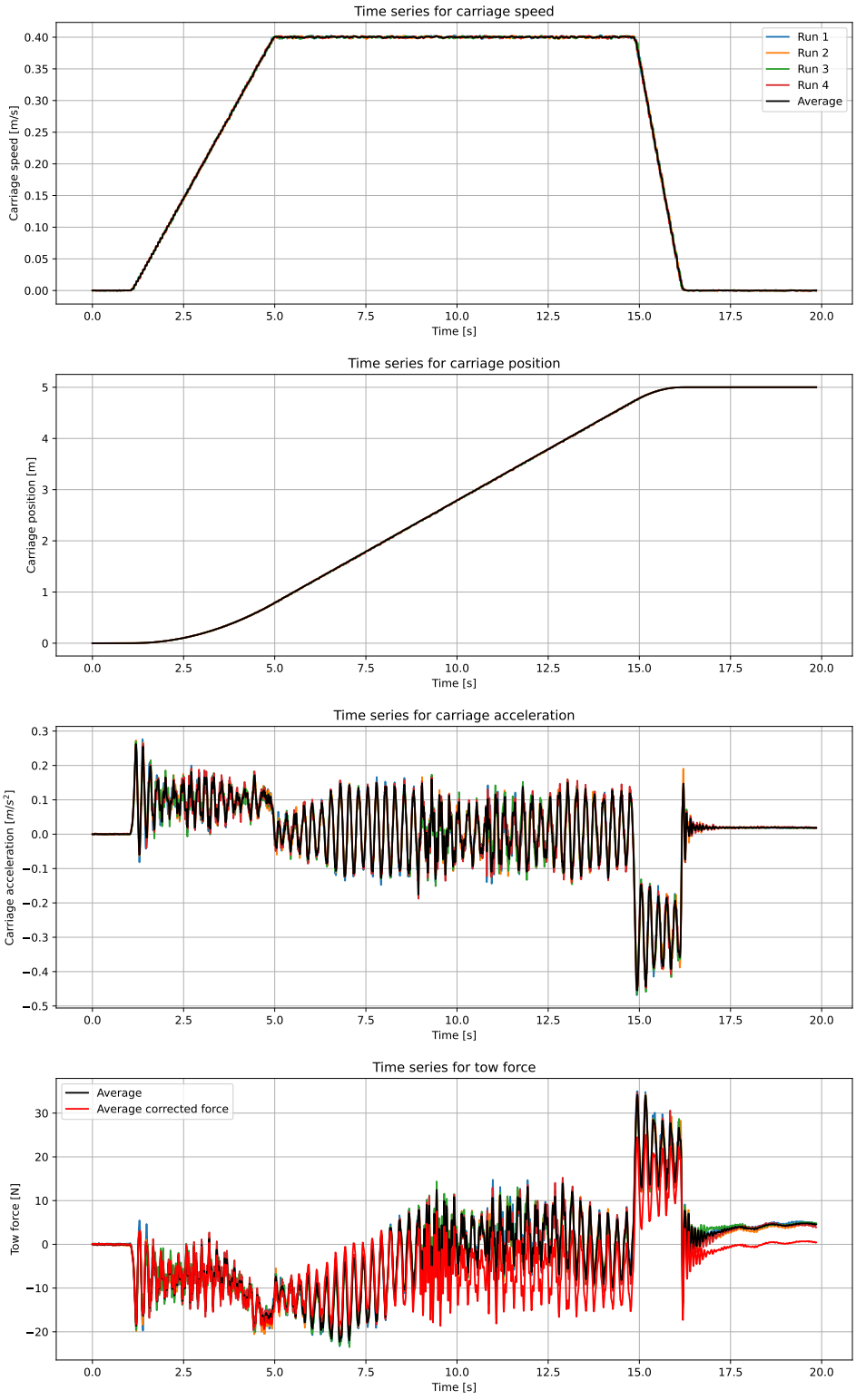

Figure C.28: Time series for model B, wet run, low acceleration, forward direction, speed 0.4 m/s

C.8 Wet run, model B, low acceleration, backward direction

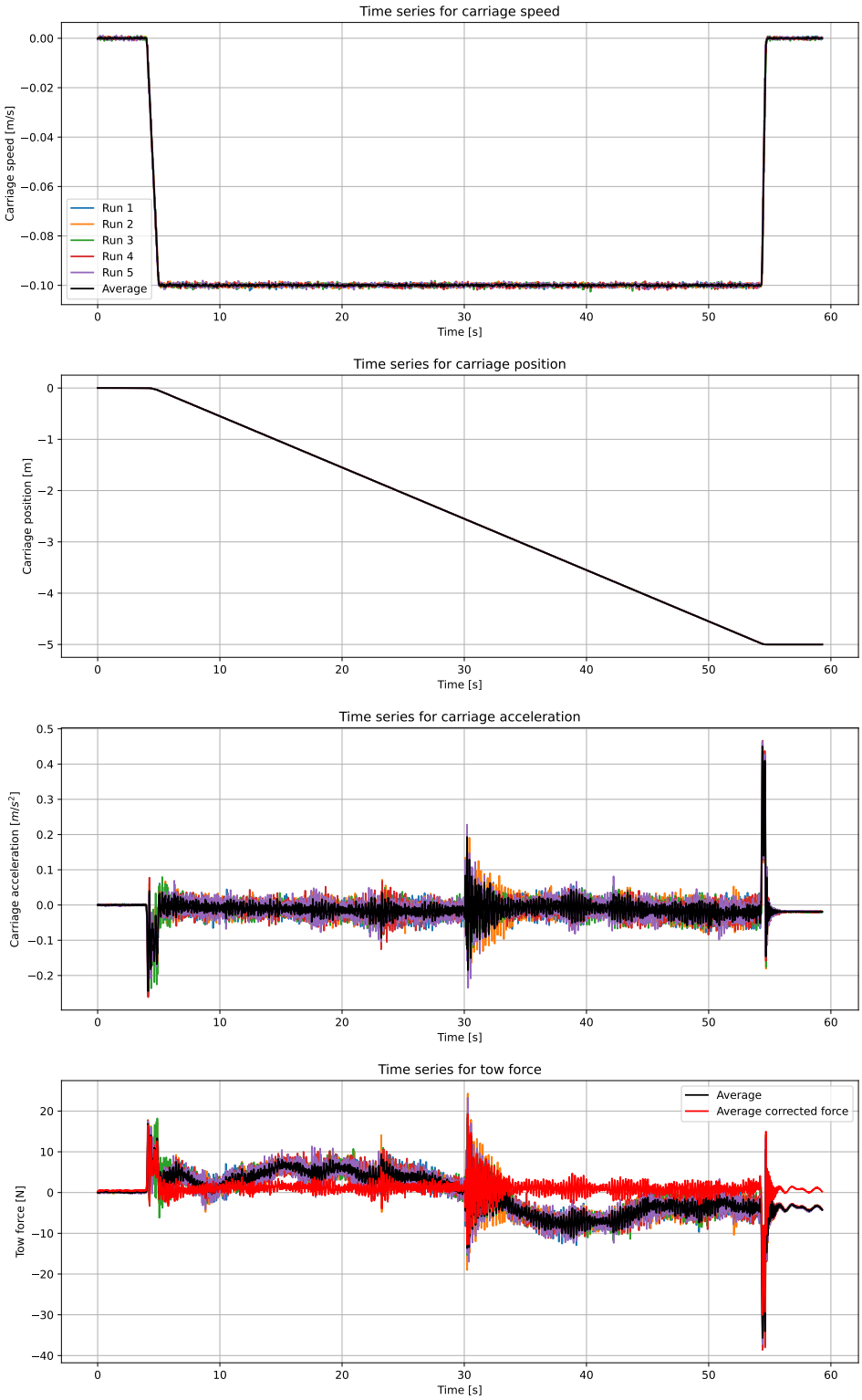

Figure C.29: Time series for model B, wet run, low acceleration, backward direction, speed 0.1 m/s

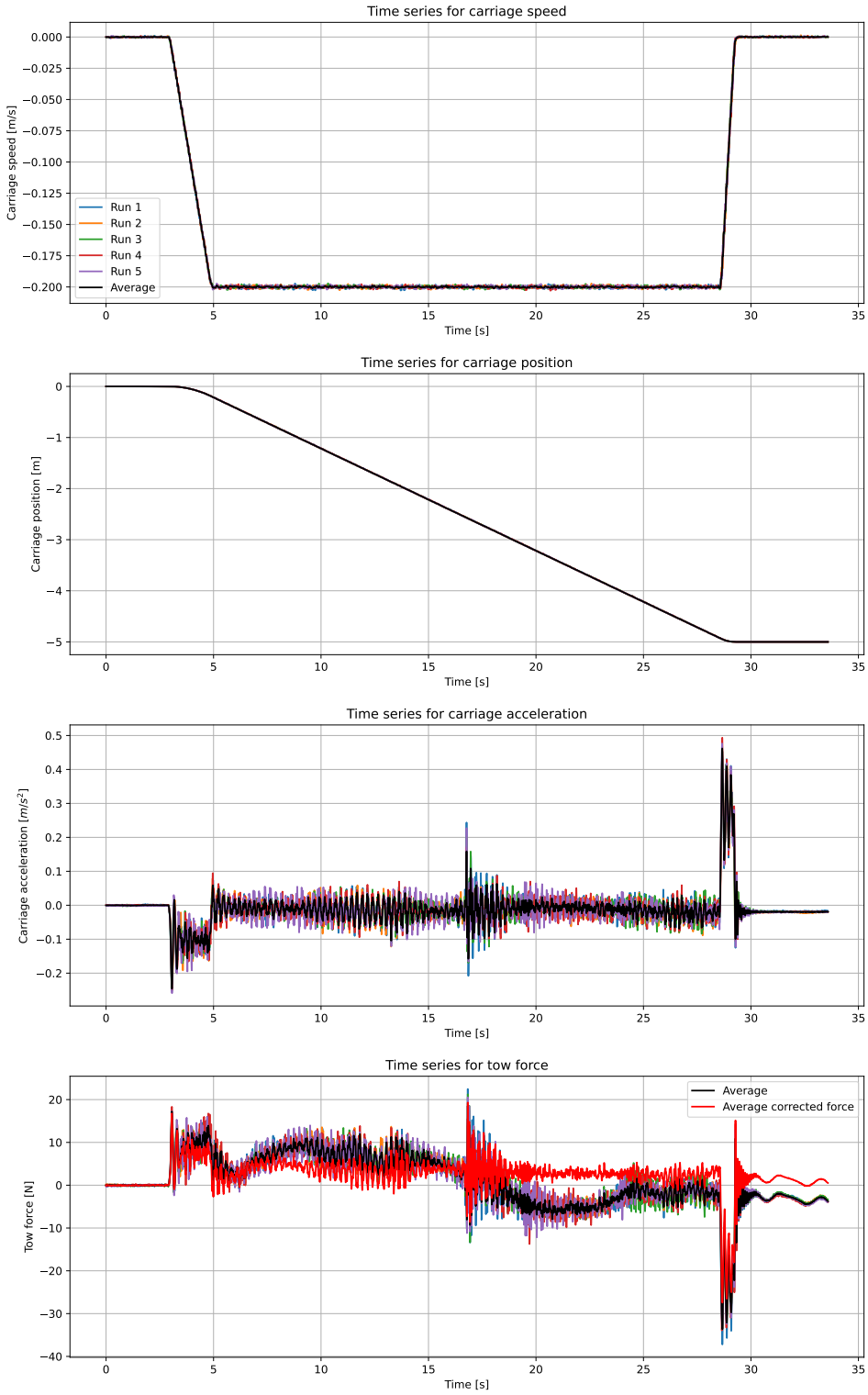

Figure C.30: Time series for model B, wet run, low acceleration, backward direction, speed 0.2 m/s

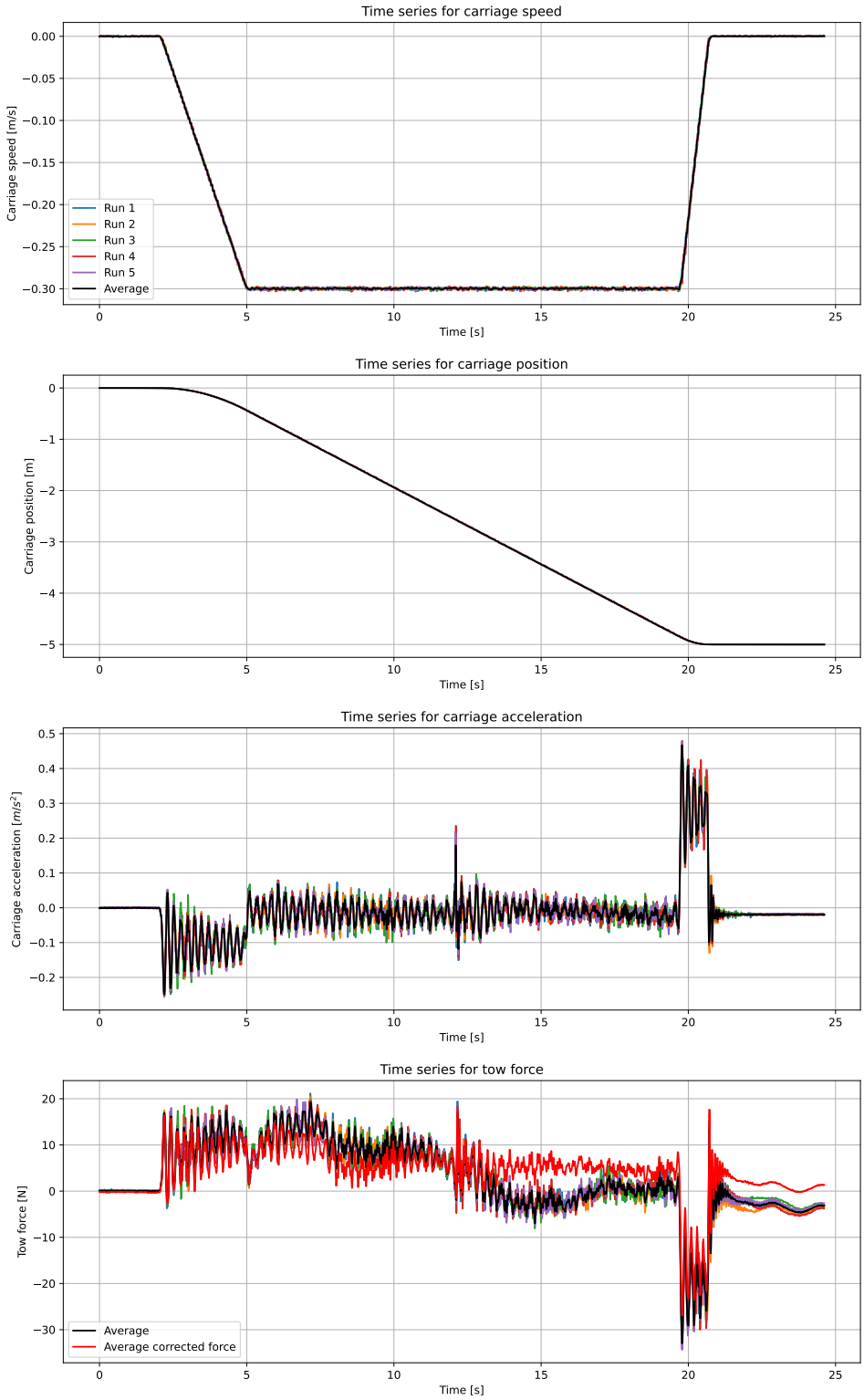

Figure C.31: Time series for model B, wet run, low acceleration, backward direction, speed 0.3 m/s

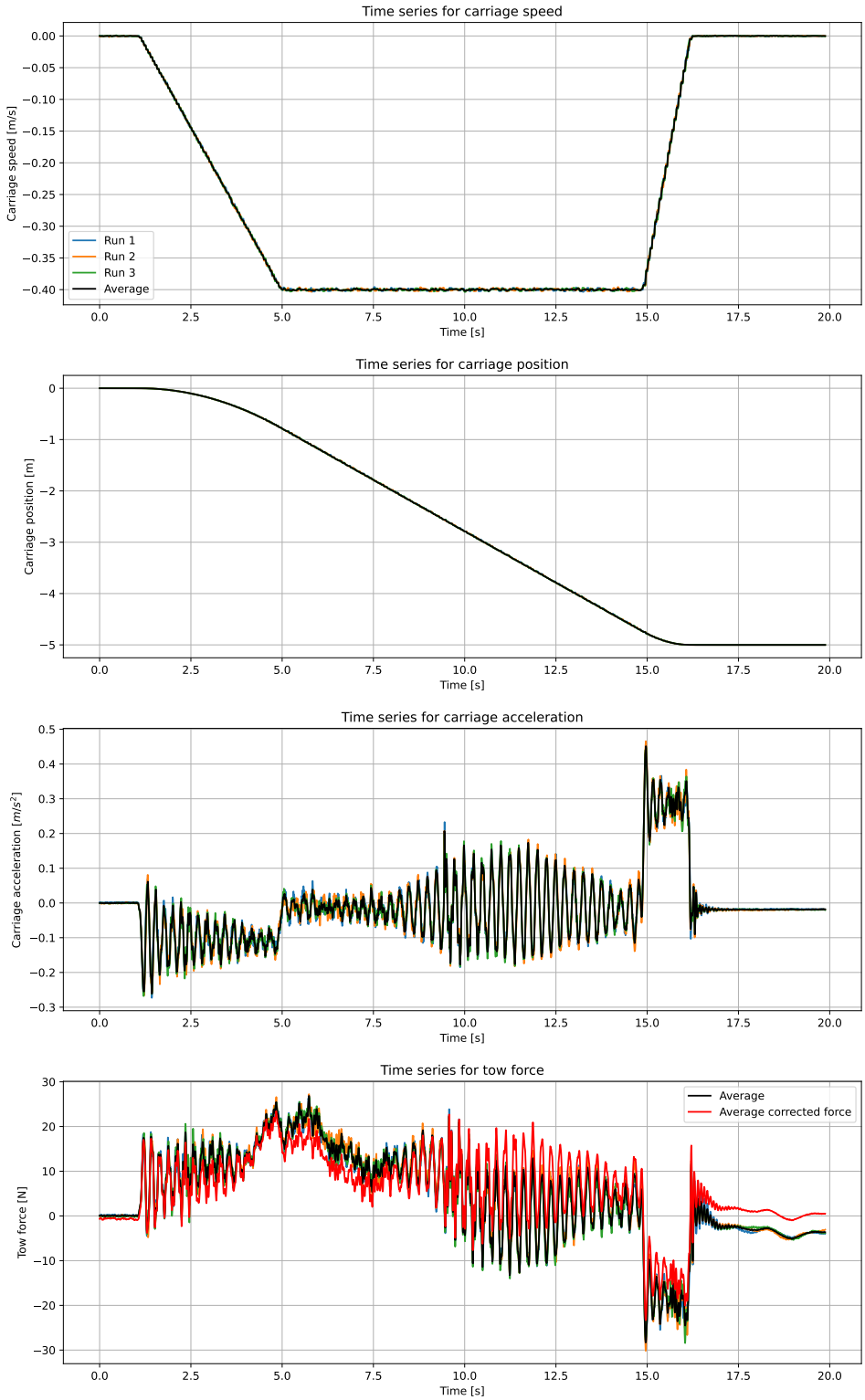

Figure C.32: Time series for model B, wet run, low acceleration, backward direction, speed 0.4 m/s

Appendix D

Time series plots for Model C

D.1 Wet run, model C, high acceleration, forward direction

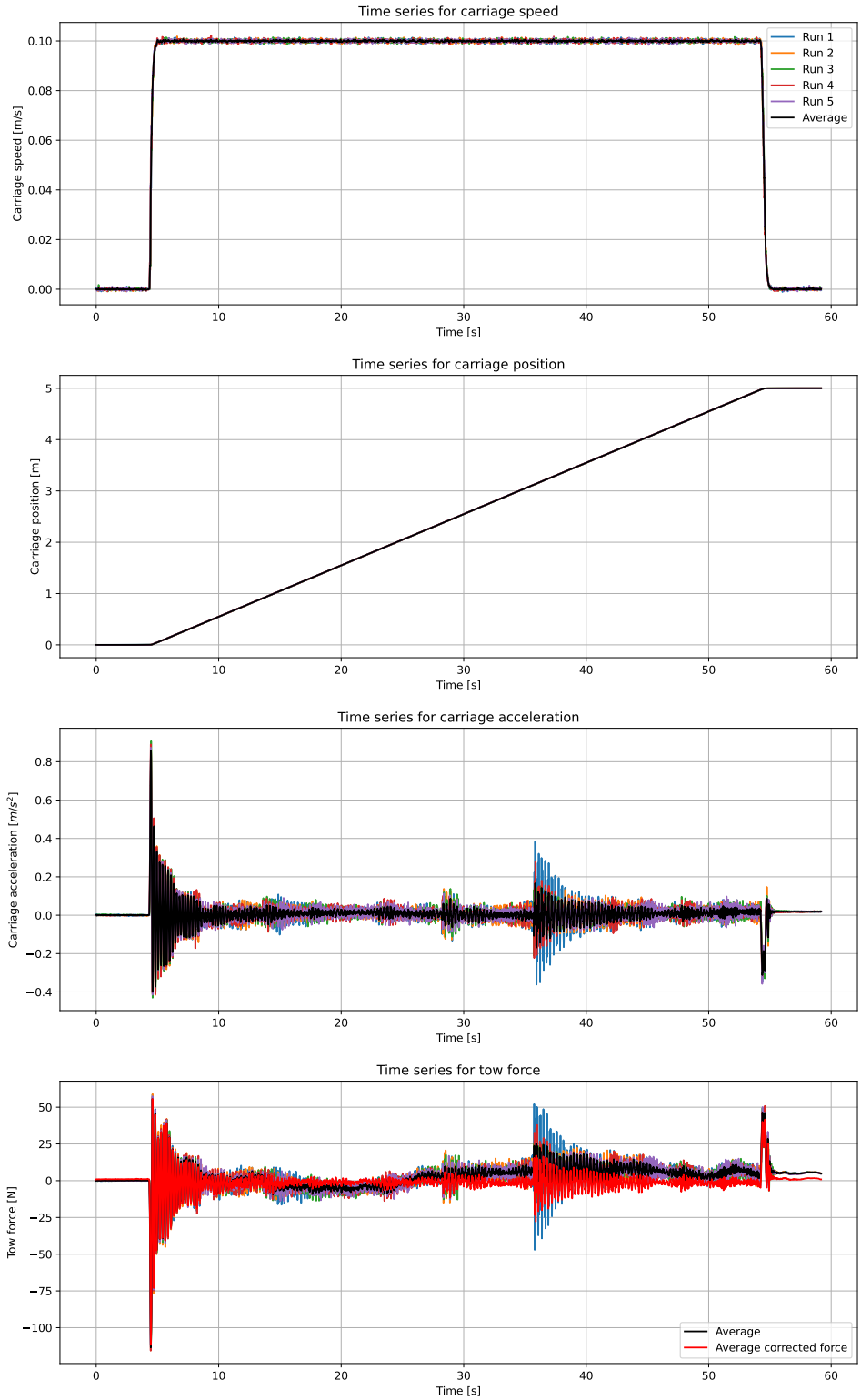

Figure D.1: Time series for model C, wet run, high acceleration, forward direction, speed 0.1 m/s

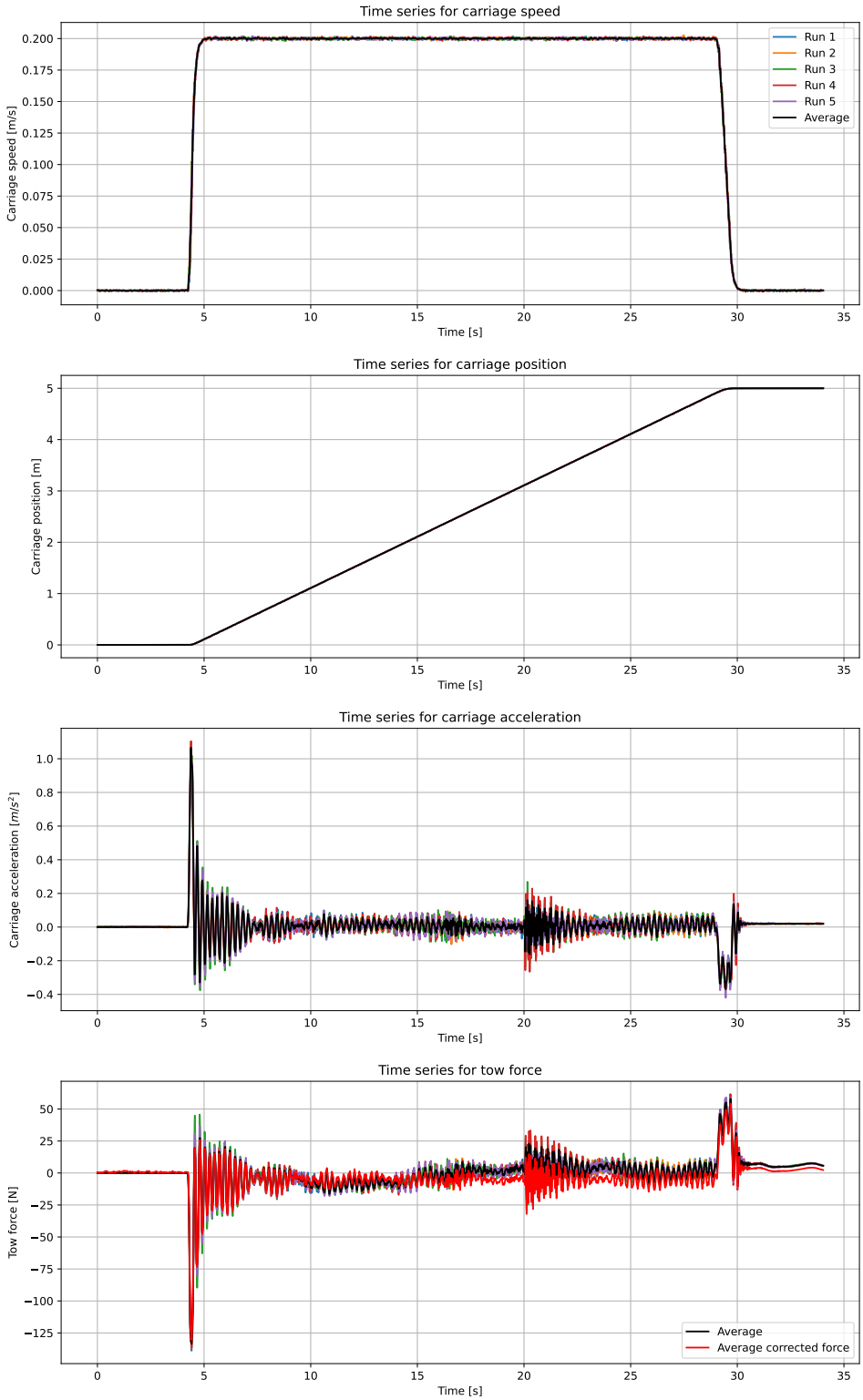

Figure D.2: Time series for model C, wet run, high acceleration, forward direction, speed 0.2 m/s

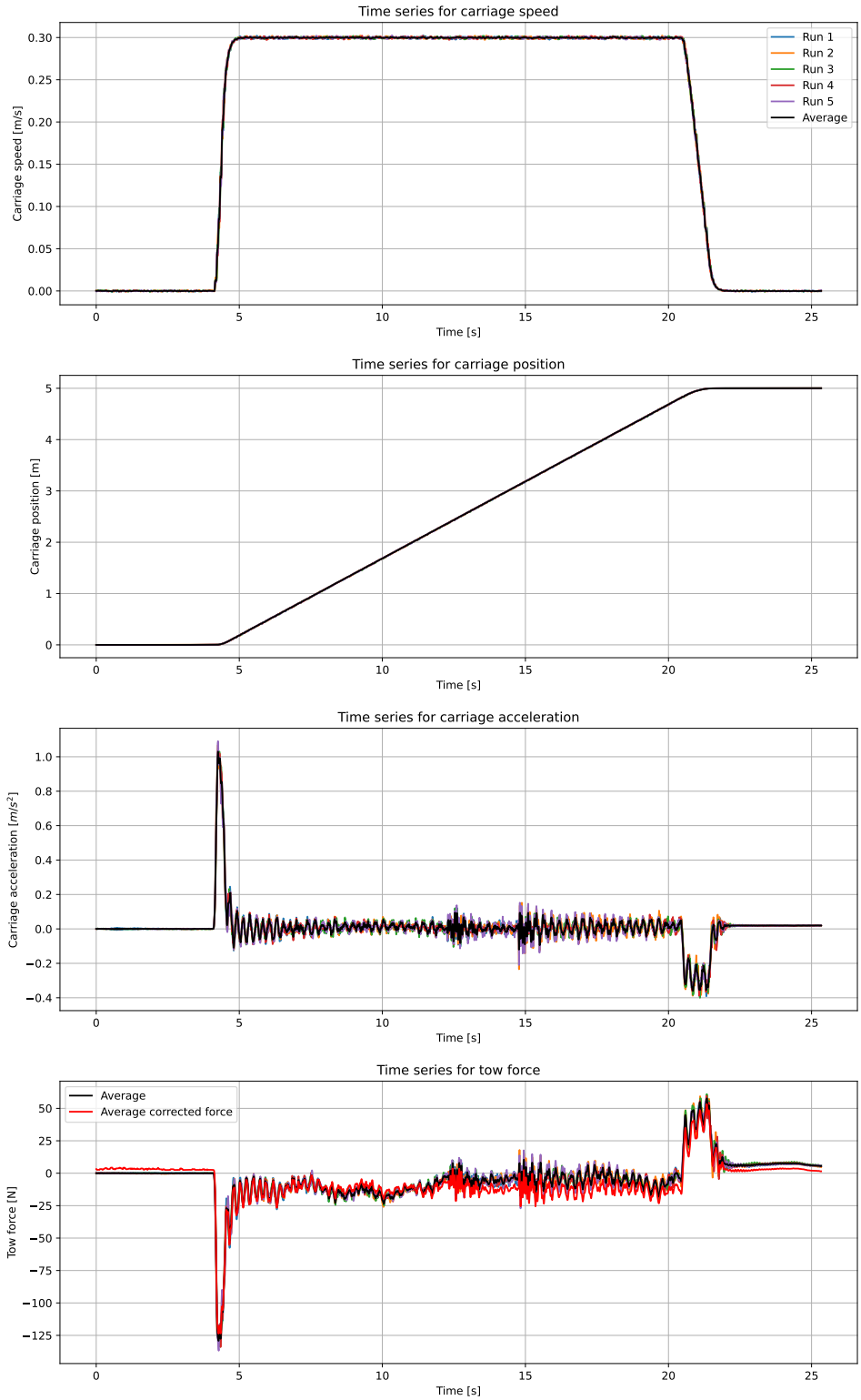

Figure D.3: Time series for model C, wet run, high acceleration, forward direction, speed 0.3 m/s

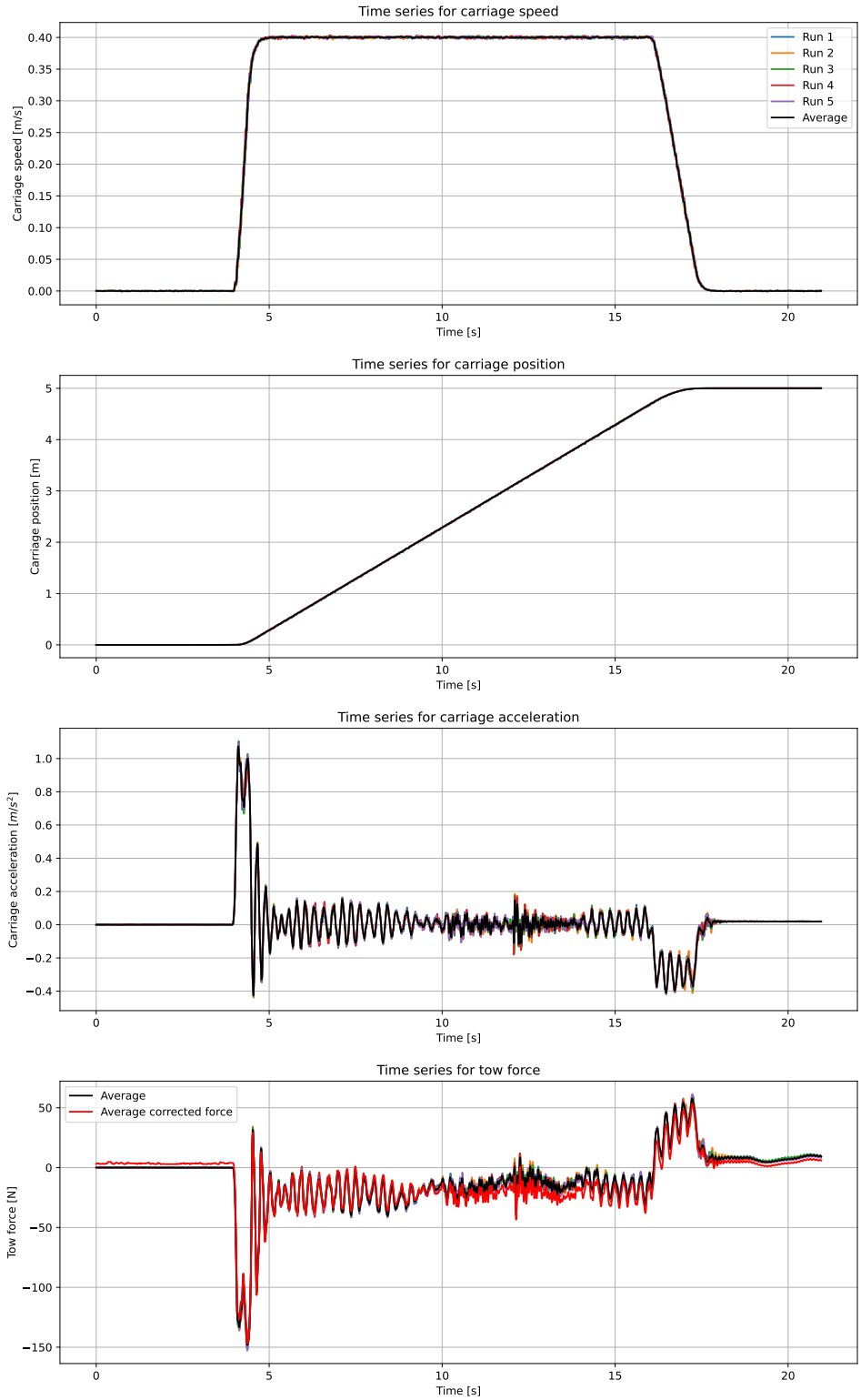

Figure D.4: Time series for model C, wet run, high acceleration, forward direction, speed 0.4 m/s

D.2 Wet run, model C, high acceleration, backward direction

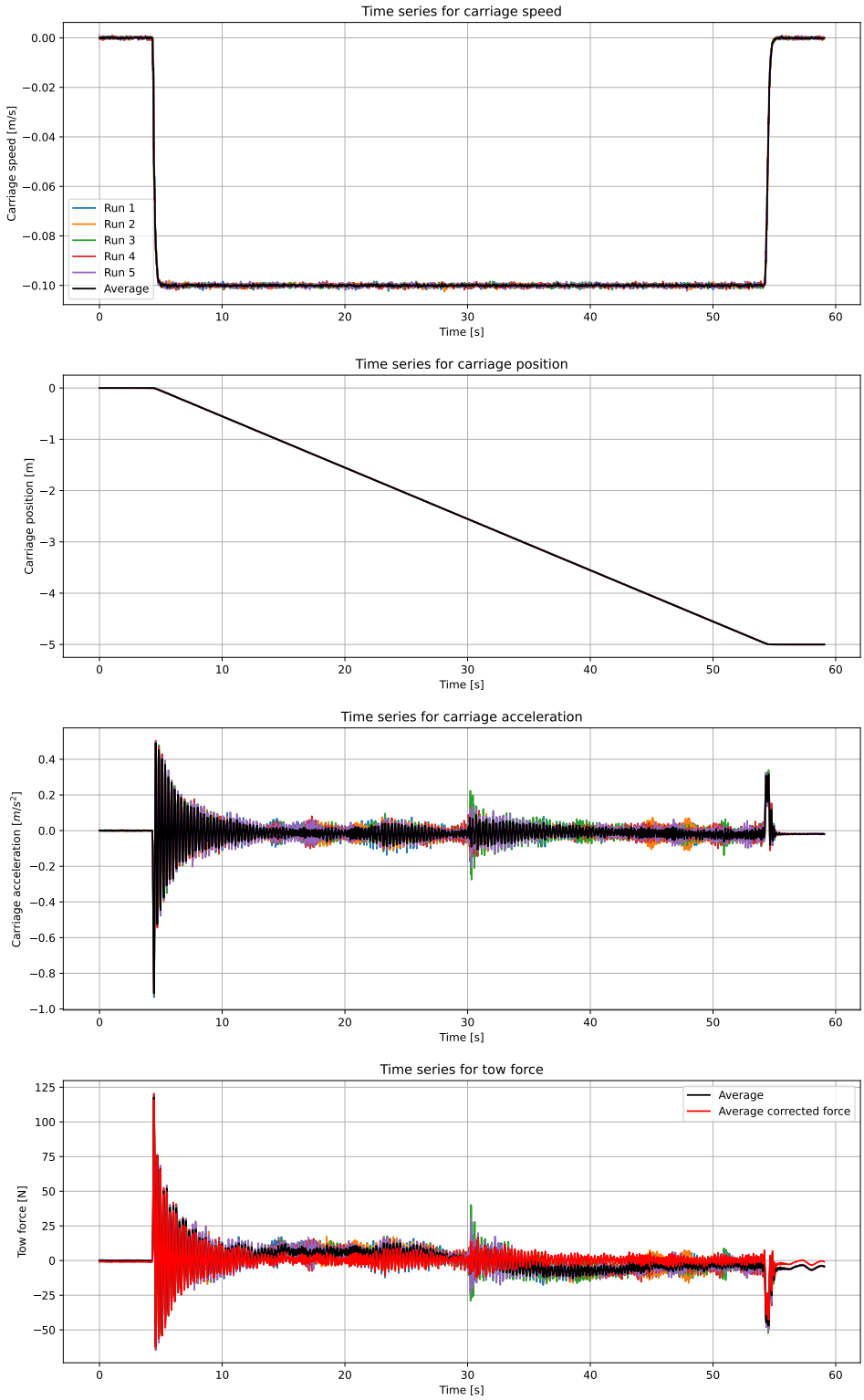

Figure D.5: Time series for model C, wet run, high acceleration, backward direction, speed 0.1 m/s

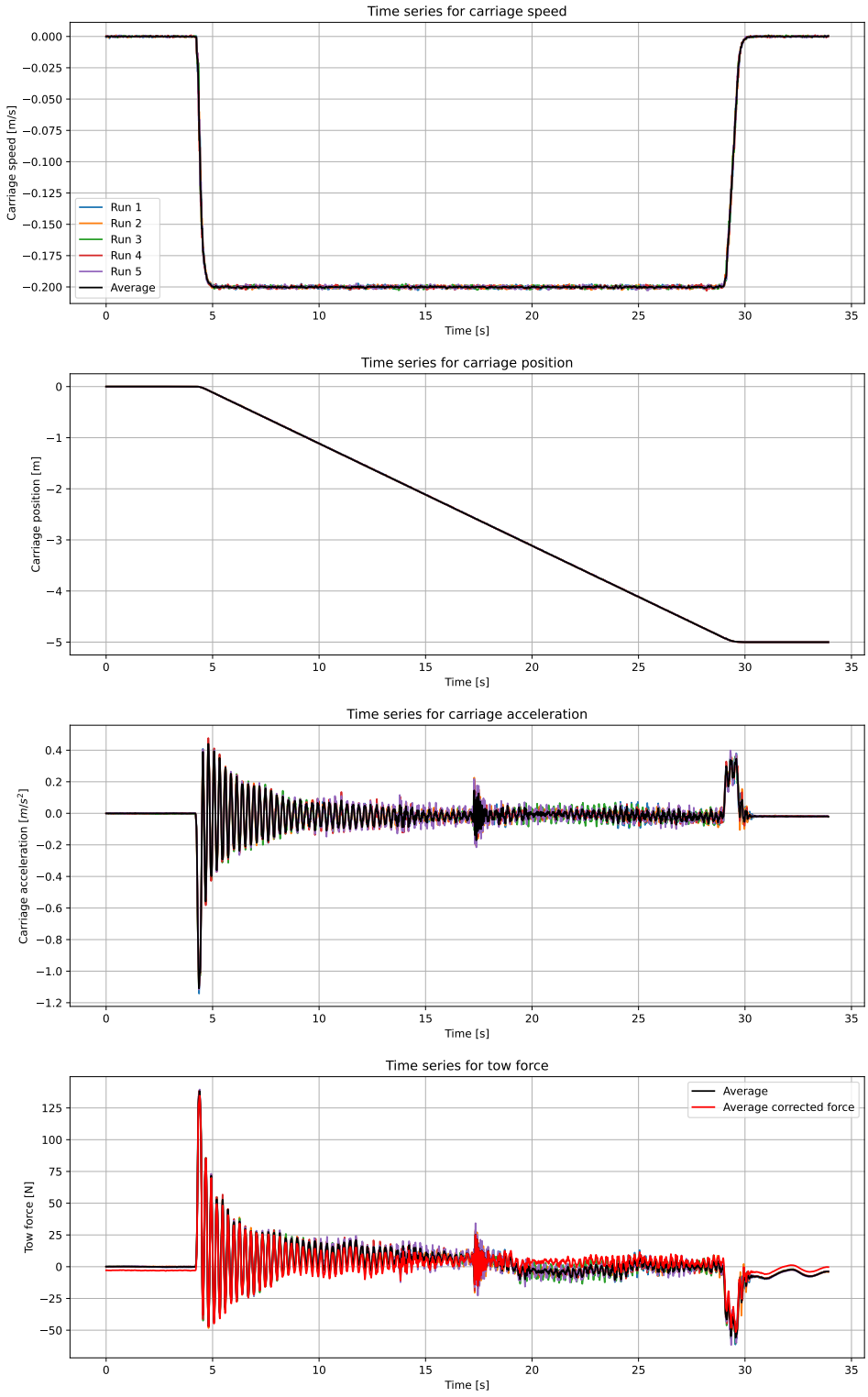

Figure D.6: Time series for model C, wet run, high acceleration, backward direction, speed 0.2 m/s

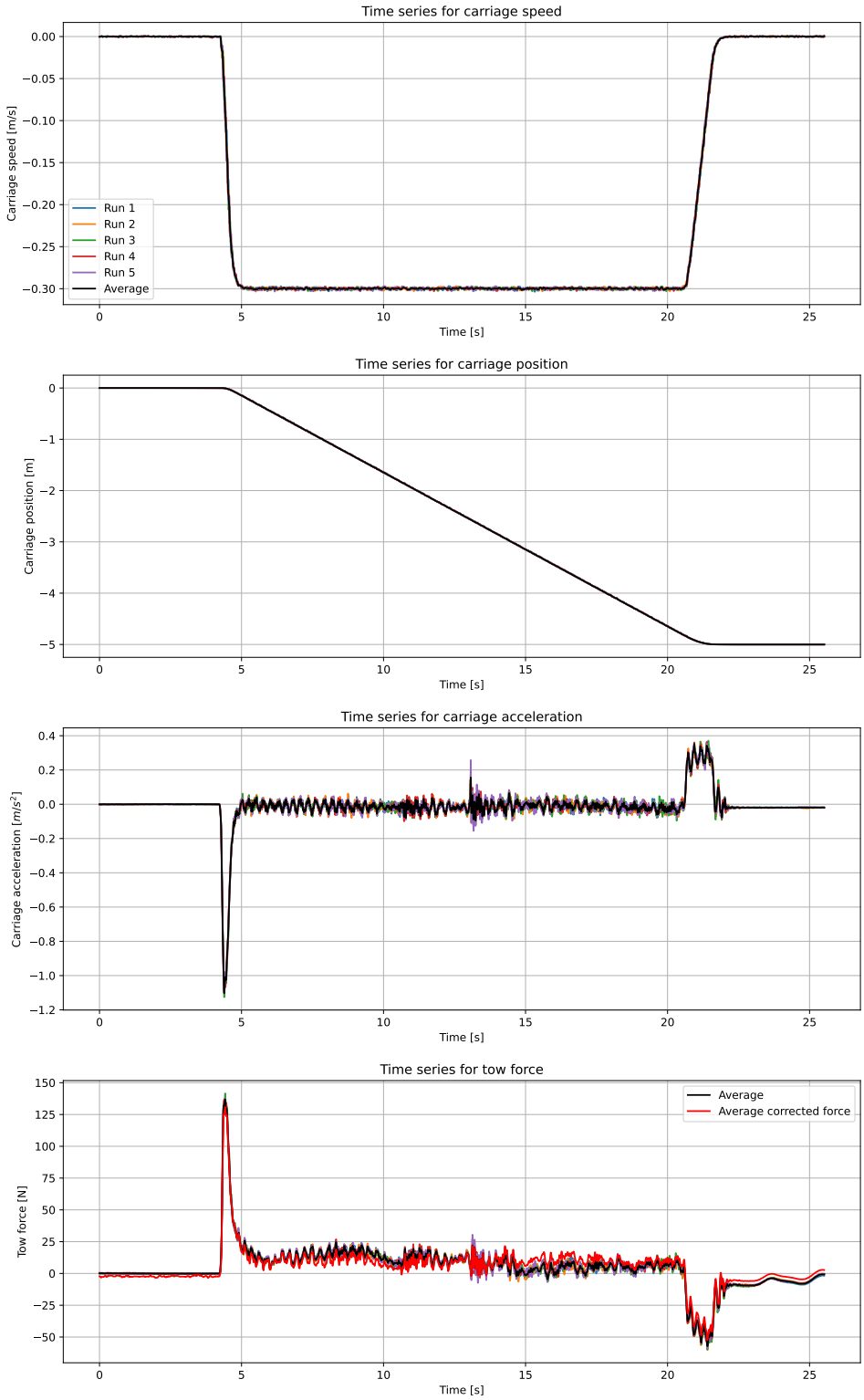

Figure D.7: Time series for model C, wet run, high acceleration, backward direction, speed 0.3 m/s

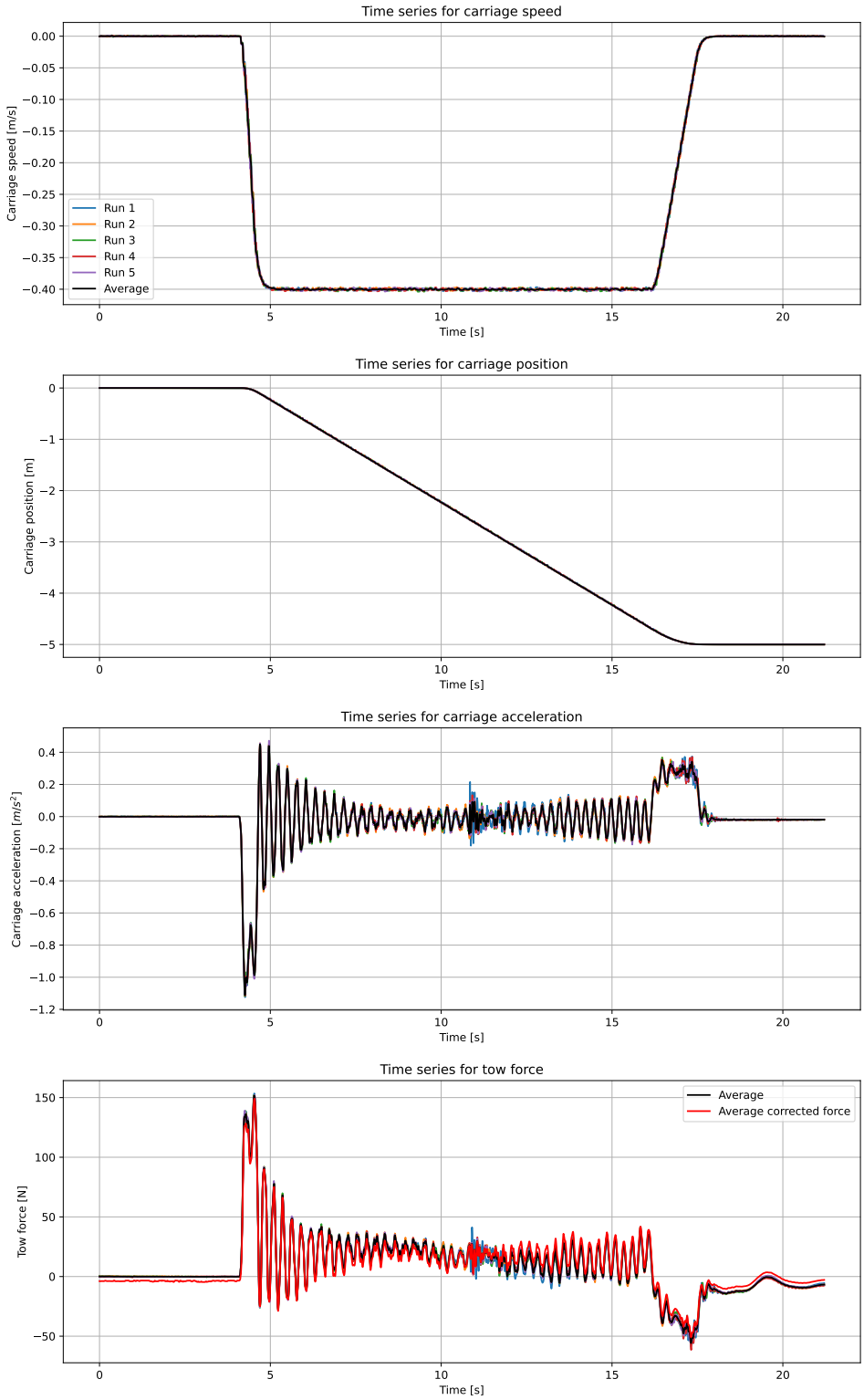

Figure D.8: Time series for model C, wet run, high acceleration, backward direction, speed 0.4 m/s

D.3 Wet run, model C, low acceleration, forward direction

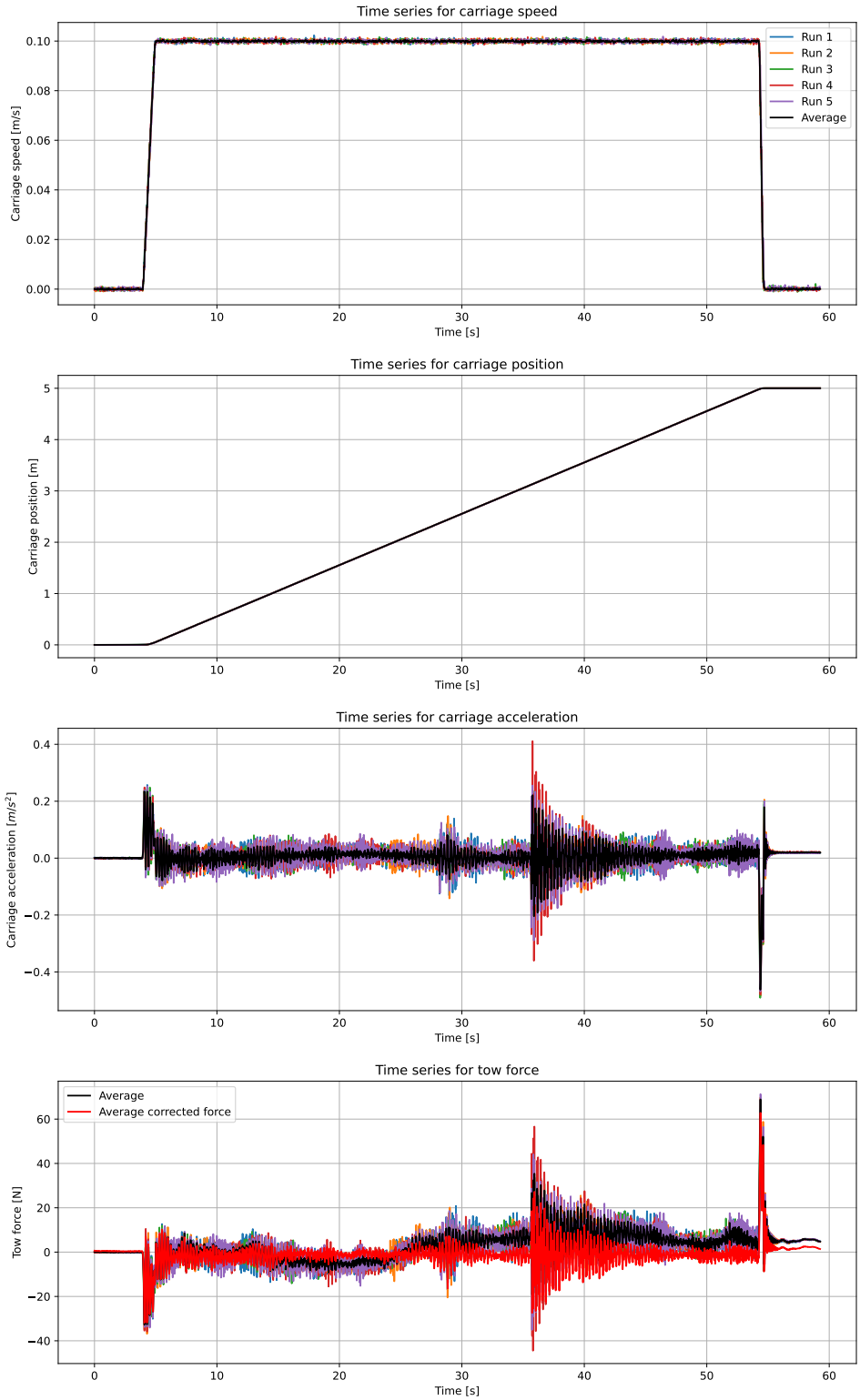

Figure D.9: Time series for model C, wet run, low acceleration, forward direction, speed 0.1 m/s

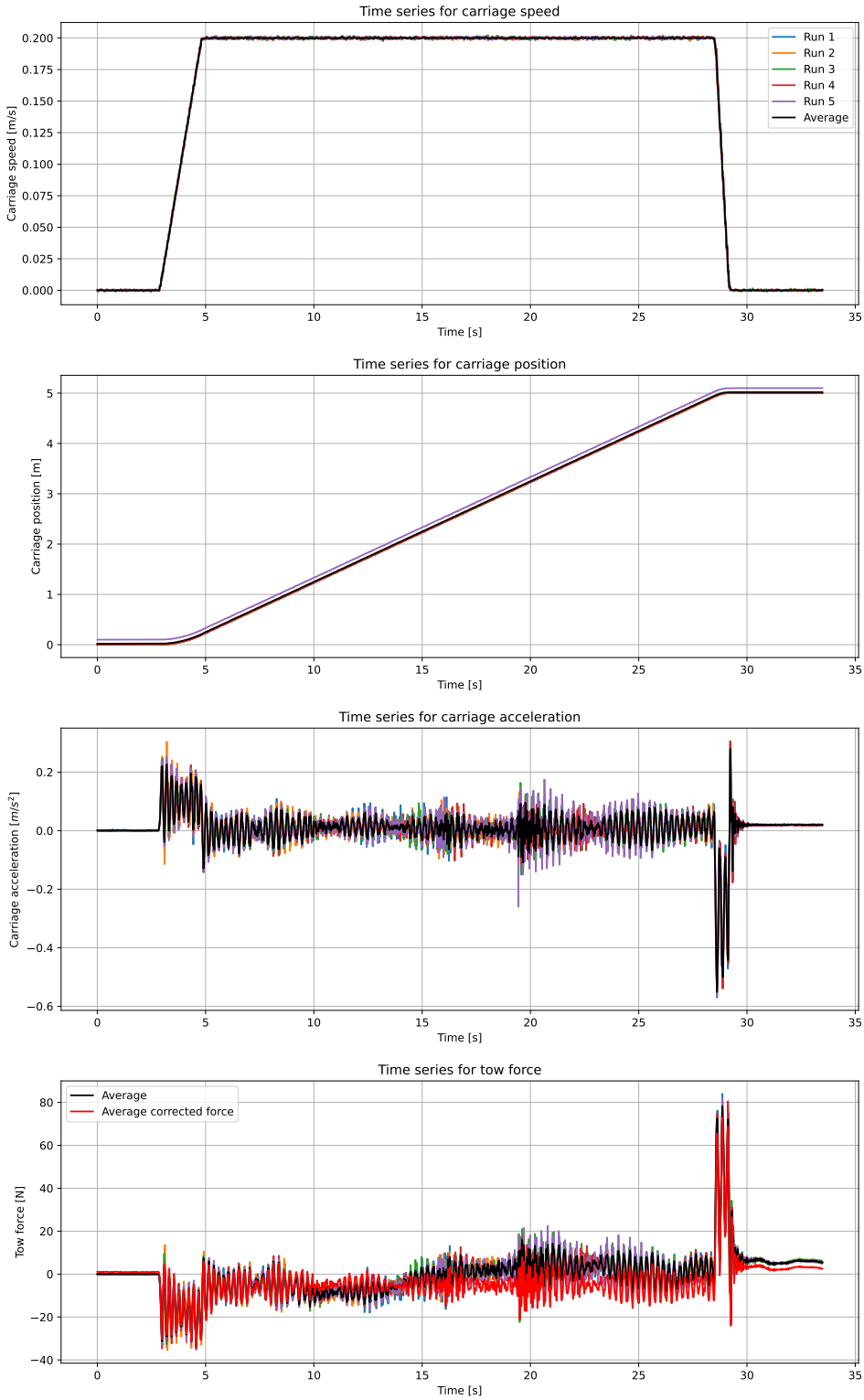

Figure D.10: Time series for model C, wet run, low acceleration, forward direction, speed 0.2 m/s

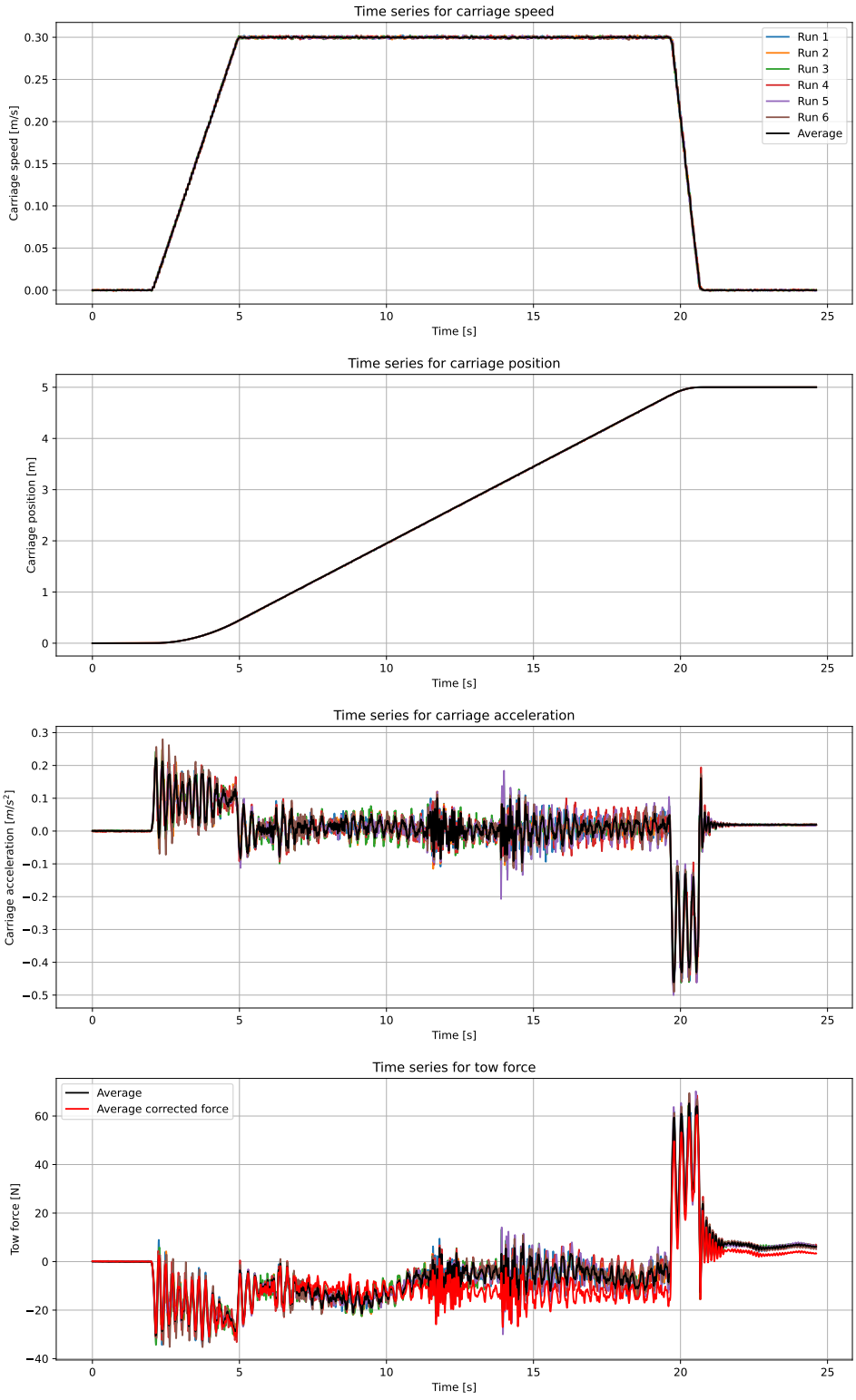

Figure D.11: Time series for model C, wet run, low acceleration, forward direction, speed 0.3 m/s

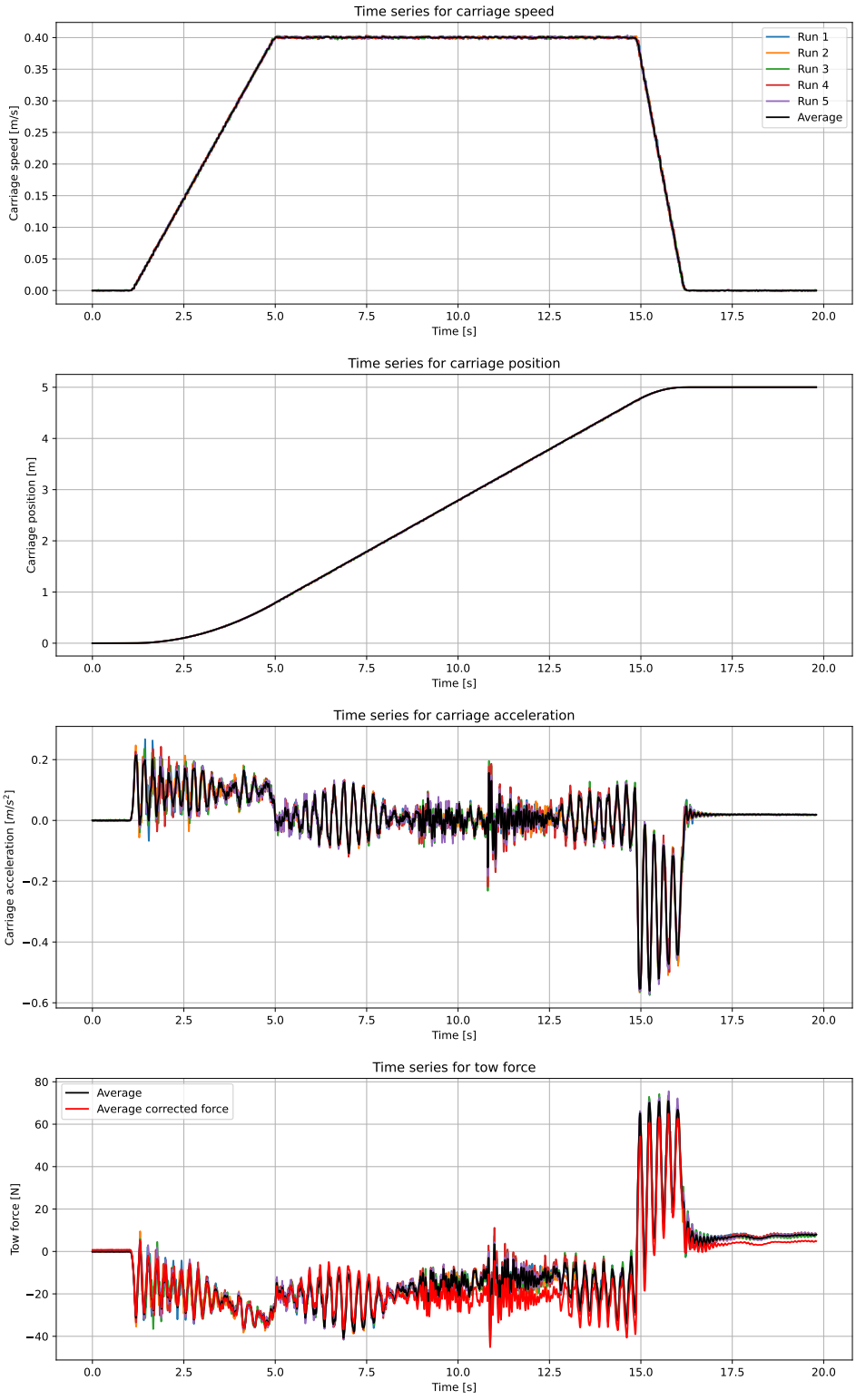

Figure D.12: Time series for model C, wet run, low acceleration, forward direction, speed 0.4 m/s

D.4 Wet run, model C, low acceleration, backward direction

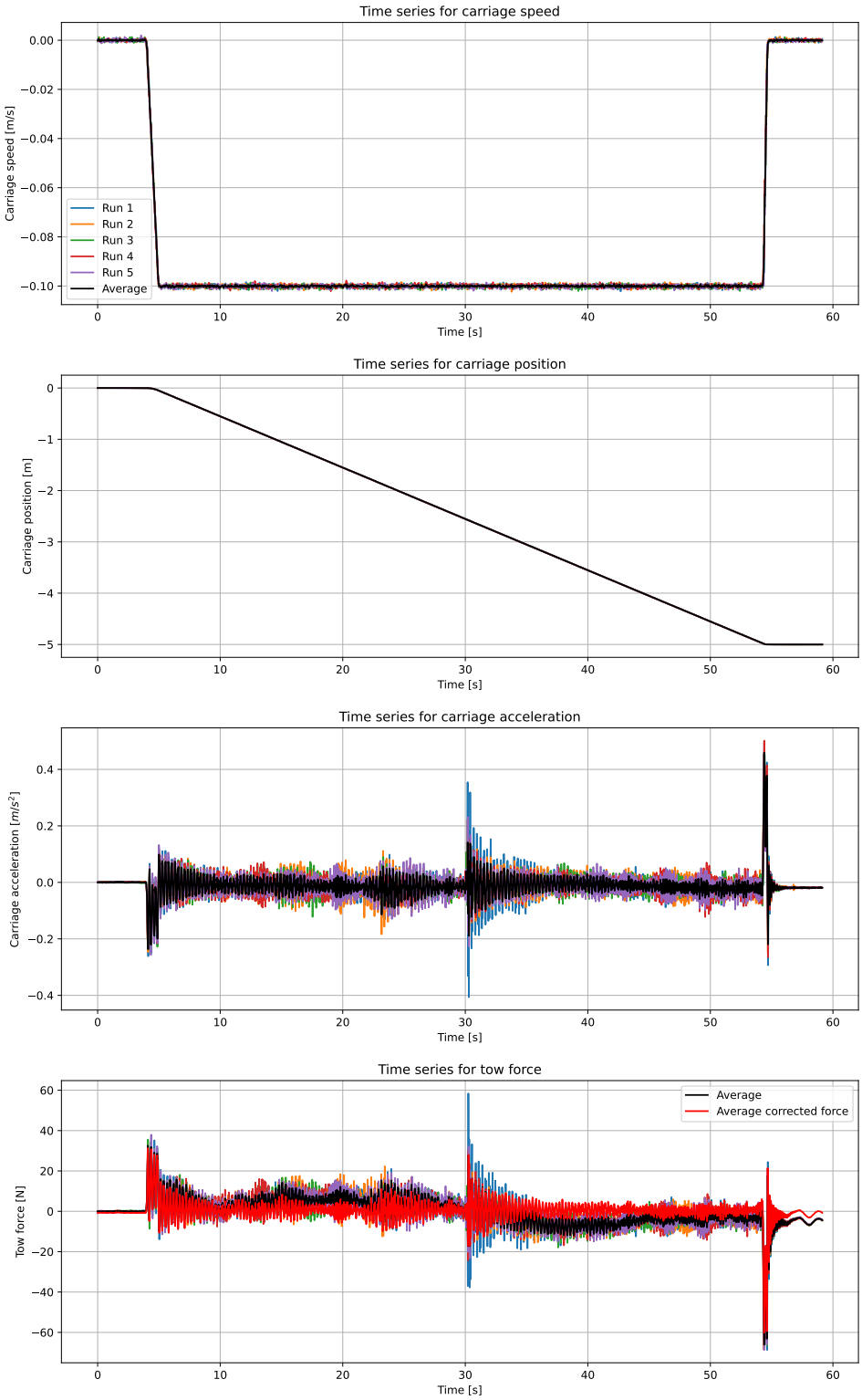

Figure D.13: Time series for model C, wet run, low acceleration, backward direction, speed 0.1 m/s

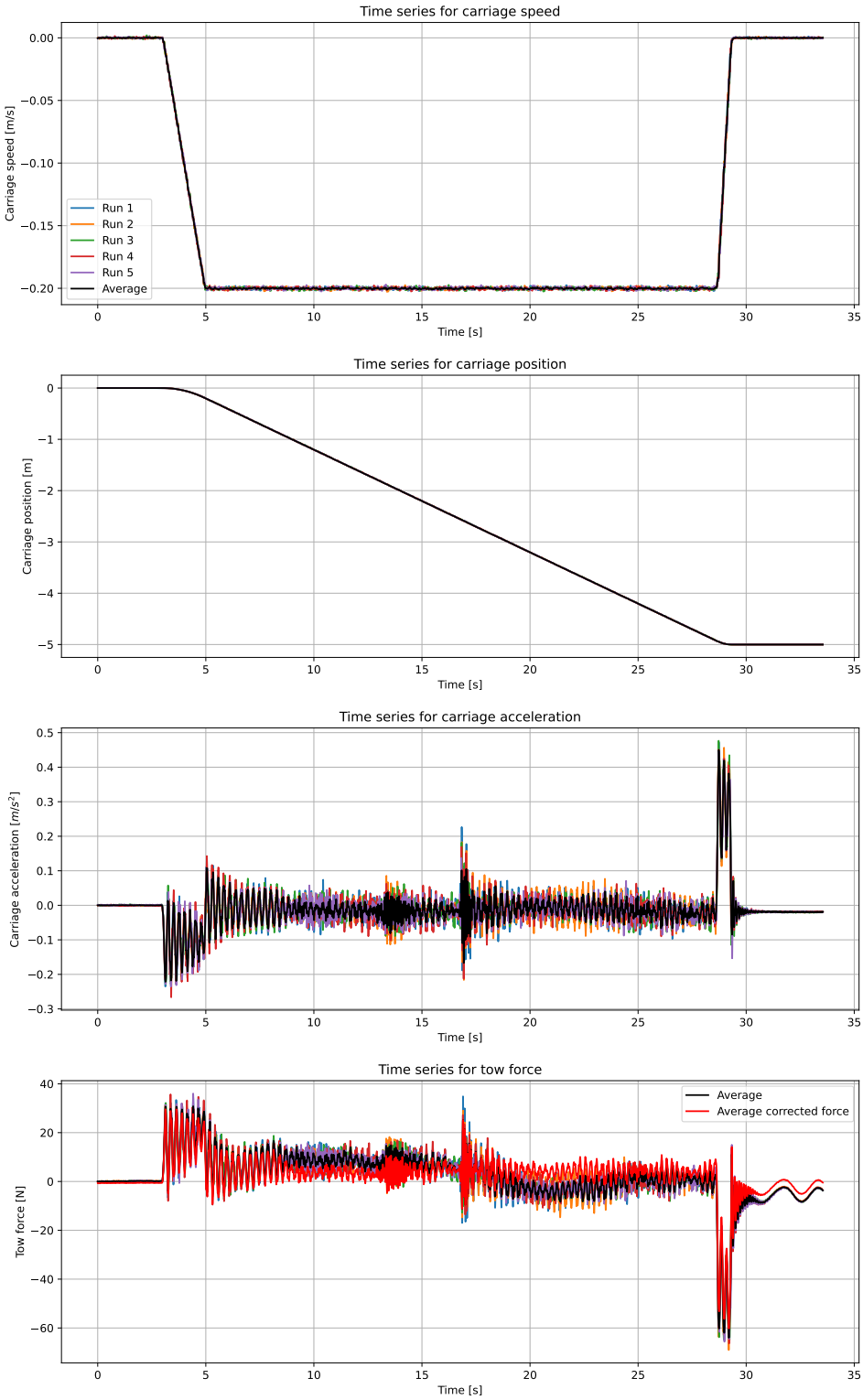

Figure D.14: Time series for model C, wet run, low acceleration, backward direction, speed 0.2 m/s

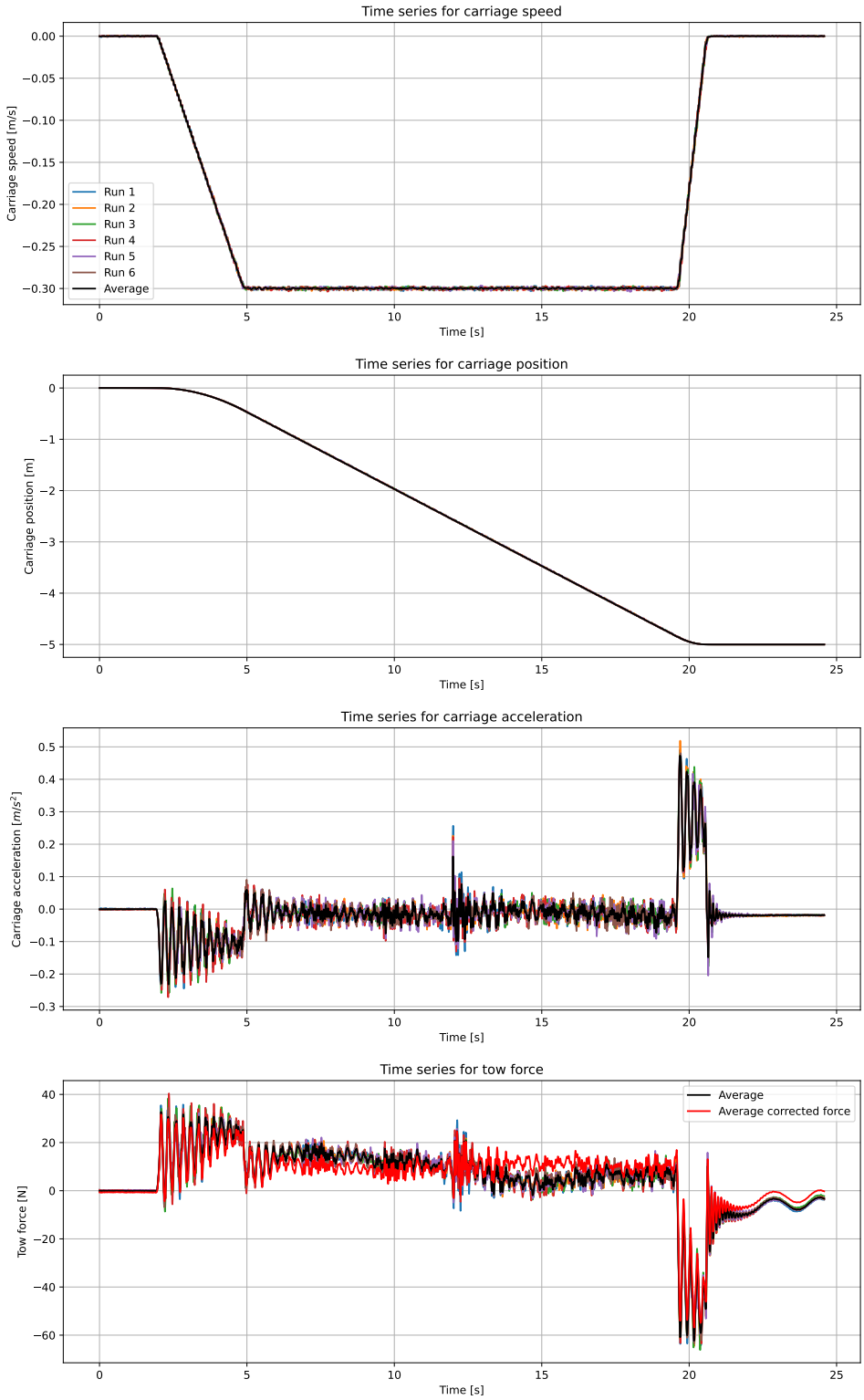

Figure D.15: Time series for model C, wet run, low acceleration, backward direction, speed 0.3 m/s

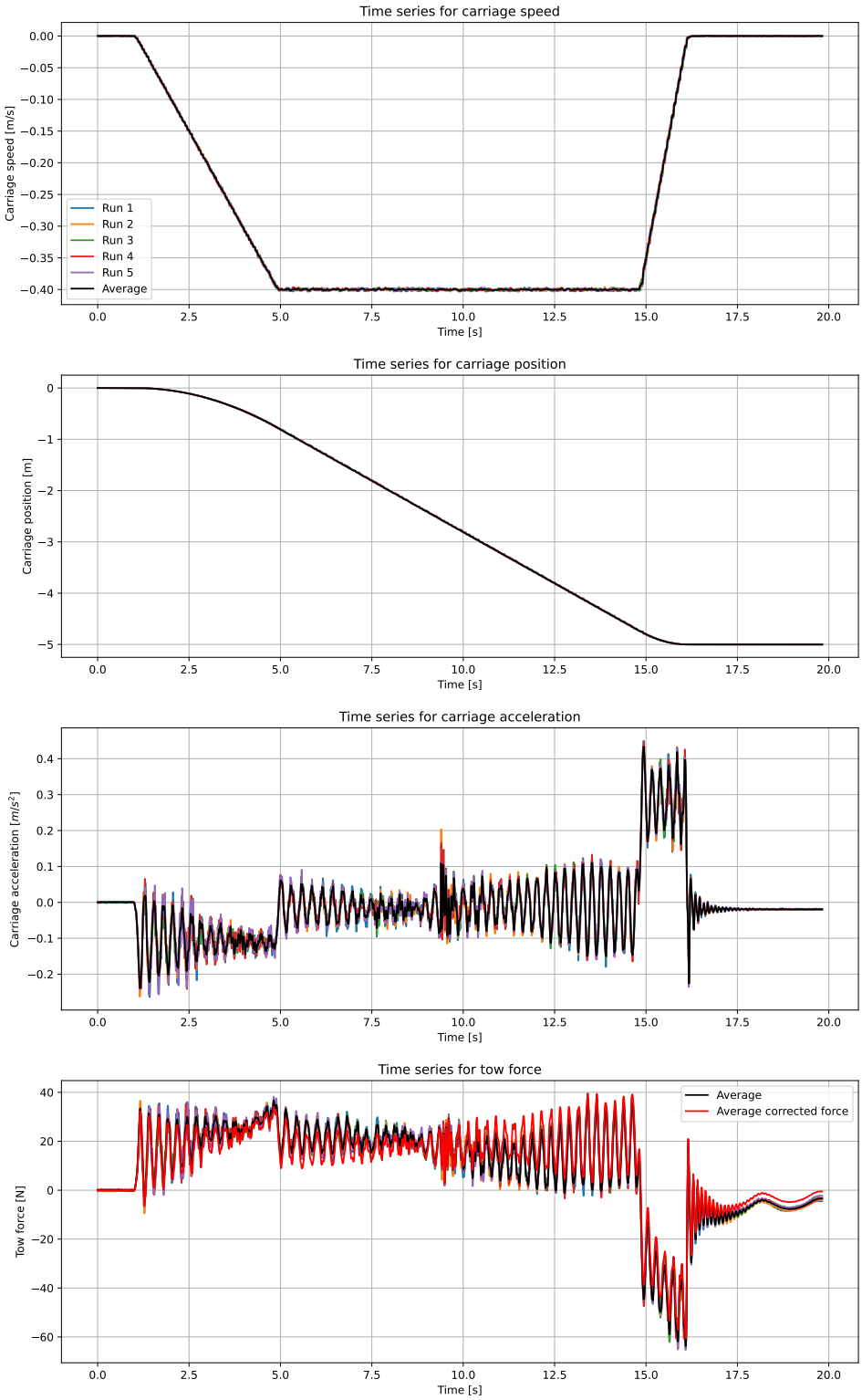

Figure D.16: Time series for model C, wet run, low acceleration, backward direction, speed 0.4 m/s

Appendix E

Time series plots for Model D

E.1 Wet run, model D, high acceleration, forward direction

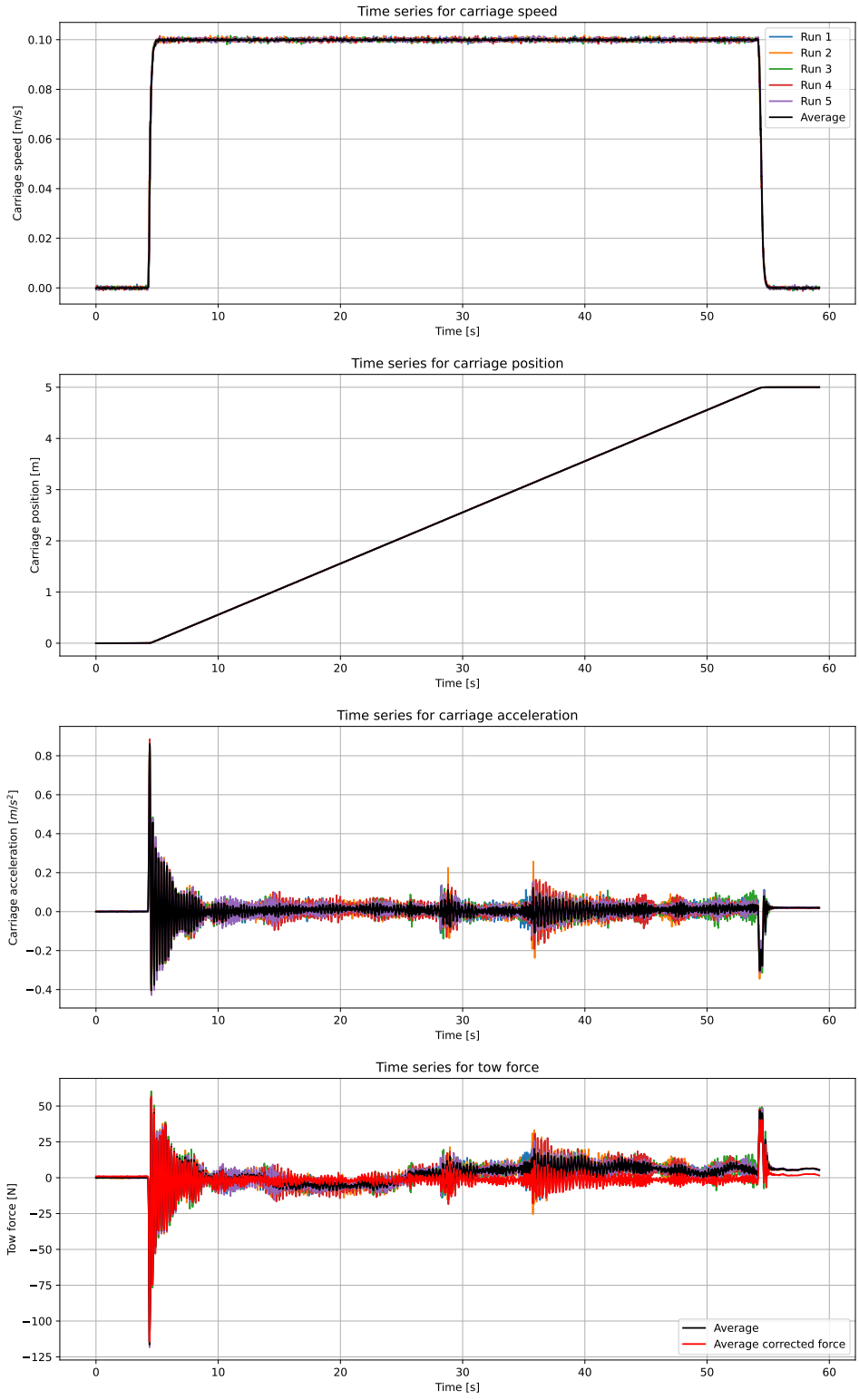

Figure E.1: Time series for model D, wet run, high acceleration, forward direction, speed 0.1 m/s

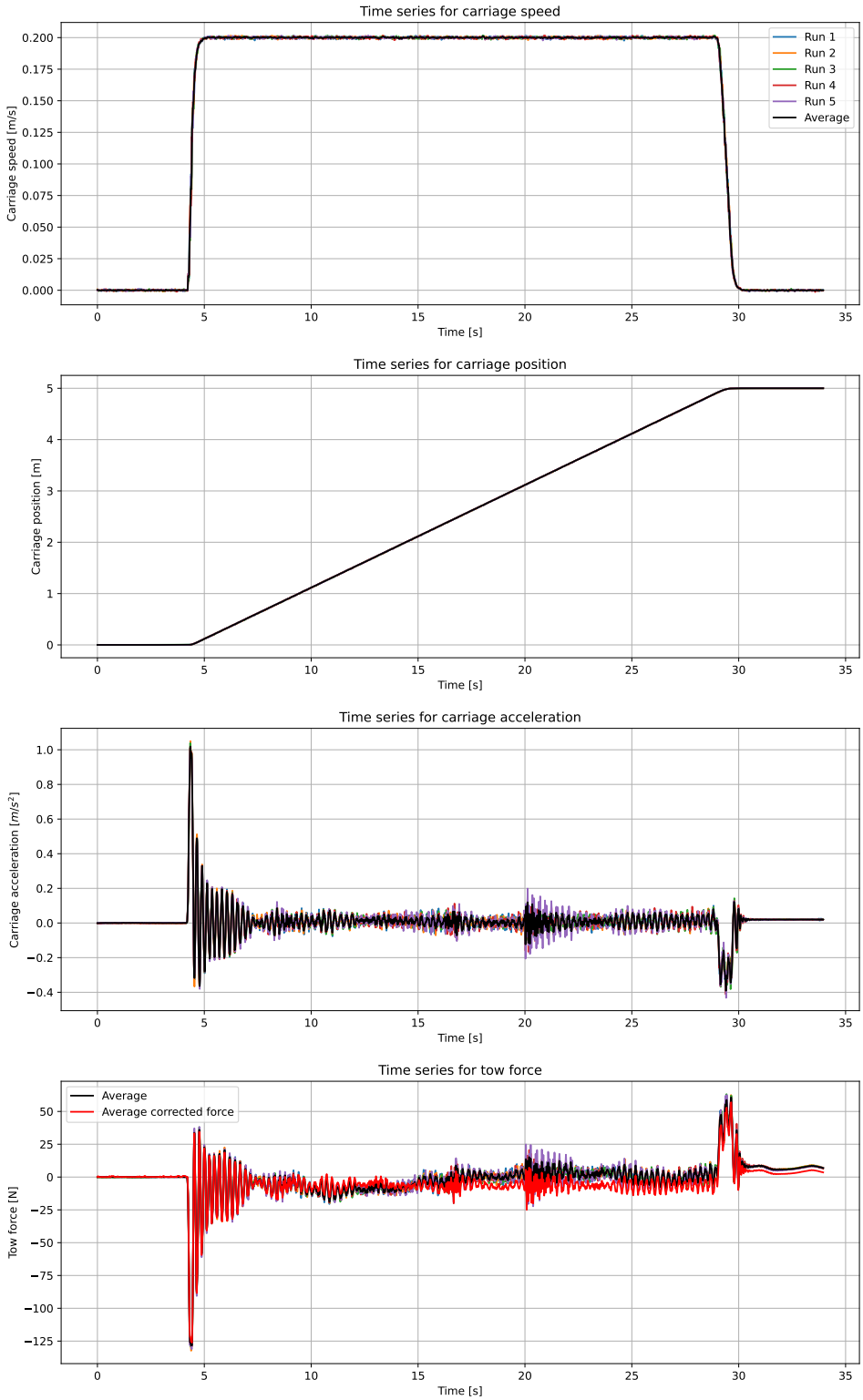

Figure E.2: Time series for model D, wet run, high acceleration, forward direction, speed 0.2 m/s

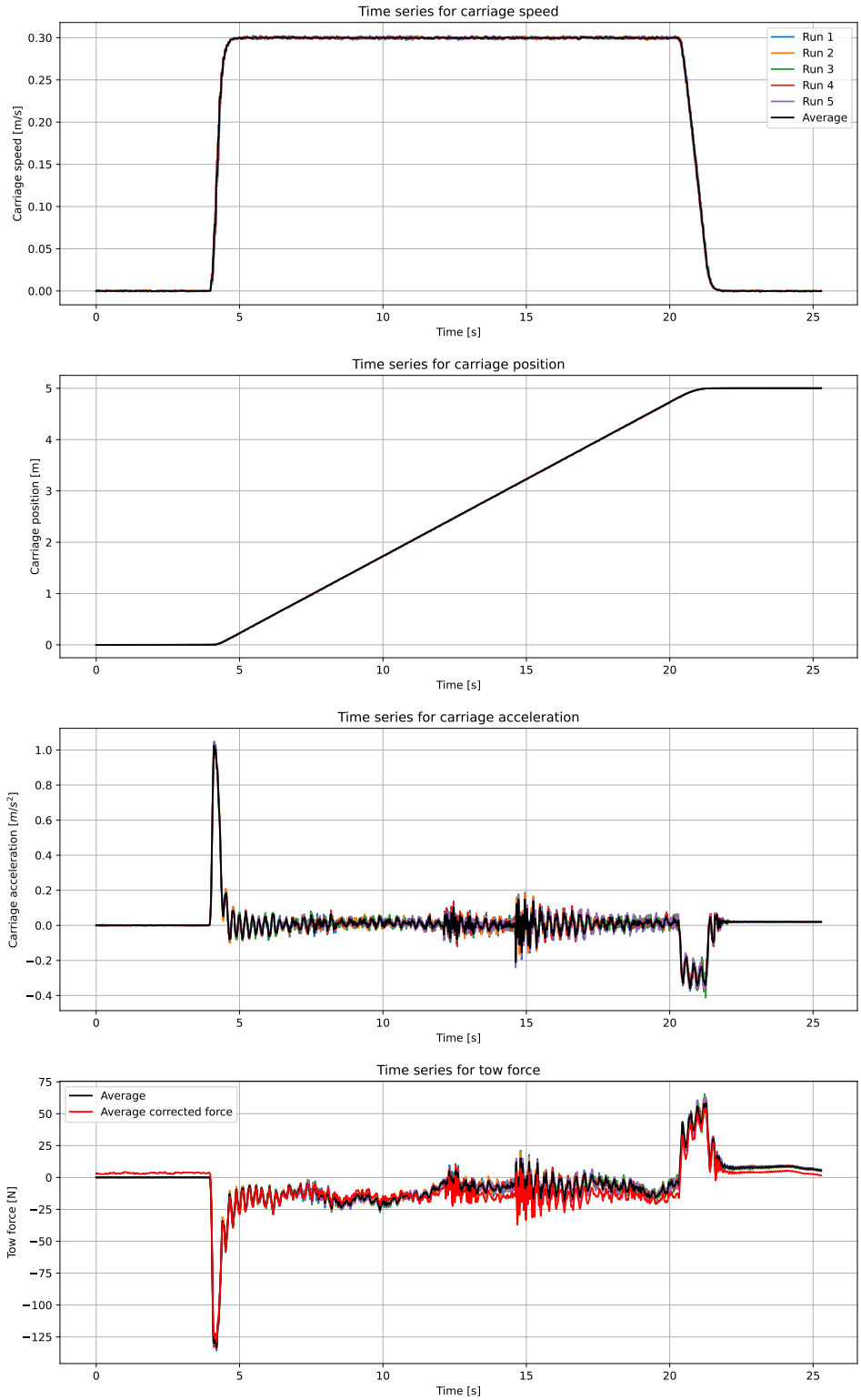

Figure E.3: Time series for model D, wet run, high acceleration, forward direction, speed 0.3 m/s

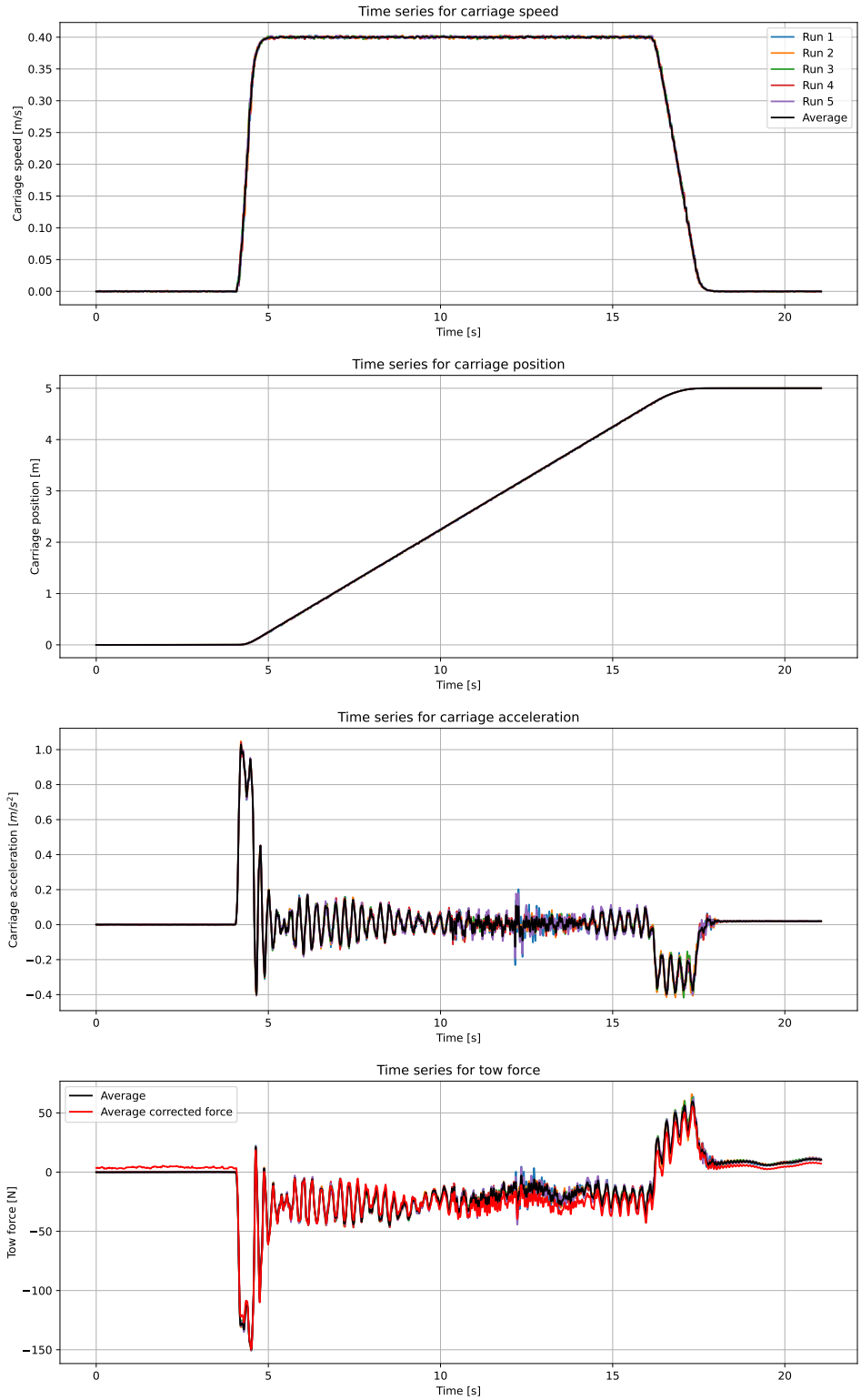

Figure E.4: Time series for model D, wet run, high acceleration, forward direction, speed 0.4 m/s

E.2 Wet run, model D, high acceleration, backward direction

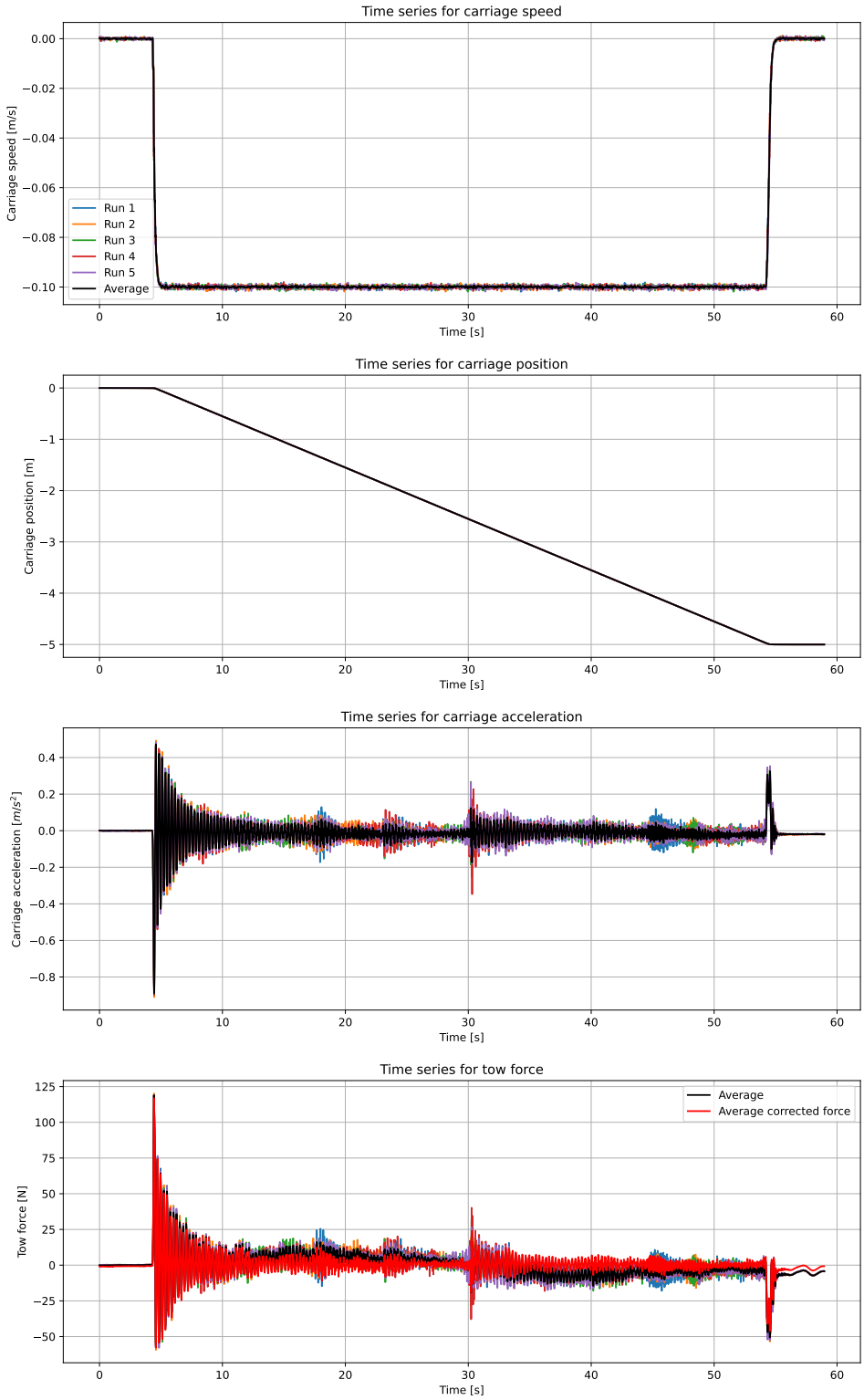

Figure E.5: Time series for model D, wet run, high acceleration, backward direction, speed 0.1 m/s

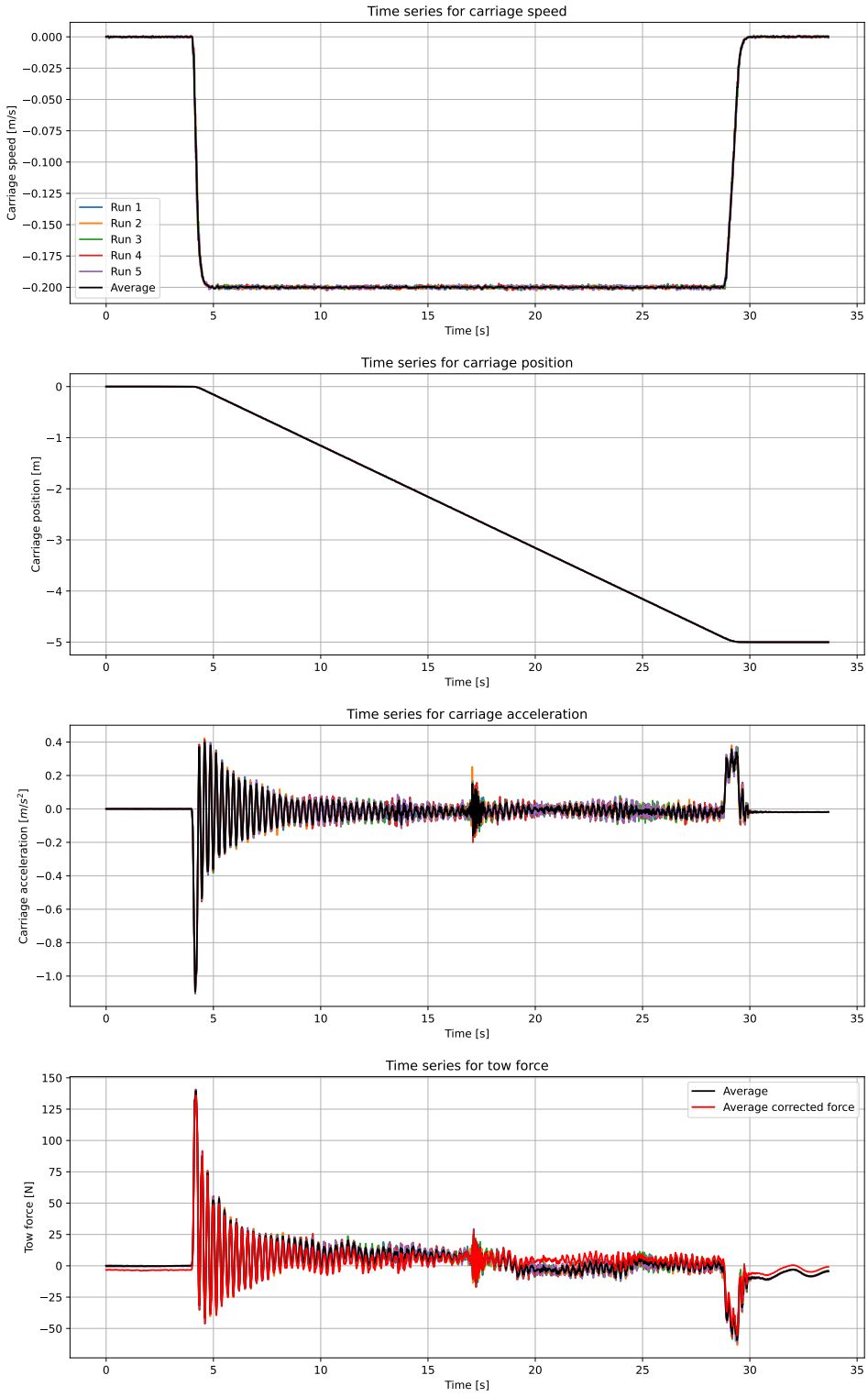

Figure E.6: Time series for model D, wet run, high acceleration, backward direction, speed 0.2 m/s

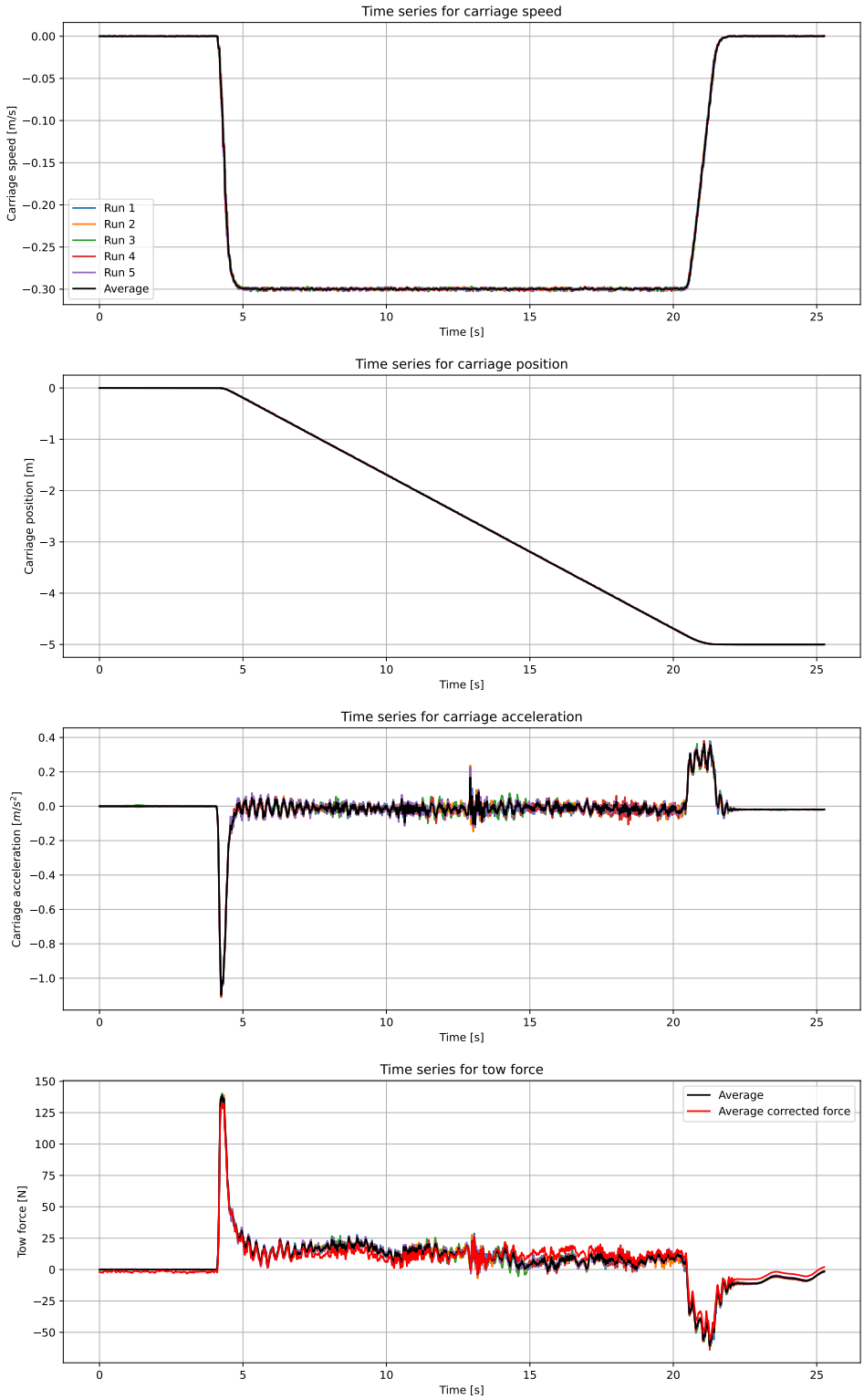

Figure E.7: Time series for model D, wet run, high acceleration, backward direction, speed 0.3 m/s

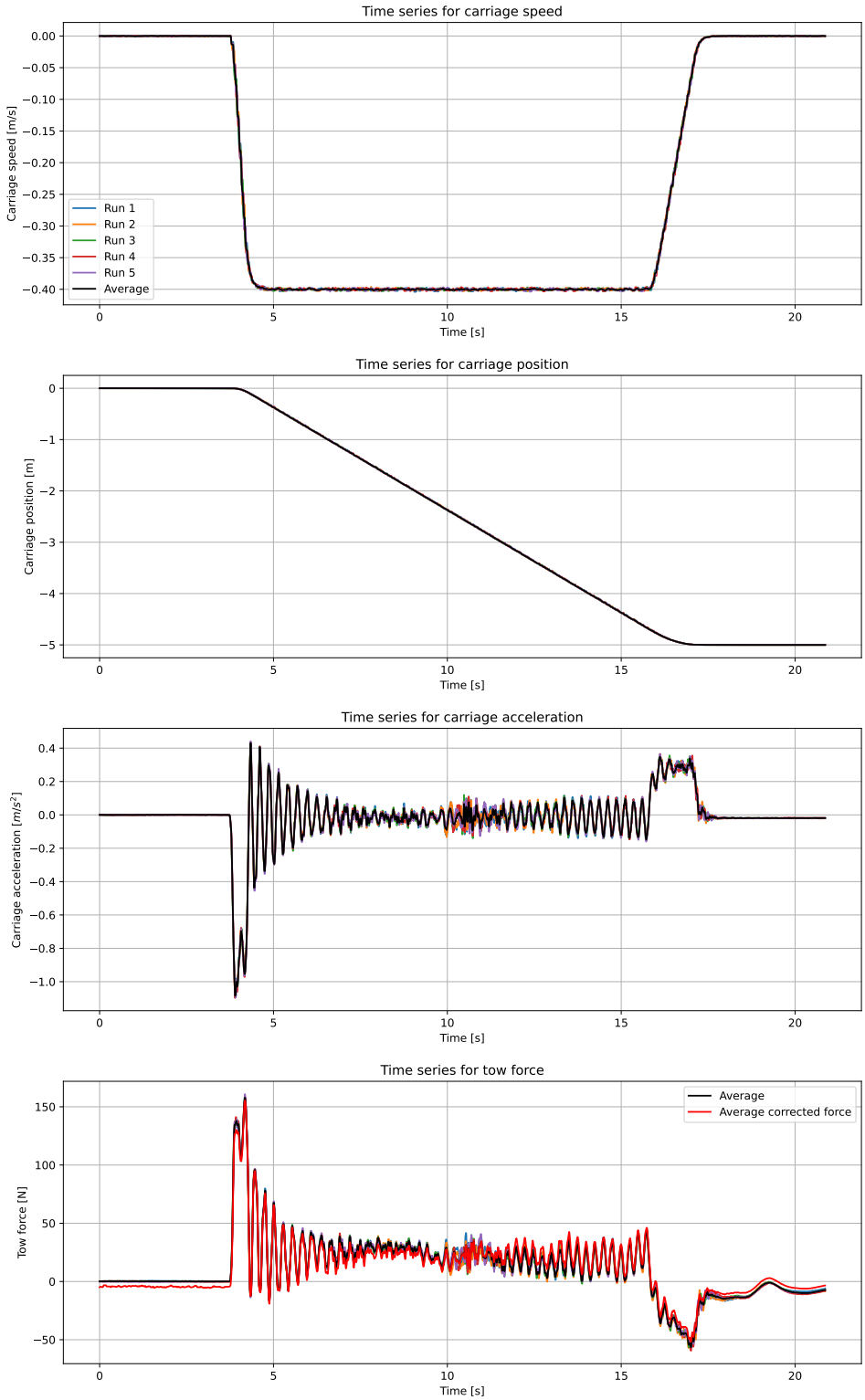

Figure E.8: Time series for model D, wet run, high acceleration, backward direction, speed 0.4 m/s

E.3 Wet run, model D, low acceleration, forward direction

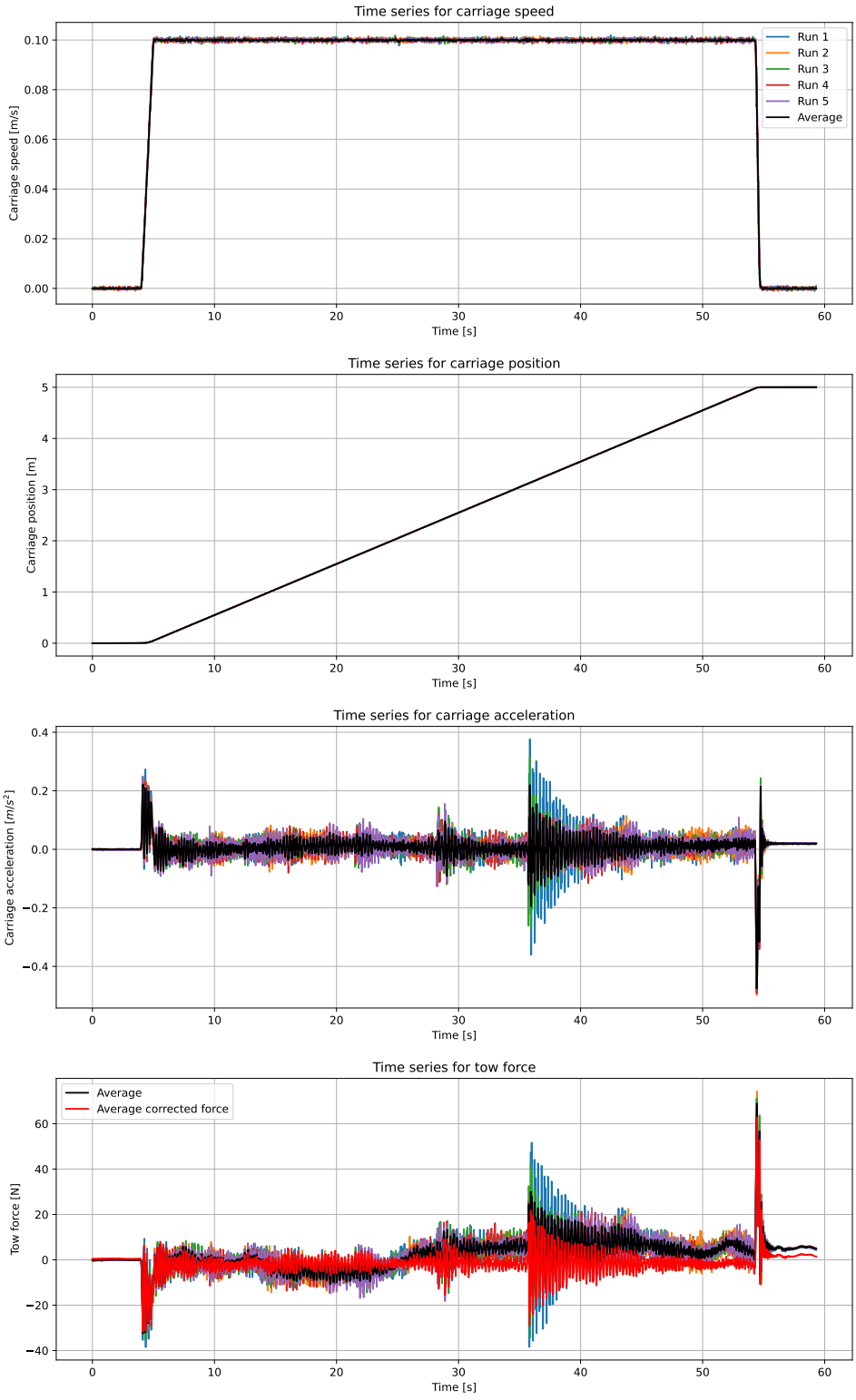

Figure E.9: Time series for model D, wet run, low acceleration, forward direction, speed 0.1 m/s

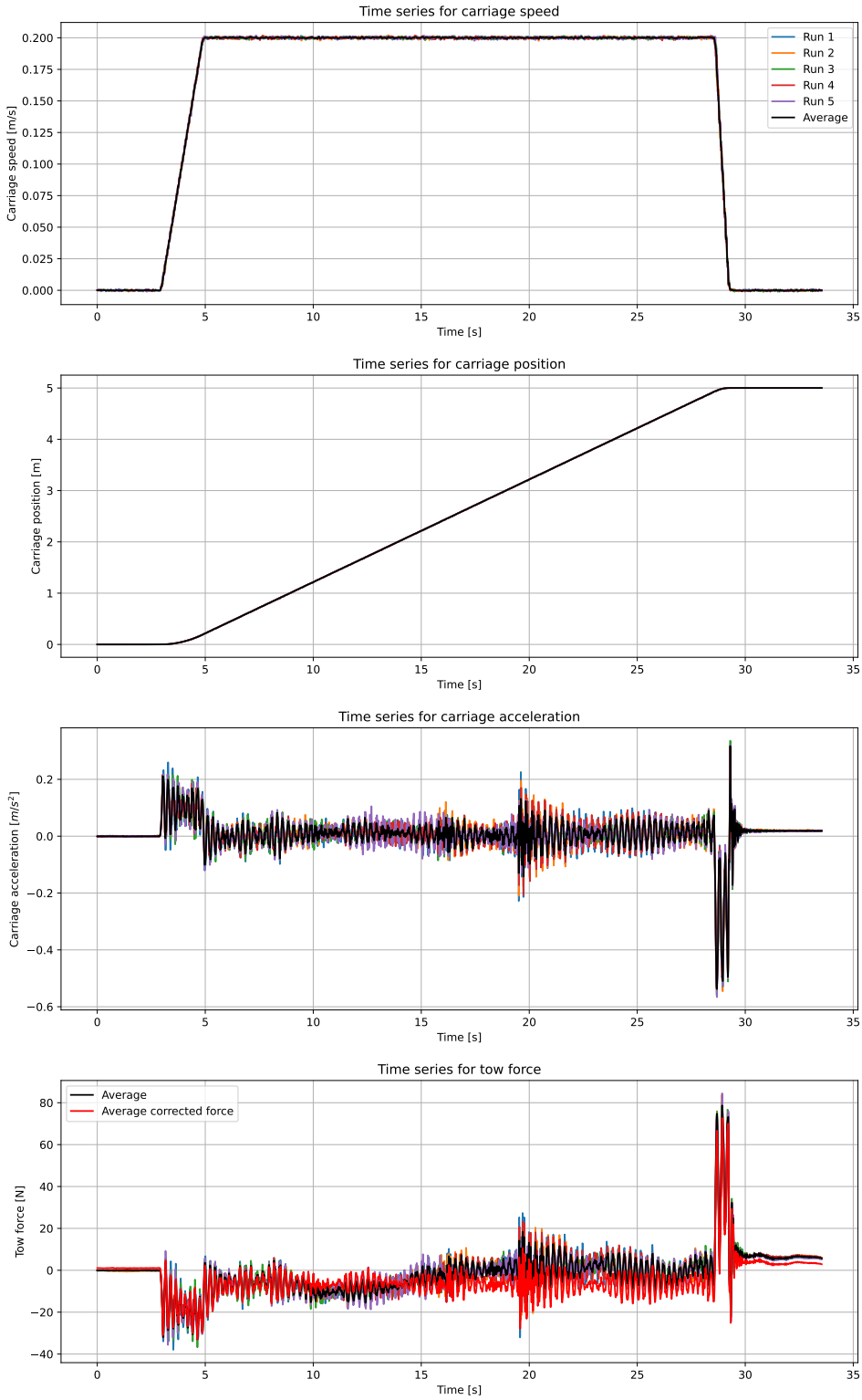

Figure E.10: Time series for model D, wet run, low acceleration, forward direction, speed 0.2 m/s

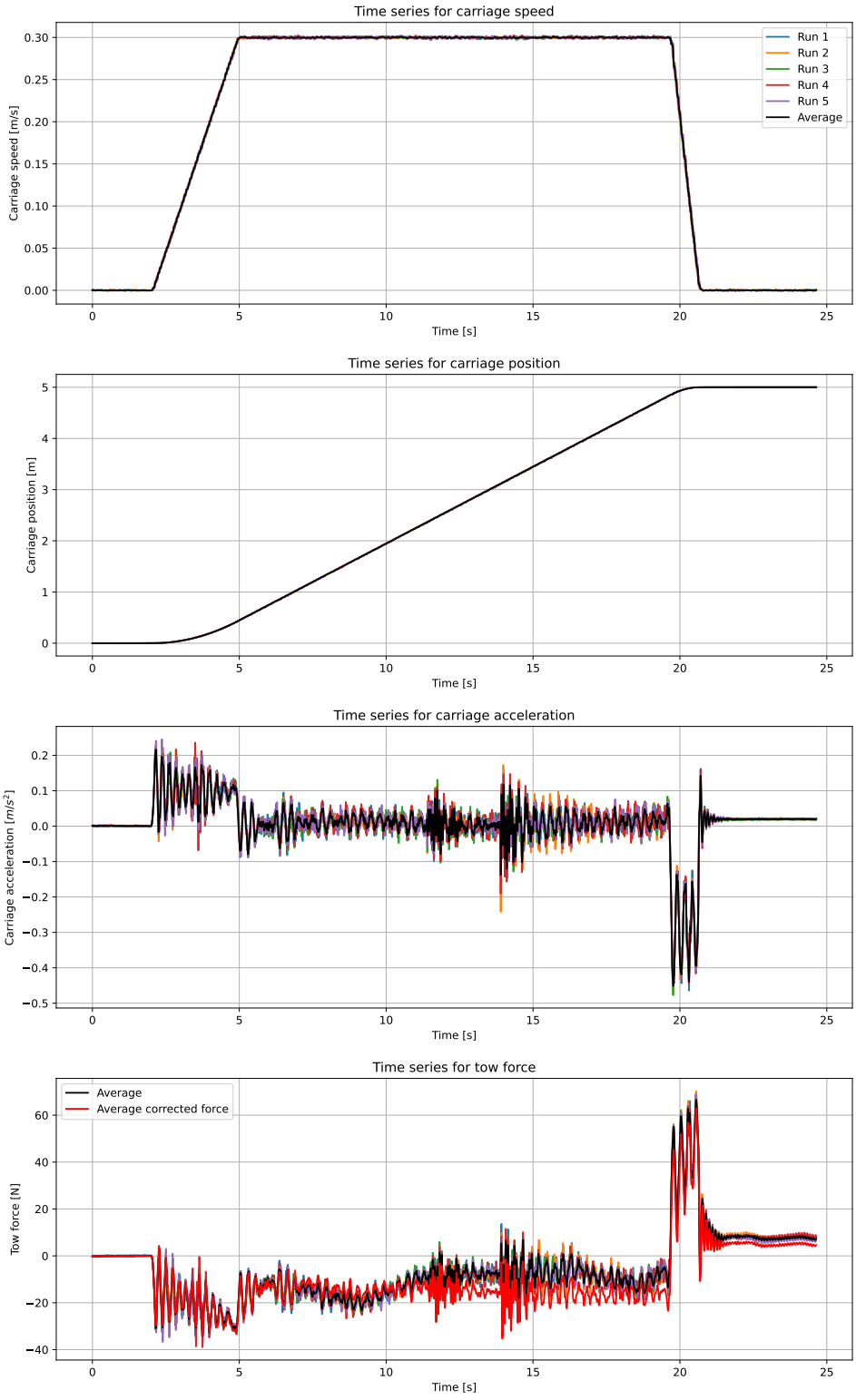

Figure E.11: Time series for model D, wet run, low acceleration, forward direction, speed 0.3 m/s

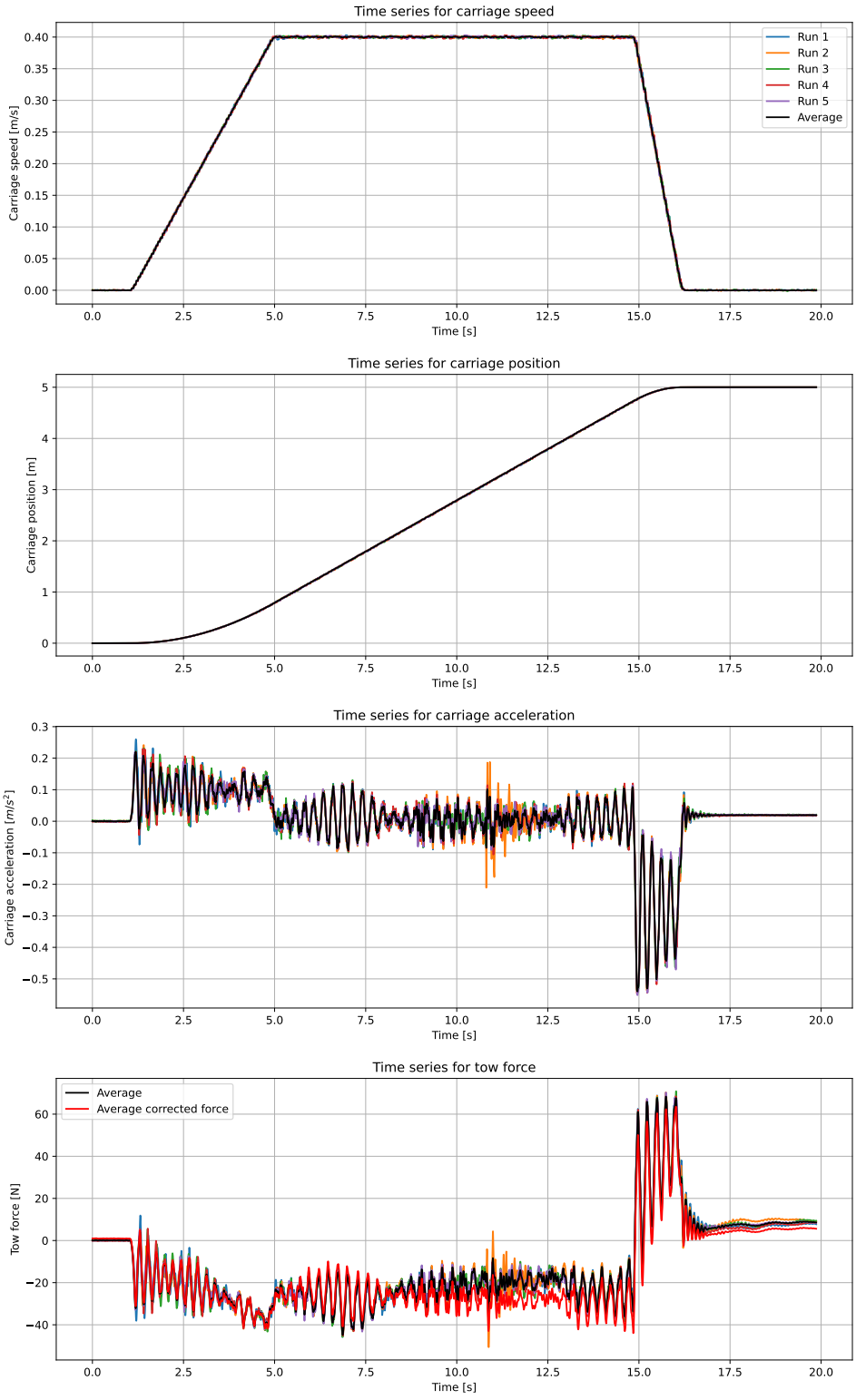

Figure E.12: Time series for model D, wet run, low acceleration, forward direction, speed 0.4 m/s

E.4 Wet run, model D, low acceleration, backward direction

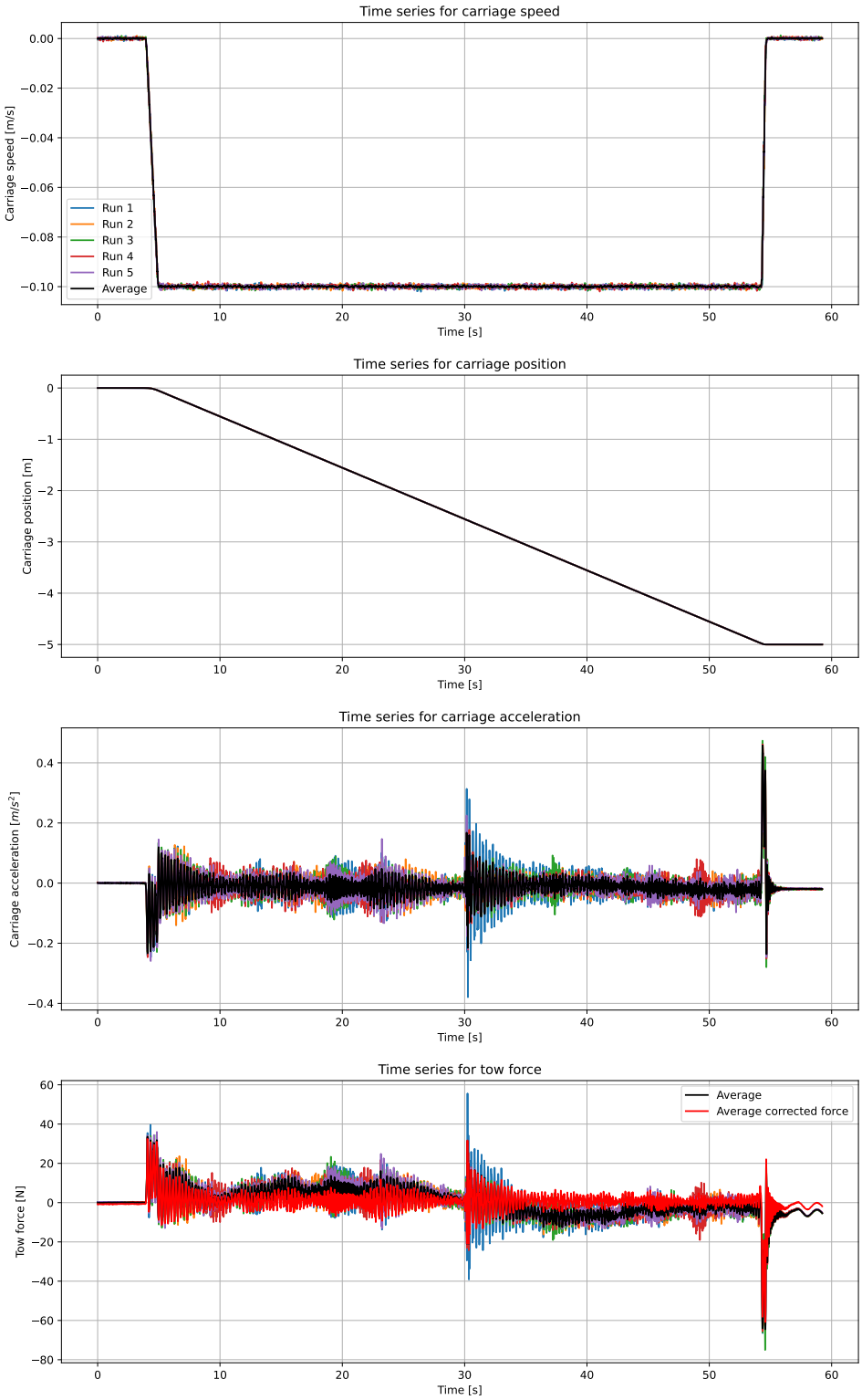

Figure E.13: Time series for model D, wet run, low acceleration, backward direction, speed 0.1 m/s

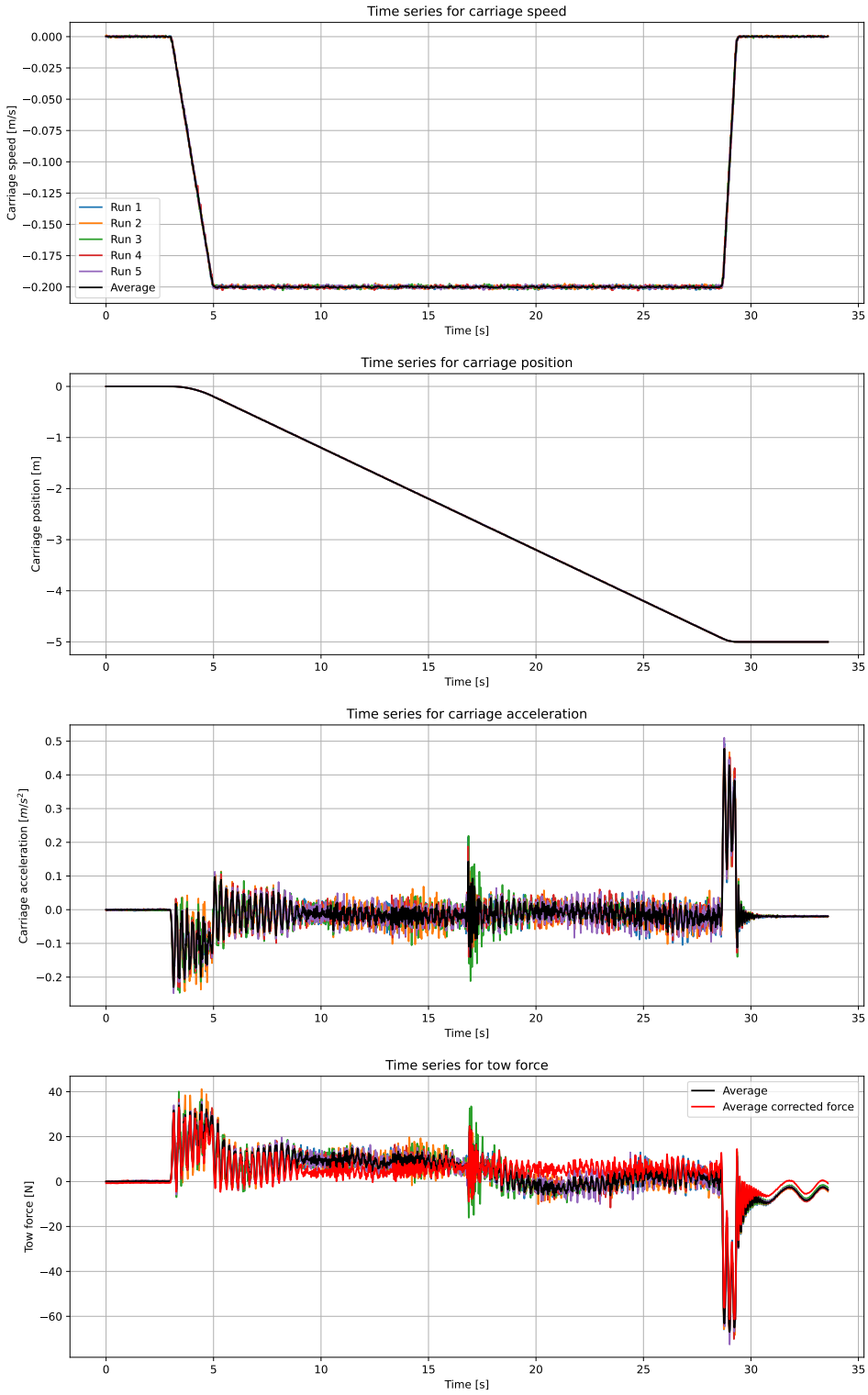

Figure E.14: Time series for model D, wet run, low acceleration, backward direction, speed 0.2 m/s

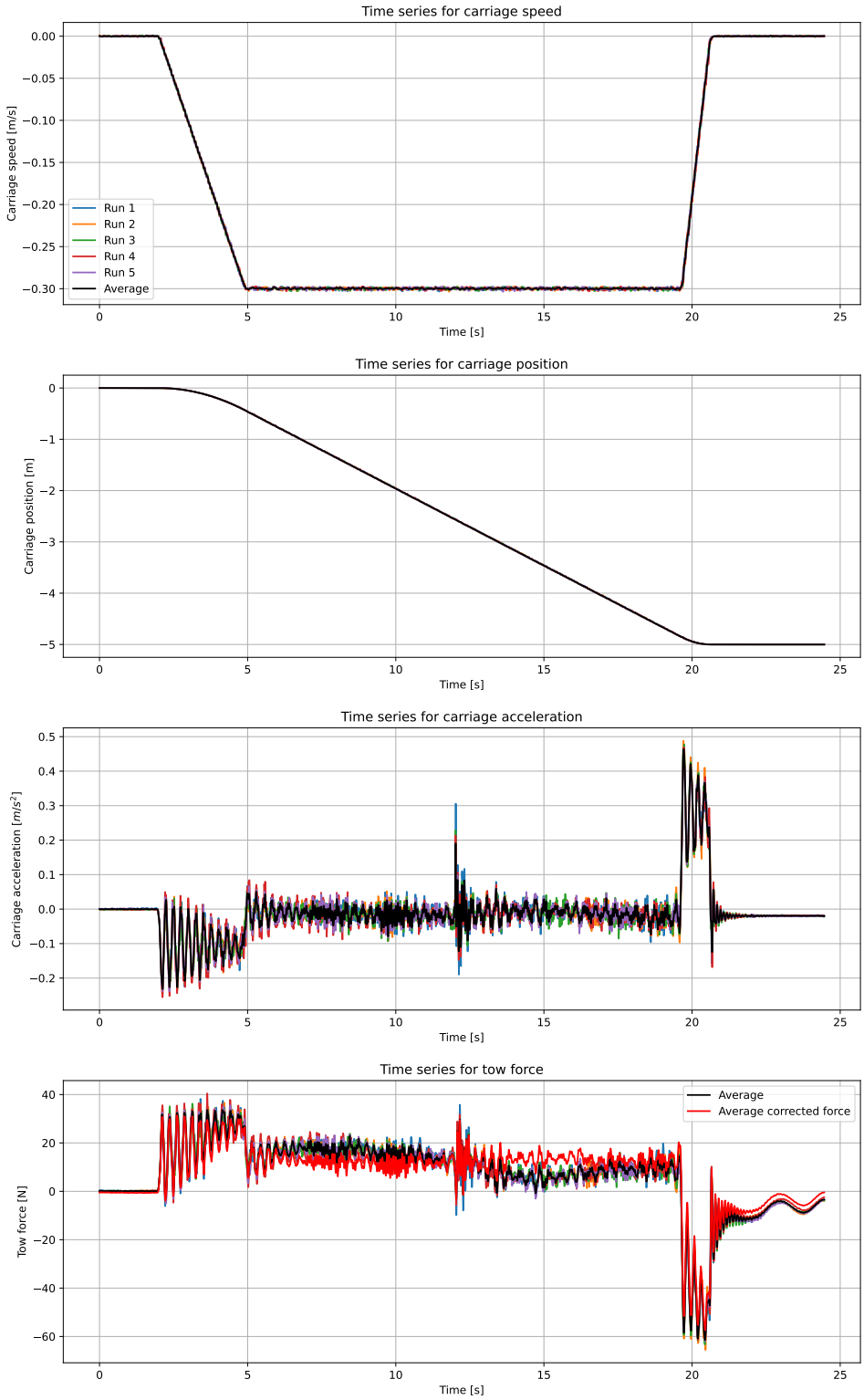

Figure E.15: Time series for model D, wet run, low acceleration, backward direction, speed 0.3 m/s

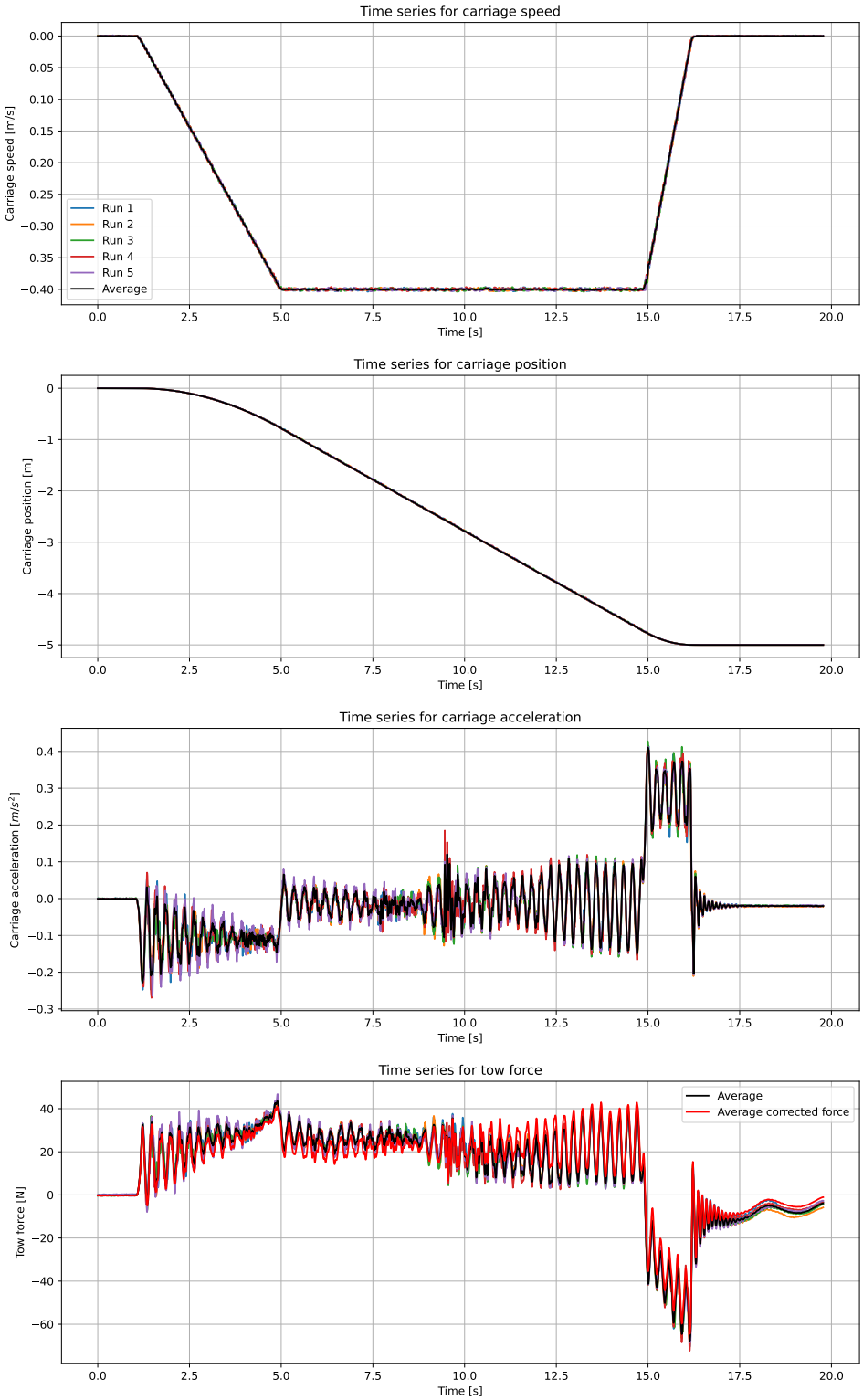

Figure E.16: Time series for model D, wet run, low acceleration, backward direction, speed 0.4 m/s

Appendix F

Results of 2D CFD simulations for Aarsnes ship sections

The reference for ship section numbers referred in the subsequent sections and the approximate location of the section along the ship length is indicated in Figure 5.14.

The drag coefficient curve for Aarsnes section section shown in Figure 4.2 is a smoothed version of the Aarsnes results for $Rn = 1.24 \cdot 10^7$. They are smoothed in order to use them in 2D+t method (see Section 3.2.2) which requires the calculation of the slopes of the drag curve. In the subsequent plots the non-smoothed original versions are presented for comparison against 2D CFD results.

F.1 Aarsnes ship section 1

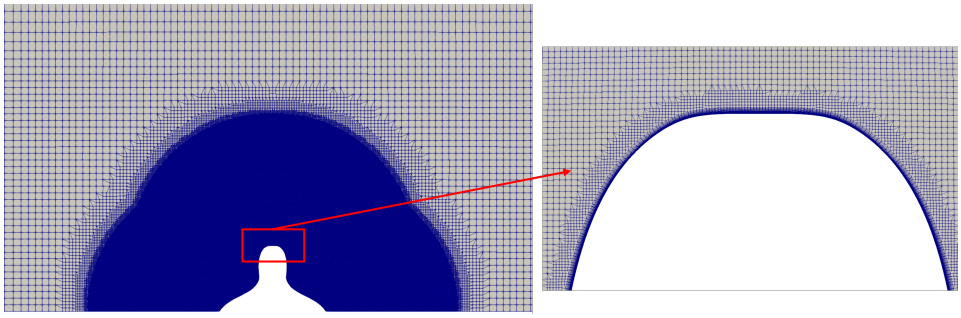

Figure F.1: Mesh around Aarsnes ship section 1. Level 4 is used for the refinement of the wake region and Level 5 is used for the surface refinement.

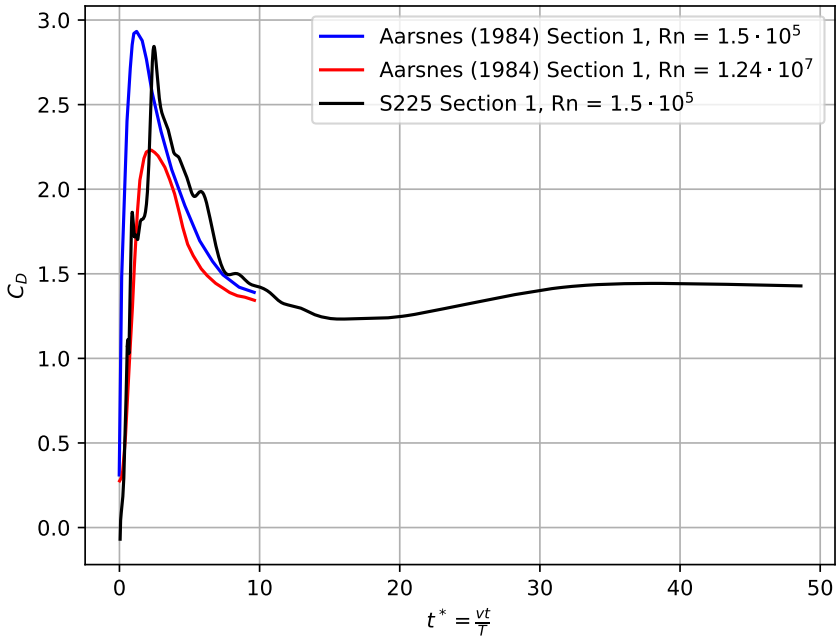

Figure F.2: Drag coefficient from 2D CFD simulation with $Rn = 1.5 \cdot 10^5$ is plotted against non-dimensional time for Aarsnes ship section 1. Drag curves obtained using vortex tracking method from Aarsnes (1984) is also indicated for $Rn = 1.5 \cdot 10^5$ and $Rn = 1.24 \cdot 10^7$.

F.2 Aarsnes ship section 2

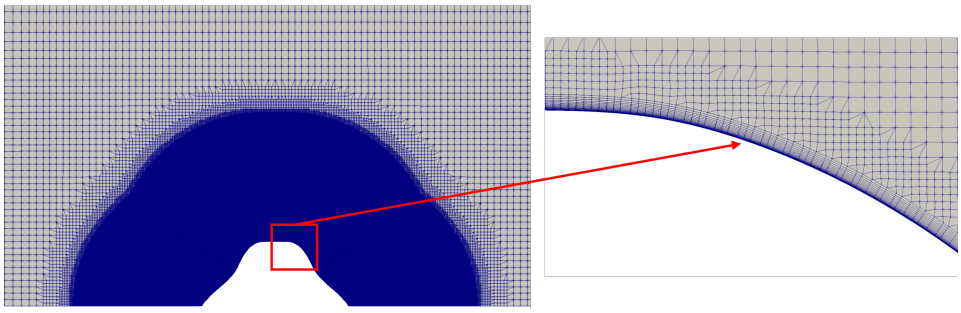

Figure F.3: Mesh around Aarsnes ship section 2. Level 4 is used for the refinement of the wake region and Level 5 is used for the surface refinement.

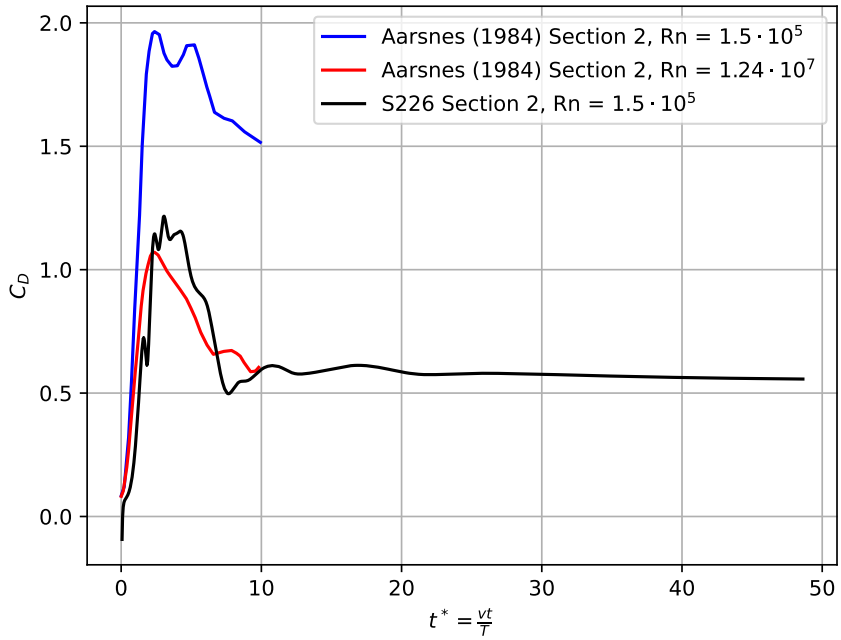

Figure F.4: Drag coefficient from 2D CFD simulation with $Rn = 1.5 \cdot 10^5$ is plotted against non-dimensional time for Aarsnes ship section 2. Drag curves obtained using vortex tracking method from Aarsnes (1984) is also indicated for $Rn = 1.5 \cdot 10^5$ and $Rn = 1.24 \cdot 10^7$.

F.3 Aarsnes ship section 10

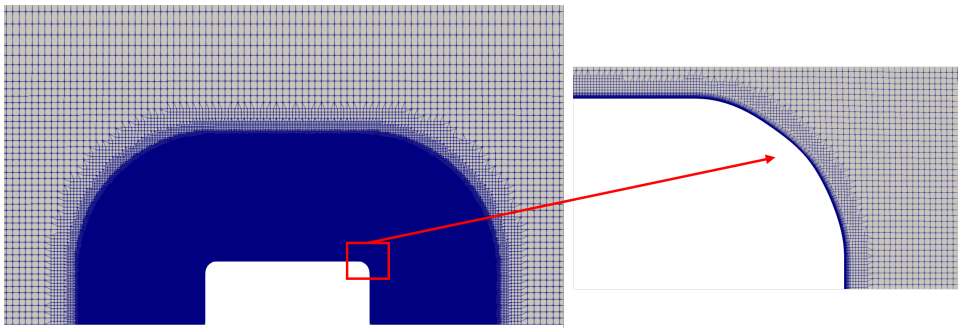

Figure F.5: Mesh around Aarsnes ship section 10. Level 4 is used for the refinement of the wake region and Level 5 is used for the surface refinement.

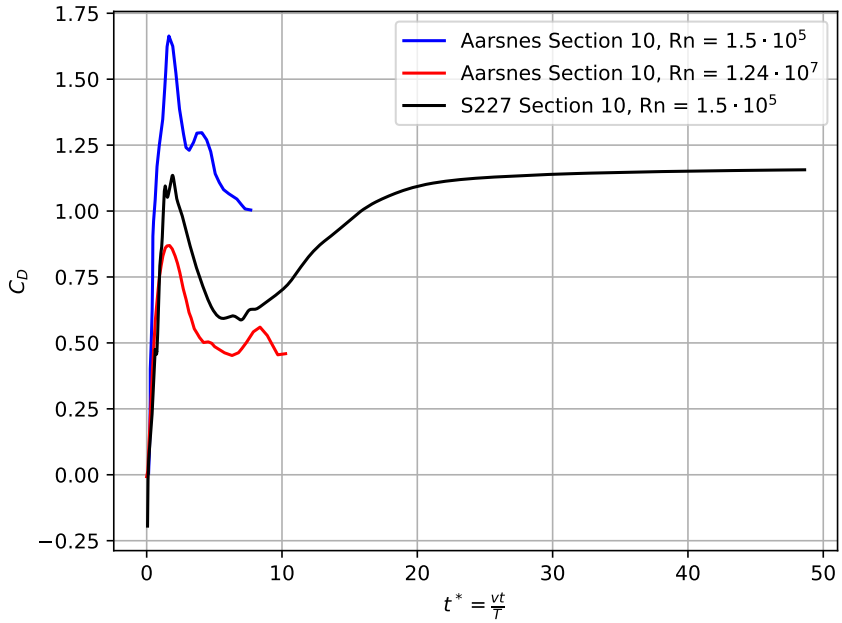

Figure F.6: Drag coefficient from 2D CFD simulation with $Rn = 1.5 \cdot 10^5$ is plotted against non-dimensional time for Aarsnes ship section 10. Drag curves obtained using vortex tracking method from Aarsnes (1984) is also indicated for $Rn = 1.5 \cdot 10^5$ and $Rn = 1.24 \cdot 10^7$.

F.4 Aarsnes ship section 19

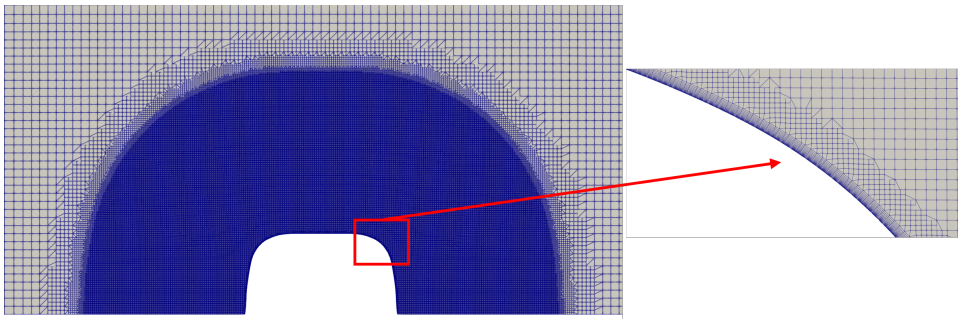

Figure F.7: Mesh around Aarsnes ship section 19. Level 4 is used for the refinement of the wake region and Level 5 is used for the surface refinement.

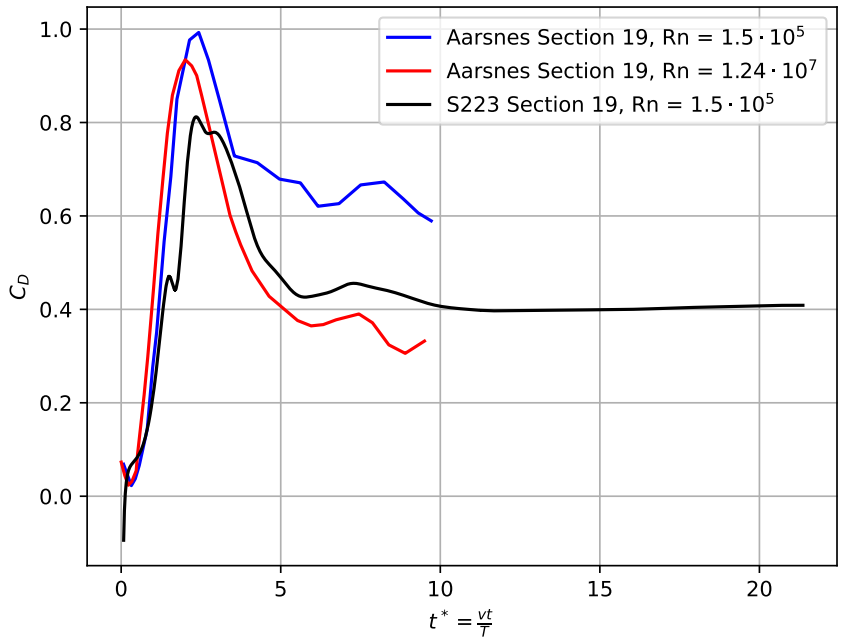

Figure F.8: Drag coefficient from 2D CFD simulation with $Rn = 1.5 \cdot 10^5$ is plotted against non-dimensional time for Aarsnes ship section 19. Drag curves obtained using vortex tracking method from Aarsnes (1984) is also indicated for $Rn = 1.5 \cdot 10^5$ and $Rn = 1.24 \cdot 10^7$.

F.5 Aarsnes ship section 20

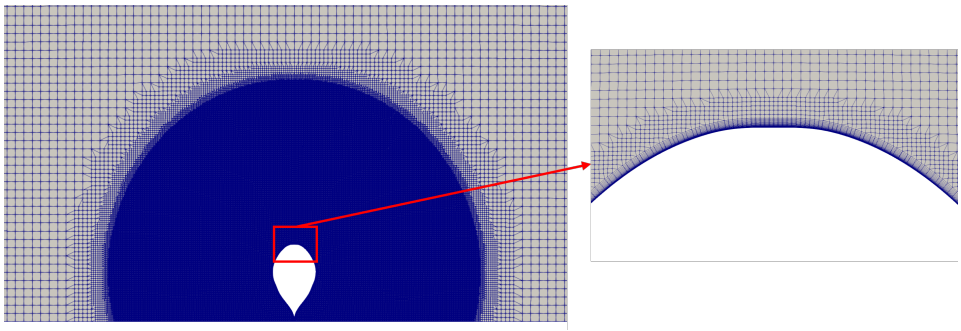

Figure F.9: Mesh around Aarsnes ship section 20. Level 4 is used for the refinement of the wake region and Level 5 is used for the surface refinement.

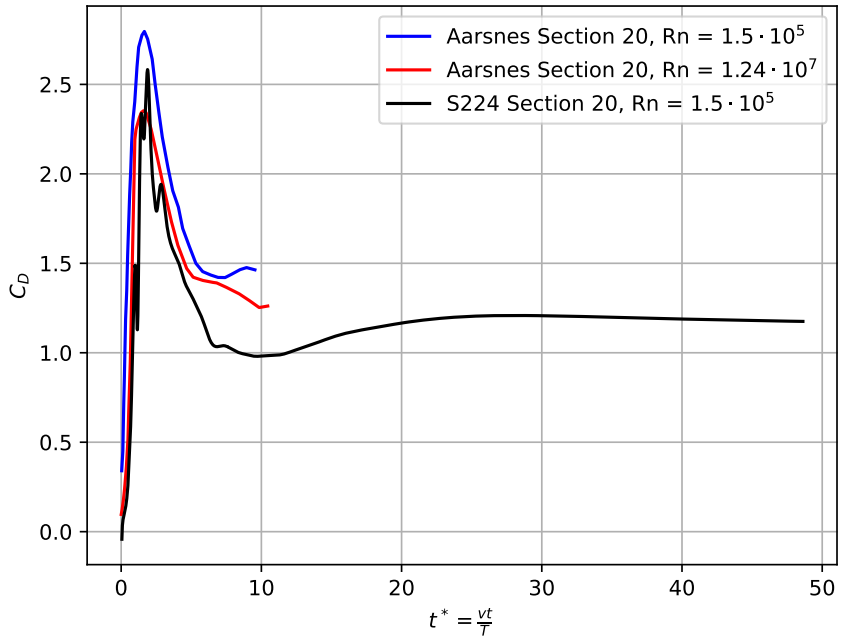

Figure F.10: Drag coefficient from 2D CFD simulation with $Rn = 1.5 \cdot 10^5$ is plotted against non-dimensional time for Aarsnes ship section 20. Drag curves obtained using vortex tracking method from Aarsnes (1984) is also indicated for $Rn = 1.5 \cdot 10^5$ and $Rn = 1.24 \cdot 10^7$.

Appendix G

Flow visualization of 2D CFD simulations

G.1 Flow field visualization around circular cylinder (S142)

Flow field visualization for simulation S142

t*	Velocity field	Vorticity field
0.6	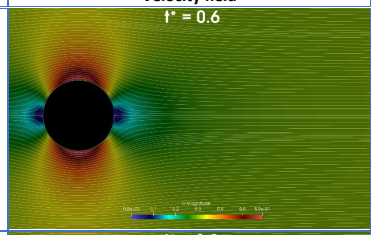	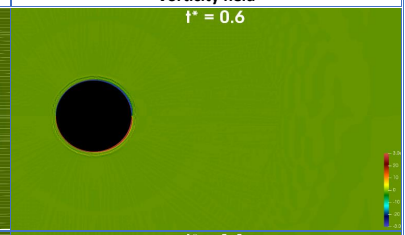
1.1	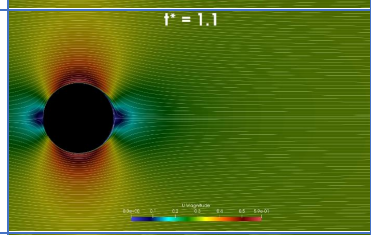	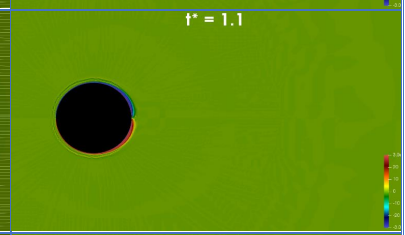
1.7	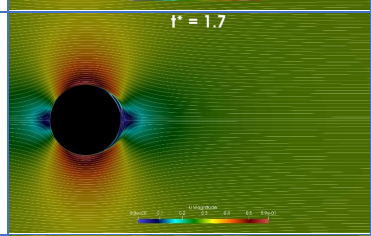	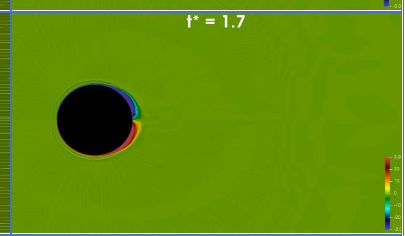
2.2	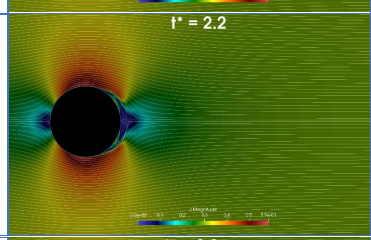	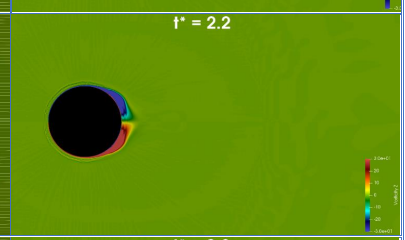
2.8	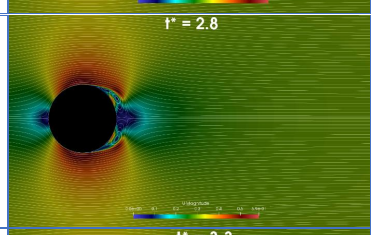	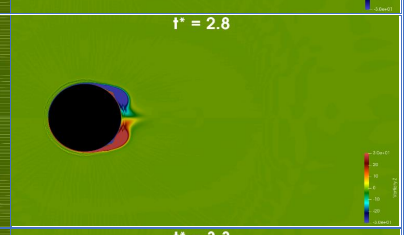
3.3	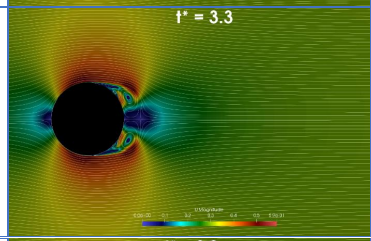	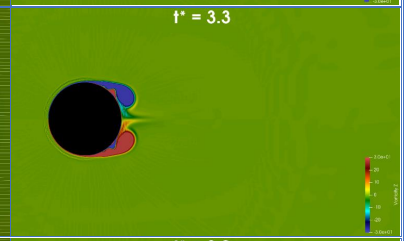
3.9	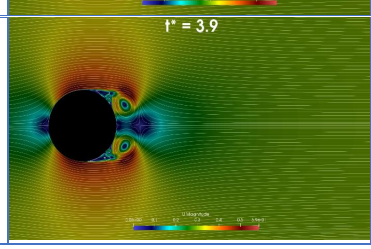	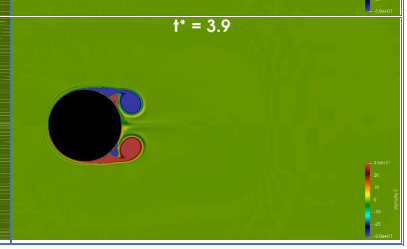

Flow field visualization for simulation S142

	Velocity field	Vorticity field
4.4	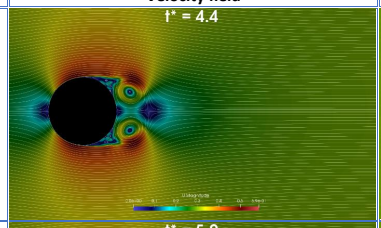	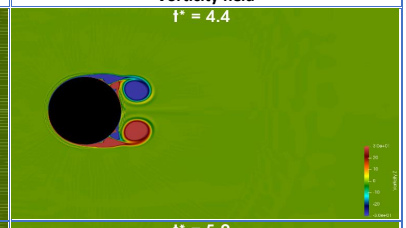
5.0	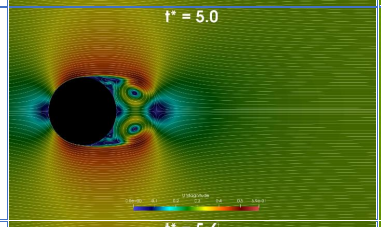	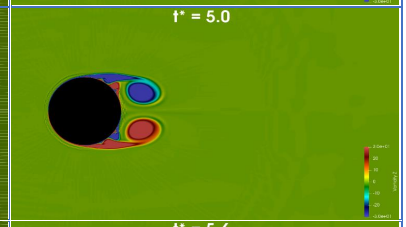
5.6	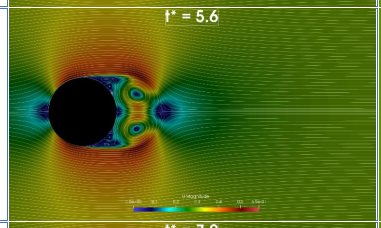	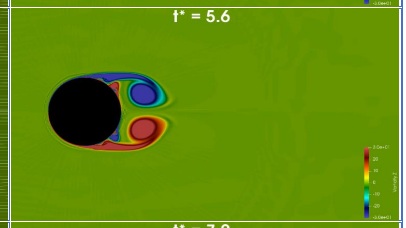
7.2	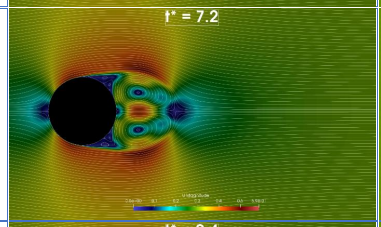	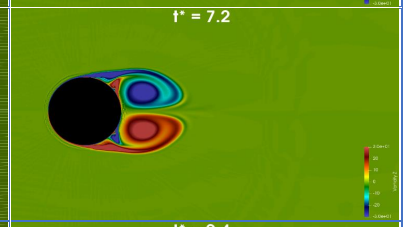
9.4	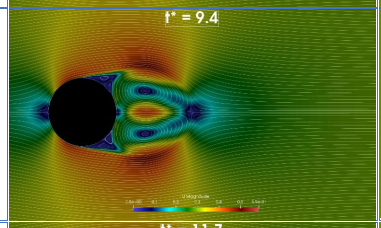	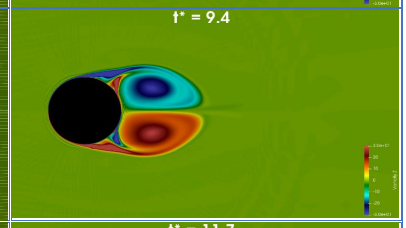
11.7	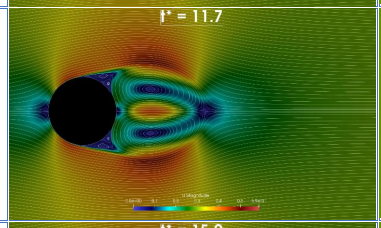	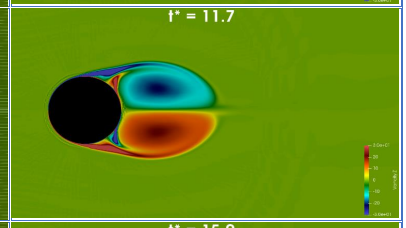
15	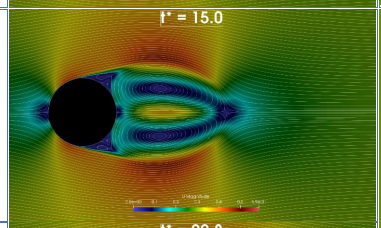	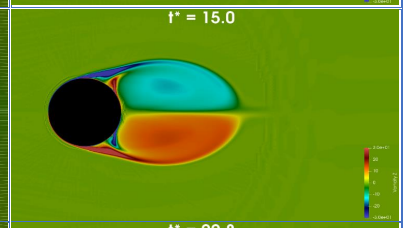
22.8	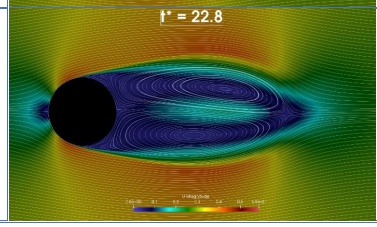	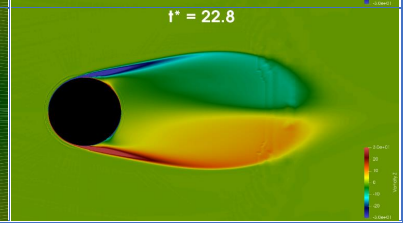

Flow field visualization for simulation S142

	Velocity field	Vorticity field
33.9	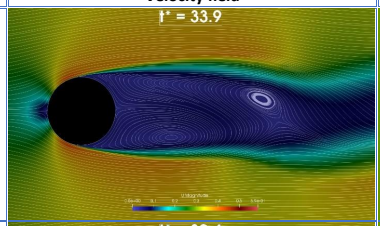	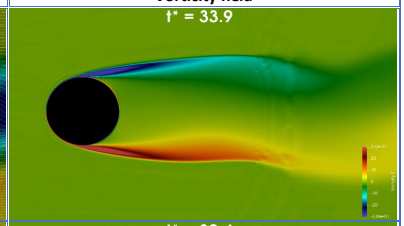
39.4	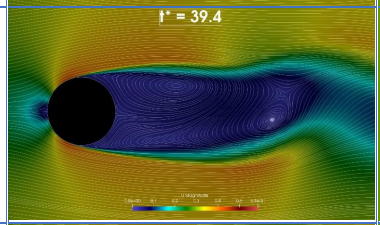	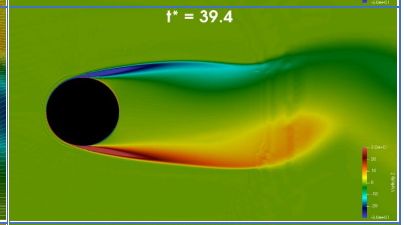
50.5	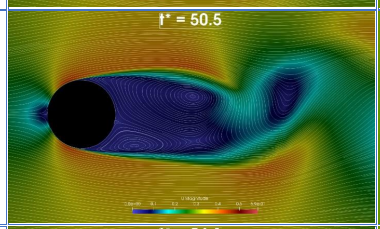	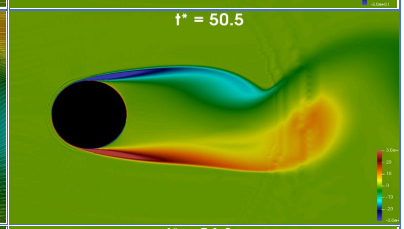
56.1	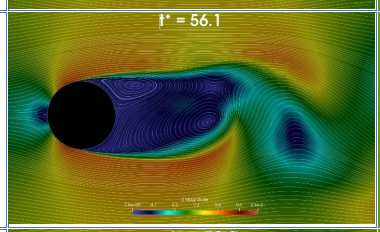	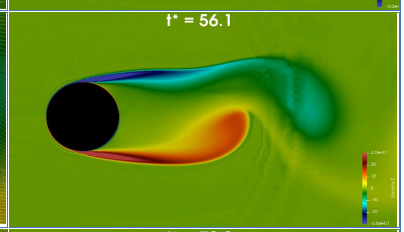
70	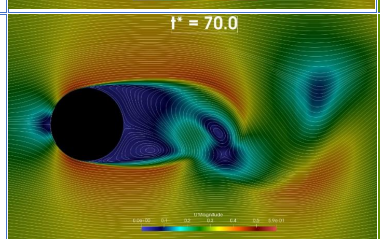	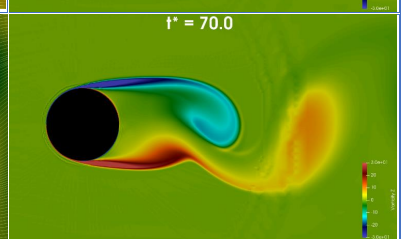
83.8	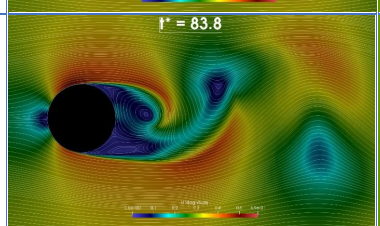	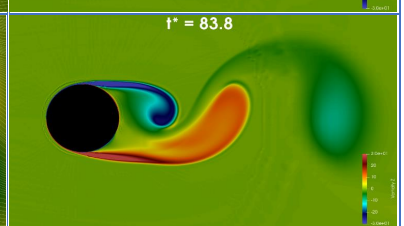
97.7	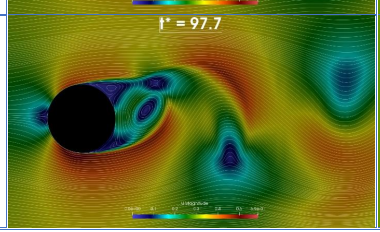	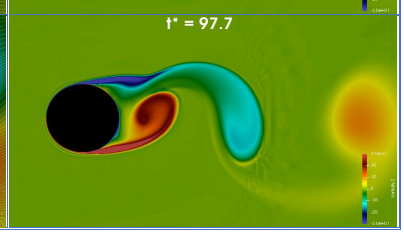

G.2 Flow field visualization around semi-circular cylinder (S141)

Flow field visualization for simulation S141

t*	Velocity field	Vorticity field
0.6	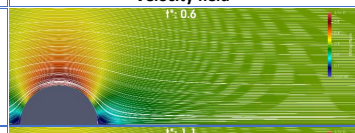	
1.1	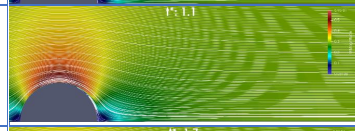	
1.7	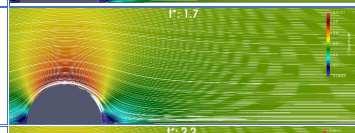	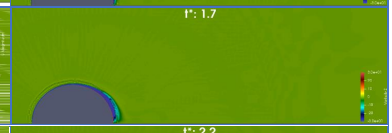
2.2	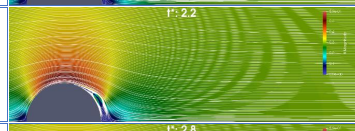	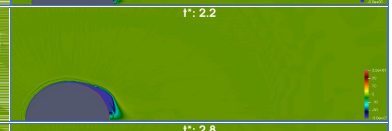
2.8	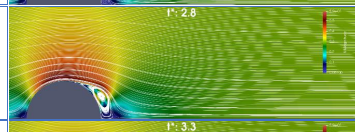	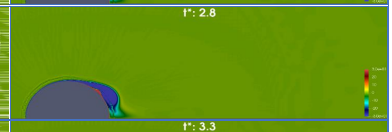
3.3	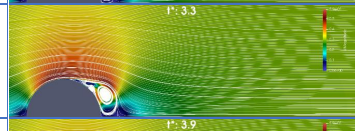	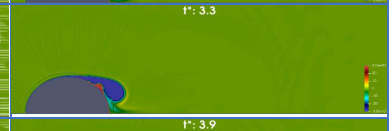
3.9	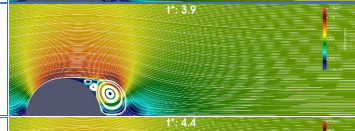	
4.4	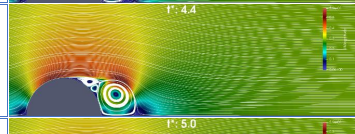	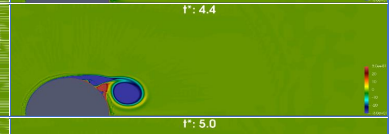
5.0	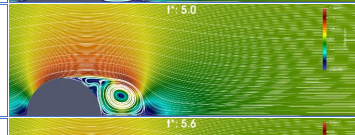	
5.6	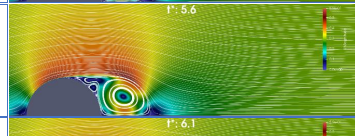	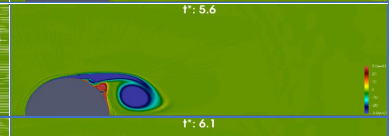
6.1	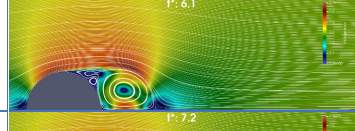	
7.2	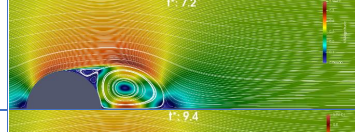	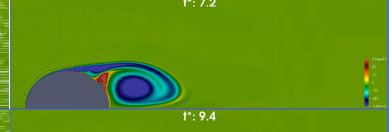
9.4	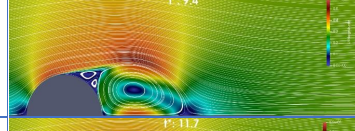	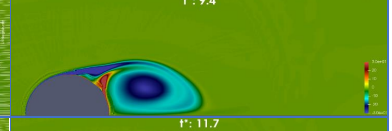
11.7	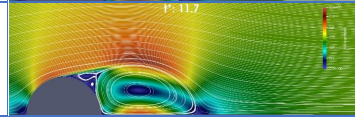	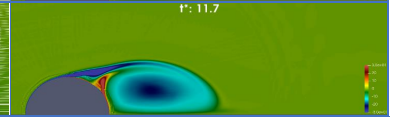

Flow field visualization for simulation S141

	Velocity field	Vorticity field
12.8	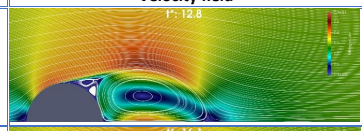	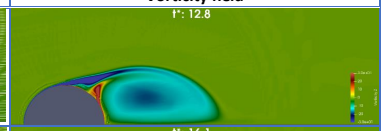
16.1	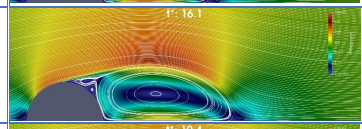	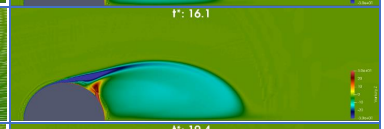
19.4	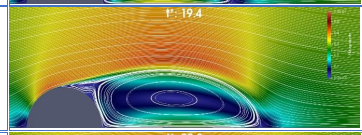	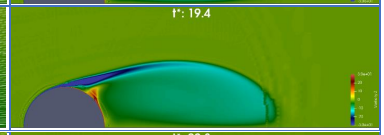
22.8	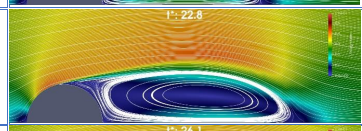	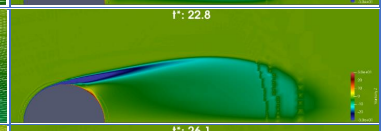
26.1	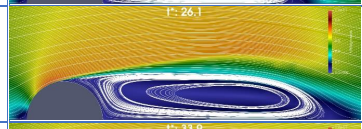	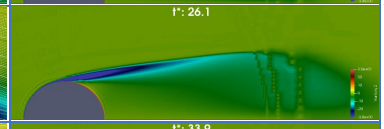
33.9	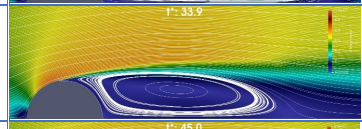	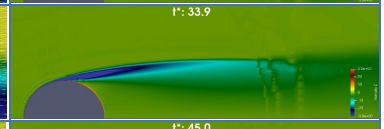
45.0	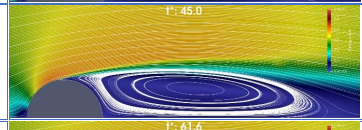	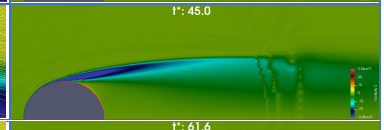
61.6	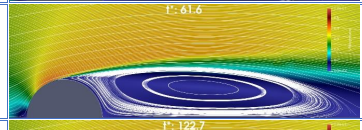	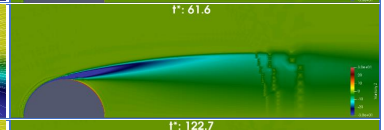
122.7	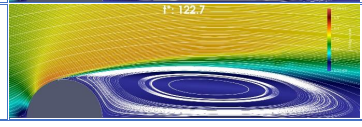	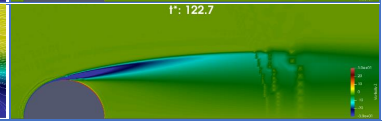

G.3 Flow around Aarsnes Section 10 and two additional derived forms

Flow visualization for Simulations S216, S228, S230

t*	B/T = 2.6 (S228 - Original Aarsnes hull)	B/T = 3.5 (S230)	B/T = 6 (S216)
0.2	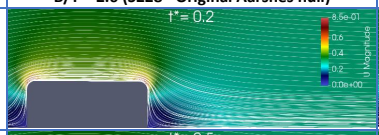	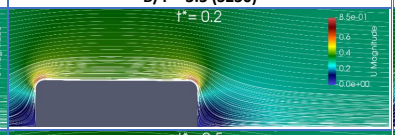	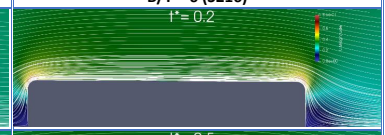
0.5	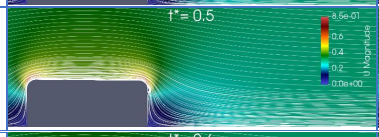	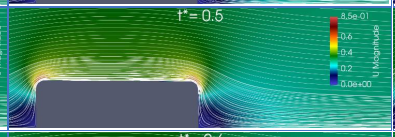	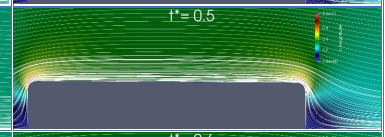
0.6	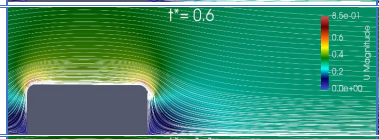	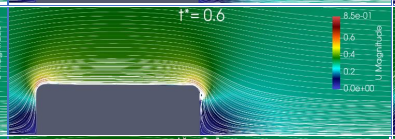	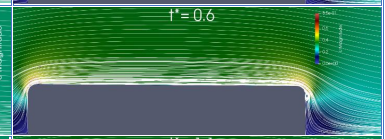
1.1	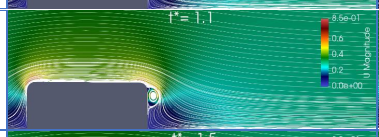	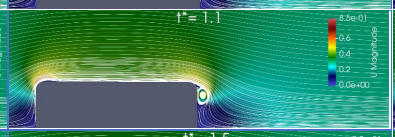	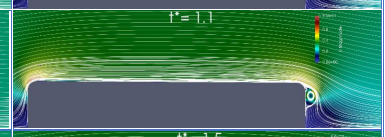
1.5	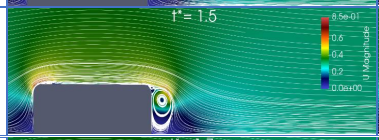	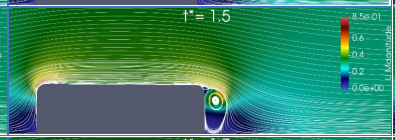	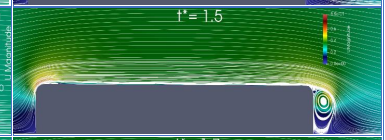
1.7	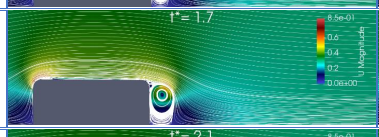	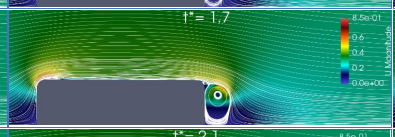	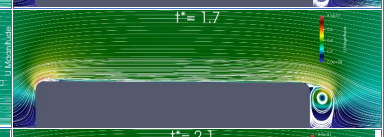
2.1	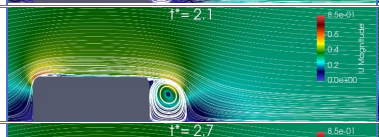	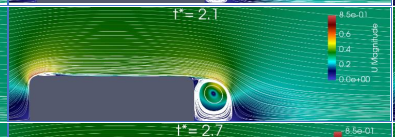	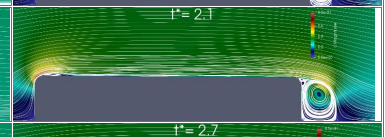
2.7	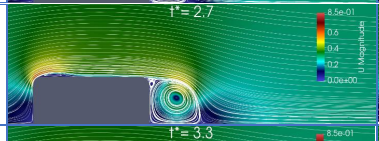	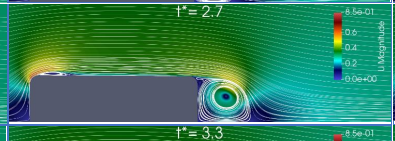	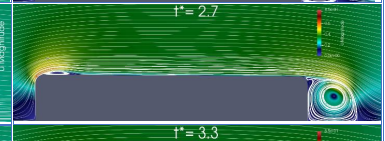
3.3	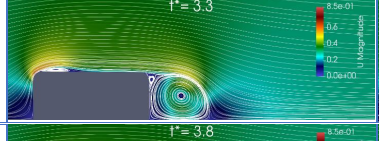	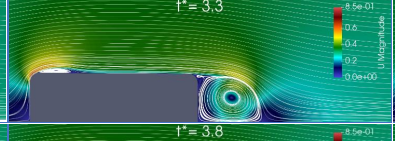	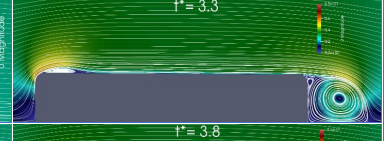
3.8	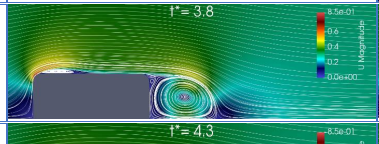	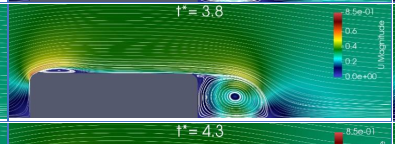	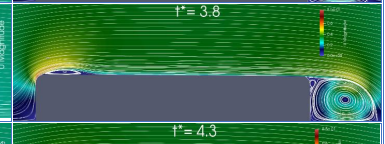
4.3	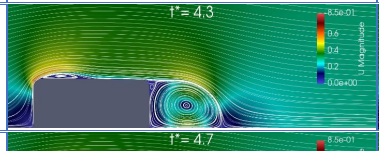	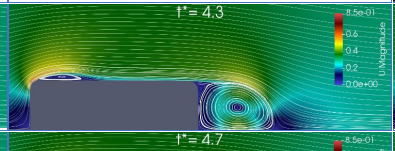	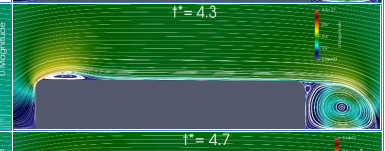
4.7	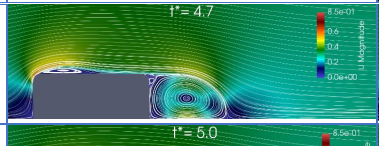	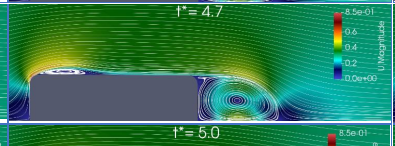	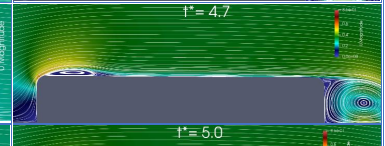
5.0	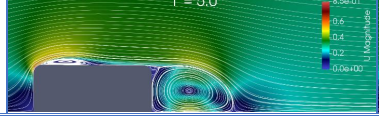	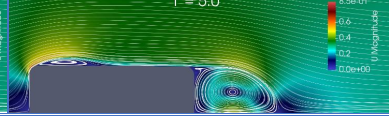	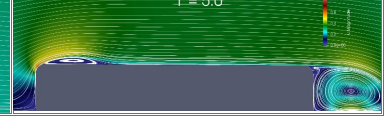

Flow visualization for Simulations S216, S228, S230

t*	B/T = 2.6 (S228 - Original Aarsnes hull)	B/T = 3.5 (S230)	B/T = 6 (S216)
5.2	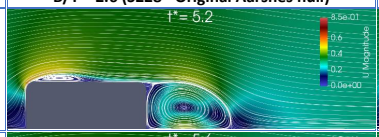	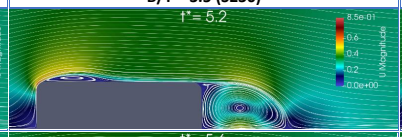	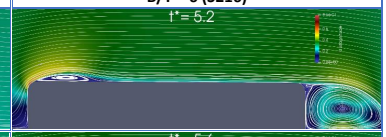
5.6	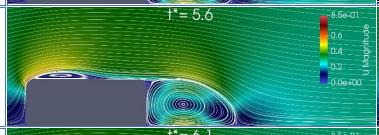	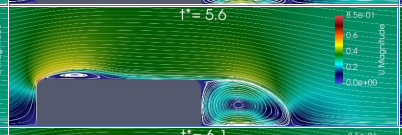	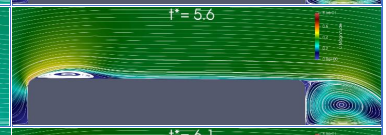
6.1	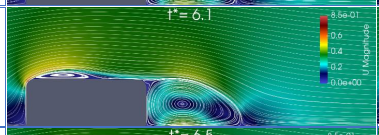	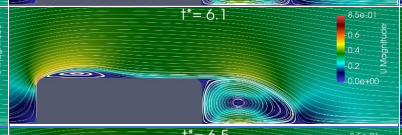	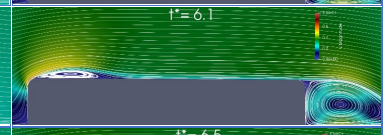
6.5	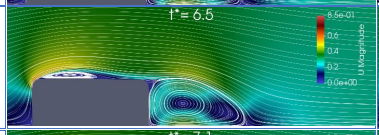	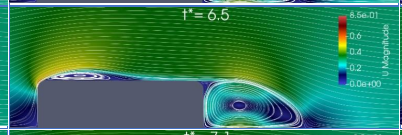	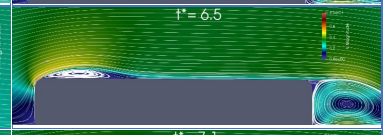
7.1	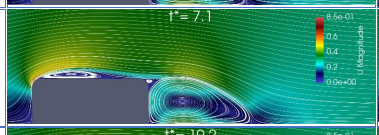	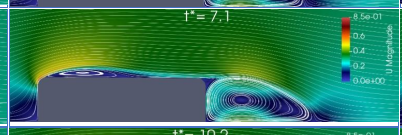	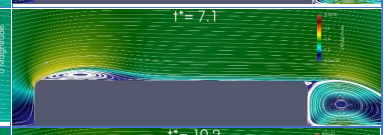
10.2	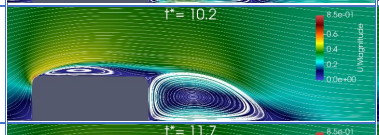	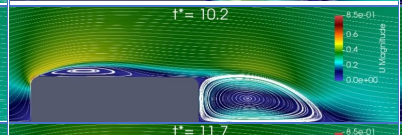	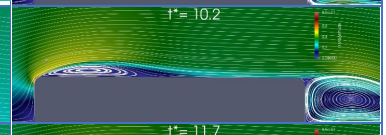
11.7	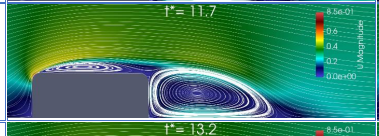	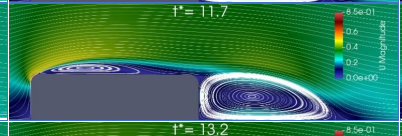	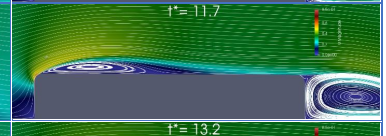
13.2	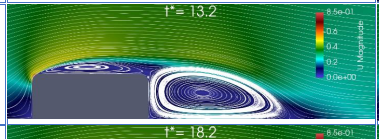	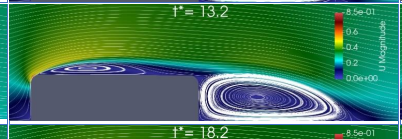	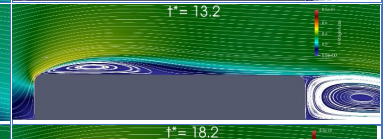
18.2	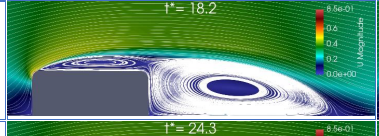	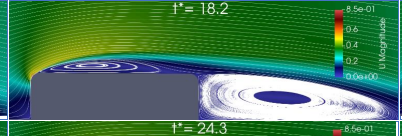	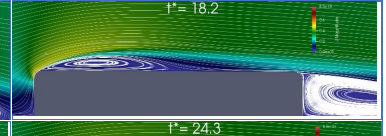
24.3	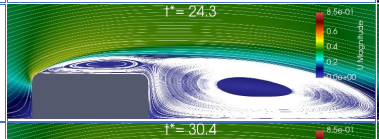	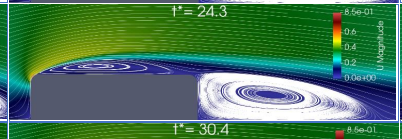	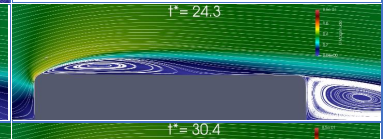
30.4	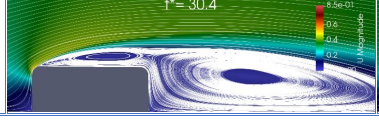	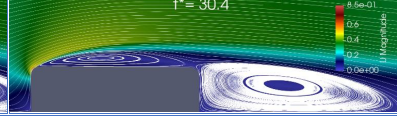	

G.4 Flow around DTC Section 10 with bilge keel (h = 1.6 m) and two additional derived forms

Flow visualization for Simulations S195, S209, S211

t*	B/T = 2.6 (S209)	B/T = 3.5 (S195 - Original DTC Section)	B/T = 6 (S211)
0.5	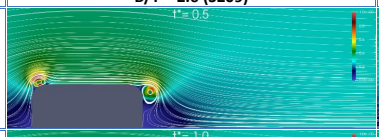	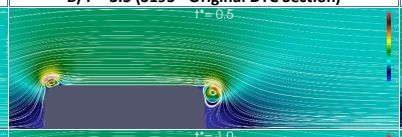	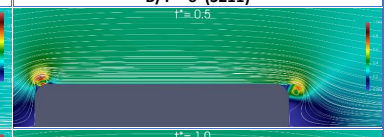
1	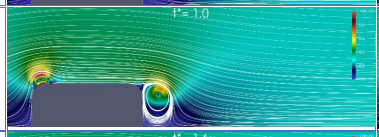	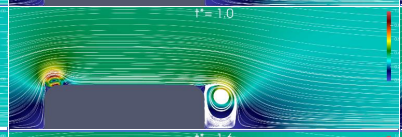	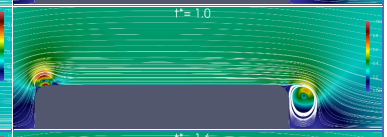
1.6	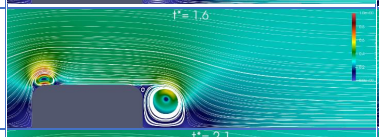	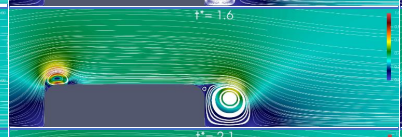	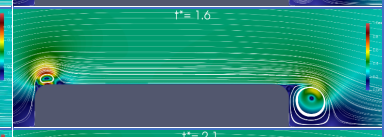
2.1	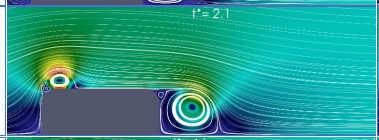	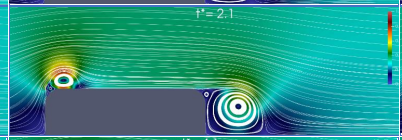	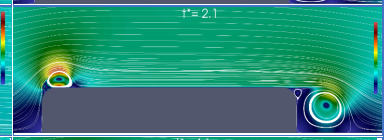
4.1	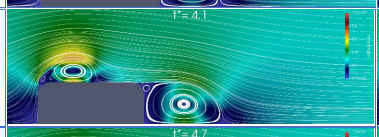	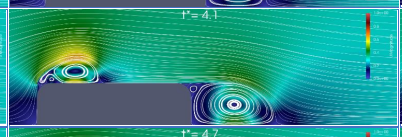	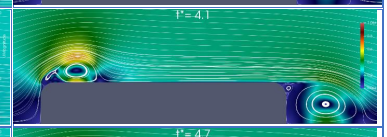
4.7	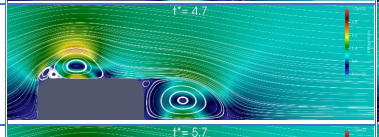	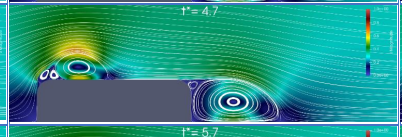	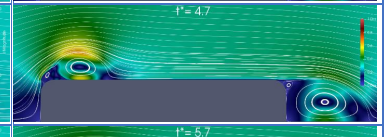
5.7	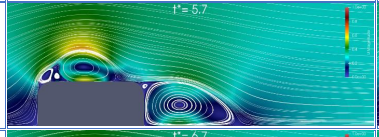	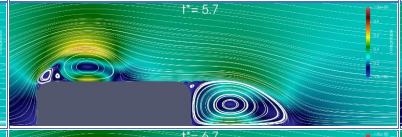	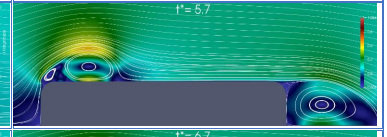
6.7	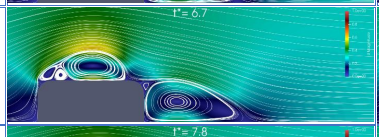	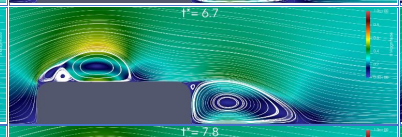	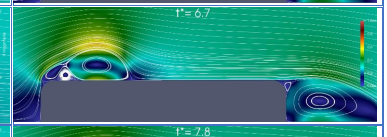
7.8	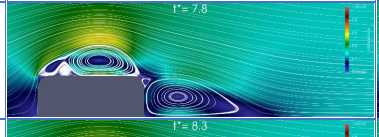	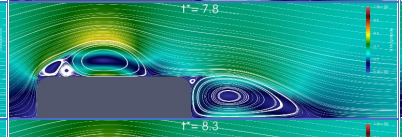	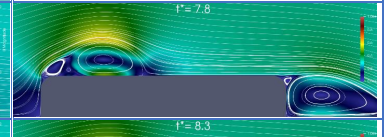
8.3	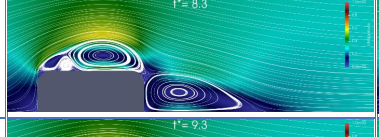	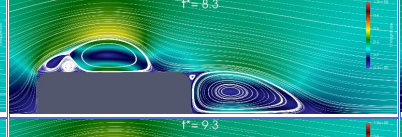	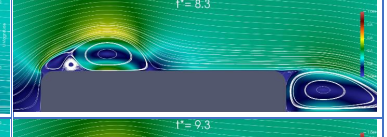
9.3	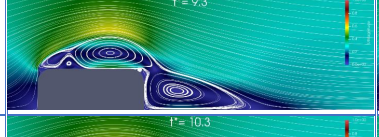	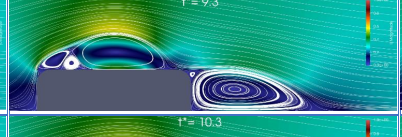	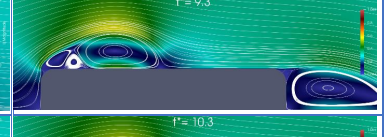
10.3	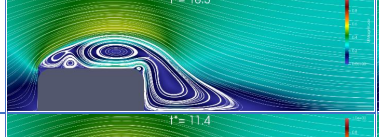	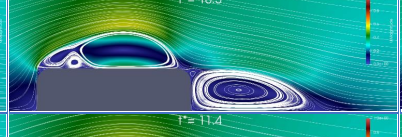	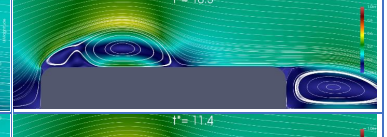
11.4		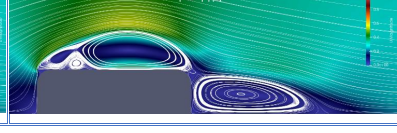	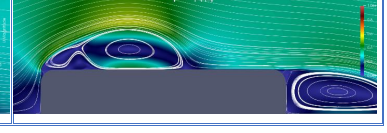

Flow visualization for Simulations S195, S209, S211

T*	B/T = 2.6	B/T = 3.0	B/T = 3.5
12.9	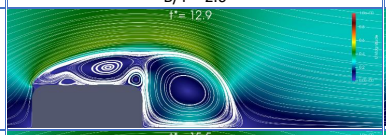	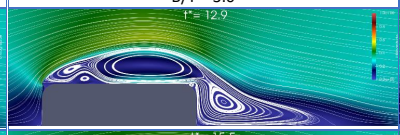	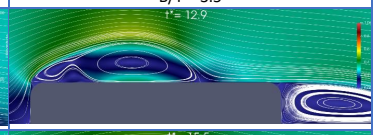
15.5	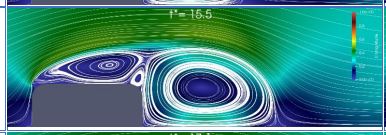	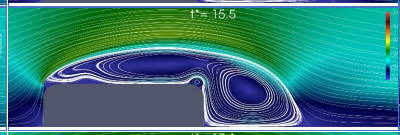	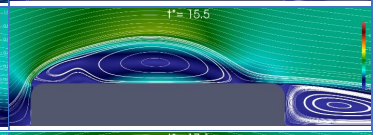
17.1	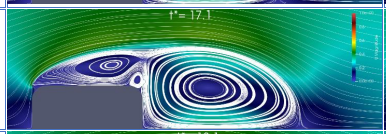	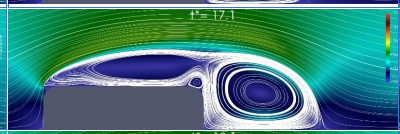	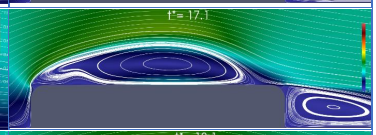
18.1	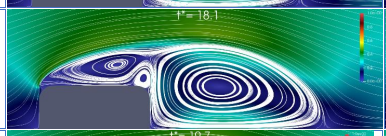	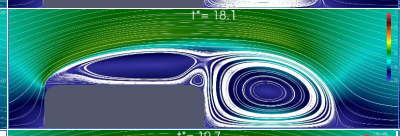	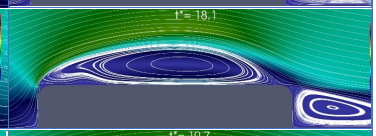
19.7	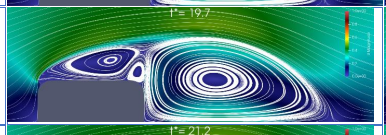	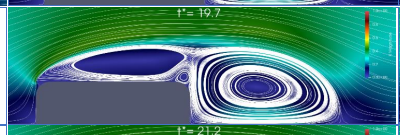	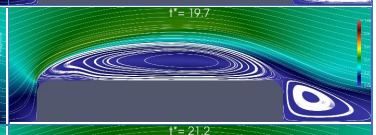
21.2	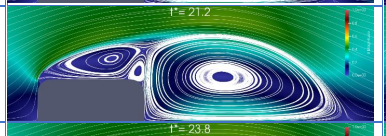	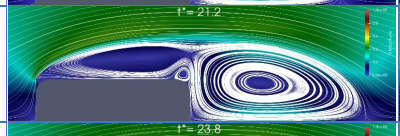	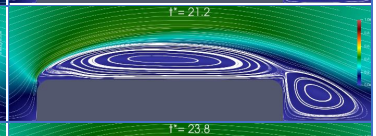
23.8	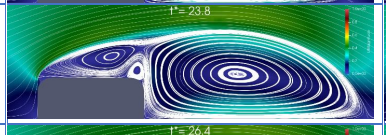	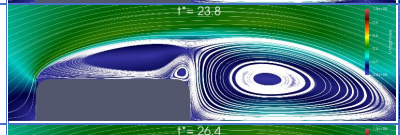	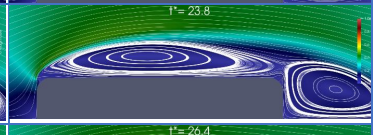
26.4	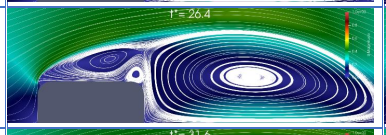	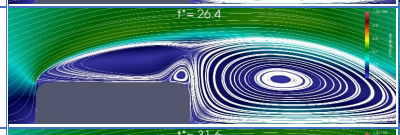	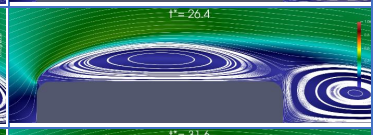
31.6	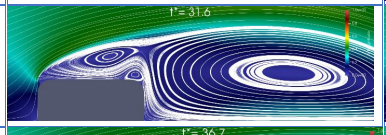	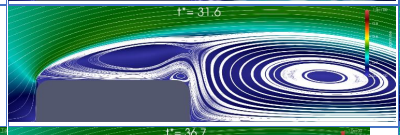	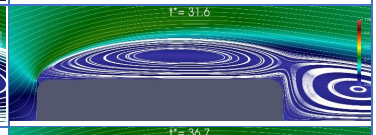
36.7	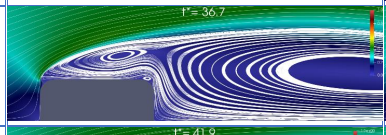	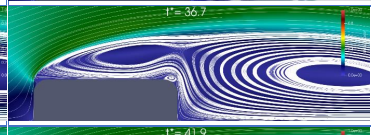	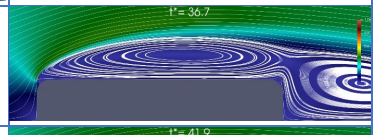
41.9	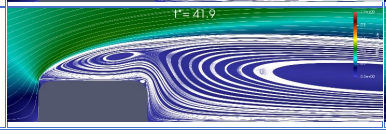	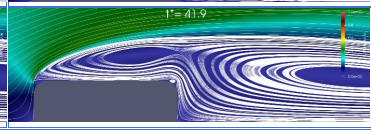	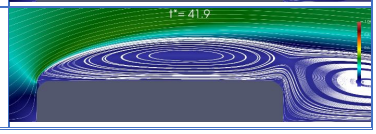

Vishnu Ramachandran Nair Rajasree

Transverse Viscous Loads in Maneuvering

NTNU
Norwegian University of
Science and Technology